INTERNATIONAL CENTER FOR NUMERICAL METHODS IN ENGINEERING

# A Finite Element Formulation for Viscous Incompressible Flows

R. Codina

Monograph CIMNE Nº-16, January 1993

# A Finite Element Formulation for Viscous Incompressible Flows

R. Codina

**Monograph CIMNE Nº-16, January 1993**

**International Center for Numerical Methods in Engineering**
Gran Capitán s/n, 08034 Barcelona, Spain

INTERNACIONAL CENTER FOR NUMERICAL METHODS IN ENGINEERING
Edificio C1, Campus Norte UPC
Gran Capitán s/n
08034 Barcelona, Spain
www.cimne.upc.es

First edition: January 1993

**A FINITE ELEMENT FORMULATION FOR VISCOUS INCOMPRESSIBLE FLOWS**
Monograph CIMNE M16

ISBN: 84-87867-21-9
Depósito legal: B-35886-94

# CONTENTS

***FOREWORD***

*CHAPTER 1*

## PENALTY FINITE ELEMENT METHODS FOR THE STATIONARY NAVIER–STOKES EQUATIONS

*CHAPTER 2*

**TRANSIENT NAVIER-STOKES EQUATIONS: FULLY DISCRETE ALGORITHM AND COMPUTATIONAL ASPECTS**

*CHAPTER 3*

## THERMALLY COUPLED FLOWS AND NONLINEAR MATERIALS

*CHAPTER 4*

**MOULD FILLING SIMULATION**

# FOREWORD

## Introduction and objectives

Although the numerical simulation of flow problems began in the sixties using finite difference or panel methods, it wasn't until the early seventies that the Finite Element Method (FEM) entered the field of computational fluid dynamics (CFD). Since then, a lot of progress has been made, both in the understanding of the difficulties lying on the application of the general finite element ideas and in the development of numerical strategies to overcome them.

This work deals with FEMs to solve viscous incompressible flow problems, an important branch of CFD whose applications are widespread in many areas of engineering and science. Numerical techniques are likely to become a serious competitor to experimentation because of their reliability and their reduced cost, and also because in some areas experiments are very difficult to make. Industries are aware of this fact and the evolution of their numerical budget reflects this interest. Nevertheless, the numerical simulation of complex real-world flow problems for many practical engineering applications lies still far in the future, not only because of the present knowledge on numerical methods but also because of today's computer facilities and capabilities. Flow problems are extremely demanding in what concerns numerical computations and the present computer technology cannot supply all the computational power that would be needed to solve many real flow problems.

All the terms of the incompressible Navier-Stokes equations involve a more or less important numerical difficulty and a lot of questions are still open. Temporal derivatives are usually dealt with using finite differences, in spite of the fact that the solution may develop high and quick variations in time and instability problems or lack of accuracy may be encountered. The incompressibility constraint, closely related to the presence of pressure forces, is another of the most important problems. Doubtless, the nonlinear convective term is the reason why the Navier-Stokes equations are so difficult to solve numerically and to analyse mathematically. Maybe the only 'nice' term is the viscous one, which gives a parabolic character to the transient equations.

The purpose of this work is twofold. First, new numerical methods are developed to treat two of the problems mentioned above, namely, the incompressibility constraint and the instability problems found when the standard Galerkin approach is applied to convection dominated flows. The second objective is to develop a general purpose finite element code, implementing the new techniques presented here and incorporating several computational features also original from this work. This general finite element model includes the numerical solution of the incompressible Navier-Stokes equations together with the energy balance equation and the tracking of free surfaces. Applications to thermally coupled flows and the flow of nonlinear materials are provided.

This work is a corrected version of the last four chapters of the author's doctoral thesis *A finite element model for incompressible flow problems.*

# Notation

The notation employed in this work is fairly standard in the mathematical literature, although perhaps not vey common in engineering circles. As far as possible, the matrix version of the abstract formulation of the problems studied is given, in particular for presenting the basic flow chart of transient and iterative algorithms.

Apart from a few exceptions, matrices and vectors are denoted by boldface characters and scalars by lightface italic characters. Cartesian notation is used when referring to a particular coordinate system, denoting by $(x_1, x_2, x_3)$ or $(x, y, z)$ the Cartesian coordinates for the three-dimensional case.

The space of square integrable functions over a domain $\omega$ of the Euclidian space has been denoted by $L^2(\omega)$, and the inner product in this space by $(\cdot,\cdot)_\omega$. The norm associated to this inner product has been indicated by

$$\|\cdot\|_\omega \equiv \|\cdot\|_{L^2(\omega)} \equiv \|\cdot\|_{0,\omega}$$

The subscript $\omega$ is often dropped if this is the domain where the problem is to be solved, always denoted by $\Omega$.

The Sobolev space of functions whose (distributional) derivatives of order up to $m$ belong to $L^2(\omega)$ has been denoted by $H^m(\omega)$. The space $H^1_0(\omega)$ consists of functions of $H^1(\omega)$ with zero trace on the boundary $\partial\omega$. Any of the symbols

$$\|\cdot\|_{m,\omega} \equiv \|\cdot\|_{H^m(\omega)}$$

has been employed to denote the norm of these spaces, although no subscript at all has been used when no confusion is possible. In general, the norm of a space $V$ has been denoted by $\|\cdot\|_V$ and the Euclidian norm of a vector by $|\cdot|$.

The classical gradient, divergence, curl and Laplacian operators have been denoted by

$$\nabla(\cdot), \quad \nabla\cdot(\cdot), \quad \nabla\times(\cdot) \quad \text{and} \quad \Delta(\cdot),$$

respectively. The symbol $\Delta t$ has been used for the time step size, not for the Laplacian of $t$. For the temporal derivative and for the partial derivative with respect to a Cartesian coordinate $x_i$ any of the symbols

$$\partial_t \equiv \frac{\partial}{\partial t}, \qquad \partial_i \equiv \frac{\partial}{\partial x_i}$$

has been used.

Various integers have been employed in the text. Some of them are

| | |
|---|---|
| $N_{sd}$ : | number of space dimensions |
| $N_{el}$ : | number of elements of the discretization |
| $N_{no}$ : | number of nodes per element |
| $N_{gp}$ : | number of integration points per element |
| $N_{tp}$ : | total number of nodes of the finite element mesh |
| $N_{fp}$ : | number of free points (without Dirichlet conditions) |
| $N_{nv}$ : | number of nodes per element with velocity unknowns |
| $N_{qp}$ : | number of nodes per element with pressure unknowns |
| $N_{vu}$ : | number of velocity unknowns ($= N_{fp} \times N_{sd}$) |
| $N_{pu}$ : | number of pressure unknowns ($= N_{el} \times N_{qp}$) |
| $N$ : | number of time steps |

A generic shape function has been denoted by $N$ (not to be confused with the number of time steps), perhaps with a superscript to indicate the node to which it is associated.

The symbol $\{\Omega^e\}$, $e = 1, ..., N_{el}$, has been used to denote a finite element partition of the domain $\Omega$. It is understood that the subdomains $\Omega^e$ are open, nonoverlapping and the union of their closures is the closure of $\Omega$. A function beloging to the finite element space is recognized by the subscript $h$, the diameter of $\{\Omega^e\}$. Vectors of nodal unknowns are denoted by the boldface capital letter corresponding to the lower case variable.

The rest of the notation is explained in the text.

## Acknowledgements

I would like to take the chance to express my appreciation to many people whose support and stimulation have made this work possible. In particular, I am indebted to Prof. Eugenio Oñate, for encouraging my research in this field. I would like also to thank some of my colleagues and friends for their help: Dr. Miguel Cervera, who collaborated with me in preparing the basic structure of the code written for this work; Uwe Schäfer, who had an important participation in the research presented in the last chapter; Dr. Gabriel Bugeda, who provided the codes for mesh generation; Javier Castro and Prof. Juan Miquel, for fruitful discussions; Knut Eckstein and Orlando Soto, for their assistence in preparing some numerical results; and Mario Galindo, for his continuous help in using computer facilities.

This research has benefited from financial support from the CIRIT (Generalitat de Catalunya), the Universitat Politècnica de Catalunya and a grant FPI from the Spanish Government. Partial support from Project BRITE, Ref. BREU-CT-91-0443, and Programme HERMES, Ref. 08W01581, are also gratefully acknowledged.

# *CHAPTER 1*

# PENALTY FINITE ELEMENT METHODS FOR THE STATIONARY NAVIER–STOKES EQUATIONS

## 1.1 Introduction

The numerical solution of the incompressible Navier-Stokes equations for many practical engineering applications is still far from being a reality. Assuming that the mathematical model represented by these equations is correct, several problems have to be faced, each one represented by different terms of the full system of equations (conservation of momentum and mass balance, i.e., incompressibility condition). Regarding the temporal discretization, the most common way to do it is by far the use of finite difference schemes, with the inconveniences of stability and/or accuracy that arise when high and quick variations in time occur. There is no doubt that the most difficult problem arises because of the nonlinear convective term. Loss of unicity of solution, hydrodynamical instabilities and turbulence are caused by this apparently innocent term. These physical phenomena are obviously reflected in the numerical algorithms and in the mathematical analysis of the problem. High Reynolds number flows are a tough problem from the physical, the mathematical and the numerical standpoints.

Another problem to be considered is the incompressibility constraint, closely related to the presence of the pressure forces. The way to overcome this problem will be the subject of this chapter. The mixed velocity-pressure finite element solution of the incompressible Navier-Stokes equations has several inconveniences due to the zero divergence condition for the velocity field. If the standard Galerkin formulation is used, the first problem to be faced is the use of compatible spaces for the velocity and the pressure, in the sense that they have to satisfy the *inf-sup* or Babuška-Brezzi (BB) stability condition [Ba1], [Ba2], [Br] (see also [BB] for a simple derivation of this condition for the discrete problem). A remedy that is gaining popularity is the use of the Galerkin Least Squares approach introduced by Hughes & Franca [HF], [HFB], [FH], [FHL] (see also [BD]), especially effective when a continuous interpolation for the pressure is used (otherwise, high order velocity interpolation or non-standard assembly algorithms have to be employed [FS]). Recently, quasi-optimal convergence of this method has been proved by Hansbo & Szepessy [HS] for the time dependent Navier-Stokes equations using space-time linear elements. In any case, the formulation depends on an algorithmic parameter whose physical meaning and optimal values are not known yet. This, and the fact that pressures appear as nodal variables (see below) may decide the user in favor of the Galerkin formulation, perhaps with an upwind technique for high Reynolds number flows.

If the Galerkin formulation is used, the matrix of the discrete algebraic system resulting from the finite element discretization has zero diagonal terms. The use of iterative solvers or inefficient renumbering algorithms seems to be the only available remedy for solving this system of equations. However, the penalty approach circumvents this problem and has other interesting features. If the pressure interpolation is discontinuous, one can eliminate the element unknowns of this field in terms of the velocity nodal unknowns. Substitution of the obtained expression in the momentum equation leads to a system whose only degrees of freedom are velocities. The reduction of the number of nodal unknowns and the fact that the method is known to work well, have made the penalty method very popular, especially in the engineering literature (see, e.g., References [CK1], [CK2], [ESG], [HLB], [Od], [OKS]). Perhaps the only drawback of this approach is the ill-conditioning of the stiffness matrix when the penalty parameter is very small. A lower bound is determined basically by the computer and the arithmetic precision used in the calculation.

There are basicaly two ways to penalize the incompressibility constraint: to start with the penalized differential equation or to wait until the weak form has been established. Both approaches do coincide for the continuous problem. However, when the finite element discretization is carried out the former automatically yields the pressure space as a consequence of the choice of the velocity interpolation. The resulting velocity-pressure pair will be in general unstable, in the sense that the BB condition will be violated. Hereafter, we will refer to this approach as *strong penalization*, whereas the use of the penalty method for the weak incompressibility equation (continuous or discrete) will be referred to as *weak penalization.* A discussion of the way a particular finite element can be implemented using strong penalization is the subject of Section 1.3.

The objective of Section 1.4 is to present and analyse an iterative weak penalty finite element method for the stationary Stokes and Navier-Stokes equations. The goal is the convergence of the iterates to the true incompressible solution. The main advantage of this approach is that larger penalty parameters can be used, thus alleviating the ill-conditioning mentioned above. The basic idea is solving the penalized equations in each iteration but adding a right-hand-side term that is basically the residual of the incompressibility equation of the previous iterate. For the Stokes equations, this approach is the only reason for an iterative scheme to be used and the conditions under which convergence is achieved are only determined by the iterative penalization. However, the Navier-Stokes equations must be solved iteratively. The question that naturally arises is whether the iterative scheme employed can be coupled with the iterative penalization or not. We prove that, under not very restrictive conditions, the answer is yes. The exposition of this section is organized as follows. The Stokes problem is considered in Section 1.4.1, where the idea of the iterative penalization is described in detail. Section 1.4.2 deals with the Navier-Stokes equations when the Picard (or successive substitution) algorithm is used for the nonlinear term and Section 1.4.3 when the Newton-Raphson scheme is employed. The uncoupling of the nonlinear and penalization iterative loops is then studied.

In this chapter the choice of the finite element spaces will not be the main interest and it is postponed until Chapter 2. Only when necessary we will refer to the stability of a certain finite element under consideration. As usual, whenever a certain element satifies the BB stability condition for the restriction arising form the zero divergence constraint, we will call it *div-stable* [BN1]. The possibility of by-passing this requirement by using an exactly divergence free finite element basis for the velocity field [GP], [RT] will not be considered in this work. The main reason is that although this formulation seems to be feasible for two-dimensional flows, the construction of velocity bases in three-dimensional problems happens to be complicated. The use of formulations other than the conforming velocity-pressure will not be treated either. Background for these methods and for the techniques to be used in this chapter can be found in References [BFo], [CO1], [CO2], [CSS], [GR], [Gu], [OC], [Pi], among other standard text books.

## 1.2 Statement of the problem and penalty methods

### 1.2.1 The continuous problem

Let $\Omega$ be an open bounded domain of $\mathbb{R}^{N_{sd}}$ ($N_{sd} = 2$ or 3) and $\Gamma = \partial\Omega$ its boundary, assumed to be locally Lipschitz. The Navier-Stokes problem for an incompressible fluid moving in $\Omega$ with, for simplicity, homogeneous boundary conditions, consists in finding a velocity field $\mathbf{u}$ and a pressure $p$ such that

$$\begin{aligned} \rho(\mathbf{u}\cdot\nabla)\mathbf{u} - \mu\Delta\mathbf{u} + \nabla p = \rho\mathbf{f} \qquad & \text{in } \Omega \\ \nabla\cdot\mathbf{u} = 0 \qquad & \text{in } \Omega \\ \mathbf{u} = \mathbf{0} \qquad & \text{on } \Gamma \end{aligned} \tag{1.1}$$

where $\mathbf{f}$ is a given body force, $\rho$ is the density of the fluid and $\mu$ is its dynamical viscosity. In order to write the weak form of problem (1.1) we introduce the spaces

$$V = H_0^1(\Omega)^{N_{sd}}, \qquad Q = L^2(\Omega) \tag{1.2}$$

and the multilinear forms

$$\begin{aligned} a(\mathbf{u},\mathbf{v}) &= \mu\int_\Omega \nabla\mathbf{u} : \nabla\mathbf{v}\, d\Omega, \\ b(q,\mathbf{v}) &= \int_\Omega q\nabla\cdot\mathbf{v}\, d\Omega, \\ c(\mathbf{u},\mathbf{v},\mathbf{w}) &= \rho\int_\Omega [(\mathbf{u}\cdot\nabla)\mathbf{v}]\cdot\mathbf{w}\, d\Omega, \\ l(\mathbf{v}) &= \rho < \mathbf{f},\mathbf{v} > \end{aligned} \tag{1.3}$$

defined on $V\times V, Q\times V, V\times V\times V$ and $V$ respectively. The symbol $<\cdot,\cdot>$ denotes the duality paring between $V$ and its topological dual $V'$ $(= H^{-1}(\Omega)^{N_{sd}})$. If the viscous term in (1.1) is written as $-\nabla\cdot(2\mu\varepsilon(\mathbf{u}))$, where $\varepsilon(\mathbf{u})$ is the symmetric part of $\nabla\mathbf{u}$, the bilinear form $a$ to be considered is

$$a(\mathbf{u},\mathbf{v}) = 2\mu\int_\Omega \varepsilon(\mathbf{u}) : \varepsilon(\mathbf{v})\, d\Omega \tag{1.4}$$

instead of that appearing in (1.3). Continuity of $a$, $b$ and $l$ is obvious. Continuity of $c$ follows from Sobolev's imbedding Theorem (if $\mathbf{u}$ and $\mathbf{v} \in V$ then $\mathbf{u}$ and $\mathbf{v} \in L^4(\Omega)^{N_{sd}}$ for $N_{sd} = 2, 3$) and from Hölder's inequality (if $u_j, v_k \in L^4(\Omega)$, then $u_j v_k \in L^2(\Omega)$, $u_j$

and $v_k$ being the components of $\mathbf{u}$ and $\mathbf{v}$). See, e.g. References [GR], [Te] for details. Since $a$, $c$ and $l$ are continuous, we can define their 'norms' by

$$\begin{aligned} N_a &= \sup \frac{a(\mathbf{v}_1, \mathbf{v}_2)}{\|\mathbf{v}_1\|_V \|\mathbf{v}_2\|_V} \\ N_c &= \sup \frac{c(\mathbf{v}_1, \mathbf{v}_2, \mathbf{v}_3)}{\|\mathbf{v}_1\|_V \|\mathbf{v}_2\|_V \|\mathbf{v}_3\|_V} \\ N_l &= \sup \frac{l(\mathbf{v}_1)}{\|\mathbf{v}_1\|_V} \end{aligned} \tag{1.5}$$

where the supremum is taken over all the $\mathbf{v}_1, \mathbf{v}_2, \mathbf{v}_3 \in V - \{0\}$ and $\|\cdot\|_V$ denotes the usual norm in $V$. We will use the symbol $\|\cdot\|_Q$ for the norm in $Q$ and $(\cdot,\cdot)$ for the inner product in the space $Q$. When no ambiguity be possible, we shall omit the subscripts in the norms.

Define the space

$$Z = \{q \in Q \mid b(q, \mathbf{v}) = 0 \quad \forall \mathbf{v} \in V\} \tag{1.6}$$

For $b$ given by (1.3), $Z = \mathbb{R}$. In the quotient space $Q/Z$ the following norm is defined

$$\|q\|_{Q/Z} = \inf_{z \in Z} \|q + z\|_Q \tag{1.7}$$

Having introduced all this notation, the weak form of problem (1.1) can be written as follows: Find $\mathbf{u} \in V$ and $p \in Q/Z$ such that

$$\begin{aligned} c(\mathbf{u}, \mathbf{u}, \mathbf{v}) + a(\mathbf{u}, \mathbf{v}) - b(p, \mathbf{v}) = l(\mathbf{v}) &\qquad \forall \mathbf{v} \in V \\ b(q, \mathbf{u}) = 0 &\qquad \forall q \in Q \end{aligned} \tag{1.8}$$

Besides the continuity of all the forms involved in (1.8), we will assume that the bilinear form $a$ is coercive and that $b$ satisfies the BB condition, i.e., there exist positive constants $K_a$ and $K_b$ such that

$$a(\mathbf{v}, \mathbf{v}) \geq K_a \|\mathbf{v}\|_V^2 \qquad \forall \mathbf{v} \in V \tag{1.9}$$

$$\sup_{\mathbf{v}} \frac{b(q, \mathbf{v})}{\|\mathbf{v}\|_V} \geq K_b \|q\|_{Q/Z} \qquad \mathbf{v} \in V - \{0\}, \forall q \in Q \tag{1.10}$$

Condition (1.9) follows from Poincaré-Friedrics inequality if $a$ is given by (1.3) and from Korn's inequality if it is given by (1.4). Condition (1.10) holds for $V$ and $Q$ given by (1.2) [La].

For the trilinear form $c$ it will be assumed that

$$c(\mathbf{u}, \mathbf{v}, \mathbf{v}) = 0 \qquad \forall \mathbf{v} \in V \tag{1.11}$$

If $\mathbf{u}$ is the solution of problem (1.8), it is easy to see that condition (1.11) is satisfied. However, we will be interested in velocity fields that do not exactly satisfy the incompressibility condition. In this case, instead of the form $c$ given in (1.3), its skew-symmetrized form will be used:

$$c_\sigma(\mathbf{u}, \mathbf{v}, \mathbf{w}) = c(\mathbf{u}, \mathbf{v}, \mathbf{w}) + \frac{1}{2}\rho \int_\Omega (\nabla \cdot \mathbf{u}) \mathbf{v} \cdot \mathbf{w} d\Omega$$

It can be easily checked that $c_\sigma(\mathbf{u},\mathbf{v},\mathbf{v}) = 0$ and that $c_\sigma(\mathbf{u},\mathbf{v},\mathbf{w}) = c(\mathbf{u},\mathbf{v},\mathbf{w})$ if $\mathbf{u}$ is the solution of problem (1.8). Continuity of $c_\sigma$ can be proved as for $c$. Thus, $c_\sigma$ can be used instead of $c$ in (1.8) and condition (1.11) will hold. In any case subscript $\sigma$ will be omitted.

Finally, we will assume that

$$\chi := \frac{N_c N_l}{K_a^2} < 1 \tag{1.12}$$

Under all these conditions, existence and uniqueness of solution of (1.8) can be proved [GR].

In what follows, the spaces $V$ and $Q$ will be those given by (1.2) or finite dimensional subspaces $V_h$ and $Q_h$ arising from the finite element discretization of $\Omega$ (internal approximation). Conditions (1.9), (1.11) and (1.12) will be automatically satisfied if $V$ and $Q$ are replaced by $V_h$ and $Q_h$. However, (1.10) has to be explicitly required for each pair of finite element spaces $V_h, Q_h$.

The condition $\chi < 1$ is certainly restrictive. It ensures uniqueness of weak solutions. However, such unicity is not likely to hold for high Reynolds numbers and in fact examples are known for which it is not true [Te]. In these cases, a more careful analysis has to be done. Fortunately, solutions of the Navier-Stokes happen to be isolated in most of the cases. For a detailed analysis of the approximation of this type of problems, the reader is referred to [BR1–3]. See also [GR].

Concerning the no-slip boundary condition in problem (1.1), the extension to the non-homogeneous condition $\mathbf{u} = \mathbf{g}$ on $\Gamma$ is straightforward and only requires some technicalities [GR]. However, the situation is somehow more involved when the traction is prescribed on a part of the boundary. An analysis of the Galerkin finite element approximation in this case can be found in [Ve2].

### 1.2.2 Penalty methods for the Stokes problem

In this chapter, we will deal with a class of penalty methods that will be briefly described here. In order to introduce the problem, it is enough to consider the Stokes equations, i.e., Eqns. (1.1) without the convective term $\rho(\mathbf{u}\cdot\nabla)\mathbf{u}$ or its weak form (1.8) with $c = 0$. In this case, Eqns. (1.1) are the optimality conditions for the minimization problem of finding $\mathbf{u} \in V$ such that $\nabla \cdot \mathbf{u} = 0$ and

$$\mathcal{L}_0(\mathbf{u}) = \inf_{\mathbf{v}} \mathcal{L}_0(\mathbf{v}) \qquad \text{over} \quad \{\mathbf{v} \in V \mid \nabla \cdot \mathbf{v} = 0\} \tag{1.13}$$

$$\mathcal{L}_0(\mathbf{v}) := \frac{1}{2} a(\mathbf{v},\mathbf{v}) - l(\mathbf{v}) \tag{1.14}$$

Introducing the Lagrangian multiplier $p$ to account for the constraint $\nabla \cdot \mathbf{u} = 0$ we are led to the following saddle point problem: Find $\mathbf{u} \in V$ and $p \in Q/Z$ such that

$$\mathcal{L}_p(\mathbf{u},p) = \inf_{\mathbf{v}\in V} \sup_{q\in Q} \mathcal{L}_p(\mathbf{v},q) \tag{1.15}$$

$$\mathcal{L}_p(\mathbf{v},q) := \frac{1}{2} a(\mathbf{v},\mathbf{v}) - l(\mathbf{v}) - b(q,\mathbf{v}) \tag{1.16}$$

Now we can consider standard techniques from optimization theory. The first is the penalty method, consisting in adding to the functional $\mathcal{L}_0$ defined by (1.14) a positive definite bilinear form evaluated on the constraint and multiplied by a large number. If, for example, we consider the $L^2$ inner product as the bilinear form and pick a small number $\epsilon > 0$, we are led to the penalized problem: Find $\mathbf{u}^\epsilon \in V$ such that

$$\mathcal{L}_{0,\epsilon}(\mathbf{u}^\epsilon) = \inf_{\mathbf{v}\in V} \mathcal{L}_{0,\epsilon}(\mathbf{v}) \tag{1.17}$$

$$\mathcal{L}_{0,\epsilon} := \frac{1}{2}a(\mathbf{v},\mathbf{v}) - l(\mathbf{v}) + \frac{1}{2\epsilon}(\nabla\cdot\mathbf{v},\nabla\cdot\mathbf{v}) \tag{1.18}$$

Finally, we could also perturb the functional $\mathcal{L}_p$ given by (1.16) in order to obtain the regularized problem: Find $\mathbf{u}^\epsilon \in V$ and $p^\epsilon \in Q_0$ such that

$$\mathcal{L}_{p,\epsilon}(\mathbf{u}^\epsilon, p^\epsilon) = \inf_{\mathbf{v}\in V}\sup_{q\in Q} \mathcal{L}_{p,\epsilon}(\mathbf{v}, q) \tag{1.19}$$

$$\mathcal{L}_{p,\epsilon}(\mathbf{v}, q) := \frac{1}{2}a(\mathbf{v},\mathbf{v}) - l(\mathbf{v}) - b(q,\mathbf{v}) - \frac{1}{2}\epsilon(q,q) \tag{1.20}$$

where we have introduced the space

$$Q_0 := \{q \in Q \mid \int_\Omega q\; d\Omega = 0\} \tag{1.21}$$

that is isomorphic to $Q/Z$ for $b$ given in (1.3). The reason for this choice of the pressure space will be clear immediately.

The Euler-Lagrange equations for the variational problem (1.17) are

$$a(\mathbf{u}^\epsilon,\mathbf{v}) + \frac{1}{\epsilon}(\nabla\cdot\mathbf{u}^\epsilon,\nabla\cdot\mathbf{v}) = l(\mathbf{v}) \qquad \forall\mathbf{v}\in V \tag{1.22}$$

whereas for problem (1.19) the optimality conditions are

$$a(\mathbf{u}^\epsilon,\mathbf{v}) - b(p^\epsilon,\mathbf{v}) = l(\mathbf{v}) \qquad \forall\mathbf{v}\in V \tag{1.23}$$

$$\epsilon(p^\epsilon, q) + b(q,\mathbf{u}^\epsilon) = 0 \qquad \forall q\in Q \tag{1.24}$$

If we take $q \equiv const.$ in (1.24) we see that

$$\epsilon\int_\Omega p^\epsilon\; d\Omega + \int_\Gamma \mathbf{n}\cdot\mathbf{u}^\epsilon\; d\Gamma = 0,$$

where $\mathbf{n}$ is the unit outward normal to $\Gamma$. Since $\mathbf{u}^\epsilon = \mathbf{0}$ on $\Gamma$, it follows that $\int_\Omega p^\epsilon\; d\Omega = 0$, i.e., $Q_0$ is the right space where $p^\epsilon$ is to be sought. For non-homogeneous boundary conditions $\mathbf{u} = \mathbf{g}$ on $\Gamma$, the given function g must satisfy the compatibility condition $\int_\Gamma \mathbf{n}\cdot\mathbf{g}\; d\Gamma = 0$ and hence $\int_\Omega p^\epsilon\; d\Omega = 0$ still holds true. Pressures that are solution of (1.1) or (1.8) are determined up to an additive constant that can be fixed seeking $p$ either in $Q_0$ or in $Q/Z$. From now onwards, the former choice will be employed since penalized solutions automatically belong to $Q_0$.

It is clear that Eqn. (1.24) implies

$$\epsilon p^\epsilon + \nabla\cdot\mathbf{u}^\epsilon = 0 \qquad \text{in the space } \; Q \tag{1.25}$$

Since for $\mathbf{u}^\epsilon \in V = H_0^1(\Omega)^{N_{sd}}$ it is $\nabla\cdot\mathbf{u}^\epsilon \in Q = L^2(\Omega)$, Eqn. (1.25) can be understood in the classical sense. Inserting the pressure $p^\epsilon$ obtained from (1.25) in terms of $\mathbf{u}^\epsilon$ into Eqn. (1.23) we recover problem (1.22). Therefore, we can state the following important fact: *for the continuous case, the penalized and the perturbed variational problems are equivalent.* The crucial point is to observe that the divergence of the velocity field belongs to the pressure space. This *will not* be true for the discrete problem and the equivalence just mentioned will cease to be valid.

The reason why we have introduced first the Stokes problem is to highlight the connexion between classical optimization techniques and the penalty methods we will consider. The Navier-Stokes equations *are not* the Euler-Lagrange equations of a functional to be minimized but nevertheless we can still consider the analogues of (1.22) and (1.23)-(1.24) with $\epsilon \neq 0$. The former problem will be the weak form of the partial differential equation

$$\rho(\mathbf{u}^\epsilon \cdot \nabla)\mathbf{u}^\epsilon - \mu\Delta\mathbf{u}^\epsilon - \frac{1}{\epsilon}\nabla(\nabla \cdot \mathbf{u}^\epsilon) = \rho\mathbf{f} \tag{1.26}$$

that is obtained by replacing the pressure $p$ in (1.1) by the expression found from the pseudo-constitutive relation

$$p^\epsilon = -\frac{1}{\epsilon}\nabla \cdot \mathbf{u}^\epsilon. \tag{1.27}$$

If the linear Elasticity problem is considered, $1/\epsilon$ has the physical meaning of being the Lamé parameter of a slightly compressible material. For a discussion about the physical meaning of several penalty methods, see Reference [HD].

Since in (1.26) the *differential equation* has been penalized, we will call this approach *strong penalization.* On the other hand, it is observed from (1.24) that the *weak form* of the incompressibility constraint has been replaced by a penalized equation. This method will be referred to as *weak penalization.* It must be stressed that both approaches are equivalent for the continuous case and that for the Stokes problem the strong penalization corresponds to the minimization of the classical penalized functional (1.18) and the weak penalization comes from seeking the saddle point of the perturbed Lagrangian (1.20).

Whichever of the two approaches just described is used, the key for proving the convergence of $\mathbf{u}^\epsilon$ and of $p^\epsilon$ to the solution $\mathbf{u}$ and $p$ of problem (1.8) as $\epsilon \to 0$ is the BB condition (1.10) (see, e.g. [Be], [BFo], [CSS], [GR], [OKS]), that in turn happens to be the key condition, together with the coercivity of $a$ (condition (1.9)), for proving existence and uniqueness of solution for this problem (1.8).

### 1.2.3 Finite element discretization

*The discrete problem*

Let $\{\Omega^e\}$ be a regular finite element partition of the domain $\Omega$, with index $e$ ranging from 1 to the number of elements $N_{el}$. For simplicity, we shall assume that $\Omega$ is a polyhedral domain. The diameter of $\{\Omega^e\}$ will be denoted by $h$, as usual.

Let now $V_h \subset V$ and $Q_h \subset Q$ be conforming finite element spaces associated to the partition $\{\Omega^e\}$. Define also

$$Z_h := \{q_h \in Q_h \mid b(q_h, \mathbf{v}_h) = 0 \qquad \forall \mathbf{v}_h \in V_h\} \tag{1.28}$$

$$Q_{0,h} := \{q_h \in Q_h \mid \int_\Omega q_h \, d\Omega = 0\} \tag{1.29}$$

Let us consider first the Stokes problem. The discrete version of (1.8) with $c = 0$ is: Find $\mathbf{u}_h \in V_h$ and $p_h \in Q_h/Z_h$ such that

$$\begin{aligned} a(\mathbf{u}_h, \mathbf{v}_h) - b(p_h, \mathbf{v}_h) &= l(\mathbf{v}_h) \qquad \forall \mathbf{v}_h \in V_h \\ b(q_h, \mathbf{u}_h) &= 0 \qquad \forall q_h \in Q_h \end{aligned} \tag{1.30}$$

The weak penalty method applied to (1.30) will read: Find $\mathbf{u}_h^\epsilon \in V_h$ and $p_h^\epsilon \in Q_{0,h}$ such that

$$\begin{aligned} a(\mathbf{u}_h^\epsilon, \mathbf{v}_h) - b(p_h^\epsilon, \mathbf{v}_h) &= l(\mathbf{v}_h) \qquad \forall \mathbf{v}_h \in V_h \\ \epsilon(p_h^\epsilon, q_h) + b(q_h, \mathbf{u}_h^\epsilon) &= 0 \qquad \forall q_h \in Q_h \end{aligned} \tag{1.31}$$

Convergence in norm of $\mathbf{u}_h^\epsilon$ to $\mathbf{u}_h$ and of $p_h^\epsilon$ to $p_h$ as $\epsilon \to 0$ is a well known result [CSS], [GR], [OKS].

The first question to be answered is whether the space $Q_{0,h}$ is isomorphic to $Q_h/Z_h$ or not. Clearly, this requires that $\dim Z_h = 1$, which is not always the case and depends on the choice of the spaces $V_h$ and $Q_h$. In Reference [JP] it is proved that this condition is also sufficient to assert that $Q_{0,h} \cong Q_h/Z_h$.

*Some finite element spaces*

There are several popular elements for which it is known that $\dim Z_h > 1$. Loosely speaking, this means that there are pressures whose discrete gradient is zero, appart from the constants. The most well known element that exhibits this pathology is the $Q_1/P_0$ pair, constructed using a bilinear continuous velocity interpolation (in 2D) and piecewise constant pressures. For this element it is known that when $\Omega$ is a square (in 2D) discretized with an even number of uniform elements along each direction, $\dim Z_h = 2$, the space $Z_h$ consisting of constants and the so called 'checkboard mode'. There is a vast literature on this controversial element, apparently first used by Hughes & Allik [HA] (cf. [BFo]). See, for example, References [BN2], [CK1], [JP], [OKS], [SG1–2], among many others. Another problem encountered when this element is used is the satisfaction of the BB condition. It is known that the discrete analogue of (1.10), namely,

$$\sup_{\mathbf{v}_h} \frac{b(q_h, \mathbf{v}_h)}{\|\mathbf{v}_h\|_V} \geq K_b \|q_h\|_{Q_h/Z_h} \qquad \mathbf{v}_h \in V_h - \{0\},\ \forall q_h \in Q_h \tag{1.32}$$

is satisfied but with $K_b = O(h)$, $h$ being the diameter of the uniform mesh [CK1], [OJ1], [JP]. It is believed that this element yields stable velocity approximations on general distorted meshes, but this fact still resists analysis. Moreover, this element can be stabilized either by using macroelements composed of this element [TR], by redefining the pressure space [KOS], [OKS] or by using iterative stabilization techniques [FB]. The reader is referred to the book of Brezzi & Fortin [BFo] (Section VI.5.4) for a clarifying discussion.

Another popular element is the $Q_2/Q_1$ pair (continuous biquadratic velocities, discontinuous piecewise bilinear pressures, in 2D). Again, it is found that $\dim Z_h = 2$ and that the constant $K_b$ in (1.32) is proportional to $h$ [CK1], [OJ1].

Perhaps the quadrilateral two-dimensional element that enjoys most popularity at the present time is the $Q_2/P_1$ pair (continuous biquadratic velocities, discontinuous piecewise linear pressures), first proposed in Reference [NPR] and known to yield very good results for incompressible flow problems [Fo2], [FF]. This element satisfies the BB condition (i.e., (1.32) with $K_b$ independent of $h$) and $\dim Z_h = 1$, showing that no spurious pressure modes are possible. See, e.g. [GR] for a rigorous analysis of its stability. A related element is the $Q_2^-/P_1$, where now a serendipid interpolation for the velocity is used. Unfortunately, this element happens to be unstable, with $\dim Z_h = 3$ and $K_b = O(h)$ [OJ1], [OJ2]. A div-stable element is obtained if the pressure is taken as piecewise constant ($Q_2^-/P_0$ element) [GR]. Box 1.1 summarizes the properties of the elements discussed so far (recall that $\dim Z_h$ refers to the case of a square discretized using a uniform mesh). See Chapter 2 for a schematic of the elements.

**Box 1.1 Stability of some quadrilateral elements**

| Element | $\dim Z_h$ | $K_b$ |
|---|---|---|
| $Q_1/P_0$ | 2 | $O(h)$ |
| $Q_2^-/P_0$ | 1 | $O(1)$ |
| $Q_2^-/P_1$ | 3 | $O(h)$ |
| $Q_2/P_0$ | 1 | $O(1)$ |
| $Q_2/P_1$ | 1 | $O(1)$ |
| $Q_2/Q_1$ | 2 | $O(h)$ |

Concerning the rate of convergence when the BB condition is satisfied, it can be expressed in the norm of $V \times Q$, i.e.,

$$\|(\mathbf{u}-\mathbf{u}_h, p-p_h)\|_{V\times Q} := \|\mathbf{u}-\mathbf{u}_h\|_V + \|p-p_h\|_Q \tag{1.33}$$

where $(\mathbf{u}, p)$ is the solution of the continuous problem and $(\mathbf{u}_h, p_h)$ the solution of (1.30). From Brezzi's result [Br], an estimate for (1.33) reduces to an estimate for the interpolation error, since

$$\|(\mathbf{u}-\mathbf{u}_h, p-p_h)\|_{V\times Q} \leq C\left(\inf_{\mathbf{v}_h\in V_h}\|\mathbf{u}-\mathbf{v}_h\|_V + \inf_{q_h\in Q_h}\|p-q_h\|_Q\right) \tag{1.34}$$

Once this is found, an estimate for the velocity in the $L^2$ norm is easily obtained through the classical Aubin-Nitsche duality argument [Br], [BFo], [Ci], [OC]. The elements $Q_2^-/P_0$ and $Q_2/P_0$ yield a suboptimal rate of convergence for the velocity in the $L^2$ norm, that is $O(h^2)$. This is due to the poor pressure approximation, which controls the error in the $V \times Q$ norm. On the other hand, the $Q_2/P_1$ yields optimal rates of convergence, namely, $\|\mathbf{u}-\mathbf{u}_h\|_0 = O(h^3)$ and $\|p-p_h\|_0 = O(h^2)$.

We postpone until Chapter 2 a more detailed discussion on available finite element interpolations and convergence properties.

*Strong penalization and RIP methods*

When dealing with the weakly penalized problem (1.31) it is clear that the velocity and pressure spaces have to be chosen independently and they have to satisfy the BB condition. Let us consider now the discrete version of problem (1.22): Find $\mathbf{u}_h^\epsilon \in V_h$ such that

$$a(\mathbf{u}_h^\epsilon, \mathbf{v}_h) + \frac{1}{\epsilon}(\nabla\cdot\mathbf{u}_h^\epsilon, \nabla\cdot\mathbf{v}_h) = l(\mathbf{v}_h) \qquad \forall \mathbf{v}_h \in V_h \tag{1.35}$$

Implicitly, relation (1.27) has been assumed. Since only velocities appear in (1.35), the pressure space is not explicitly defined in this approach. In fact, it is determined by (1.27). Symbolically, we can write $Q_h = \operatorname{div} V_h$, meaning that pressures are the divergence of vector fields belonging to the velocity space $V_h$. The resulting $V_h - Q_h$ pair will be in general unstable.

The way to (partially) overcome this problem was first devised in the pioneering works of Zienkiewicz *et al.* [ZTT] in the context of plate and shell bending theory for the Reissner-Mindlin formulation and Fried [Fr] in incompressible Elasticity. In its actual form, it consists in integrating the volumetric term $(\nabla \cdot \mathbf{u}_h^\epsilon, \nabla \cdot \mathbf{v}_h)$ using a low order quadrature rule. The method was first called *selective underintegration* (or reduced underintegration, if this rule is used to compute all the terms) and was lately popularized by Oden [Od] under the acronym *RIP* (Reduced Integration Penalty) method.

To see the connexion between (1.35) and (1.31), let $\boldsymbol{\xi}_j^e$, $j = 1, ..., N_{qp}$ be the quadrature points placed within element $e$, $e = 1, ..., N_{el}$, to calculate $(\nabla \cdot \mathbf{u}_h^\epsilon, \nabla \cdot \mathbf{v}_h)$ and let $\omega_j^e > 0$ be the corresponding weights. Denote by $(\cdot,\cdot)_*$ the approximate $L^2$ inner product associated to this rule, i.e.,

$$(f_1, f_2)_* := \sum_{e=1}^{N_{el}} \sum_{j=1}^{N_{qp}} \omega_j^e f_1(\boldsymbol{\xi}_j^e) f_2(\boldsymbol{\xi}_j^e) \tag{1.36}$$

Instead of (1.35) we will consider:

$$a(\mathbf{u}_h^\epsilon, \mathbf{v}_h) + \frac{1}{\epsilon}(\nabla \cdot \mathbf{u}_h^\epsilon, \nabla \cdot \mathbf{v}_h)_* = l(\mathbf{v}_h) \qquad \forall \mathbf{v}_h \in V_h \tag{1.37}$$

Now, let $Q_h$ be the pressure space defined by discontinuous piecewise polynomials $N_{qp}$–unisolvent (for example, in 2D, constants if $N_{qp} = 1$, linear if $N_{qp} = 3$, bilinear if $N_{qp} = 4$ and so on) and consider also the problem

$$a(\mathbf{u}_h^\epsilon, \mathbf{v}_h) - (p_h^\epsilon, \nabla \cdot \mathbf{v}_h)_* = l(\mathbf{v}_h) \qquad \forall \mathbf{v}_h \in V_h \tag{1.38}$$

$$\epsilon(p_h^\epsilon, q_h)_* + (q_h, \nabla \cdot \mathbf{u}_h^\epsilon)_* = 0 \qquad \forall q_h \in Q_h \tag{1.39}$$

From Eqn. (1.39) we have that

$$0 = (\epsilon p_h^\epsilon + \nabla \cdot \mathbf{u}_h^\epsilon, q_h)_* = \sum_{e=1}^{N_{el}} \sum_{j=1}^{N_{qp}} \omega_j^e \left[\epsilon p_h^\epsilon(\boldsymbol{\xi}_j^e) + \nabla \cdot \mathbf{u}_h^\epsilon(\boldsymbol{\xi}_j^e)\right] q_h(\boldsymbol{\xi}_j^e)$$

for all $q_h \in Q_h$, from where it follows that

$$p_h^\epsilon(\boldsymbol{\xi}_j^e) = -\frac{1}{\epsilon}\nabla \cdot \mathbf{u}_h^\epsilon(\boldsymbol{\xi}_j^e) \tag{1.40}$$

for $j = 1, ..., N_{qp}$, $e = 1, ..., N_{el}$. Inserting this expression in Eqn. (1.38) we obtain (1.37). Therefore, we have proved that *problems (1.37) and (1.38)-(1.39) are equivalent*. As a trivial consequence, the following result follows from the comparison of (1.31) and (1.38)-(1.39): *If the numerical quadrature rule is such that*

$$(q_h, q_h')_* = (q_h, q_h') \qquad \text{and} \qquad (q_h, \nabla \cdot \mathbf{v}_h)_* = (q_h, \nabla \cdot \mathbf{v}_h) \tag{1.41}$$

*for all $q_h$, $q_h' \in Q_h$ and $\mathbf{v}_h \in V_h$, then the weak penalty method (1.31) and the RIP method (1.37) are equivalent.*

This equivalence theorem was first established by Malkus & Hughes [MH], although the proof presented here is closer to the one given by Oden [Od]. See also [ESG] and [Fo3] for an interesting discussion.

The definition of the pressure space $Q_h$ is obvious once the numerical quadrature rule has been chosen. Of course the real problem is to check whether condition (1.41) is satisfied or not. For the $Q_1/P_0$ element, the equivalence happens to be exact for general distorted meshes [BFo], [JP], since it is easy to see that if a one-point quadrature rule is used to evaluate the volumetric term, condition (1.41) holds true. In Section 1.3 we will discuss what happens for quadratic quadrilateral elements.

*Matrix formulation*

The penalty methods discussed so far can be applied to the Navier-Stokes equations as well. Corresponding to problems (1.31) and (1.37) we will have, respectively,

**Method 1** (weak penalization): *Find* $\mathbf{u}_h^\epsilon \in V_h$ *and* $p_h^\epsilon \in Q_{0,h}$ *such that*

$$\begin{aligned} c(\mathbf{u}_h^\epsilon, \mathbf{u}_h^\epsilon, \mathbf{v}_h) + a(\mathbf{u}_h^\epsilon, \mathbf{v}_h) - b(p_h^\epsilon, \mathbf{v}_h) &= l(\mathbf{v}_h) \qquad \forall \mathbf{v}_h \in V_h \\ \epsilon(p_h^\epsilon, q_h) + b(q_h, \mathbf{u}_h^\epsilon) &= 0 \qquad \forall q_h \in Q_h \end{aligned} \tag{1.43}$$

**Method 2** (strong penalization): *Find* $\mathbf{u}_h^\epsilon \in V_h$ *such that*

$$c(\mathbf{u}_h^\epsilon, \mathbf{u}_h^\epsilon, \mathbf{v}_h) + a(\mathbf{u}_h^\epsilon, \mathbf{v}_h) + \frac{1}{\epsilon} d(\mathbf{u}_h^\epsilon, \mathbf{v}_h) = l(\mathbf{v}_h) \qquad \forall \mathbf{v}_h \in V_h \tag{1.44}$$

where the notation

$$d(\mathbf{u}_h, \mathbf{v}_h) := (\nabla \cdot \mathbf{u}_h, \nabla \cdot \mathbf{v}_h), \tag{1.45}$$

has been introduced. Define now the following integers associated to the finite element mesh:

| | |
|---|---|
| $N_{fp}$ | : total number of free nodes, |
| $N_{vu} := N_{fp} \times N_{sd}$ | : total number of velocity unknowns, |
| $N_{pu} := N_{qp} \times N_{el}$ | : total number of pressure unknowns. |

Each term in Eqns. (1.43) and (1.44) will yield a matrix or a vector once the finite element basis (shape functions) has been chosen. Let $\mathbf{U}$ and $\mathbf{P}$ be the vectors whose components are the velocity and pressure nodal unknowns, respectively, and denote by $\mathbf{U}^\epsilon$ and $\mathbf{P}^\epsilon$ their 'penalized' counterparts. The matrices that will appear in the final algebraic system of equations and the term from where they come are given in Box 1.2. The vector $\mathbf{F}_p$ accounts for possible non-homegeneous velocity boundary conditions.

Having introduced all these arrays, the matrix version of problems (1.43) and (1.44) will be

**Method 1** (weak penalization): *Solve the nonlinear algebraic system*

$$\begin{aligned} \mathbf{K}_c(\mathbf{U}^\epsilon)\,\mathbf{U}^\epsilon + \mathbf{K}_d\mathbf{U}^\epsilon - \mathbf{G}\mathbf{P}^\epsilon &= \mathbf{F}_u \\ \mathbf{G}^T\mathbf{U}^\epsilon + \epsilon\mathbf{M}_p\mathbf{P}^\epsilon &= \mathbf{F}_p \end{aligned} \tag{1.46}$$

**Method 2** (strong penalization): *Solve the nonlinear algebraic system*

$$\mathbf{K}_c(\mathbf{U}^\epsilon)\,\mathbf{U}^\epsilon + \mathbf{K}_d\mathbf{U}^\epsilon + \frac{1}{\epsilon}\mathbf{K}_v\mathbf{U}^\epsilon = \mathbf{F}_u \tag{1.47}$$

Although expressions (1.46) will be kept in what follows, their implementation uses the fact that the pressure interpolation is discontinuous. This allows to eliminate the pressure degrees of freedom, thus making the method much more efficient from the computational standpoint. For discontinuous pressures, the second equation in (1.46) holds for each element. If we denote by superscript $e$ the element arrays, before imposing the boundary conditions we will have that

$$\mathbf{G}^{(e)^T}\mathbf{U}^{(e)^\epsilon} + \epsilon\mathbf{M}_p^{(e)}\mathbf{P}^{(e)^\epsilon} = \mathbf{0} \tag{1.48}$$

and hence

$$\mathbf{P}^{(e)^\epsilon} = -\frac{1}{\epsilon}\mathbf{M}_p^{(e)^{-1}}\mathbf{G}^{(e)^T}\mathbf{U}^{(e)^\epsilon} \tag{1.49}$$

Let $\mathcal{A}$ denote the standard finite element assembly operator. From (1.48) and (1.49) we have that:

$$\left[\mathbf{K}_c\left(\mathbf{U}^\epsilon\right) + \mathbf{K}_d + \frac{1}{\epsilon}\mathcal{A}_{e=1}^{N_{el}}\left(\mathbf{G}^{(e)}\mathbf{M}_p^{(e)^{-1}}\mathbf{G}^{(e)^T}\right)\right]\mathbf{U}^\epsilon = \mathbf{F}_u \tag{1.50}$$

Once $\mathbf{U}^{\epsilon(i)}$ is found by solving Eqn. (1.50), the pressure nodal values can be computed for each element from the expression (1.49). It should be remarked that the matrix of system (1.50) has to be factored only once for Newtonian Stokesian flows and that the inversion of $\mathbf{M}_p^{(e)}$ is trivial (it is a $(N_{sd}+1)\times(N_{sd}+1)$ matrix if linear pressures are used). Due to this simplification when the pressure is discontinuous, the weak penalty method is rarely applied when the pressure space consists of continuous functions.

**Box 1.2 Matrices and vectors for the algebraic system**

| Matrix | comes from | and has dimensions |
|---|---|---|
| $\mathbf{K}_c(\mathbf{U})$ | $c(\mathbf{u},\cdot,\cdot)$ | $N_{vu}\times N_{vu}$ |
| $\mathbf{K}_d$ | $a(\cdot,\cdot)$ | $N_{vu}\times N_{vu}$ |
| $\mathbf{K}_v$ | $d(\cdot,\cdot)$ | $N_{vu}\times N_{vu}$ |
| $\mathbf{G}$ | $b(\cdot,\cdot)$ | $N_{vu}\times N_{pu}$ |
| $\mathbf{M}_p$ | $(\cdot,\cdot)$ | $N_{pu}\times N_{pu}$ |
| $\mathbf{F}_u$ | $l(\cdot)$ | $N_{vu}$ |
| $\mathbf{F}_p$ | Bound. cond. | $N_{pu}$ |

**Remark 1.1**

From the preceeding discussion and comparing expressions (1.47) and (1.50), it is clear that the equality

$$\mathcal{A}_{e=1}^{N_{el}}\left(\mathbf{G}^{(e)}\mathbf{M}_p^{(e)^{-1}}\mathbf{G}^{(e)^T}\right) = \mathbf{K}_v \tag{1.51}$$

will hold if the quadrature rule $(\cdot,\cdot)_*$ verifies conditions (1.41). Checking this matrix relation for the particular case of the $Q_1/P_0$ element was the first step towards the understanding of the equivalence between strong and weak penalizations [Hu1]. □

*Some bibliographical notes on the BB condition*

The BB condition introduced earlier plays a fundamental role in the theory of mixed and penalty methods. Here we want to mention briefly the most important works that sketch its evolution towards the actual knowledge. The first fundamental paper to be referred is due to Babuška [Ba1], where a general variational problem is considered. He introduced two general conditions on the bilinear form that defines the problem that may be viewed as a generalization of the classical Lax-Milgram Lemma. The particular case of saddle point problems was considered by Brezzi [Br], who presented the condition under the form that has been used here, that is, condition (1.10). He proved a general existence and uniqueness theorem and the error estimate (1.34). It was early recognized that the main difficulty that arises when considering the discrete finite element problem is that, although the stability condition holds for the continuous problem, it is not automatically inherited by the discrete version. The stability of the continuous Stokes equations had already been proved by Ladyzhenskaya [La]. This is why the BB condition is sometimes called LBB (Ladyzhenskaya-Babuška-Brezzi) condition.

Later, this stability condition has been applied to a wide variety of mixed problems. Babuška *et al.* [BOP] proved convergence of several mixed methods using mesh dependent norms for different methods that were known to work well. However, most of the effort was placed on finding methods for effectively checking the stability condition. With regards to the incompressibility constraint, the first method that enjoyed widespread use is due to Fortin [Fo1], who showed that in some cases the BB condition follows if a continuous operator can be built from the space $V$ to $V_h$. This method has been used, for example, to prove the stability of the so called *mini-element* [ABF]. Another important method was designed by Crouzieux & Raviart [CR], who also introduced a widely used stabilization technique based on the introduction of bubble functions. Bercovier & Pironneau [BP] first proved the stability of the Taylor-Hood elements [TH]. Later, their analysis was simplifyed by Verfürth [Ve1]. Recently, Brezzi & Falk have proved the stability of higher-order Taylor-Hood elements [BFa]. The stability of some low-order elements was also proved by Boland & Nicolaides [BN3], using the method they introduced in [BN1]. Let us also mention a promising technique due to Stenberg [St1], [St2] (see also [St3] for a self-contained presentation) that together with Fortin's method seems to be the simplest tool for proving div-stability of finite elements.

A review of mixed methods using the velocity-pressure and the tension-velocity approaches can be found in References [BB] and [Ar], respectively.

Finally, let us mention another technique introduced by Zienkiewicz *et al.* [ZQT] that *is not* sufficient to assert div-stability but that turns out to be of practical interest is most of the cases. It is based on a degrees-of-freedom counting, requiring solvability of the discrete problem (not stability!) for any 'patch' of elements. The idea underlying this method is the patch test introduced by Irons (see, e.g. [IL], [Ra], [TSZ]).

An engineering-oriented approach to the use of mixed finite element interpolations can be found in the books of Hughes [Hu2] and Zienkiewicz & Taylor [ZT].

## 1.3 An example of strong penalization: The biquadratic element for two–dimensional incompressible flows

The first tentative title for this section was *An example of failure: the ...* This already gives an idea of the conclusions that may be drawn from the results to be presented here.

At first glance, the use of a certain quadrature rule for the volumetric term (1.45) to emulate a pure mixed velocity-pressure interpolation seems to be quite attractive. Nevertheless, it turns out that problems arise when trying to do this. The purpose of this section is to convince the reader that the slightly higher computational effort associated to the weak penalization (1.43) method when it is compared to the strong penalization (1.44) is certainly worth affording.

Here, we will restrict ourselves to the Lagrangian biquadratic interpolation for the velocity. Several reduced integration rules for the volumetric term will be treated, trying to reproduce the $Q_2/P_0$, $Q_2/Q_1$ and $Q_2/P_1$ elements. In order to illustrate the exposition, the well known cavity flow test will be used to exemplify the application of the ideas of the text.

Since the strong penalization will not be used any more in this work, a simple although complete numerical algorithm will be presented for the Navier-Stokes equations, including the pressure calculation and the treatment of problems with a high cell Reynolds number using a Petrov-Galerkin technique.

### 1.3.1 Gauss–Legendre quadrature for the volumetric term

First we shall consider a one-point quadrature rule. Clearly, the pressure space $Q_h$ in this case will consist of discontinuous piecewise constant functions. The element to be reproduced will be the $Q_2/P_0$ pair, which is div-stable. Let us introduce the notation

$$b_*(q_h, \mathbf{v}_h) := (q_h, \nabla \cdot \mathbf{v}_h)_*, \qquad q_h \in Q_h, \;\; \mathbf{v}_h \in V_h \tag{1.52}$$

Since the divergence of biquadratic functions contains a complete second degree polynomial, the second condition in (1.41) will not be satisfied and the strong and weak penalizations will not be exactly equivalent. There is a consistency error due to the numerical quadrature rule that will be given by the power $\alpha$ in the estimate

$$|b(q_h, \mathbf{v}_h) - b_*(q_h, \mathbf{v}_h)| \leq Ch^{\alpha} \|q_h\|_Q \|\mathbf{v}_h\|_V, \qquad q_h \in Q_h, \;\; \mathbf{v}_h \in V_h \tag{1.53}$$

Clearly, $\alpha > 0$ is needed if the mixed interpolation is to be approximated as $h \to 0$. For the particular element under consideration, the one-point rule integrates exactly bilinear functions. Therefore, $\alpha = 1$.

In Reference [Fo3], it is proved that condition (1.53) is sufficient to assert that the bilinear form $b_*(\cdot,\cdot)$ will satisfy the BB condition for $h$ sufficiently small if $b(\cdot,\cdot)$ does. However, it can be proved that $b_*(\cdot,\cdot)$ is stable for *any* $h$ using the following stronger result (cf. [BFo], Prop. II.2.19): *If there exists an homeomorphism* $\Pi_h : V_h \longrightarrow V_h$ *such that*

$$b(q_h, \mathbf{v}_h) = b_*(q_h, \Pi_h \mathbf{v}_h), \qquad q_h \in Q_h, \;\; \mathbf{v}_h \in V_h \tag{1.54}$$

*then* $b_*(\cdot,\cdot)$ *satisfies the BB condition iff* $b(\cdot,\cdot)$ *does.*

In [BFo], $\Pi_h$ is constructed explicitly for uniform meshes, thus proving that the resulting scheme will be stable in this case. The integration error (1.53) will nevertheless remain.

Consider now the Gauss-Legendre $2 \times 2$ integration rule for the volumetric term. The associated pressure space will consist of piecewise bilinear pressures. Since this rule can integrate exactly bicubic polynomials, conditions (1.41) will be verified for uniform meshes (although a small quadrature error will remain if they are distorted) and the $Q_2/Q_1$ pair will be exactly reproduced. However, it has already been mentioned that this element suffers from having a small stability constant $K_b$, which tends to zero as $h \to 0$ and also from the fact that spurious pressure modes may appear.

The $3 \times 3$ quadrature rule is inadequate, since it leads to the $Q_2/Q_2$ element, known to be completely unstable and to yield meaningless answers (locking phenomenon).

We have tested the $Q_2/P_0$ and $Q_2/Q_1$ elements for the driven cavity flow problem. Results are shown in Figure 1.1 (Stokes problem). In all the cases, we have taken $\mu = 1$ and a uniform mesh of $21 \times 21$ nodal points ($10 \times 10$ biquadratic elements) to discretize the domain $[0,1] \times [0,1]$. Body forces are zero. The penalty parameter has been taken $\epsilon = 10^{-8}$. Homogeneous Dirichlet conditions have been prescribed everywhere on the boundary except in the upper edge, where two types of boundary conditions have been tested:

$$A - \textit{Leaky lid cavity}: \mathbf{u} = (1,0) \text{ for } y = 1, \quad 0 \le x \le 1$$
$$B - \textit{Ramp condition}: \mathbf{u} = (1,0) \text{ for } y = 1, \quad 0 < x < 1$$

It is known that the singularity on the boundary conditions of problem B is more difficult to reproduce by numerical schemes than the one of problem A.

Figures 1.1.(1) and 1.1.(2) show the velocity vectors obtained for problem A using the one-point and $2 \times 2$ rules, respectively. Results are good in both cases, although the former seems to yield overdiffusive answers. This is known to happen for the pure $Q_2/P_0$ interpolation and it is even more accentuated now due to the integration error (1.53). For problem B, the one-point rule still gives a stable approximation (Figure 1.1.(3)), but oscillations appear when the $2 \times 2$ rule is employed (Figure 1.1.(4)). From these facts it may be concluded that neither the one-point nor the $2 \times 2$ rules are especially robust and accurate. Accuracy is the problem associated to the former, whereas the latter shows a lack of stability.

### 1.3.2 About the (im)possibility of emulating the $Q_2/P_1$ element

In this section we shall prove that the $Q_2/P_1$ *cannot* be reproduced using the strong penalty method with a reduced integration rule for the volumetric term. First, a three point quadrature rule will be presented, showing also that it is optimal. Using this rule, it will be proved that the consistency error (1.53) is bounded below by a positive constant *independent of* $h$ and that tends to zero when the three quadrature points collapse in a single one. Therefore, for $\epsilon \to 0$ and $h \to 0$ the numerical solution *will not* converge to the exact incompressible solution and the error will rely on the position of the integration points.

Some numerical experiments for the driven cavity flow have been conducted to show the disastrous behavior of the algorithm for different positions of the quadrature points.

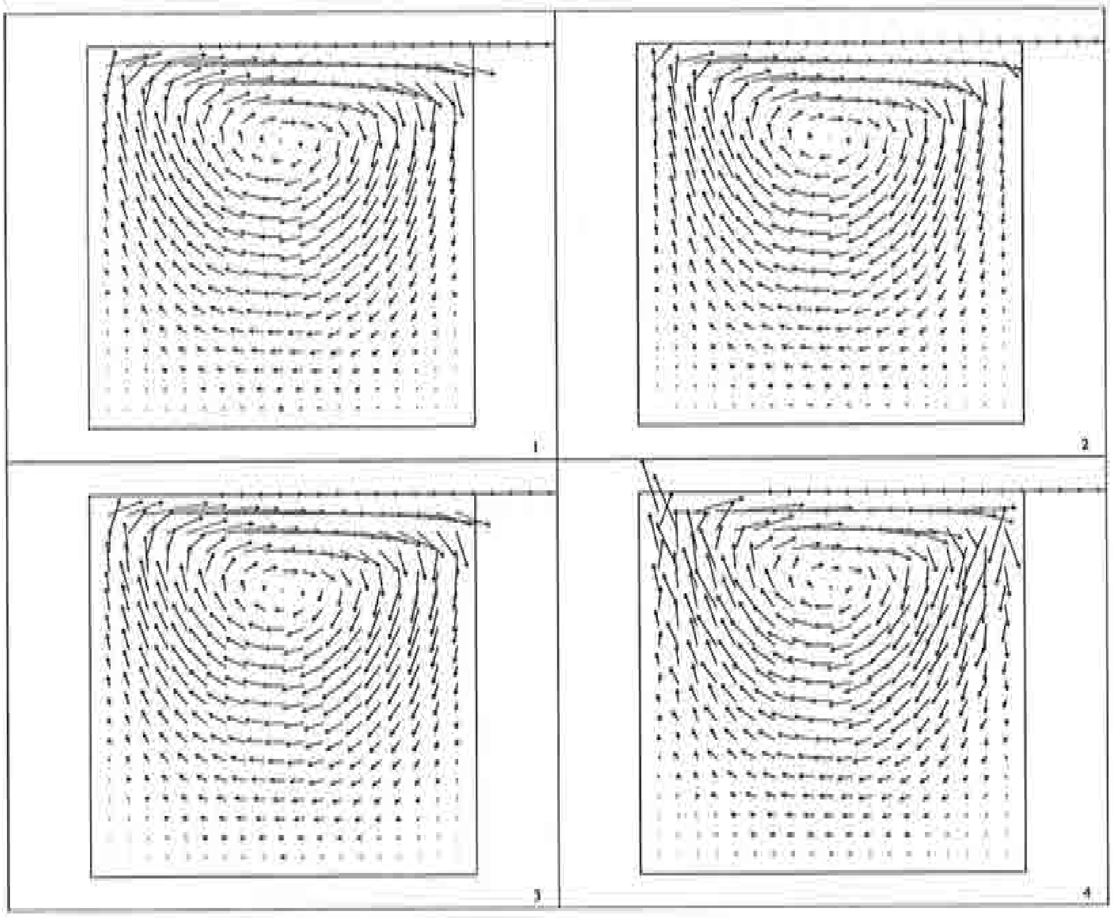

Figure 1.1 Results for the driven cavity flow problem. Stokes flow. (1): one-point rule, problem A; (2): $2 \times 2$ rule, problem A; (3): one-point rule, problem B; (4): $2 \times 2$ rule, problem B

*A three point quadrature rule*

Let $\Omega_0 := [-1,1] \times [-1,1]$ be the parent domain where the numerical integration is to be carried out. As usual, every subdomain $\Omega^e$ of the finite element partition will be mapped to $\Omega_0$ using the standard isoparametric mapping. We denote by $P_m$ the set of polynomials of degree $m$ and by $Q_m$ the set of tensor product polynomials of degree $m$ in each Cartesian direction $x$ and $y$.

**Proposition 1.1** *The numerical quadrature rule*

$$\int_{\Omega_0} f(x,y)dxdy \approx \frac{4}{3}\sum_{i=1}^{3} f(x_i,y_i) \tag{1.55}$$

*with*

$$\begin{aligned}(x_1,y_1) &= (0,r),\\ (x_2,y_2) &= (-r\cos(\pi/6), -r\sin(\pi/6)),\\ (x_3,y_3) &= (r\cos(\pi/6), -r\sin(\pi/6)),\end{aligned} \tag{1.56}$$

*is exact for any $f \in Q_1(\Omega_0)$ and for all $r \in [0,1]$. For $r = \sqrt{2/3}$, it is also exact for any $f \in P_2(\Omega_0)$. Moreover, it is optimal, in the sense that polynomials of the form $f(x,y) = p(x,y) + axy^2 + bx^2y$, with $p \in P_2(\Omega_0)$ and $a$ and $b$ constants, cannot be exactly integrated using three points.*

*Proof:* Let $f(x,y) = p(x,y) + axy^2 + bx^2y$, with $p \in P_2(\Omega_0)$. Denote by $(x_i, y_i)$, $i = 1,2,3$ the coordinates of the quadrature points and by $\omega_i$ their weights. Imposing that

$$\int_{\Omega_0} f(x,y)dxdy = \sum_{i=1}^{3} \omega_i f(x_i, y_i)$$

the following relations are found:

$$\begin{aligned}
\omega_1 + \omega_2 + \omega_3 &= 4 && (a)\\
x_1\omega_1 + x_2\omega_2 + x_3\omega_3 &= 0 && (b)\\
y_1\omega_1 + y_2\omega_2 + y_3\omega_3 &= 0 && (c)\\
x_1y_1\omega_1 + x_2y_2\omega_2 + x_3y_3\omega_3 &= 0 && (d)\\
x_1^2\omega_1 + x_2^2\omega_2 + x_3^2\omega_3 &= 4/3 && (e)\\
y_1^2\omega_1 + y_2^2\omega_2 + y_3^2\omega_3 &= 4/3 && (f)\\
x_1y_1^2\omega_1 + x_2y_2^2\omega_2 + x_3y_3^2\omega_3 &= 0 && (g)\\
x_1^2y_1\omega_1 + x_2^2y_2\omega_2 + x_3^2y_3\omega_3 &= 0 && (h)
\end{aligned}$$

Let us first show that it is impossible to fulfil all these conditions with three different points.

Assume $\omega_i \neq 0$, $i = 1,2,3$. If $x_j \neq 0$ for some $j$, requiring non-trivial solvability from conditions $(b)$, $(d)$ and $(g)$ it is found that

$$\omega_1\omega_2\omega_3(y_2 - y_1)(y_3 - y_1)(y_3 - y_2) = 0$$

Assume, without loss of generality, that $y_2 = y_3 \neq y_1$. If $y_j \neq 0$ for some $j$, conditions $(c)$, $(d)$ and $(h)$ imply

$$\omega_1\omega_2\omega_3(x_2 - x_1)(x_3 - x_1)(x_3 - x_2) = 0$$

Suppose that $x_1 = x_2 \neq x_3$ ($x_2 = x_3$ would mean that points 2 and 3 collapse). Since $\omega_i \neq 0$, from conditions $(d)$, $(g)$ and $(h)$ it follows that

$$x_1^2 x_3 y_1 y_2^2 (y_2 - y_1)(x_3 - x_1) = 0$$

If $y_1 = y_2$ or $x_1 = x_3$ two points would collapse. Assume that $x_1 = x_2 = 0$, $x_3 \neq 0$. From Eqns. $(g)$ and $(h)$ it is found that $y_2 = y_3 = 0$, and from $(c)$ $y_1 = 0$. Hence, points 1 and 2 have inevitably collapsed.

Once it is known that two points must coincide, it is easy to see that system $(a) - (h)$ does not have any solution. For example, take $\omega_3 = 0$. From $(d)$ and $(g)$ it follows that $y_1 = y_2$ and from $(d)$ and $(h)$ $x_1 = x_2$. With a single point only bilinear polynomials can be exactly integrated.

The Proposition follows by checking that conditions $(a) - (d)$ hold for $\omega_1 = \omega_2 = \omega_3 = 4/3$ and $(x_i, y_i)$ given by (1.56). If $r = \sqrt{2/3}$, also $(e)$ and $(f)$ hold. □

**Remark 1.2**

The quadrature rule defined by (1.55)–(1.56) seems to have been used before (cf. [Ki]), although the author was not aware of this fact at the moment of undertaking this work. □

*Inconsistency of* $b_*(\cdot,\cdot)$

If the volumetric term is integrated using a three-point quadrature rule, the pressure space will consist of piecewise linear polynomials. For $r = \sqrt{2/3}$, the first condition (1.41) will be fulfilled for uniform meshes. However, the bilinear form $b_*(\cdot,\cdot)$ cannot approximate the bilinear form $b(\cdot,\cdot)$ for a fixed $r > 0$. This is what the following result states.

**Proposition 1.2** *Assume that the quadrature rule of Proposition 1.1 is used for the volumetric term. Then, there is a constant* $C(r)$ *independent of* $h$*, with* $C(r) \to 0$ *as* $r \to 0$*, such that*

$$\sup_{q_h, \mathbf{v}_h} \frac{|b(q_h, \mathbf{v}_h) - b_*(q_h, \mathbf{v}_h)|}{\|q_h\|_Q \|\mathbf{v}_h\|_V} \geq C(r),$$

*where the supremum is taken over all the* $q_h \in Q_h - \{0\}$ *and* $\mathbf{v}_h \in V_h - \{\mathbf{0}\}$.

*Proof:* Since the functions in $Q_h$ are discontinuous, we can take $q_h^0$ constant on an element $\Omega^e$ and zero everywhere else. Take also $\mathbf{v}_h^0 = N_9\mathbf{a}$, where $N_9(x,y)$ is the shape function associated to the central node of the element and $\mathbf{a} \neq \mathbf{0}$ is a constant vector. Without loss of generality, we shall assume $\Omega^e$ to be affine with the parent domain $\Omega_0$, where natural coordinates $\xi, \eta$ are taken. We will have that

$$b(q_h^0, \mathbf{v}_h^0) = q_h^0 \int_{\Omega^e} \nabla \cdot (N_9\mathbf{a}) d\Omega = q_h^0 \int_{\partial\Omega^e} \mathbf{n} \cdot (N_9\mathbf{a}) d\Gamma = 0$$

and

$$b_*(q_h^0, \mathbf{v}_h^0) = C_1 \; q_h^0 \; \frac{1}{3} \text{meas}(\Omega^e) \; |\sum_{i=1}^{3} \nabla N_9(\xi_i, \eta_i)| |\hat{\mathbf{a}}| \cos\beta,$$

where the constant $C_1$ takes into account the angles of the edges in $\Omega^e$, $|\hat{\mathbf{a}}|$ is the Euclidian norm of the vector transformed of $\mathbf{a}$ to the parent domain and $\beta$ is the angle between $\hat{\mathbf{a}}$ and $\sum_{i=1}^{3} \nabla N_9(\xi_i, \eta_i)$. Since

$$\nabla N_9(\xi, \eta) = \left(-2\xi(1-\eta^2), -2\eta(1-\xi^2)\right),$$

it is found that

$$|\sum_{i=1}^{3} \nabla N_9(\xi_i, \eta_i)| = \frac{3}{2} r$$

Considering that

$$\|q_h^0\|_Q = |q_h^0| \; \text{meas}(\Omega^e)^{\frac{1}{2}}, \qquad \|\mathbf{v}_h^0\|_V = C_2 \; |\hat{\mathbf{a}}| \; \text{meas}(\Omega^e)^{\frac{1}{2}},$$

with $C_2$ depending on $\beta$ and the $V$−norm of $N_9$ in $\Omega_0$, we will have that

$$\sup_{q_h, \mathbf{v}_h} \frac{|b(q_h, \mathbf{v}_h) - b_*(q_h, \mathbf{v}_h)|}{\|q_h\|_Q \|\mathbf{v}_h\|_V} \geq \sup_{\beta} \frac{|b_*(q_h^0, \mathbf{v}_h^0)|}{\|q_h^0\|_Q \|\mathbf{v}_h^0\|_V} = Cr$$

for a certain constant $C$. □

It is clear from this result that the higher $r$ is (with $0 \leq r \leq 1$), the more inaccurate will be approximation to the incompressibility condition. To verify this numerically, the driven cavity flow using the introduced method has been solved. Results are shown in Figure 1.2. In Figures 1.2.(1) and 1.2.(2), $r = \sqrt{2/3}$ has been used. The first case corresponds to the leaky lid boundary conditions and the second to the ramp condition. Although no oscillations are apparent in any of the two cases, it is obvious that the incompressibility constraint has been excessively relaxed. The central vortex has moved down with respect to the reference results of Figure 1.1. To check the effect of the value of $r$, the problem with the ramp condition has been run again with $r = 0.5$ and $r = 0.9$ (Figures 1.2.(3) and 1.2.(4), respectively). As expected, the zero divergence condition is totally violated in the latter case, where results are meaningless. Looking at Figures 1.2.(3), 1.2.(2) and 1.2.(4) we see how increasing value of $r$ (0.5, $\sqrt{2/3}$ and 0.9, respectively) this constraint is more and more relaxed.

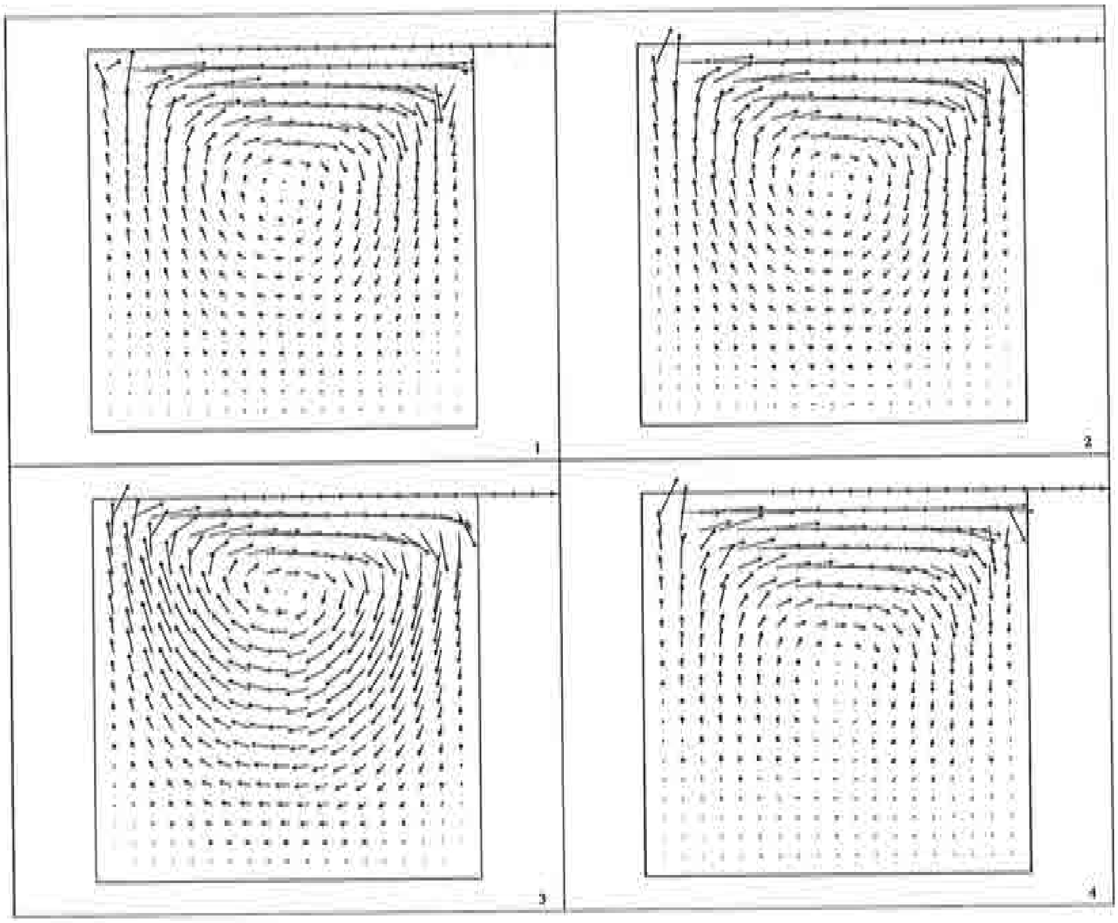

Figure 1.2 Results for the driven cavity flow problem. Stokes flow. Three-point quadrature rule for the volumetric term. (1): $r = \sqrt{2/3}$, leaky lid condition; (2): $r = \sqrt{2/3}$, ramp condition; (2): $r = 0.5$, ramp condition; (2): $r = 0.9$, ramp condition.

### 1.3.3 Pressure calculation

Once the velocity has been calculated by solving problem (1.47), relation (1.40) gives the values of the pressure at the reduced integration points. There are two questions to be considered. First, the pressures will be discontinuous across interelement boundaries and thus a smoothing facility has to be introduced, mainly for plotting purposes. The second aspect is that some of the elements that can be emulated through underintegration of the volumetric term exhibit spurious pressure modes (cf. Box 1.1). Sometimes, the smoothing technique utilized may be enough to remove these modes, but this in general will not be true, especially near the boundaries [HLB]. On the other hand, the penalty approach automatically precludes the appearence of these spurious pressures. Nevertheless, pressure convergence cannot be ensured [JP], [OKS] and the pressure space has to be redefined in order to obtain this convergence (under stricter regularity assumptions than usual for the exact solution [JP]).

Here, both problems will be treated and applied to the $Q_2/Q_1$ and $Q_2/P_0$ elements. Also, the possibility of solving a Poisson equation for the pressure will be discussed. As far as we are aware, this method has only been applied to the $Q_1/P_0$ element by Sohn & Heinrich [SH]. Since it is impossible for this element to approximate the second derivatives for the velocity field that are required for this method, they had to calculate them via the interpolation of the nodal *first* derivatives and using a least squares technique. This problem is circumvented if quadratic elements are used.

For a detailed and up-to-date discussion of the Poisson problem for the pressure the reader is referred to the paper of Gresho & Sani [GS], where both theoretical and practical questions are treated. Of special interest is the discussion on the boundary conditions to be imposed to the pressure.

*Pressure filter and Least-squares smoothing (LSS)*

Consider first the $Q_2/Q_1$ element and assume that the velocity field $\mathbf{u}_h$ is known in the parent domain $\Omega_0$, where the numerical integration has been performed. Eqn. (1.40) will give the value of the pressure at the quadrature points. As explained earlier, spurious modes may be present for the non-penalized problem and pollute the penalized solution. In order to remove them, what we do is to project the space of piecewise bilinear pressures onto the space of piecewise *linear* pressures, since it is known that no spurious modes appear for the $Q_2/P_1$ element. We have successfully tested the following method.

Let $p_i^e$, $i = 1, 2, 3, 4$, be the pressure values in the parent domain corresponding to element $e$ computed using (1.40). Let also $\gamma = \sqrt{3}/2$ and

$$(\xi_1, \eta_1) = (-\gamma, -\gamma), \qquad (\xi_2, \eta_2) = (\gamma, -\gamma),$$
$$(\xi_3, \eta_3) = (-\gamma, \gamma), \qquad (\xi_4, \eta_4) = (\gamma, \gamma)$$

be the coordinates of the quadrature rule points. From $p_i^e$ we construct the following piecewise linear pressure:

$$p_l^e(\xi, \eta) = a_0 + a_1\xi + a_2\eta \tag{1.57}$$

with

$$\begin{aligned} a_0 &:= \frac{1}{4}\sum_{i=1}^{4} p_i^e, && \text{(mean value)} \\ a_1 &:= \frac{1}{2}\left(\frac{p_2^e - p_1^e}{2\gamma} + \frac{p_4^e - p_3^e}{2\gamma}\right) && (\xi\text{-derivative}) \\ a_2 &:= \frac{1}{2}\left(\frac{p_3^e - p_1^e}{2\gamma} + \frac{p_4^e - p_2^e}{2\gamma}\right) && (\eta\text{-derivative}) \end{aligned}$$

Now we have a discontinuous piecewise linear pressure given by (1.57), for which no spurious modes are expected. In order to obtain a continuous pressure field $p_s(x,y)$, we use a standard Least-squares method [Hu2], [ZT], described in more detail in Chapter 2. The pressure $p_s(x,y)$ is interpolated using the biquadratic element. If $N^{(i)}(x,y)$ denotes the shape function of the $i$th node of the finite element mesh, the vector of smoothed pressure nodal unknowns, say $\mathbf{P}_s$, will be found by solving the algebraic system

$$\mathbf{M}\mathbf{P}_s = \mathbf{R}_s, \tag{1.58}$$

where the symmetric and positive-definite matrix $\mathbf{M}$ has components $M_{ij} = \int_\Omega N^{(i)}N^{(j)}d\Omega$ and

$$\begin{aligned} R_{s,j} &= \mathcal{A}_{e=1}^{N_{el}} \int_{\Omega^e} N^{(j)}(x,y)\; p_l^e(x,y)d\Omega \\ &= \mathcal{A}_{e=1}^{N_{el}} \int_{\Omega_0} N^{(j)}(\xi,\eta)\; p_l^e(\xi,\eta)\; |J(\xi,\eta)|d\Omega, \end{aligned}$$

$J(\xi,\eta)$ being the Jacobian determinant of the isoparametric mapping and $p_l^e(\xi,\eta)$ being given by (1.57).

For the $Q_2/P_0$ element, this smoothing is also applied, although now the pressure is constant and given directly by (1.40).

*Pressure Poisson equation*

Taking the divergence of the momentum equation in (1.1) yields

$$\Delta p = \nabla\cdot[\rho\mathbf{f} + \mu\Delta\mathbf{u} - \rho(\mathbf{u}\cdot\nabla)\mathbf{u}] \qquad \text{in } \Omega \tag{1.59}$$

i.e., a Poisson equation for the pressure. If we assume the velocity field to be solenoidal and sufficiently smooth, we would have that $\nabla\cdot(\mu\Delta\mathbf{u}) = \mu\Delta(\nabla\cdot\mathbf{u}) = 0$. However, we will keep the term $\mu\Delta\mathbf{u}$ in (1.59) for the moment.

In Reference [GS], it is concluded that the correct boundary condition for (1.59) is the imposition of the conservation of the normal component of the momentum. Multiplying the first equation in (1.1) by the unit outward normal $\mathbf{n}$ and evaluating on the boundary (understanding this process as a limit) we are led to

$$\frac{\partial p}{\partial n} = \mathbf{n}\cdot[\rho\mathbf{f} + \mu\Delta\mathbf{u} - \rho(\mathbf{u}\cdot\nabla)\mathbf{u}] \qquad \text{on } \partial\Omega \tag{1.60}$$

The solution of the Neumann problem (1.59)–(1.60) is unique up to an additive constant that can be fixed by specifying the value of the pressure at a certain point.

Let $\hat{Q} = H^1(\Omega)$ and $\hat{Q}_0 = H^1(\Omega)/\mathbb{R}$. The weak form of problem (1.59)–(1.60) is: Find $p \in \hat{Q}_0$ such that

$$\int_\Omega \nabla q \cdot \nabla p \; d\Omega = \int_{\partial\Omega} q \left[ \frac{\partial p}{\partial n} - \mathbf{n} \cdot \mathcal{F}_m \right] d\Gamma + \int_\Omega \nabla q \cdot \mathcal{F}_m \; d\Omega \qquad \forall q \in \hat{Q} \tag{1.61}$$

where

$$\mathcal{F}_m(\mathbf{u}) := \rho \mathbf{f} + \mu \Delta \mathbf{u} - \rho(\mathbf{u} \cdot \nabla)\mathbf{u}$$

is the vector whose divergence appears in the right-hand-side of (1.59). Since (1.60) establishes that $\partial p/\partial n = \mathbf{n} \cdot \mathcal{F}_m$, the boundary term in (1.61) vanishes.

Construct now conforming finite element spaces $\hat{Q}_{0,h} \subset \hat{Q}_0$ and $\hat{Q}_h \subset \hat{Q}$ using the biquadratic element. The discrete counterpart of problem (1.61) is to find $p_h \in \hat{Q}_{0,h}$ such that

$$(\nabla q_h, \nabla p_h) = (\nabla q_h, \mathcal{F}_m(\mathbf{u}_h)) \qquad \forall q_h \in \hat{Q}_h \tag{1.62}$$

Let us discuss now the approximation properties that can be expected from the solution of problem (1.62). It is well established (see, e.g. [Ci]) that the error $\|p - p_h\|_0$ is of order $O(h^3)$ for a given function $\mathcal{F}_m(\mathbf{u}_h)$. However, the real problem is the approximation of $\mathcal{F}_m(\mathbf{u}_h)$ to $\mathcal{F}_m(\mathbf{u})$, with $\mathbf{u}_h \in V_h$. If we assume that the inverse estimate [Ci]

$$\|\mathbf{v}_h\|_{s,\Omega^e} \leq C \; h^{-1} \|\mathbf{v}_h\|_{s-1,\Omega^e}$$

holds for any $\mathbf{v}_h \in V_h$, we can roughly expect that

$$\|\mathcal{F}_m(\mathbf{u}) - \mathcal{F}_m(\mathbf{u}_h)\|_0 \sim h^{-2} \; \|\mathbf{u} - \mathbf{u}_h\|_0$$

since $\mathcal{F}_m(\mathbf{u}_h)$ involves second derivatives of $\mathbf{u}_h$. Therefore, the error in the pressure associated to problem (1.62) will be driven by the approximation of $\mathcal{F}_m(\mathbf{u}_h)$ to $\mathcal{F}_m(\mathbf{u})$.

For the $Q_2/Q_1$ element, the best we can hope for is the interpolation error $\|\mathbf{u} - \mathbf{u}_h\|_0 = O(h^3)$, if no instabilities are present. Therefore, $\|\mathcal{F}_m(\mathbf{u}) - \mathcal{F}_m(\mathbf{u}_h)\|_0 = O(h)$. However, for the $Q_2/P_0$ element the error will be $\|\mathbf{u} - \mathbf{u}_h\|_0 = O(h^2)$, due to the poor pressure approximation. In this case, $\|\mathcal{F}_m(\mathbf{u}) - \mathcal{F}_m(\mathbf{u}_h)\|_0 = O(1)$, i.e., no convergence can be expected of $\mathcal{F}_m(\mathbf{u}_h)$ to $\mathcal{F}_m(\mathbf{u})$.

Numerical experiments show that this quasi-heuristic considerations are pessimistic, at least for the Stokes problem.

**Remarks 1.3**

(1) If we would have taken $\mathcal{F}_m(\mathbf{u}) = \rho\mathbf{f} - \rho(\mathbf{u} \cdot \nabla)\mathbf{u}$, without the viscous term, second derivatives should be calculated not in $\Omega$ but on $\partial\Omega$, since the boundary term in (1.61) would be

$$\int_{\partial\Omega} q \; \mu \; \mathbf{n} \cdot \Delta\mathbf{u} \; d\Gamma$$

The situation now is even worse than before, since roughly speaking approximations on the boundary have a gap 1/2 with respect to approximations in the interior of the domain (cf. Remark 1.4.(3)). In fact, in Reference [SH] it is concluded that the method we have considered yields better numerical results than this one.

(2) Although we have considered the velocity $\mathbf{u}_h$ known, the way the Poisson equation for the pressure is usually used is to guess a velocity field and solve (1.62). The pressure so calculated is used to recompute the velocity. This procedure is

repeated until convergence is achieved. This is a common way to uncouple the velocity and pressure calculations. □

*Numerical performance*

We have computed the pressure for the driven cavity flow with leaky lid boundary conditions using the two methods just described. Figures 1.3.(1) and 1.3.(2) show the results obtained using the pressure filtering and the least-squares smoothing for the one-point and the 2 × 2 integration rules, respectively. As it was already observed for the velocity field, results are overdiffusive for the first option. Figures 1.3.(3) and 1.3.(4) correspond to the same cases using the pressure Poisson equation. Results are 'smoother' than before and qualitatively similar. It must be pointed out that for the one-point rule pressure convergence cannot be guaranteed and for the 2 × 2 rule it is reduced to $O(h)$. Nevertheless, results seem to be fairly good.

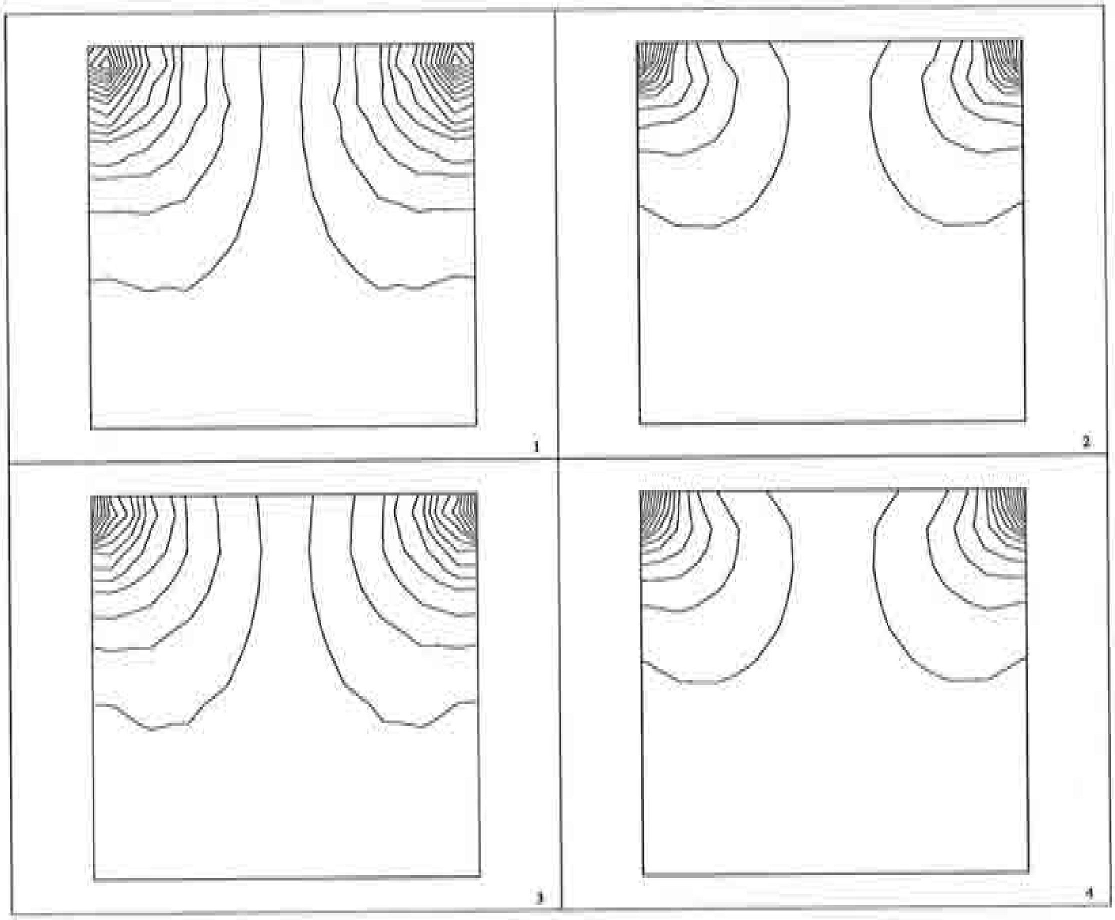

Figure 1.3 Pressures for the driven cavity flow problem (biquadratic element). Stokes flow. (1): one-point rule, least-squares smoothing; (2): 2 × 2 rule, least-squares smoothing; (3): one-point rule, pressure Poisson equation; (4): 2 × 2 rule, pressure Poisson equation.

### 1.3.4 Numerical procedures for the Navier–Stokes equations

To close this incursion into the use of the strong penalty method, we shall briefly describe the numerical techniques we have employed when dealing with the Navier-Stokes equations (1.1). The matrix notation introduced at the end of Section 1.2.3 will be kept.

*Linearization technique*

In order to solve the nonlinear algebraic system (1.47), the simplest linearization method has been employed:

*Given* $\mathbf{U}^{\epsilon(0)}$, *for* $i = 1, 2, \ldots$ *solve for* $\mathbf{U}^{\epsilon(i)}$*:*

$$\mathbf{K}_d\mathbf{U}^{\epsilon(i)} + \frac{1}{\epsilon}\mathbf{K}_v\mathbf{U}^{\epsilon(i)} = \mathbf{F}_u - \mathbf{K}_c\left(\mathbf{U}^{\epsilon(i-1)}\right)\mathbf{U}^{\epsilon(i-1)} \tag{1.63}$$

This method has the important advantdge that the matrix of the algebraic system to be solved at each iteration, viz. $\mathbf{K}_d + (1/\epsilon)\mathbf{K}_v$, is symmetric and positive-definite. Thus, it has to be factored only once and the computational effort of each iteration is reduced to a forward and a backward substitution. In our computations, we have used the frontal algorithm for symmetric matrices due to Irons [Ir] and described in [HO].

Convergence has been checked using the criterion

$$|\mathbf{U}^{\epsilon(i)} - \mathbf{U}^{\epsilon(i-1)}| \leq TOL|\mathbf{U}^{\epsilon(i)}| \tag{1.64}$$

where $TOL$ is a given tolerance and $|\cdot|$ denotes the Euclidian norm of a vector.

*Continuation method*

The main drawback of algorithm (1.63) is that it only converges (and linearly) if the initial guess $\mathbf{U}^{\epsilon(0)}$ is close enough to the final solution. We take $\mathbf{U}^{\epsilon(0)} = \mathbf{0}$ and thus the effective initial guess is the Stokesian solution $\mathbf{U}^{\epsilon(1)}$. Convergence will only be possible for moderate values of the Reynolds number $Re$. It turns out that in practice the algorithm only converges for very small values of $Re$. In order to 'push' the scheme to higher values, we have employed a very simple continuation method, based on incrementing $Re$ up to the final value in several steps. The density $\rho$ has been used as the incrementing factor.

A detailed analysis of different iterative techniques and continuation methods for the strong penalty approach can be found in the papers by Carey & Krishnan [CK3], [CK4], where several numerical results are presented.

*Petrov-Galerkin weighting*

When the convective terms of a transport-diffusion equation are important, the standard Galerkin method fails and numerical oscillations occur. We shall not undertake here a detailed description of available numerical remedies, for which we refer to [Co2]. The method we shall use is the Streamline Diffusion (SD) method as described in the quoted reference for the scalar convection-diffusion equation.

The extension of the SD method to the Navier-Stokes equations is by no means unique, in the sense that several schemes have been proposed in the recent literature. We will come back to this point later in Chapter 2.

Although the iterative method described earlier does not allow for solving highly convective flows, it may be possible that the mesh diameter be large and therefore the *cell Reynolds number*

$$(Re)^e := \rho \frac{|\mathbf{u}^e| h^e}{2\mu} \tag{1.65}$$

be also large. As usual, superscript $e$ denotes characteristic values for an element. From the discussion in Reference [Co2], for values $(Re)^e > 2$ numerical oscillations may be expected when quadratic elements are used.

The SD method that has been implemented is based on the perturbation of the test function $\mathbf{v}_h \in V_h$ to

$$\mathbf{v}_h + \tau(\mathbf{u}_h \cdot \nabla)\mathbf{v}_h, \tag{1.66}$$

the second term only affecting the element interiors. The parameter $\tau$ in (1.66) is the so called *intrinsic time*, which involves *upwind functions* that are calculated as explained in [Co2], replacing the Péclet number $\gamma$ by the cell Reynolds number given by (1.65). Problem (1.44) will be modified as follows: Find $\mathbf{u}_h \in V_h$ such that

$$\begin{aligned} c(\mathbf{u}_h^\epsilon, \mathbf{u}_h^\epsilon, \mathbf{v}_h) + a(\mathbf{u}_h^\epsilon, \mathbf{v}_h) + \frac{1}{\epsilon} d(\mathbf{u}_h^\epsilon, \mathbf{v}_h) \\ + \sum_{e=1}^{N_{el}} \mathcal{S}_e(\mathbf{u}_h^\epsilon, \mathbf{v}_h) = l(\mathbf{v}_h) \qquad \forall \mathbf{v}_h \in V_h \end{aligned} \tag{1.67}$$

where $\mathcal{S}_e$ is the nonlinear functional

$$\begin{aligned} \mathcal{S}_e(\mathbf{u}_h, \mathbf{v}_h) := (\tau^e(\mathbf{u}_h^e \cdot \nabla)\mathbf{v}_h, \rho(\mathbf{u}_h \cdot \nabla)\mathbf{u}_h - \mu \Delta \mathbf{u}_h - \rho \mathbf{f})_{\Omega^e} \\ + \left( \tau^e(\mathbf{u}_h^e \cdot \nabla)\mathbf{v}_h, -\frac{1}{\epsilon} \nabla(\nabla \cdot \mathbf{u}_h) \right)_{*,\Omega^e} \end{aligned} \tag{1.68}$$

Observe that the dependence of $\tau$ on $\mathbf{u}_h$, who is now the unknown of the problem, will be complicated.

Denote by $\mathbf{S}(\mathbf{U}) \cdot \mathbf{V}$ the matrix version of the functional $\sum_{e=1}^{N_{el}} \mathcal{S}_e(\mathbf{u}_h, \mathbf{v}_h)$ once the finite element discretization has been performed. In order to preserve the advantatges of scheme (1.63) when the SD method is used, it has been modified as follows:

*Given* $\mathbf{U}^{\epsilon(0)}$, *for* $i = 1, 2, \ldots$ *solve for* $\mathbf{U}^{\epsilon(i)}$:

$$\mathbf{K}_d \mathbf{U}^{\epsilon(i)} + \frac{1}{\epsilon} \mathbf{K}_v \mathbf{U}^{\epsilon(i)} = \mathbf{F}_u - \mathbf{K}_c \left( \mathbf{U}^{\epsilon(i-1)} \right) \mathbf{U}^{\epsilon(i-1)} - \mathbf{S} \left( \mathbf{U}^{\epsilon(i-1)} \right) \tag{1.69}$$

We have found numerically that the convergence rate of the initial scheme is not deteriorated because of the SD term, but rather improved.

*Final algorithm*

Having in mind all the techniques discussed so far, the final algorithm will read as indicated in Box 1.3. We have used the following notation: $\delta\rho$ is the density increment of each continuation step, $\mathbf{L}$ is the discrete Laplacian matrix, $\mathbf{P}_p$ are the nodal values of the pressure computed using the Poisson equation (1.62) and $\mathbf{R}_p$ is the right-hand-side arising from the discretization of this equation. Terms between parenthesis and italic characters denote logical variables.

**Box 1.3 Algorithm for the Navier–Stokes equations**

```
• Compute $\mathbf{K}_d$ using full integration
• Compute $\mathbf{K}_v$ using reduced integration
• Factorise and store $\mathbf{A} := \mathbf{K}_d + (1/\epsilon)\mathbf{K}_v$
• Set $\rho_c := 0$ and $\mathbf{U}^{\epsilon(0)} := \mathbf{0}$
• WHILE $\rho_c < \rho$ DO:
      • $i := 0$
      • $\rho_c \leftarrow \rho_c + \delta\rho$
      • WHILE (not converged) DO:
            • $i \leftarrow i + 1$
            • Compute $\mathbf{R}^{(i-1)} := \mathbf{F}_u - \mathbf{K}_c\left(\mathbf{U}^{\epsilon(i-1)}\right)\mathbf{U}^{\epsilon(i-1)} - \mathbf{S}\left(\mathbf{U}^{\epsilon(i-1)}\right)$
            • Solve $\mathbf{A}\mathbf{U}^{\epsilon(i)} = \mathbf{R}^{(i-1)}$
            • If $|\mathbf{U}^{\epsilon(i)} - \mathbf{U}^{\epsilon(i-1)}| \leq TOL|\mathbf{U}^{\epsilon(i)}|$ then (converged)
        END while (not converged)
      • New initial guess: $\mathbf{U}^{\epsilon(0)} \leftarrow \mathbf{U}^{\epsilon(i)}$
  END while $\rho_c < \rho$
• Compute the pressure:
      • IF (LSS) then
            • Solve $\mathbf{M}\mathbf{P}_s = \mathbf{R}_s$
      • ELSE if (Poisson) then
            • Solve $\mathbf{L}\mathbf{P}_p = \mathbf{R}_p$
        END
  END
```

*Numerical experiments*

Some very simple numerical experiments have been conducted for the driven cavity flow with leaky lid boundary conditions. The pressure has been computed solving the Poisson equation (1.62). The Reynolds number based on the length of the square ($= 1$) and the prescribed velocity in the upper edge ($= (1, 0)$) is equal to the density $\rho$ for $\mu = 1$. In all the cases, $TOL = 0.001$ has been chosen. The penalty parameter is $\epsilon = 10^{-8}$.

First we solve the Navier-Stokes problem for $Re = 200$ and using the mesh of $21 \times 21$ nodal points employed before (using biquadratic elements). Ten continuation steps and two iterations per step have been required for convergence. In this case, no oscillations appear when using the standard Galerkin formulation. Figures 1.4.(1) and 1.4.(2) show the velocity vectors using the one-point and the $2 \times 2$ quadrature rules. The first case, as it has been already observed in former examples, yields overdiffusive and inaccurate results. In Figures 1.4.(3) and 1.4.(4) the pressure contours have been plotted. Observe that results are bad for the one-point rule and seem to be correct for the $2 \times 2$ rule. Recall that for the former case, no pressure convergence can be guaranteed, whereas for the latter the best one can hope for is an $O(h)$ approximation. These results seem to confirm the discussion of Section 1.3.3.

Next, a $Re = 250$ problem has been run on a new uniform mesh of $11 \times 11$ nodal points ($5 \times 5$ biquadratic elements). Only the $2 \times 2$ point rule has been used. Figures 1.5.(1) and 1.5.(3) show the velocity vectors and the pressure contours obtained using

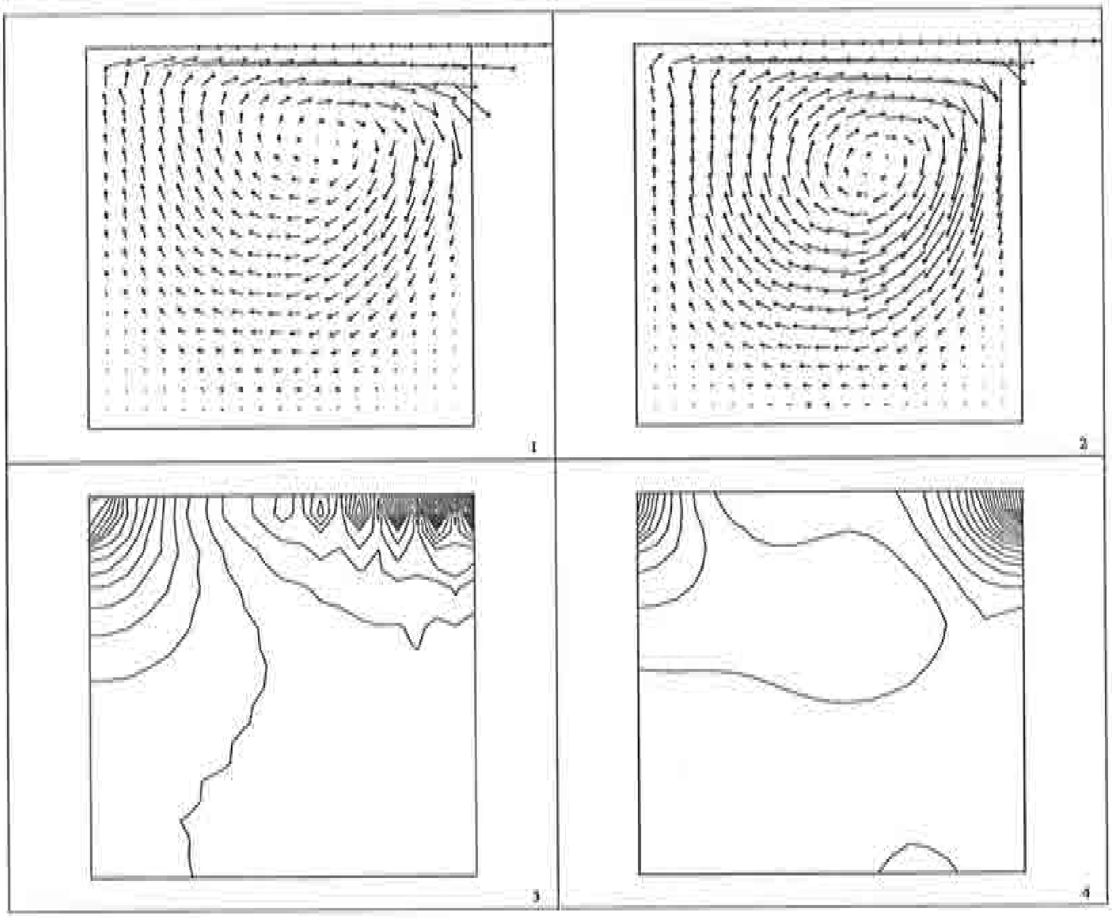

Figure 1.4 Navier-Stokes results using the 21 × 21 mesh, $Re = 200$. The pressure has been computed solving a Poisson equation. (1): Velocities using the one-point rule; (2): Velocities using the 2 × 2 point rule; (3): Pressure contours using the one-point rule; (4): Pressure contours using the 2 × 2 point rule.

the Galerkin formulation. In this case, the cell Reynolds number exceeds two for some elements in the upper right corner, where oscillations can be observed. These are removed if the SD method is used (Figures 1.5.(2) and 1.5.(4)). The upwind functions have been determined according to the methodology proposed in Section 1.4.2.

## 1.4 Weak penalization: analysis of an iterative penalty method

Because of the problems encountered when the strong penalty method is used, we shall move now to the weak penalization approach (hereafter referred to just as penalty method). It is not our purpose to investigate its behavior, which will be appreciated from the numerical examples in this and the following chapters, but rather to present

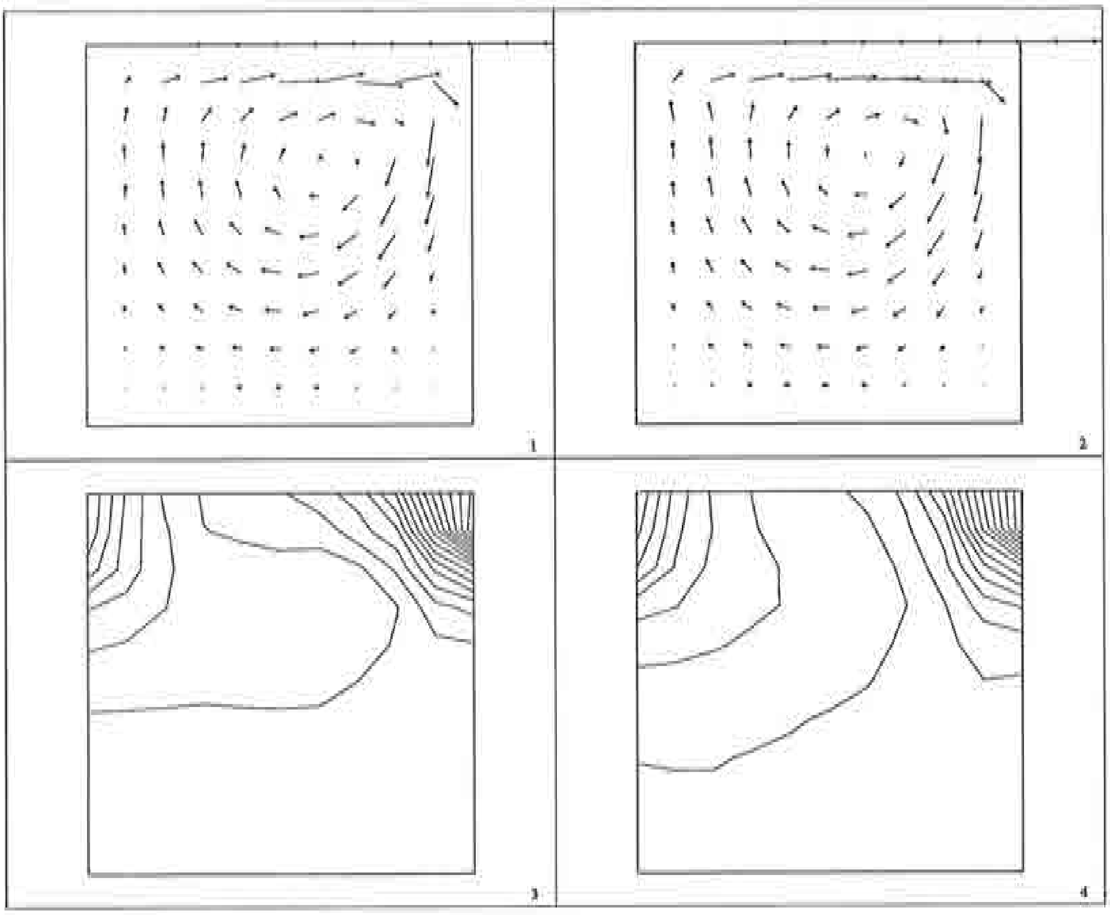

Figure 1.5 Navier-Stokes results using the $11 \times 11$ mesh, $Re = 250$. The pressure has been computed solving a Poisson equation and the $2 \times 2$ quadrature rule has been employed. (1): Velocities using the Galerkin formulation; (2): Velocities using the SD method; (3): Pressure contours using the Galerkin formulation; (4): Pressure contours using the SD method.

and analyse an *iterative* version that will be used throughout this work. The method described by Eqns. (1.43) will be called *classical penalty method.*

The main drawback of the penalty method is the ill-conditioning of the stiffness matrix when the penalty parameter is very small. For Newtonian flows, a fairly wide range of values of this parameter are known to yield good results (that is, the incompressibility equation is sufficiently well approximated) and to be easily handled if direct solvers are employed. Experience shows that the range $\epsilon = 10^{-6}\mu^{-1}$ to $\epsilon = 10^{-9}\mu^{-1}$ is recommended [HLB]. Two questions arise. The first is what happens for non-Newtonian flows. In this case, the viscosity may vary several orders of magnitude in the fluid domain, especially if the physical properties of the material are considered to be thermally sensitive. The above rule for choosing the penalty parameter has to be applied using the smallest value of the viscosity (in order to avoid ill-conditioning), which is unknown before the calculation. Besides that, the incompressibility constraint will be excessively relaxed in the high viscosity zones. Another question to be considered is whether iterative solvers can be safely used or not. Usually, their convergence is very sensitive to the condition number of the stiffness matrix, which grows as the penalty parameter decreases.

The objective of this section is to present an iterative penalty finite element method whose basic motivation is alleviating the problems mentioned above. The incompressibility equation is penalized in each iteration but the residual of the previous iterate is added as a forcing term. The interesting issue is what happens when the iterative penalization is coupled with the iterative procedure due to the nonlinearity of the problem. As in Reference [Co1], we analyse here what happens when the Picard and the Newton-Raphson algorithms are employed.

We will use the notation of the continuous problem. All the results also apply for its discrete finite element approximation.

### 1.4.1 Iterative penalization for the Stokes problem

The problem we consider in this section is (1.8) with $c = 0$, i.e., to find $\mathbf{u} \in V$ and $p \in Q_0$ such that

$$\begin{aligned} a(\mathbf{u},\mathbf{v}) - b(p,\mathbf{v}) &= l(\mathbf{v}) \qquad \forall \mathbf{v} \in V \\ b(q,\mathbf{u}) &= 0 \qquad \forall q \in Q \end{aligned} \tag{1.70}$$

The iterative penalty method that will be analysed is particularly simple to introduce for this linear problem.

*Motivation and statement of the algorithm*

If the penalty method is applied to solve (1.70), one has to find $\mathbf{u}^{\epsilon(1)} \in V$ and $p^{\epsilon(1)} \in Q$ such that

$$\begin{aligned} a(\mathbf{u}^{\epsilon(1)},\mathbf{v}) - b(p^{\epsilon(1)},\mathbf{v}) &= l(\mathbf{v}) \qquad \forall \mathbf{v} \in V \\ \epsilon(p^{\epsilon(1)},q) + b(q,\mathbf{u}^{\epsilon(1)}) &= 0 \qquad \forall q \in Q \end{aligned} \tag{1.71}$$

Once $\mathbf{u}^{\epsilon(1)}$ and $p^{\epsilon(1)}$ are found, define $\delta\mathbf{u}$ and $\delta p$ such that $\mathbf{u} = \mathbf{u}^{\epsilon(1)} + \delta\mathbf{u}$ and $p = p^{\epsilon(1)} + \delta p$. Then, $\delta\mathbf{u}$ and $\delta p$ will be the solution of

$$\begin{aligned} a(\delta\mathbf{u},\mathbf{v}) - b(\delta p,\mathbf{v}) &= 0 \qquad \forall \mathbf{v} \in V \\ b(q,\delta\mathbf{u}) &= \epsilon(p^{\epsilon(1)},q) \qquad \forall q \in Q \end{aligned}$$

Now, this problem can also be solved using the penalty method. If $\delta\mathbf{u}^\epsilon, \delta p^\epsilon$ is the penalized solution and we define $\mathbf{u}^{\epsilon(2)} = \mathbf{u}^{\epsilon(1)} + \delta\mathbf{u}^\epsilon$, $p^{\epsilon(2)} = p^{\epsilon(1)} + \delta p^\epsilon$, we will have that

$$\begin{aligned} a(\mathbf{u}^{\epsilon(2)},\mathbf{v}) - b(p^{\epsilon(2)},\mathbf{v}) &= l(\mathbf{v}) \qquad \forall \mathbf{v} \in V \\ \epsilon(p^{\epsilon(2)},q) + b(q,\mathbf{u}^{\epsilon(2)}) &= \epsilon(p^{\epsilon(1)},q) \qquad \forall q \in Q \end{aligned} \tag{1.72}$$

The argument used to arrive at problem (1.72) may be applied iteratively. This leads to the following algorithm:

*Given $p^{\epsilon(0)} \in Q_0$, for $i = 1, 2, \ldots$ find $(\mathbf{u}^{\epsilon(i)}, p^{\epsilon(i)}) \in V \times Q_0$ such that*

$$\begin{aligned} a(\mathbf{u}^{\epsilon(i)},\mathbf{v}) - b(p^{\epsilon(i)},\mathbf{v}) &= l(\mathbf{v}) \qquad \forall \mathbf{v} \in V \\ \epsilon(p^{\epsilon(i)},q) + b(q,\mathbf{u}^{\epsilon(i)}) &= \epsilon(p^{\epsilon(i-1)},q) \qquad \forall q \in Q \end{aligned} \tag{1.73}$$

Existence and uniqueness of solution follows considering the problem in the space $V \times Q$ and applying Lax-Milgram's Lemma. This algorithm will be analysed below and extended to the Navier-Stokes equations. Before that, some other existing methods will be discussed.

*Some remarks on related methods*

Algorithm (1.73) may be viewed as a variant of the Augmented Lagrangian method (see, e.g. References [Gl], [Te]) provided that Uzawa's algorithm is used to update the pressure. This was implicitly done in early works whose basic motivation was also the computational problems encountered when small penalties are used (for example, the method was applied to linear incompressible Elasticity in Reference [Sa] and the discrete algebraic system was considered in Reference [Fe]. See also Reference [ZVT]). An important difference between our approach and the Augmented Lagrangian method is that, as will be seen below, we *will not* require the bilinear form $a(\cdot,\cdot)$ to be symmetric (although it certainly is, for the problem we consider) and thus an associated minimization problem is not needed for deriving (1.73).

The residual out-of-balance argument used to arrive at algorithm (1.73) is completely general and has physical meaning for nonlinear cases, either if the nonlinearity comes from the momentum equations (Navier-Stokes problem) or from the constitutive law of the material. The step from problem (1.72) to problem (1.73) may be applied to nonlinear problems as well, although in these cases $\delta\mathbf{u}$ and $\delta p$ will be the solution of a nonlinear problem that in turn has to be linearized. Our leading idea is trying to converge in this process to the true incompressible solution. See the Appendix of Reference [CCO].

There are possibly many ways for 're-discovering' algorithm (1.73). Another one is to introduce a false transient for the pressure (not for the momentum equation) assuming the fluid to be slightly compressible and then to discretize the temporal derivative using the backward Euler scheme. Except for this discretization, this is nothing but the artificial compressibility method introduced by Chorin [Ch]. The penalty parameter $\epsilon$ in this case would be the inverse of $c^2\Delta t$, where $c$ is the speed of sound in the fluid and $\Delta t$ the time step (see Reference [HD] for further discussion). This approach makes sense for algorithm (1.73) and for the algorithm considered in Section 1.4.4. However, it ceases to be valid when the second equation in (1.73) is coupled with a linearized form of the Navier-Stokes equations, whereas the residual argument used above can be easily extended to these cases.

*Convergence of the algorithm*

Before studying the convergence of the iterates of (1.73), let us state two simple results:

**Lemma 1.1** *If $q \in Q_0$ then $\|q\|_{Q/Z} = \|q\|$.*

*Proof:* It follows directly from the definition of $\|\cdot\|_{Q/Z}$ and the fact that, in our case, $Z = \mathbb{R}$:

$$\begin{aligned}\|q\|_{Q/Z} &= \inf_{c\in\mathbb{R}} \|q+c\| \\ &= \inf_{c\in\mathbb{R}} \{\|q\|^2 + \|c\|^2 + 2(q,c)\}^{\frac{1}{2}}\end{aligned}$$

$$= \inf_{c \in \mathbb{R}} \{||q||^2 + ||c||^2\}^{\frac{1}{2}}$$
$$= ||q||. \qquad \square$$

This lemma will allow us to omit the subscript $Q/Z$ when using condition (1.10). We will also need the following *a priori* estimates:

**Lemma 1.2** *Let* $\mathbf{u}$ *and* $p$ *be the solution of the Stokes problem (1.70). Then*

$$||\mathbf{u}|| \leq \frac{N_l}{K_a} \tag{1.74}$$

$$||p|| \leq \frac{N_l}{K_b}\left(1 + \frac{N_a}{K_a}\right) \tag{1.75}$$

*Proof:* Taking $\mathbf{v} = \mathbf{u}$ in (1.70) we get

$$K_a||\mathbf{u}||^2 \leq a(\mathbf{u},\mathbf{u}) = l(\mathbf{u}) \leq N_l||\mathbf{u}||$$

and (1.74) follows. On the other hand, condition (1.10) implies that there exists $\mathbf{v} \in V - \{0\}$ such that

$$\begin{aligned} K_b||p||||\mathbf{v}|| &\leq b(p,\mathbf{v}) \\ &= a(\mathbf{u},\mathbf{v}) - l(\mathbf{v}) \\ &\leq (N_l + N_a||\mathbf{u}||)\,||\mathbf{v}|| \end{aligned}$$

and using (1.74) we obtain (1.75). □

We now proceed to the main result of this subsection.

**Theorem 1.1** *Let* $(\mathbf{u},p) \in V \times Q_0$ *be the solution of the Stokes problem (1.70) and* $(\mathbf{u}^{\epsilon(i)}, p^{\epsilon(i)}) \in V \times Q_0$ *the solution of (1.73). Define*

$$\bar{\epsilon} := \epsilon\frac{N_a^2}{K_a K_b^2}$$

*If* $\bar{\epsilon} < 1$ *then*

$$\lim_{i\to\infty} ||p - p^{\epsilon(i)}|| = 0, \qquad \lim_{i\to\infty} ||\mathbf{u} - \mathbf{u}^{\epsilon(i)}|| = 0$$

*Moreover, convergence is linear with* $\bar{\epsilon}$*:*

$$||p - p^{\epsilon(i)}|| \leq \bar{\epsilon}\; ||p - p^{\epsilon(i-1)}|| \tag{1.76}$$

$$||\mathbf{u} - \mathbf{u}^{\epsilon(i)}|| \leq \bar{\epsilon}\frac{K_b}{N_a}||p - p^{\epsilon(i-1)}|| \tag{1.77}$$

*Proof:* Substracting the equations of (1.70) and (1.73) one finds:

$$\begin{aligned} a(\mathbf{u} - \mathbf{u}^{\epsilon(i)}, \mathbf{v}) - b(p - p^{\epsilon(i)}, \mathbf{v}) = 0 \quad \forall \mathbf{v} \in V \\ \epsilon(p^{\epsilon(i-1)} - p^{\epsilon(i)}, q) + b(q, \mathbf{u} - \mathbf{u}^{\epsilon(i)}) = 0 \quad \forall q \in Q \end{aligned} \tag{1.78}$$

On the other hand, we have that:

$$\begin{aligned}0 &\le (p - p^{\epsilon(i)}, p - p^{\epsilon(i)})\\ &= (p^{\epsilon(i-1)} - p^{\epsilon(i)}, p - p^{\epsilon(i)}) + (p - p^{\epsilon(i-1)}, p - p^{\epsilon(i)})\end{aligned}$$

and then

$$(p^{\epsilon(i)} - p^{\epsilon(i-1)}, p - p^{\epsilon(i)}) \le (p - p^{\epsilon(i-1)}, p - p^{\epsilon(i)}) \tag{1.79}$$

This inequality will be used several times. Taking $\mathbf{v} = \mathbf{u} - \mathbf{u}^{\epsilon(i)}$ and $q = p - p^{\epsilon(i)}$ in (1.78) and using (1.79) we get:

$$\begin{aligned}K_a\|\mathbf{u} - \mathbf{u}^{\epsilon(i)}\|^2 &\le a(\mathbf{u} - \mathbf{u}^{\epsilon(i)}, \mathbf{u} - \mathbf{u}^{\epsilon(i)})\\ &= b(p - p^{\epsilon(i)}, \mathbf{u} - \mathbf{u}^{\epsilon(i)})\\ &= \epsilon(p^{\epsilon(i)} - p^{\epsilon(i-1)}, p - p^{\epsilon(i)})\\ &\le \epsilon(p - p^{\epsilon(i-1)}, p - p^{\epsilon(i)})\\ &\le \epsilon\|p - p^{\epsilon(i-1)}\|\,\|p - p^{\epsilon(i)}\| \end{aligned}\tag{1.80}$$

Using the BB condition, there exists $\mathbf{v} \in V - \{\mathbf{0}\}$ such that

$$\begin{aligned}K_b\|p - p^{\epsilon(i)}\|\,\|\mathbf{v}\| &\le b(p - p^{\epsilon(i)}, \mathbf{v})\\ &= a(\mathbf{u} - \mathbf{u}^{\epsilon(i)}, \mathbf{v})\\ &\le N_a\|\mathbf{u} - \mathbf{u}^{\epsilon(i)}\|\,\|\mathbf{v}\|\end{aligned}$$

and hence

$$\|p - p^{\epsilon(i)}\| \le \frac{N_a}{K_b}\|\mathbf{u} - \mathbf{u}^{\epsilon(i)}\| \tag{1.81}$$

Combining (1.80) and (1.81) relations (1.76) and (1.77) are found. Applying inductively this inequalities, we get

$$\begin{aligned}\|p - p^{\epsilon(i)}\| &\le \bar{\epsilon}^i\|p - p^{\epsilon(0)}\|\\ \|\mathbf{u} - \mathbf{u}^{\epsilon(i)}\| &\le \bar{\epsilon}^i\frac{K_b}{N_a}\|p - p^{\epsilon(0)}\|\end{aligned}$$

The theorem follows from the fact that $\bar{\epsilon} < 1$. □

If we take $p^{\epsilon(0)} = 0$ and apply Lemma 1.2, we see that

$$\begin{aligned}\|p - p^{\epsilon(i)}\| &\le C_1\bar{\epsilon}^i\\ \|\mathbf{u} - \mathbf{u}^{\epsilon(i)}\| &\le C_2\bar{\epsilon}^i\end{aligned}\tag{1.82}$$

where the constants $C_1$ and $C_2$ are

$$\begin{aligned}C_1 &:= \frac{N_l}{K_b}\left(1 + \frac{N_a}{K_a}\right)\\ C_2 &:= \frac{N_l}{N_a}\left(1 + \frac{N_a}{K_a}\right)\end{aligned}$$

The rates of convergence (1.82) will be checked numerically in Section 1.5.

The result stated by Theorem 1.1 can also be proved for the fully discrete system and in matrix form, only requiring simple linear algebra concepts. This has been done in Reference [CCO], where it is also explained why the penalty parameter must be taken proportional to $\mu^{-1}$.

### 1.4.2 A Picard-based iterative algorithm for the Navier-Stokes equations

The Stokes problem is linear and to iterate is a price to be paid if one wants to satisfy (weakly) the constraint $\nabla \cdot \mathbf{u} = 0$ up to a certain tolerance with a given penalty parameter $\epsilon$. However, an iterative algorithm is needed for the Navier-Stokes equations and if the iteration loop could be coupled with the iterative penalization, we would have satisfied the incompressibility constraint at a low computational cost. The purpose of this section is to investigate whether this is possible or not when the Picard scheme is used to deal with the nonlinear term. Theorem 1.2 below gives sufficient conditions under which the final algorithm is convergent.

The problem to be considered now is (1.8) with $c$ given by (1.3) (or its skew-symmetric form):

*Find* $(\mathbf{u}, p) \in V \times Q_0$ *such that*

$$\begin{aligned} c(\mathbf{u},\mathbf{u},\mathbf{v}) + a(\mathbf{u},\mathbf{v}) - b(p,\mathbf{v}) &= l(\mathbf{v}) \qquad \forall \mathbf{v} \in V \\ b(q,\mathbf{u}) &= 0 \qquad \forall q \in Q \end{aligned} \tag{1.83}$$

The Picard or successive substitution algorithm for this problem is:

*Given* $\mathbf{u}^{(0)} \in V$, *for* $i = 1, 2, \ldots$ *find* $(\mathbf{u}^{(i)}, p^{(i)}) \in V \times Q_0$ *such that*

$$\begin{aligned} c(\mathbf{u}^{(i-1)},\mathbf{u}^{(i)},\mathbf{v}) + a(\mathbf{u}^{(i)},\mathbf{v}) - b(p^{(i)},\mathbf{v}) &= l(\mathbf{v}) \qquad \forall \mathbf{v} \in V \\ b(q,\mathbf{u}^{(i)}) &= 0 \qquad \forall q \in Q \end{aligned} \tag{1.84}$$

We note that sometimes the name *Picard algorithm* is reserved for the case when all arguments of the nonlinear term are evaluated in the previous iteration (see Eqn. (1.62)). Convergence of algorithm (1.84) for any initial guess $\mathbf{u}^{(0)}$ assuming that condition (1.12) holds is a well known result (see, e.g. [CK4] for the case of strong penalty methods). The scheme we propose and analyse is the following:

*Given* $(\mathbf{u}^{\epsilon(0)}, p^{\epsilon(0)}) \in V \times Q_0$, *for* $i = 1, 2, \ldots$ *find* $(\mathbf{u}^{\epsilon(i)}, p^{\epsilon(i)}) \in V \times Q_0$ *such that*

$$\begin{aligned} c(\mathbf{u}^{\epsilon(i-1)},\mathbf{u}^{\epsilon(i)},\mathbf{v}) + a(\mathbf{u}^{\epsilon(i)},\mathbf{v}) - b(p^{\epsilon(i)},\mathbf{v}) &= l(\mathbf{v}) \qquad \forall \mathbf{v} \in V \\ \epsilon(p^{\epsilon(i)},q) + b(q,\mathbf{u}^{\epsilon(i)}) &= \epsilon(p^{\epsilon(i-1)},q) \qquad \forall q \in Q \end{aligned} \tag{1.85}$$

Once again, existence and uniqueness of solution for (1.85) follows considering the problem in the space $V \times Q$ and applying Lax-Milgram's Lemma, since coercivity of the associated bilinear form is a consequence of (1.9) and (1.11). Before proving convergence in norm of the iterates of (1.85) to the solution of (1.83) we state the following *a priori* estimates to be used later:

**Lemma 1.3** *Let* $(\mathbf{u}, p)$ *and* $(\mathbf{u}^{\epsilon(i)}, p^{\epsilon(i)})$ *be the solutions of (1.83) and (1.85), respectively. Then*

$$\|\mathbf{u}\| \leq \frac{N_l}{K_a} \tag{1.86}$$

$$\|\mathbf{u}^{\epsilon(i)}\| \leq \frac{N_l}{K_a} + \sqrt{\frac{\epsilon}{K_a}} \left( \|p - p^{\epsilon(i-1)}\| + \|p\| \right) \tag{1.87}$$

*Proof:* Estimate (1.86) is obtained exactly as (1.74) noting (1.11). To prove (1.87), take $\mathbf{v} = \mathbf{u}^{\epsilon(i)}$ and $q = p^{\epsilon(i)}$ in (1.85). We get:

$$\begin{aligned} l(\mathbf{u}^{\epsilon(i)}) &= a(\mathbf{u}^{\epsilon(i)}, \mathbf{u}^{\epsilon(i)}) + \epsilon(p^{\epsilon(i)} - p^{\epsilon(i-1)}, p^{\epsilon(i)}) \\ &= a(\mathbf{u}^{\epsilon(i)}, \mathbf{u}^{\epsilon(i)}) + \frac{\epsilon}{2}\|p^{\epsilon(i)} - p^{\epsilon(i-1)}\|^2 + \frac{\epsilon}{2}\left(\|p^{\epsilon(i)}\|^2 - \|p^{\epsilon(i-1)}\|^2\right) \\ &\geq a(\mathbf{u}^{\epsilon(i)}, \mathbf{u}^{\epsilon(i)}) - \frac{\epsilon}{2}\|p^{\epsilon(i-1)}\|^2 \end{aligned}$$

and hence

$$\begin{aligned} 2K_a\|\mathbf{u}^{\epsilon(i)}\|^2 &\leq 2N_l\|\mathbf{u}^{\epsilon(i)}\| + \epsilon\|p^{\epsilon(i-1)}\|^2 \\ &\leq \frac{N_l^2}{K_a} + K_a\|\mathbf{u}^{\epsilon(i)}\|^2 + \epsilon\|p^{\epsilon(i-1)}\|^2 \end{aligned}$$

and (1.87) follows easily applying the triangle inequality to $\|p^{\epsilon(i-1)} - p + p\|$. □

We next establish convergence of algorithm (1.85).

**Theorem 1.2** *Let $(\mathbf{u}, p) \in V \times Q_0$ and $(\mathbf{u}^{\epsilon(i)}, p^{\epsilon(i)}) \in V \times Q_0$ be the solutions of (1.83) and (1.85) respectively. Assume that*

$$\epsilon < \frac{K_a K_b^2}{N_c^2}$$

*and for any $\alpha \geq 2$ define the following constants:*

$$\begin{aligned} M &:= \left[\frac{N_l}{K_a} + \sqrt{\frac{\epsilon}{K_a}}\left(\alpha\frac{N_a}{K_b}\|\mathbf{u} - \mathbf{u}^{\epsilon(0)}\| + \|p - p^{\epsilon(0)}\| + \|p\|\right)\right]\left[1 - \sqrt{\frac{\epsilon}{K_a}}\frac{N_c}{K_b}\right]^{-1} \\ C_\alpha &:= \frac{1}{K_b}(N_c M + \alpha N_a) \\ \beta &:= \frac{1}{2} + \frac{1}{2}\left(1 + \frac{2}{\alpha}\right)^{\frac{1}{2}} \\ \bar{\epsilon} &:= \epsilon\frac{1}{K_a}C_\alpha^2 \\ \bar{\chi} &:= \beta(\chi + \bar{\epsilon}) \end{aligned}$$

*with $\chi$ defined in (1.12). Suppose that $\bar{\chi} < 1$ and that the initial guess for the velocity satisfies $\|\mathbf{u}^{\epsilon(0)}\| \leq M$. Then, the following holds:*

$$\|\mathbf{u}^{\epsilon(i)}\| \leq M, \quad i = 1, 2, ... \tag{1.88}$$

$$\lim_{i\to\infty}\|p - p^{\epsilon(i)}\| = 0, \quad \lim_{i\to\infty}\|\mathbf{u} - \mathbf{u}^{\epsilon(i)}\| = 0 \tag{1.89}$$

*Moreover, convergence is linear with $\bar{\chi}$, that is, there exist constants $C$ and $C'$ such that, for i=1,2,...*

$$\begin{aligned} \|p - p^{\epsilon(i)}\| &\leq C\bar{\chi}^i \\ \|\mathbf{u} - \mathbf{u}^{\epsilon(i)}\| &\leq C'\bar{\chi}^i \end{aligned} \tag{1.90}$$

*Proof:* Only (1.90) has to be proved, since (1.89) follows from the fact that $\bar{\chi} < 1$. We proceed by induction. By hypothesis, (1.88) holds for $i = 0$. Assume that it is true up to $i-1$, with $i \geq 1$ fixed. Substracting the equations of (1.85) from (1.83) and using the fact that for a bilinear form $g$ we have $g(u_1, v_1) - g(u_2, v_2) = g(u_1 - u_2, v_1) + g(u_2, v_1 - v_2)$, we get:

$$\begin{aligned} c(\mathbf{u} - \mathbf{u}^{\epsilon(i-1)}, \mathbf{u}, \mathbf{v}) + c(\mathbf{u}^{\epsilon(i-1)}, \mathbf{u} - \mathbf{u}^{\epsilon(i)}, \mathbf{v}) \\ + a(\mathbf{u} - \mathbf{u}^{\epsilon(i)}, \mathbf{v}) - b(p - p^{\epsilon(i)}, \mathbf{v}) = 0 \qquad \forall \mathbf{v} \in V \\ \epsilon(p^{\epsilon(i-1)} - p^{\epsilon(i)}, q) + b(q, \mathbf{u} - \mathbf{u}^{\epsilon(i)}) = 0 \qquad \forall q \in Q \end{aligned}$$

Taking $\mathbf{v} = \mathbf{u} - \mathbf{u}^{\epsilon(i)}$ and $q = p - p^{\epsilon(i)}$ we obtain

$$a(\mathbf{u} - \mathbf{u}^{\epsilon(i)}, \mathbf{u} - \mathbf{u}^{\epsilon(i)}) = \epsilon(p^{\epsilon(i)} - p^{\epsilon(i-1)}, p - p^{\epsilon(i)}) - c(\mathbf{u} - \mathbf{u}^{\epsilon(i-1)}, \mathbf{u}, \mathbf{u} - \mathbf{u}^{\epsilon(i)})$$

and using the coercivity of $a$, (1.12) and Lemma 1.3:

$$\begin{aligned} K_a\|\mathbf{u} - \mathbf{u}^{\epsilon(i)}\|^2 &\leq N_c\|\mathbf{u}\|\|\mathbf{u} - \mathbf{u}^{\epsilon(i-1)}\|\|\mathbf{u} - \mathbf{u}^{\epsilon(i)}\| + \epsilon\|p - p^{\epsilon(i-1)}\|\|p - p^{\epsilon(i)}\| \\ &\leq K_a\chi\|\mathbf{u} - \mathbf{u}^{\epsilon(i-1)}\|\|\mathbf{u} - \mathbf{u}^{\epsilon(i)}\| + \epsilon\|p - p^{\epsilon(i-1)}\|\|p - p^{\epsilon(i)}\| \quad (1.91) \end{aligned}$$

The BB condition implies that there exists $\mathbf{v} \in V - \{0\}$ such that

$$\begin{aligned} &K_b\|p - p^{\epsilon(i)}\| \, \|\mathbf{v}\| \leq b(p - p^{\epsilon(i)}, \mathbf{v}) \\ &\quad = a(\mathbf{u} - \mathbf{u}^{\epsilon(i)}, \mathbf{v}) + c(\mathbf{u} - \mathbf{u}^{\epsilon(i-1)}, \mathbf{u}, \mathbf{v}) + c(\mathbf{u}^{\epsilon(i-1)}, \mathbf{u} - \mathbf{u}^{\epsilon(i)}, \mathbf{v}) \\ &\quad \leq \left( N_c\|\mathbf{u}\|\|\mathbf{u} - \mathbf{u}^{\epsilon(i-1)}\| + N_c\|\mathbf{u}^{\epsilon(i-1)}\|\|\mathbf{u} - \mathbf{u}^{\epsilon(i)}\| + N_a\|\mathbf{u} - \mathbf{u}^{\epsilon(i)}\| \right) \|\mathbf{v}\| \end{aligned}$$

Using again Lemma 1.3 and (1.88) for $i-1$:

$$\|p - p^{\epsilon(i)}\| \leq \frac{K_a}{K_b}\chi\|\mathbf{u} - \mathbf{u}^{\epsilon(i-1)}\| + \frac{N_c M}{K_b}\|\mathbf{u} - \mathbf{u}^{\epsilon(i)}\| + \frac{N_a}{K_b}\|\mathbf{u} - \mathbf{u}^{\epsilon(i)}\| \qquad (1.92)$$

Inequalities (1.91) and (1.92) can be written as

$$U^{(i)^2} \leq \chi U^{(i-1)} U^{(i)} + \epsilon \frac{1}{K_a} P^{(i-1)} P^{(i)} \qquad (1.93)$$

$$P^{(i)} \leq \frac{K_a}{K_b}\chi U^{(i-1)} + \left( \frac{N_c M}{K_b} + \frac{N_a}{K_b} \right) U^{(i)} \qquad (1.94)$$

where we have defined

$$U^{(j)} := \|\mathbf{u} - \mathbf{u}^{\epsilon(j)}\|, \quad P^{(j)} := \|p - p^{\epsilon(j)}\|$$

for $j = i$ or $i-1$. Using (1.94) in (1.93) we get:

$$U^{(i)^2} \leq A_1 U^{(i)} + A_2 \qquad (1.95)$$

where

$$\begin{aligned} A_1 &:= \chi U^{(i-1)} + \epsilon \frac{1}{K_a} P^{(i-1)} \left( \frac{N_c M}{K_b} + \frac{N_a}{K_b} \right) \\ A_2 &:= \epsilon \frac{1}{K_a} P^{(i-1)} \chi \frac{K_a}{K_b} U^{(i-1)} \end{aligned}$$

Since

$$A_1 \leq A_0 := \chi U^{(i-1)} + \epsilon \frac{1}{K_a} P^{(i-1)} C_\alpha$$

we see from (1.95) that

$$U^{(i)^2} \leq A_0 U^{(i)} + A_2 \tag{1.96}$$

$A_0^2$ contains the term

$$2\chi U^{(i-1)} \epsilon \frac{1}{K_a} P^{(i-1)} C_\alpha$$

and, since $K_a \leq N_a$ we get

$$\begin{aligned} A_2 &\leq \frac{\epsilon}{K_a} P^{(i-1)} \chi \frac{N_a}{K_b} U^{(i-1)} \\ &\leq \frac{\epsilon}{K_a} P^{(i-1)} \chi \frac{1}{\alpha} C_\alpha U^{(i-1)} \end{aligned}$$

Hence $A_0^2 \geq 2\alpha A_2$ and from (1.96) we obtain:

$$\begin{aligned} U^{(i)} &\leq \frac{1}{2} A_0 + \frac{1}{2} \left( A_0^2 + 4A_2 \right)^{\frac{1}{2}} \\ &\leq \left[ \frac{1}{2} + \frac{1}{2} \left( 1 + \frac{2}{\alpha} \right)^{\frac{1}{2}} \right] A_0 \\ &= \beta A_0 \end{aligned}$$

Substitution of this inequality in (1.94) and writing the expression of $A_0$ leads to

$$\begin{aligned} U^{(i)} &\leq \beta \chi U^{(i-1)} + \beta \epsilon \frac{1}{K_a} C_\alpha P^{(i-1)} \\ &= \beta \chi U^{(i-1)} + \beta \bar{\epsilon} C_\alpha^{-1} P^{(i-1)} \\ P^{(i)} &\leq \frac{K_a}{K_b} \chi U^{(i-1)} + \beta \chi C_1 U^{(i-1)} + \beta \epsilon \frac{1}{K_a} C_1 C_\alpha P^{(i-1)} \\ &\leq \beta \chi C_2 U^{(i-1)} + \beta \epsilon \frac{1}{K_a} C_\alpha C_\alpha P^{(i-1)} \\ &\leq \beta \chi C_\alpha U^{(i-1)} + \beta \bar{\epsilon} P^{(i-1)} \end{aligned}$$

From this and assuming that (1.90) holds up to $i-1$ one easily gets that (1.90) is also true for the given $i$ with the constants appearing in (1.90) $C = C_\alpha \|\mathbf{u} - \mathbf{u}^{\epsilon(0)}\| + \|p - p^{\epsilon(0)}\|$, $C' = \|\mathbf{u} - \mathbf{u}^{\epsilon(0)}\| + C_\alpha^{-1} \|p - p^{\epsilon(0)}\|$. It only remains to show that (1.88) holds for this iteration. Applying Lemma 1.3 and the fact that $P^{(i-1)} \leq C_\alpha U^{(0)} + P^{(0)}$ we obtain:

$$\begin{aligned} \|\mathbf{u}^{\epsilon(i)}\| &\leq \frac{N_l}{K_a} + \sqrt{\frac{\epsilon}{K_a}} \left[ C_\alpha \|\mathbf{u} - \mathbf{u}^{\epsilon(0)}\| + \|p - p^{\epsilon(0)}\| + \|p\| \right] \\ &= \frac{N_l}{K_a} + \sqrt{\frac{\epsilon}{K_a}} \left[ \left( \frac{N_c}{K_b} M + \alpha \frac{N_a}{K_b} \right) \|\mathbf{u} - \mathbf{u}^{\epsilon(0)}\| + \|p - p^{\epsilon(0)}\| + \|p\| \right] \\ &= M \end{aligned}$$

and the induction is complete. □

It is interesting to compare the result stated by this theorem with what one obtains for the Picard algorithm (1.84). First of all, in this case convergence is achieved regardless of the initial guess $\mathbf{u}^{(0)}$, whereas for (1.85) we have seen that $\mathbf{u}^{\epsilon(0)}$ has to have a norm bounded by the constant $M$. For practical purposes, this does not present any trouble, since one usually starts taking $\mathbf{u}^{\epsilon(0)} = \mathbf{0}$.

For (1.84) it is known that (1.90) holds with $\chi$ instead of $\bar{\chi}$. However, from the definition of $C_\alpha, \beta$ and $\bar{\epsilon}$ we see that if $\alpha$ is taken of order $\epsilon^{-q}$, with $q < \frac{1}{2}$, then $\bar{\epsilon} \to 0$ and $\beta \to 1$ as $\epsilon \to 0$, that is, $\bar{\chi} \to \chi$. So, for $\epsilon$ small the convergence of algorithm (1.85) is the same as that of (1.84). One can obtain $\alpha$ such that $\bar{\chi}$ be minimized (under the restriction $\alpha \geq 2$). For example, taking the norms and the coercivity constants of the forms involved in the problem equal to unity, one obtains that the optimal condition for achieving convergence is $\chi < 0.7511$ for $\epsilon = 10^{-1}$ and $\chi < 0.9744$ for $\epsilon = 10^{-4}$. The fact that, in any case, $\bar{\chi} \geq \chi$ is the cost of converging to the true incompressible solution using a penalized scheme.

### 1.4.3 A Newton-Raphson-based iterative algorithm for the Navier-Stokes equations

The objective of this section is to analyse the algorithm obtained when the Newton-Raphson scheme is coupled with the iterative penalization in the sense used previously for the Picard scheme. Once again, we will see that the usual convergence requirements of the Newton-Raphson method have to be slightly restricted. In this case, there is another important issue to be considered. It is well known that convergence is quadratic for Newton-Raphson's iterates. The question is whether this rate of convergence will be inherited by the scheme we propose. The answer is that this is true up to a certain iteration. From there onwards, the convergence rate will only be linear. However, the numerical experiments we have performed, some of which are presented in Section 1.5, indicate that the situation is not so bad as it might seem. For small penalty parameters, usually much larger than those used in classical penalty methods, convergence is achieved before its rate turns from quadratic to linear.

The Newton-Raphson algorithm applied to problem (1.83) reads as follows:

*Given $\mathbf{u}^{(0)} \in V$, for $i = 1, 2, \ldots$ find $(\mathbf{u}^{(i)}, p^{(i)}) \in V \times Q_0$ such that*

$$\begin{aligned} c(\mathbf{u}^{(i-1)}, \mathbf{u}^{(i)}, \mathbf{v}) + c(\mathbf{u}^{(i)}, \mathbf{u}^{(i-1)}, \mathbf{v}) + a(\mathbf{u}^{(i)}, \mathbf{v}) - b(p^{(i)}, \mathbf{v}) & \\ = c(\mathbf{u}^{(i-1)}, \mathbf{u}^{(i-1)}, \mathbf{v}) + l(\mathbf{v}) & \qquad \forall \mathbf{v} \in V \\ b(q, \mathbf{u}^{(i)}) = 0 & \qquad \forall q \in Q \end{aligned} \tag{1.97}$$

That this algorithm is convergent if the initial guess is sufficiently close to the exact solution and that convergence is quadratic is a well known result. In [GR], this is proved when the solution of (1.84) belongs to a nonsingular branch. The modified algorithm we will consider is the following:

*Given $(\mathbf{u}^{\epsilon(0)}, p^{\epsilon(0)}) \in V \times Q_0$, for $i = 1, 2, \ldots$ find $(\mathbf{u}^{\epsilon(i)}, p^{\epsilon(i)}) \in V \times Q_0$ such that*

$$\begin{aligned} c(\mathbf{u}^{\epsilon(i-1)}, \mathbf{u}^{\epsilon(i)}, \mathbf{v}) + c(\mathbf{u}^{\epsilon(i)}, \mathbf{u}^{\epsilon(i-1)}, \mathbf{v}) + a(\mathbf{u}^{\epsilon(i)}, \mathbf{v}) - b(p^{\epsilon(i)}, \mathbf{v}) & \\ = c(\mathbf{u}^{\epsilon(i-1)}, \mathbf{u}^{\epsilon(i-1)}, \mathbf{v}) + l(\mathbf{v}) & \qquad \forall \mathbf{v} \in V \\ \epsilon(p^{\epsilon(i)}, q) + b(q, \mathbf{u}^{\epsilon(i)}) = \epsilon(p^{\epsilon(i-1)}, q) & \qquad \forall q \in Q \end{aligned} \tag{1.98}$$

Our analysis will be based on the assumption that (1.12) holds.

**Theorem 1.3** *Let $(\mathbf{u},p) \in V \times Q_0$ and $(\mathbf{u}^{\epsilon(i)}, p^{\epsilon(i)}) \in V \times Q_0$ be the solutions of (1.83) and (1.98) respectively. Let $\alpha \geq 2$ be given and define the following constants:*

$$\begin{aligned}
C &:= \frac{2N_c}{K_a(1-\chi)} \\
C_\alpha &:= \frac{K_a}{2K_b}(1+3\chi) + \alpha\frac{N_a}{K_b} \\
\beta &:= \frac{1}{2} + \frac{1}{2}\left(1+\frac{2}{\alpha}\right)^{\frac{1}{2}} \\
\bar{\epsilon} &:= \epsilon\frac{CC_\alpha^2}{N_c}
\end{aligned}$$

*Assume that the following conditions are satisfied:*

$$(H1) \qquad \|\mathbf{u}-\mathbf{u}^{\epsilon(0)}\| < \frac{1}{C\beta}\frac{\sigma}{\gamma}, \quad \text{with} \quad \sigma < 1, \ \ \gamma > 1$$

$$(H2) \qquad \bar{\epsilon} < \frac{\gamma-1}{\beta\gamma}\sigma$$

$$(H3) \qquad \bar{\epsilon}\|p-p^{\epsilon(0)}\| < \frac{\gamma-1}{\beta^2\gamma^2}\frac{C_\alpha}{C}\sigma^2 \quad \text{or} \quad \|p-p^{\epsilon(0)}\| < \frac{C_\alpha}{C\beta}\frac{\sigma}{\gamma}$$

*Under these conditions, we have that, for $i = 1, 2, \ldots$*

$$(T1) \qquad \|\mathbf{u}-\mathbf{u}^{\epsilon(i)}\| < \frac{1}{C\beta}\frac{\sigma}{\gamma}, \quad \|p-p^{\epsilon(i)}\| < \frac{C_\alpha}{C\beta}\frac{\sigma}{\gamma}$$

$$(T2) \qquad K_a - N_c\|\mathbf{u}^{\epsilon(i)}\| > \frac{K_a}{2}(1-\chi)$$

$$(T3) \qquad \lim_{i\to\infty}\|p-p^{\epsilon(i)}\| = 0, \quad \lim_{i\to\infty}\|\mathbf{u}-\mathbf{u}^{\epsilon(i)}\| = 0$$

*Moreover, if for a certain $I$*

$$(H4) \qquad \bar{\epsilon} < \frac{\gamma-1}{\beta\gamma}\sigma^{2I-1}$$

*then convergence is quadratic up to this $I$:*

$$(T4) \qquad \|\mathbf{u}-\mathbf{u}^{\epsilon(i)}\| < \frac{1}{C\beta}\frac{\sigma^{2^i}}{\gamma}, \quad \|p-p^{\epsilon(i)}\| < \frac{C_\alpha}{C\beta}\frac{\sigma^{2^i}}{\gamma}, \quad 1 \leq i \leq I$$

*Proof:* We proceed by induction. For $i = 0$, $(T1)$ is precisely $(H1)$ and $(H3)$ if the second option in this hypothesis is taken. In fact, for $i = 1, 2, \ldots$ we will see that any of the two possibilities in $(H3)$ are sufficient for proving $(T1)$. On the other hand, $(T2)$ for $i = 0$ follows from $(H1)$ and (1.86):

$$\begin{aligned}
K_a - N_c\|\mathbf{u}^{\epsilon(0)}\| &\geq K_a - N_c\|\mathbf{u}-\mathbf{u}^{\epsilon(0)}\| - N_c\|\mathbf{u}\| \\
&> K_a - \frac{N_c}{\beta}\frac{K_a(1-\chi)}{2N_c} - K_a\chi \\
&> \frac{1}{2}K_a(1-\chi)
\end{aligned} \tag{1.99}$$

since $\beta > 1$. Now, let $i$ be fixed and assume $(T1)$ and $(T2)$ hold up to $i-1$. In order to prove existence and uniqueness of solution for (1.98), let us write this problem as follows: Find $(\mathbf{u}^{\epsilon(i)}, p^{\epsilon(i)}) \in V \times Q_0$ such that

$$\mathcal{B}_{i-1}(\mathbf{u}^{\epsilon(i)}, p^{\epsilon(i)}; \mathbf{v}, q) = \mathcal{L}_{i-1}(\mathbf{v}, q) \quad \forall (\mathbf{v}, q) \in V \times Q$$

where

$$\begin{aligned}\mathcal{B}_{i-1}(\mathbf{u}, p; \mathbf{v}, q) :&= c(\mathbf{u}^{\epsilon(i-1)}, \mathbf{u}, \mathbf{v}) + c(\mathbf{u}, \mathbf{u}^{\epsilon(i-1)}, \mathbf{v}) + a(\mathbf{u}, \mathbf{v}) \\ &\quad - b(p, \mathbf{v}) + \epsilon(p, q) + b(q, \mathbf{u}) \\ \mathcal{L}_{i-1}(\mathbf{v}, q) :&= l(\mathbf{v}) + c(\mathbf{u}^{\epsilon(i-1)}, \mathbf{u}^{\epsilon(i-1)}, \mathbf{v}) + \epsilon(p^{\epsilon(i-1)}, q)\end{aligned}$$

If we prove that $\mathcal{B}_{i-1}$ is coercive in $V \times Q$, existence and uniqueness will follow from Lax-Milgram's Lemma. We see that

$$\begin{aligned}\mathcal{B}_{i-1}(\mathbf{v}, q; \mathbf{v}, q) &= c(\mathbf{v}, \mathbf{u}^{\epsilon(i-1)}, \mathbf{v}) + a(\mathbf{v}, \mathbf{v}) + \epsilon(q, q) \\ &\geq (K_a - N_c\|\mathbf{u}^{\epsilon(i-1)}\|)\|\mathbf{v}\|^2 + \epsilon\|q\|^2 \\ &\geq \min\{K_a - N_c\|\mathbf{u}^{\epsilon(i-1)}\|, \epsilon\}(\|\mathbf{v}\|^2 + \|q\|^2)\end{aligned}$$

and the fact that $K_a - N_c\|\mathbf{u}^{\epsilon(i-1)}\| > 0$ is a consequence of $(T2)$ used inductively.

Applying the same arguments as in Theorem 1.2 to arrive at (1.91) and (1.92) we now obtain:

$$\begin{aligned}K_a\|\mathbf{u} - \mathbf{u}^{\epsilon(i)}\|^2 &\leq N_c\|\mathbf{u} - \mathbf{u}^{\epsilon(i-1)}\|^2\|\mathbf{u} - \mathbf{u}^{\epsilon(i)}\| \\ &\quad + N_c\|\mathbf{u} - \mathbf{u}^{\epsilon(i)}\|^2\|\mathbf{u}^{\epsilon(i-1)}\| + \epsilon\|p - p^{\epsilon(i-1)}\|\|p - p^{\epsilon(i)}\| \qquad (1.100) \\ K_b\|p - p^{\epsilon(i)}\| &\leq N_c\|\mathbf{u}\|\|\mathbf{u} - \mathbf{u}^{\epsilon(i)}\| + N_c\|\mathbf{u} - \mathbf{u}^{\epsilon(i-1)}\|^2 \\ &\quad + N_c\|\mathbf{u}^{\epsilon(i-1)}\|\|\mathbf{u} - \mathbf{u}^{\epsilon(i)}\| + N_a\|\mathbf{u} - \mathbf{u}^{\epsilon(i)}\| \qquad (1.101)\end{aligned}$$

If we call

$$\begin{aligned}&U^{(j)} := \|\mathbf{u} - \mathbf{u}^{\epsilon(j)}\|, \quad P^{(j)} := \|p - p^{\epsilon(j)}\|, \quad j = i \text{ or } i-1 \\ &A_1 := K_a - N_c\|\mathbf{u}^{\epsilon(i-1)}\| \\ &A_2 := N_c U^{(i-1)^2} + \epsilon P^{(i-1)}\left(\frac{N_c}{K_b}\|\mathbf{u}\| + \frac{N_c}{K_b}\|\mathbf{u}^{\epsilon(i-1)}\| + \frac{N_a}{K_b}\right) \\ &A_3 := \epsilon P^{(i-1)}\frac{N_c}{K_b}U^{(i-1)^2}\end{aligned}$$

we find from the previous inequalities that

$$A_1 U^{(i)^2} \leq A_2 U^{(i)} + A_3 \qquad (1.102)$$

From $(T2)$ it is $A_1 > 0$. Note now that, from $(T1)$ and (1.86):

$$\begin{aligned}\frac{N_c}{K_b}\|\mathbf{u}\| + \frac{N_c}{K_b}\|\mathbf{u}^{\epsilon(i-1)}\| + \frac{N_a}{K_b} &< \frac{N_c}{K_b}\|\mathbf{u}\| + \frac{N_c}{K_b}\frac{1}{C} + \frac{N_c}{K_b}\|\mathbf{u}\| + \frac{N_a}{K_b} \\ &= \frac{2K_a}{K_b}\chi + \frac{N_a}{K_b} + \frac{K_a(1-\chi)}{2K_b} \\ &< C_a\end{aligned}$$

and so we have

$$A_2 < A_0 := N_c U^{(i-1)^2} + \epsilon P^{(i-1)} C_\alpha$$

$A_0^2$ contains the term

$$2 N_c U^{(i-1)^2} \epsilon P^{(i-1)} \alpha \frac{N_a}{K_b}$$

Since $K_a \leq N_a$ we have that

$$2A_1 A_3 < 2K_a \epsilon P^{(i-1)} \frac{N_c}{K_b} U^{(i-1)^2} < \frac{1}{\alpha} A_0^2$$

and hence, from (1.102) and using that $A_2 < A_0$ and $(T2)$:

$$\begin{aligned}
U^{(i)} &< \frac{1}{2}\frac{A_0}{A_1} + \frac{1}{2A_1}\left(A_0^2 + 4A_1A_3\right)^{\frac{1}{2}} \\
&< \frac{1}{2}\frac{A_0}{A_1} + \frac{1}{2A_1}\left(1 + \frac{2}{\alpha}\right)^{\frac{1}{2}} A_0 \\
&= \beta \frac{A_0}{A_1} \\
&< \frac{2\beta}{K_a(1-\chi)}\left(N_c U^{(i-1)^2} + \epsilon P^{(i-1)} C_\alpha\right) \\
&= C\beta U^{(i-1)^2} + \epsilon\beta \frac{C}{N_c} C_\alpha P^{(i-1)}
\end{aligned}$$

On the other hand, for the pressures we obtain from (1.101) that:

$$\begin{aligned}
P^{(i)} &\leq \frac{N_c}{K_b} U^{(i-1)^2} + \left(\frac{N_c}{K_b}\|\mathbf{u}^{\epsilon(i-1)}\| + \frac{N_c}{K_b}\|\mathbf{u}\| + \frac{N_a}{K_b}\right) U^{(i)} \\
&< \frac{N_c}{K_b} U^{(i-1)^2} + C_1 U^{(i)} \\
&< \frac{N_c}{K_b} U^{(i-1)^2} + C_1 C\beta U^{(i-1)^2} + \epsilon\beta C_\alpha \frac{C_1}{N_c} P^{(i-1)}
\end{aligned}$$

Noting that

$$\frac{N_a}{K_b}\beta C = \beta \frac{N_a}{K_b} \frac{2N_c}{K_a(1-\chi)} > \frac{N_c}{K_b}$$

we finally obtain that (1.100) and (1.101) imply:

$$U^{(i)} < C\beta U^{(i-1)^2} + \bar{\epsilon}\beta C_\alpha^{-1} P^{(i-1)} \tag{1.103}$$

$$P^{(i)} < CC_\alpha \beta U^{(i-1)^2} + \bar{\epsilon}\beta P^{(i-1)} \tag{1.104}$$

Now, using $(H2)$ and $(T1)$ for $i-1$ one gets:

$$\begin{aligned}
U^{(i)} &< C\beta \frac{1}{C^2\beta^2}\frac{\sigma^2}{\gamma^2} + \frac{\gamma-1}{\gamma}\sigma \frac{C_\alpha^{-1}C_\alpha}{C\beta}\frac{\sigma}{\gamma} \\
&= \frac{1}{C\beta}\frac{\sigma^2}{\gamma} \\
P^{(i)} &< CC_\alpha\beta \frac{1}{C^2\beta^2}\frac{\sigma^2}{\gamma^2} + \frac{\gamma-1}{\gamma}\sigma \frac{C_\alpha}{C\beta}\frac{\sigma}{\gamma} \\
&= \frac{C_\alpha}{C\beta}\frac{\sigma^2}{\gamma}
\end{aligned}$$

Since $\sigma < 1$, the induction for $(T1)$ is closed. Observe that either of the two possibilities in $(H3)$ suffices for proving this part of the thesis. $(T2)$ is obtained from $(T1)$ using the same steps as in (1.99). In order to prove $(T3)$, from (1.103) and (1.104) we see that the required condition is:

$$\theta^{(i)} := C\beta U^{(i)} + \bar{\epsilon}\beta < 1$$

From $(T1)$ and $(H2)$ it follows that $\theta^{(i)} < \sigma < 1$, so convergence of the algorithm is ensured. Inequalities (1.103) and (1.104) show that the rate of convergence will be at least linear.

Now, suppose that $(H4)$ holds. For $1 \leq i \leq I$ we obtain from (1.103) and (1.104) and assuming $(T4)$ to be true up to $i-1$, that:

$$\begin{aligned} U^{(i)} &< C\beta \frac{1}{C^2\beta^2}\frac{\sigma^{2^i}}{\gamma^2} + \frac{\gamma-1}{\gamma}\sigma^{2^{i-1}}\frac{C_\alpha^{-1}C_\alpha}{C\beta}\frac{\sigma^{2^{i-1}}}{\gamma} \\ &= \frac{1}{C\beta}\frac{\sigma^{2^i}}{\gamma} \\ P^{(i)} &< CC_\alpha\beta\frac{1}{C^2\beta^2}\frac{\sigma^{2^i}}{\gamma^2} + \frac{\gamma-1}{\gamma}\sigma^{2^{i-1}}\frac{C_\alpha}{C\beta}\frac{\sigma^{2^{i-1}}}{\gamma} \\ &= \frac{C_\alpha}{C\beta}\frac{\sigma^{2^i}}{\gamma} \end{aligned}$$

This proves $(T4)$ and completes the proof of the theorem. □

This theorem states that if the initial guess is close enough to the final solution and $\epsilon$ is sufficiently small, algorithm (1.98) will converge. The situation is similar for the standard Newton-Raphson scheme (1.97). The only difference in the requirement for the initial velocity guess is that $(H1)$ has to hold but with $\beta = 1$. Nevertheless, the same remarks as in Theorem 1.2 apply and in our case $\alpha$ can be taken such that $\beta \to 1$ when $\epsilon \to 0$. Another observation is that in $(H3)$ we can choose either having a 'good' initial pressure guess or limiting the value of $\epsilon$.

### 1.4.4 Uncoupling of the iterative penalization

In Sections 1.4.2 and 1.4.3 we have seen that if the iterative penalization is coupled with the iterative scheme used to deal with the convective term of the Navier-Stokes equations, the conditions under which this scheme converges have to be restricted. There is also the possibility of uncoupling the iteration due to the nonlinearity of the equations and the imposition on the incompressibility constraint. The purpose of this section is the analysis of the following algorithm:

*Given $p^{\epsilon(0)} \in Q_0$, for $i = 1, 2, ...$ find $(\mathbf{u}^{\epsilon(i)}, p^{\epsilon(i)}) \in V \times Q_0$ such that*

$$\begin{aligned} c(\mathbf{u}^{\epsilon(i)}, \mathbf{u}^{\epsilon(i)}, \mathbf{v}) + a(\mathbf{u}^{\epsilon(i)}, \mathbf{v}) - b(p^{\epsilon(i)}, \mathbf{v}) &= l(\mathbf{v}) \qquad &\forall \mathbf{v} \in V \\ \epsilon(p^{\epsilon(i)}, q) + b(q, \mathbf{u}^{\epsilon(i)}) &= \epsilon(p^{\epsilon(i-1)}, q) \qquad &\forall q \in Q \end{aligned} \tag{1.105}$$

For a given $i$, existence and uniqueness of solution is a consequence of assumption (1.12) [GR]. For each iteration of this algorithm a nonlinear problem has to be solved.

We will assume that the solution found in this process is exact. In this case, we obtain a result similar to the one encountered for the Stokes problem in Section 1.4.1:

**Theorem 1.4** *Let $(\mathbf{u},p) \in V \times Q_0$ and $(\mathbf{u}^{\epsilon(i)}, p^{\epsilon(i)}) \in V \times Q_0$ be the solutions of (1.83) and (1.105), respectively. Define the following constants:*

$$\begin{aligned}
M &:= \frac{N_l}{K_a} + \sqrt{\frac{\epsilon}{K_a}}(\|p - p^{\epsilon(0)}\| + \|p\|) \\
C_1 &:= K_a(1-\chi) \\
C_2 &:= \frac{K_a}{K_b}\chi + \frac{N_c}{K_b}M + \frac{N_a}{K_b} \\
\bar{\epsilon} &:= \frac{\epsilon}{C_1}C_2^2
\end{aligned}$$

*If $\bar{\epsilon} < 1$ then:*

$$\|\mathbf{u}^{\epsilon(i)}\| \leq M, \quad i = 1, 2, \ldots \tag{1.106}$$

$$\lim_{i\to\infty} \|p - p^{\epsilon(i)}\| = 0, \quad \lim_{i\to\infty} \|\mathbf{u} - \mathbf{u}^{\epsilon(i)}\| = 0 \tag{1.107}$$

*Moreover, convergence is linear with $\bar{\epsilon}$:*

$$\begin{aligned}
\|p - p^{\epsilon(i)}\| &\leq \bar{\epsilon}^i \|p - p^{\epsilon(0)}\| \\
\|\mathbf{u} - \mathbf{u}^{\epsilon(i)}\| &\leq C_2^{-1}\bar{\epsilon}^i \|p - p^{\epsilon(0)}\|
\end{aligned} \tag{1.108}$$

*Proof:* First observe that (1.87) holds for the solution $\|\mathbf{u}^{\epsilon(i)}\|$ of (1.105). This can be proved exactly as in Lemma 1.3. Thus, (1.106) is verified for $i = 1$. Let $i > 1$ be given and assume this is true up to this iteration. If the ideas used to arrive at (1.91) and (1.92) in Theorem 1.2 are now applied, one finds:

$$K_a\|\mathbf{u} - \mathbf{u}^{\epsilon(i)}\|^2 \leq N_c\|\mathbf{u}\|\|\mathbf{u} - \mathbf{u}^{\epsilon(i)}\|^2 + \epsilon\|p - p^{\epsilon(i-1)}\|\|p - p^{\epsilon(i)}\| \tag{1.109}$$

$$\begin{aligned}
K_b\|p - p^{\epsilon(i)}\| \leq\; & N_c\|\mathbf{u}\|\|\mathbf{u} - \mathbf{u}^{\epsilon(i)}\| + N_c\|\mathbf{u}^{\epsilon(i)}\|\|\mathbf{u} - \mathbf{u}^{\epsilon(i)}\| \\
& + N_a\|\mathbf{u} - \mathbf{u}^{\epsilon(i)}\|
\end{aligned} \tag{1.110}$$

Combining inequalities (1.109) and (1.110), using the estimates (1.86) for $\mathbf{u}$ and (1.106) for $\mathbf{u}^{\epsilon(i)}$ and considering the definition of the constants in the statement of the theorem, we arrive at:

$$\begin{aligned}
\|p - p^{\epsilon(i)}\| &\leq \bar{\epsilon}\|p - p^{\epsilon(i-1)}\| \\
\|\mathbf{u} - \mathbf{u}^{\epsilon(i)}\| &\leq \bar{\epsilon}C_2^{-1}\|p - p^{\epsilon(i-1)}\|
\end{aligned}$$

from where (1.108) follows. Since $\bar{\epsilon} < 1$ we have that $\|p - p^{\epsilon(i)}\| < \|p - p^{\epsilon(0)}\|$ and we obtain from (1.87) that (1.106) holds for $i + 1$. This closes the induction. Finally, (1.108) implies (1.107) for $\bar{\epsilon} < 1$. □

## 1.5 Numerical examples

The three examples presented in this section concern the numerical behavior of the iterative penalty method analysed heretofore. The implementation of the scheme is treated in detail in Chapter 2, where the calculation of the pressure, the streamfunction and the vorticity $\boldsymbol{\omega} := \nabla \times \mathbf{u}$ is described in detail. Only results using the $Q_2/P_1$ will be shown. Similar answers are obtained using other elements that satisfy the BB condition (see Chapter 2).

Convergence has been checked only in velocities, using the norm of the residual over the norm of the last iterate as the parameter to decide whether this convergence has been achieved or not (cf. Eqn. (1.64)). In the figures presented thereafter, this parameter in % is what is called *residual*. Since we are mainly interested in the satisfaction of the incompressibility constraint, also the $L^2$ norm of the discrete divergence of the velocity has been computed.

All the calculations have been carried out on a CONVEX-C120 computer using double arithmetic precision.

**Example 1.1** *Two-dimensional driven cavity flow*

In this example, the Stokes problem with $\mu = 1$ in the unit square $[0,1]\times[0,1]$ has been solved. The boundary conditions have been taken as $\mathbf{u} = (1,0)$ for $y = 1, 0 \leq x \leq 1$ ($x$, $y$ being the Cartesian coordinates) and $\mathbf{u} = (0,0)$ on the rest of the boundary (leaky-lid conditions). External body forces have been taken zero. The domain has been discretized using a uniform mesh of $25 \times 25$ nodal points ($12 \times 12$ elements). The velocity vectors, streamlines, pressure contours and vorticity contours for this problem have been plotted in Figure 1.6. Figure 1.7 shows the convergence history for the values of the penalty parameter $\epsilon = 10^{-1}$, $10^{-2}$, $10^{-3}$ and $10^{-4}$. Observe that the difference in the slope of the curves agrees with the theoretical prediction (1.82).

Once the finite element discretization has been performed, the term $\nabla \cdot \mathbf{u}$ leads to $\mathbf{BU}$, where $\mathbf{B} = \mathbf{G}^T$ is the discrete divergence matrix (cf. Box 1.2). In order to study the convergence of the iterates to the incompressible solution, the norm of $\mathbf{BU}^{\epsilon(i)}$ has been computed. Figure 1.8 shows the results obtained for different values of the penalty parameter. The curves correspond to 1, 2 and 3 iterations in the algorithm (1.73). Once again, their relative slope agrees with what (1.82) predicts. Observe that $\|\mathbf{BU}^{\epsilon(i)}\|$ will be bounded by $\epsilon G \|p^{\epsilon(i)} - p^{\epsilon(i-1)}\|$, where $G$ is the norm of the Gramm matrix $\mathbf{M}_p$ given in Box 1.2 whose components are the scalar products of the basis functions for the pressure (see (1.73)).

**Example 1.2** *Three-dimensional driven cavity flow*

The numerical simulation of three dimensional flows is a challenge, even for simple problems, mainly because of the large amount of computer memory required. One may afford long CPU times in research environments, but the real problem is to make the problem fit in the limits of the available computer memory.

Iterative solvers for algebraic linear systems have the important feature of being much less memory demanding than direct methods. On the other hand, they are very sensitive to the condition number of the system matrix. The number of iterations to be performed to achieve convergence is highly increased when this condition number grows.

In this example we present some preliminary results obtained for the Stokes flow in a 3D cavity using the iterative penalty method and solving the algebraic system

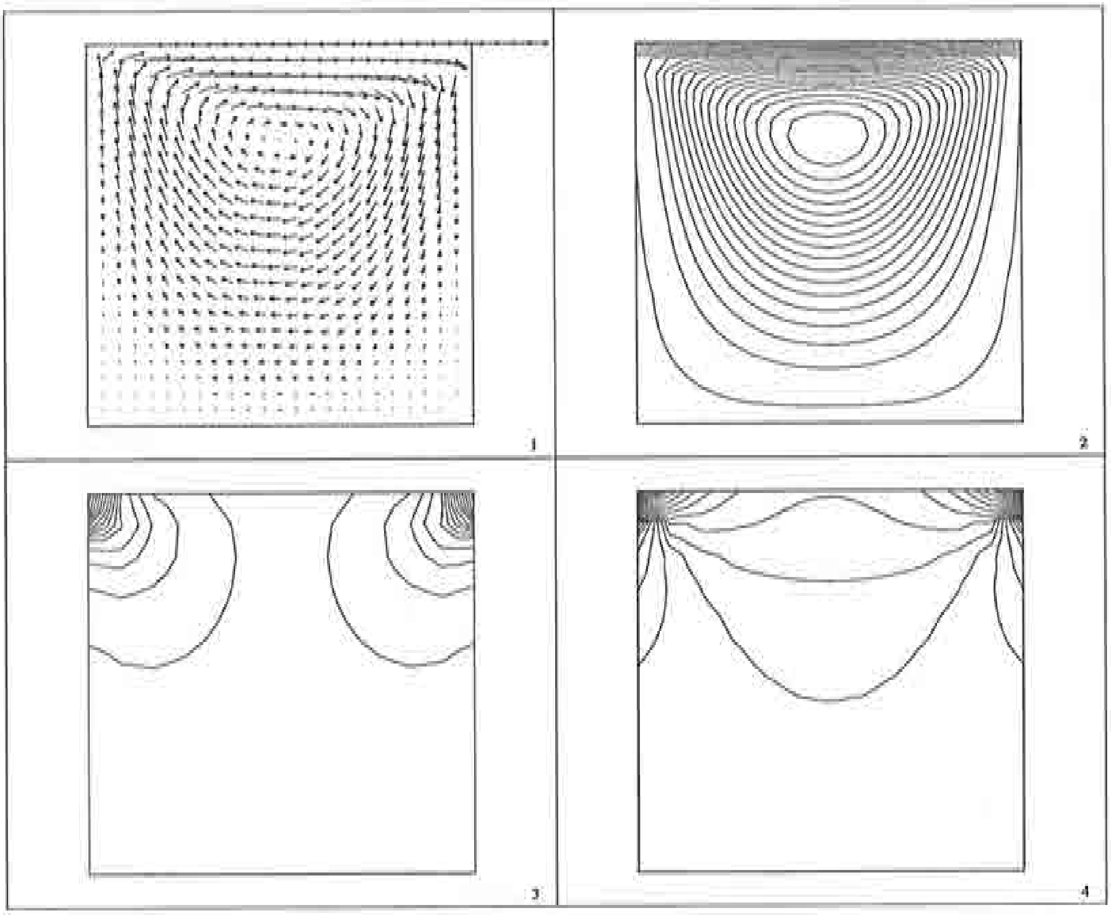

Figure 1.6 Numerical solution of the two-dimensional cavity flow problem. (1): Velocity vectors; (2): Streamfunction contours; (3): Pressure contours; (4): Vorticity contours.

using the conjugate gradient algorithm (see Reference [RTF] for similar experiments). The domain is the unit cube $[0,1]^3$ discretized using a uniform mesh of $21 \times 21 \times 21$ nodal points ($10 \times 10 \times 10$ $Q_2/P_1$ elements). The boundary conditions are $\mathbf{u} = (0,1,0)$ for $z = 1$, $0 \le x \le 1$, $0 \le y \le 1$ and $\mathbf{u} = \mathbf{0}$ on the rest of the boundary. The viscosity has been taken $\mu = 1$ and body forces are zero. Pressure contours are shown in Figure 1.9.

The total memory required for this problem has been 81.27 Mb (Mega-bytes), a considerable figure if we consider that it has been run on a computer with 128 Mb of central memory. Most of this memory (78.91 Mb) has been needed to allocate the element arrays (shape functions, derivatives, element matrices, etc.). The memory required for the conjugate gradient solver has been only 149 Kb (Kilo-bytes).

It is clear that the smaller $\epsilon$ be, the larger will be the condition number of the stiffness matrix and therefore less congugate gradient (CG) iterations will be needed, but more iterative penalization (IP) iterations will be required to reach a prescribed convergence tolerance. Here, the tolerance for the CG algorithm has been taken as

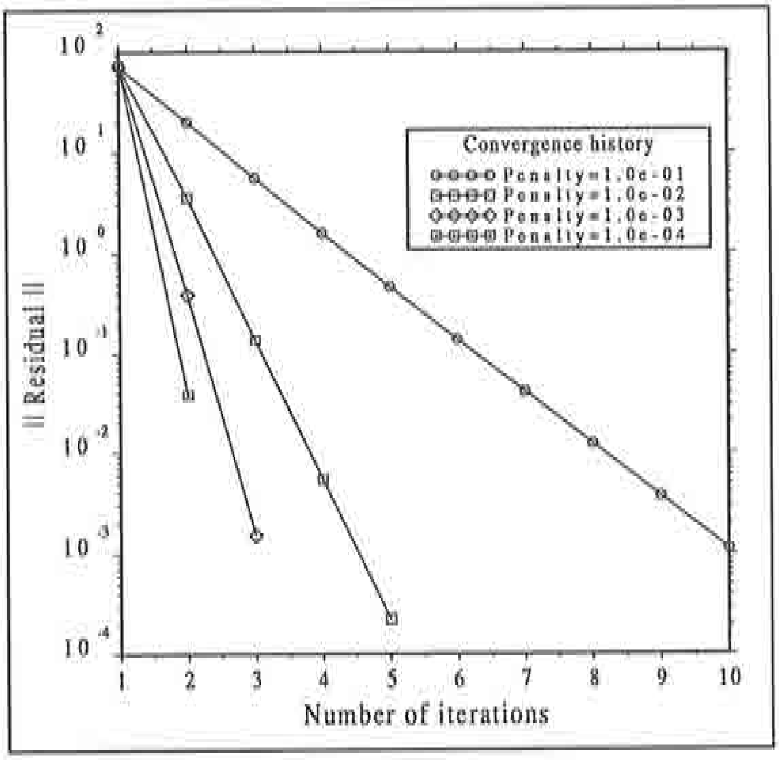

Figure 1.7 Convergence history for the two-dimensional cavity flow example using different penalty parameters.

$10^{-6}$ and the convergence tolerance as $10^{-3}$ %. The results obtained are the following:

| Penalty | CG iterations | IP iterations | CPU (seconds) |
|---|---|---|---|
| $10^{-2}$ | 418 | 6 | 8778 |
| $10^{-4}$ | 2913 | 3 | 25924 |
| $10^{-6}$ | 6303 | 2 | 36594 |

The CPU times are only referred to the solver algorithm. From these results it is apparent that it is worth using a 'large' penalty parameter, since the final CPU time is smaller, thanks to the small number of CG iterations. This compensates the fact that more iterations have to be performed to satisfy the incompressibility constraint up to the prescribed tolerance.

The number of CG and IP iterations and the CPU time have been plotted in Figure 1.10, as well as the convergence history for the values of $\epsilon$ considered.

**Example 1.3** *Flow over a backward-facing step*

The purpose of this example is to present some numerical results concerning the algorithms studied in Sections 1.4.2 and 1.4.3 for the incompressible Navier-Stokes equations. We have chosen this well known benchmark problem because a large number of numerical results are available. The computational domain we have taken is the rectangle $[0, 22] \times [0, 1.5]$ with a step of length 3 and height 0.5 placed in the lower left corner. A detail of the mesh used in the calculation is shown in Figure 1.11.(1). This mesh is composed of 408 biquadratic elements (for the velocity interpolation) and 1721 nodal points.

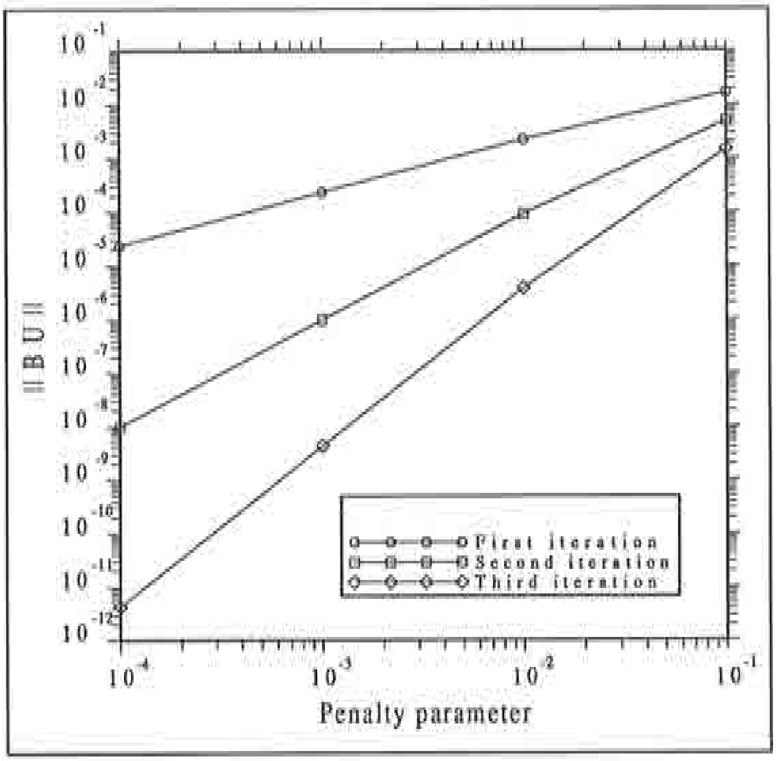

**Figure 1.8** Norm of the discrete divergence for the 2D cavity flow example for different number of iterations.

On the left boundary $x = 0$ a parabolic velocity profile with maximum value $(1, 0)$ has been prescribed. The viscosity has been taken as $\mu = 0.005$ and the density $\rho = 1$. Thus, the Reynolds number based on the inflow profile and the step height is $Re = 100$. The outflow boundary $x = 22$, $0 < y < 1.5$ has been left free. We have employed the expression (1.4) for the viscous term. In this case, the associated natural boundary condition is zero traction. On the rest of the boundary, the no-slip condition $\mathbf{u} = \mathbf{0}$ has been imposed. External body forces are zero.

The computed pressure contours and a detail of the streamlines are plotted in Figures 1.11.(2) to 1.11.(4). These results have been obtained using a penalty parameter $\epsilon = 10^{-4}$ and with a tolerance of $10^{-4}$%. The iterative scheme employed has been (1.98). Now we discuss the performance of the algorithms (1.85) and (1.98) for this problem when the classical penalty method and the iterative penalization proposed in this chapter are used. In the former case, the right-hand-side in the second equation of both (1.85) and (1.98) is zero.

Consider first algorithm (1.85). Figure 1.12.(1) shows the convergence history in the discrete $L^2$ norm when both the classical and the iterative penalty methods are used. No difference can be observed in the plot even though the parameter that defines convergence in the former case is $\chi$ whereas in the latter it is $\bar{\chi} > \chi$ (see (1.90)). The values of the relative norm of the residual in iteration number 18 are $0.87215 \times 10^{-2}$ for the classical penalty method and $0.87108 \times 10^{-2}$ for the iterative penalization. However, the important issue is the evolution of $\|\mathbf{B}\mathbf{U}^{\epsilon(i)}\|$ shown in Figure 1.12.(2). For the classical penalty method this norm remains constant (and, as expected, of order $\epsilon$). On the other hand, the velocity solution of algorithm (1.85)

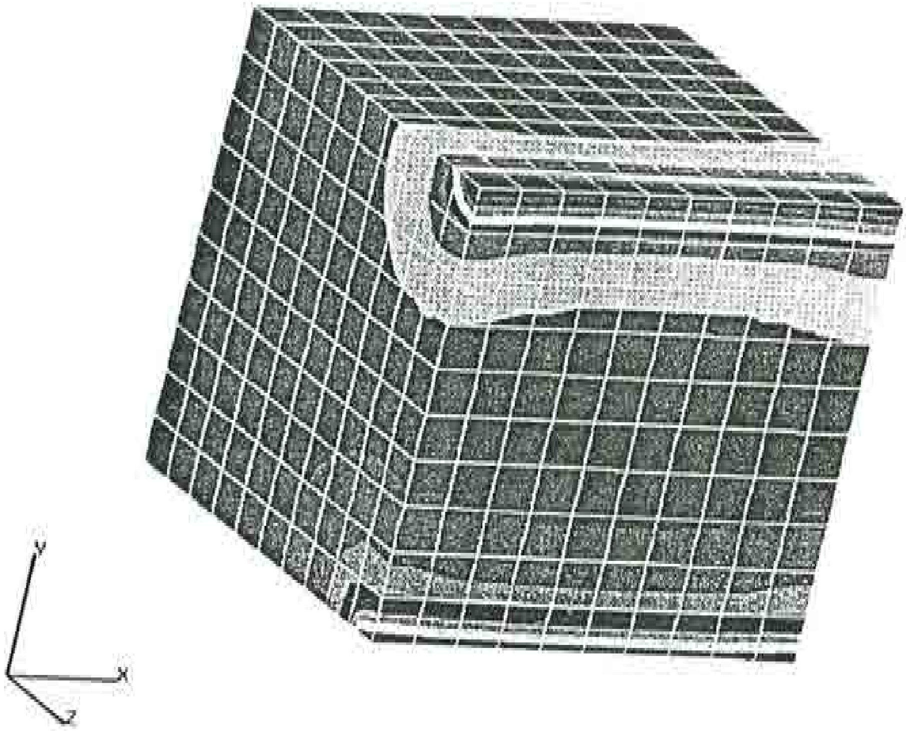

Figure 1.9 Pressure contours for the 3D cavity flow problem.

converges linearly to a (weakly) solenoidal field. The same experiments have been performed using the Newton-Raphson-based algorithm (1.98). If the initial guess is taken as $\mathbf{u}^{\epsilon(0)} = \mathbf{0}$, $p^{\epsilon(0)} = 0$ the scheme does not converge. In order to obtain a good initial guess, at least two iterations of algorithm (1.85) have to be performed, both for the classical and the iterative penalty methods. For $\epsilon = 10^{-4}$, the convergence history of the two methods shown in Figure 1.12.(3) is the same. The relative norm of the residual reaches the value $0.9986 \times 10^{-8}$ at iteration number 7 for the classical penalty method and $0.9781 \times 10^{-8}$ if (1.98) is used. The evolution of the norm of the discrete divergence (Figure 1.12.(4)) is certainly very different for the two methods. Whereas the penalty method yields a constant value, the iterative penalization converges quadratically to a zero divergence velocity field.

Similar results are obtained when the penalty parameter is $\epsilon = 10^{-1}$. Figures 1.13.(1) and 1.13.(2) show the convergence history and the evolution of $\|\mathbf{BU}^{\epsilon(i)}\|$ for the Picard-based algorithm (1.85). It is interesting to observe that for this large penalty number the residual norm using (1.85) is only slightly larger than using the classical penalty method. For the Newton-Raphson-based method, results are shown in Figures 1.13.(3) and 1.13.(4) and are especially interesting. The convergence rate for the iterates of (1.98) (see Figure 1.13.(3)) is quadratic up to iteration number 6 (except for the two first iterations, in which scheme (1.85) has been used). From there on, this rate turns to be linear. This possibility was already predicted in Theorem 1.3. The classical penalty method has a global quadratic convergence rate, but $\|\mathbf{BU}^{\epsilon(i)}\|$ keeps constant in the iterative process (Figure 1.13.(4)) at an unacceptable value.

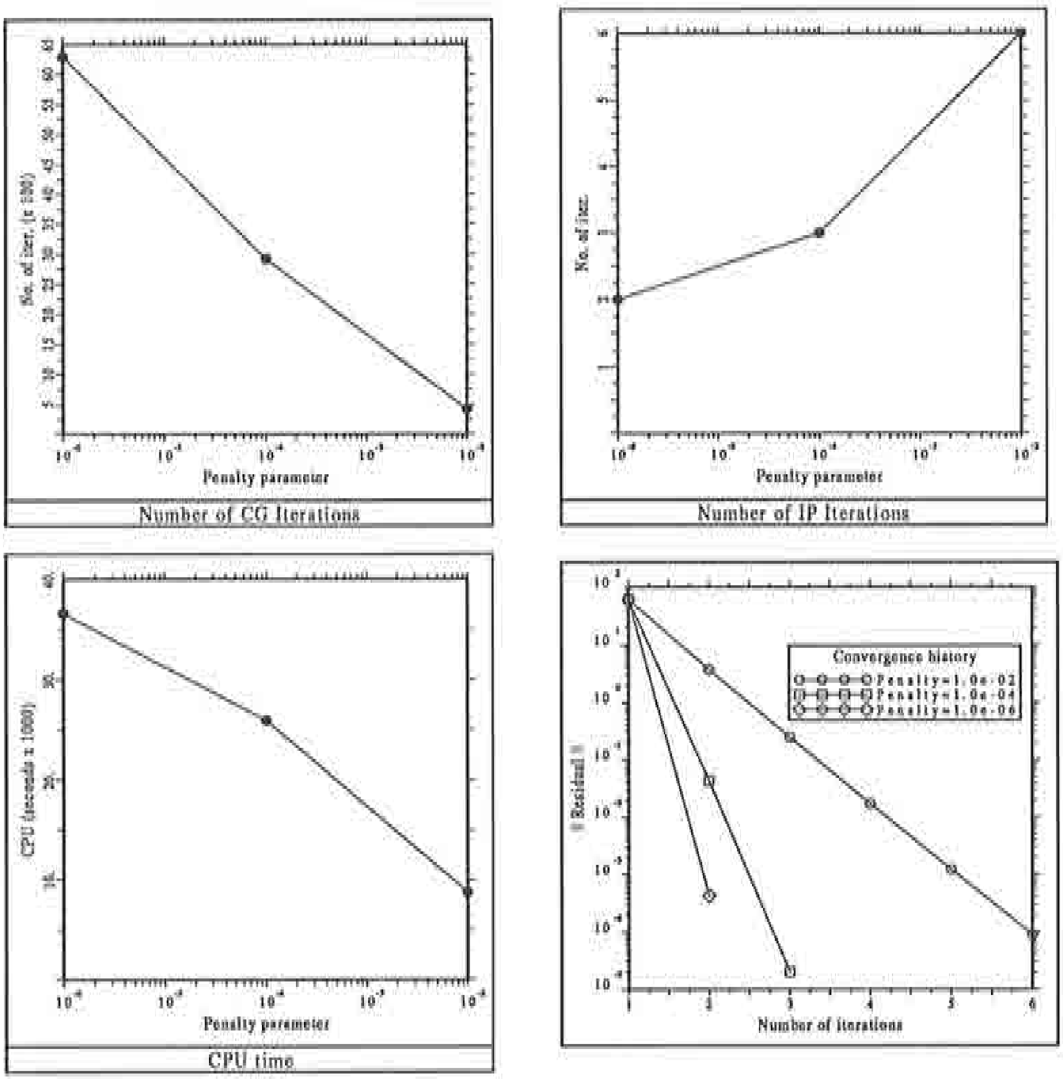

Figure 1.10 Results for the 3D cavity flow problem.

## 1.6 Summary and conclusions

The interest of this chapter has been focussed on the use of penalty methods to deal with the incompressibility constraint of the Navier-Stokes equations, with special reference to their computational behavior. We have started considering the strong penalty method and the related selective underintegration (RIP method), since this approach seems simpler than the weak penalization. *A priori*, there are no reasons to reject it. Nevertheless, the main conclusion of Section 1.3 is that the weak penalty method is to be preferred.

The new results and methods that have been introduced in this direction are:

- *Stability of some 2D elements.* Numerical experiments have demonstrated that the $Q_2/Q_1$ element suffers from having a small stability constant. The $Q_2/P_0$ element is robust, although very inaccurate (overdiffusive). Furthermore, it cannot be exactly reproduced using a RIP method. The integration error may be

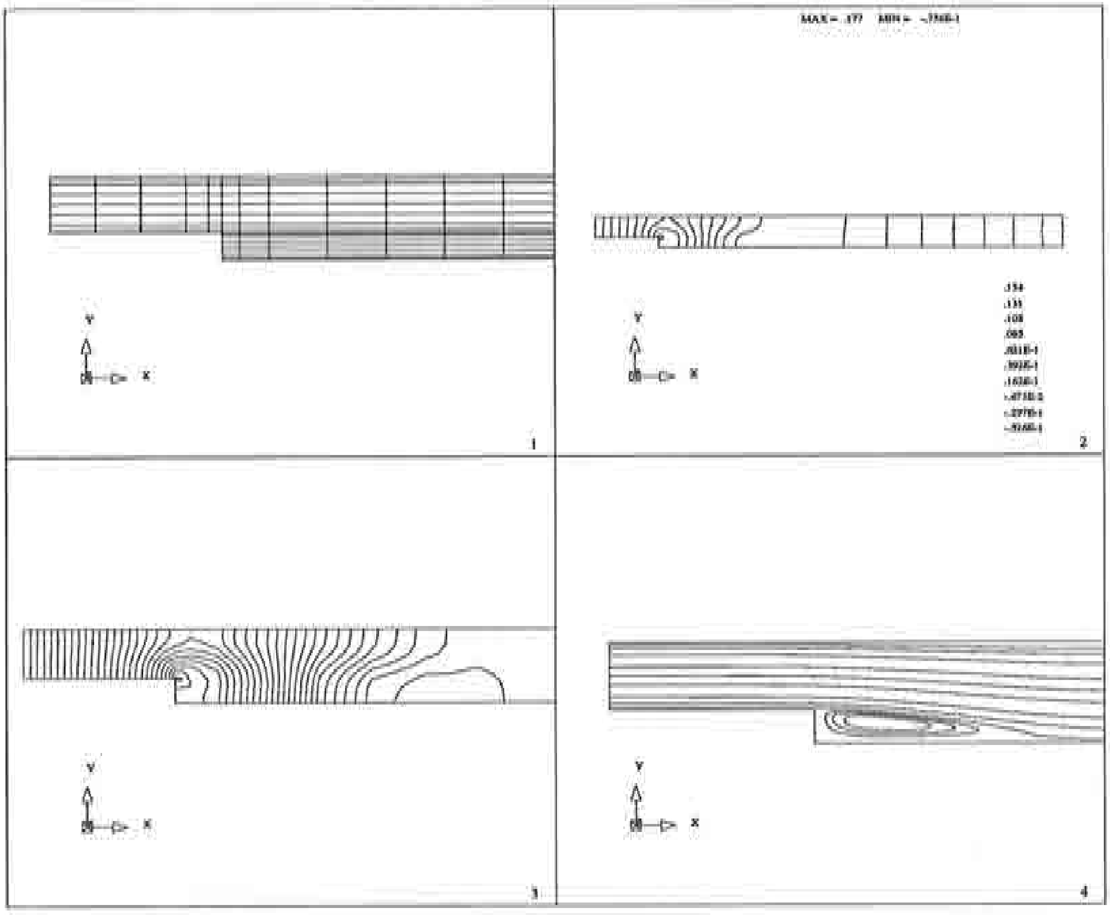

Figure 1.11 Numerical solution of the backward-facing step problem. (1): Detail of the mesh; (2): Pressure contours; (3): Detail of pressure contours; (4): Detail of streamlines.

responsible in part for this wrong behavior. It has also been proved theoretically and confirmed through numerical experiments that the $Q_2/P_1$ element cannot be emulated using the strong penalty method.

- *Pressure calculation.* A filtering technique has been proposed to compute the pressure for the $Q_2/Q_1$ element that has proved to be effective. Also, the possibility of solving a Poisson equation for the pressure after the velocity is known has been studied.
- *Petrov-Galerkin weighting.* Based on the results of [Co2], a Streamline Diffusion method has been introduced for the Navier-Stokes equations when the strong penalization is used.

It is important to point out that the numerical experiments presented in Section 1.3 are only those that have been considered *representative*, but many other tests have also been conducted that, for brevity, have not been included here.

However, the most important results are those concerning the iterative (weak) penalty method proposed and analysed in Section 1.4. We believe that this method has very interesting features. The penalty method for the incompressible Navier-Stokes

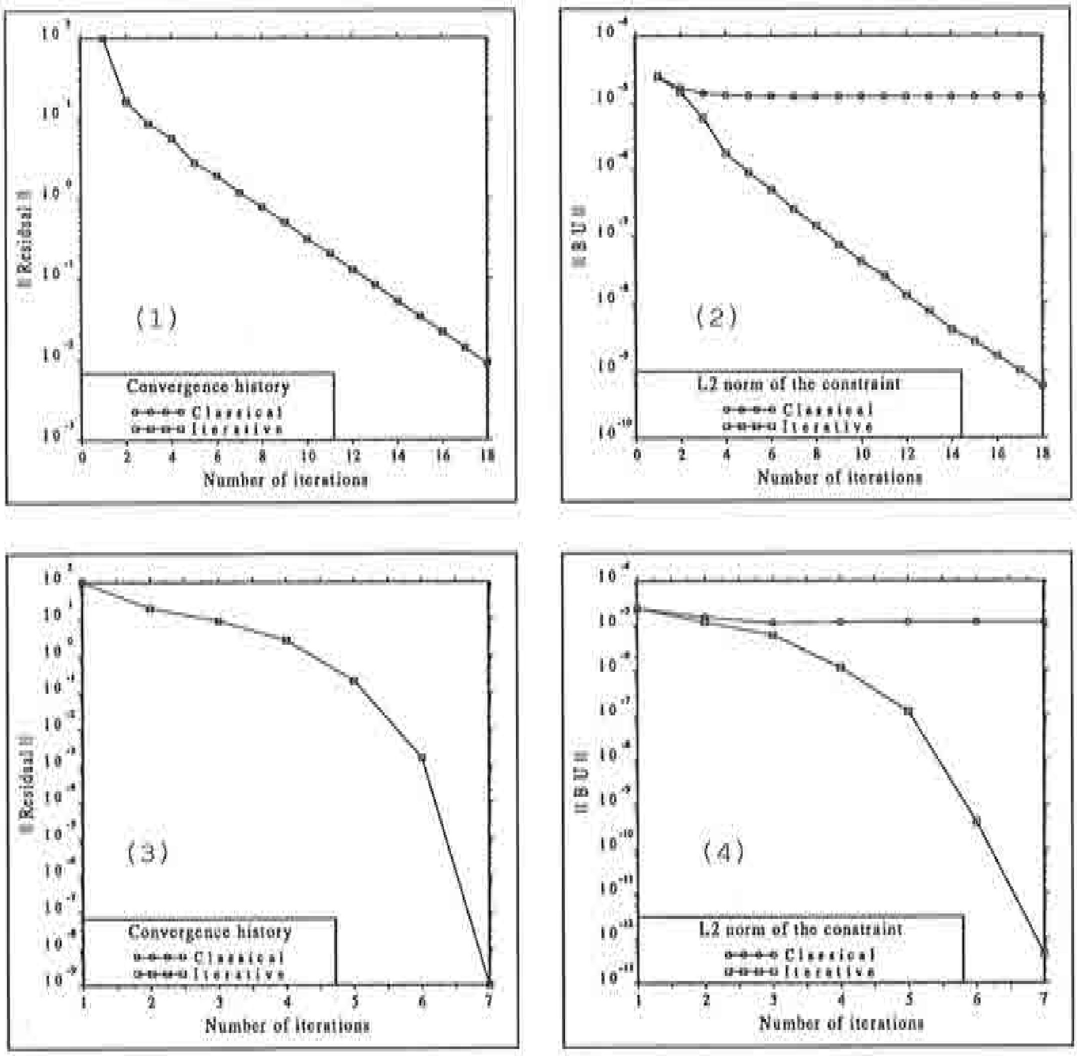

Figure 1.12 Comparison of the classical and iterative penalty methods for the backward-facing step problem with $\epsilon = 10^{-4}$. (1): Convergence history for the Picard algorithm; (2): Norm of the constraint for the Picard algorithm; (3): Convergence history for the Newton-Raphson algorithm; (4): Norm of the constraint for the Newton-Raphson algorithm.

equations in its classical form is attractive. It reduces the number of nodal unknowns and yields good results. This is a very important attribute if three-dimensional problems have to be solved on medium-size computers. However, small penalty parameters lead to ill-conditioned stiffness matrices. Usually, this ill-conditioning is not a trouble if direct solvers are used. But, still thinking in the numerical simulation of 3-D flows, iterative solvers are almost imperative when a real problem has to be faced. These solvers are very sensitive to the condition number of the stiffness matrix and this seriously limits the feasibility of the classical penalty method. The iterative penalization presented here tries to circumvent, at least in part, this inconvenience. It allows the use of much larger penalty parameters, thus yielding matrices whose condition numbers are much smaller. Whether this will be enough for using iterative solvers or not

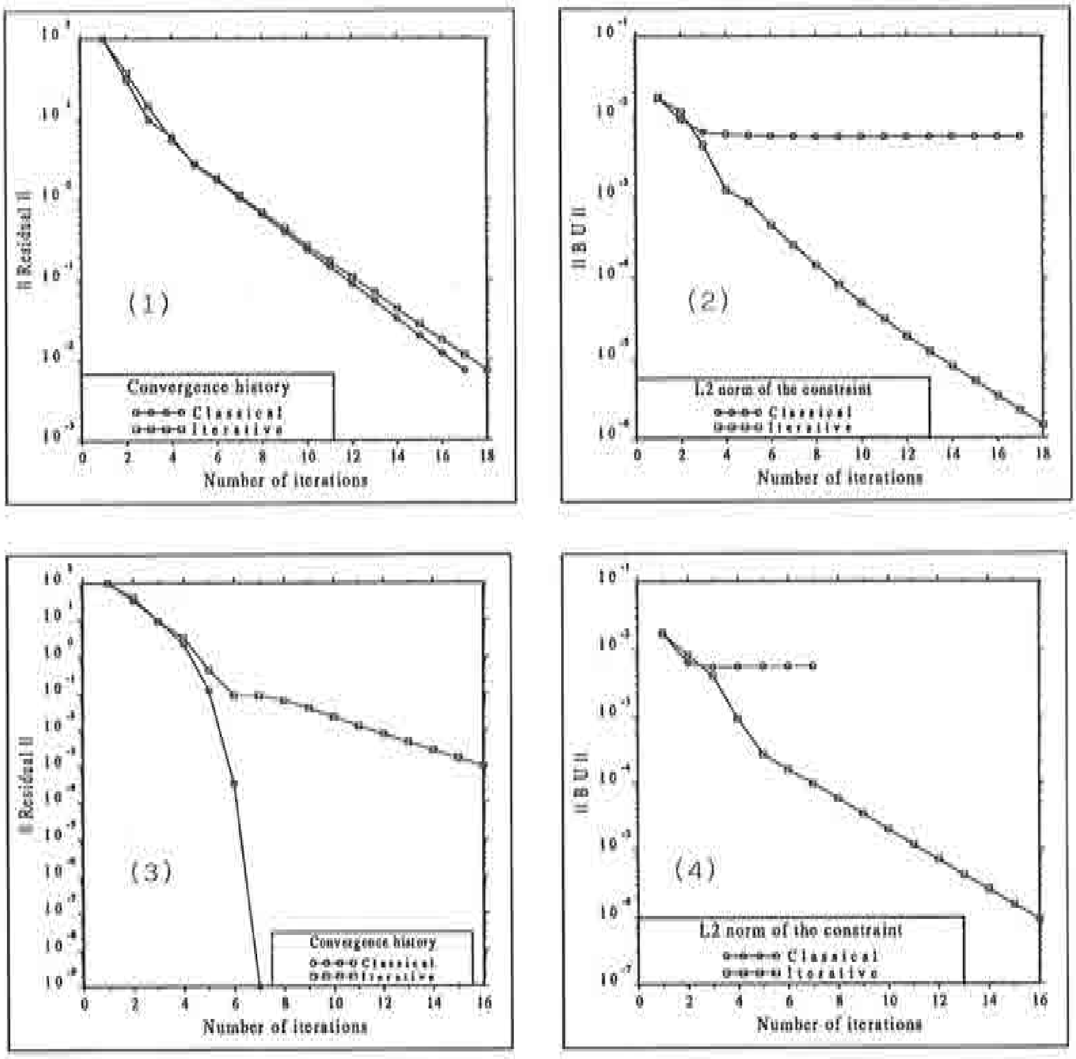

Figure 1.13 Comparison of the classical and iterative penalty methods for the backward-facing step problem with $\epsilon = 10^{-1}$. (1): Convergence history for the Picard algorithm; (2): Norm of the constraint for the Picard algorithm; (3): Convergence history for the Newton-Raphson algorithm; (4): Norm of the constraint for the Newton-Raphson algorithm.

is something that experience has to provide. Results for the 3D cavity flow example presented in Section 1.5 (for the Stokes problem) using the conjugate gradient method are certainly encouraging.

The iterative penalization presented here may be obtained from different approaches conceptually different. For the Stokes problem, it reduces to the Augmented Lagrangian method combined with the Uzawa algorithm to uncouple the pressure. It can also be interpreted as the introduction of an artificial compressibility and a false transient only for the pressure whenever the temporal derivative is discretized using the backward Euler scheme. However, we prefer the residual argument described in Section 1.4.1 since it is still valid when the iterative equation for the pressure is coupled with a linearized form of the momentum equations in the Navier-Stokes problem. The convergence analysis of the iterative penalty method coupled with this linearization of the convective term has shown that:

- *Picard-based algorithm.* The analysis of the algorithm (Theorem 1.2) reveals that the rate of convergence is smaller than for the classical penalty method.
- *Newton-Raphson based algorithm.* The attraction ball of the exact solution happens to be smaller than for the classical penalization. Quadratic convergence can only be ensured up to a certain iteration (Theorem 1.3).

However, numerical experiments indicate that these effects are only apparent when the penalty parameter is 'very large', compared with the standards of the classical approach. Anyway, if needed, there is also the possibility of uncoupling the iterative penalization (Theorem 1.4) and obtain a rate of convergence that only depends on the penalty parameter.

In practice, it is common to use penalties of order $10^{-6}\mu^{-1}$ to $10^{-9}\mu^{-1}$. We have already said that these values can be easily handled using direct solvers. However, there are some practical cases in which the viscosity varies several orders of magnitude in the fluid domain, as in quasi-Newtonian fluids with thermal dependent physical properties. In these cases, the above rule has to be applied using the smallest value of the viscosity, thus relaxing in excess the incompressibility constraint in the high viscosity zones. We will start up again with this argument in Chapter 3.

## References

[Ar] D.N. Arnold. Mixed finite element methods for elliptic problems. *Comput. Meths. Appl. Mech. Engrg.*, vol. 82 (1990), 281–300

[ABF] D.N. Arnold., F. Brezzi and M. Fortin. A stable finite element for the Stokes equations. *Calcolo*, vol. 21 (1984), 337–344

[Ba1] I. Babuška. Error bounds for finite element method. *Numer. Math.*, vol. 16 (1971), 322–333

[Ba2] I. Babuška. The finite element method with Lagrangian multipliers. *Numer. Math.*, vol. 20 (1973), 179–192

[BOP] I. Babuška, J. Osborn and J. Pitkäranta. Analysis of mixed methods using mesh dependent norms *Math. Comp.*, vol. 35 (1980), 1039–1062

[Be] M. Bercovier. Perturbation of a mixed variational problem, application to mixed finite element methods. *RAIRO Anal. Numer.*, vol. 12 (1978), 211–236

[BP] M. Bercovier and O. Pironneau. Error estimates for finite element method solution of the Stokes problem in the primitive variables. *Numer. Math.*, vol. 33 (1979), 211–224

[BN1] J.M. Boland and R.A. Nicolaides. Stability of finite elements under divergence constraints. *SIAM J. Numer. Anal.*, vol. 20 (1983), 722–731

[BN2] J.M. Boland and R.A. Nicolaides. On the stability of bilinear-constant velocity-pressure finite elements. *Numer. Math.*, vol. 44 (1984), 219–222

[BN3] J.M. Boland and R.A. Nicolaides. Stable and semistable low order finite elements for viscous flows. *SIAM J. Numer. Anal.*, vol. 22 (1985), 474–492

[Br] F. Brezzi. On the existence, uniqueness and approximation of saddle point problems arising from Lagrange multipliers. *RAIRO Anal. Numer.*, vol. 8

(1974), 129–151

[BB] F. Brezzi and K.J. Bathe. A discourse on the stability conditions for mixed finite element formulations. *Comput. Meths. Appl. Mech. Engrg.*, vol. 82 (1990), 27–57

[BD] F. Brezzi and J. Douglas. Stabilized mixed methods for the Stokes problem. *Numer. Math.*, vol. 53 (1988), 225–235

[BFa] F. Brezzi and R. Falk. Stability of higher-order Taylor-Hood elements. *SIAM J. Numer. Anal.*, vol. 28 (1991), 581–590

[BFo] F. Brezzi and M. Fortin. *Mixed and hybrid finite element methods* (Springer-Verlag, 1991).

[BR1] F. Brezzi, J. Rappaz and P.A. Raviart. Finite dimensional approximation of nonlinear problems. Part I: Branches of non-singular solutions. *Numer. Math.*, vol. 36 (1981), 1–25

[BR2] F. Brezzi, J. Rappaz and P.A. Raviart. Finite dimensional approximation of nonlinear problems. Part II: Limit points. *Numer. Math.*, vol. 37 (1981), 1–28

[BR3] F. Brezzi, J. Rappaz and P.A. Raviart. Finite dimensional approximation of nonlinear problems. Part III: Simple bifurcation points. *Numer. Math.*, vol. 38 (1981), 1–30

[CK1] G.F. Carey and R. Krishnan. Penalty approximation of Stokes flow. *Comput. Meths. Appl. Mech. Engrg.*, vol. 35 (1982), 169–206

[CK2] G.F. Carey and R. Krishnan. Penalty finite element method for the Navier-Stokes equations. *Comput. Meths. Appl. Mech. Engrg.*, vol. 42 (1984), 183–224

[CK3] G.F. Carey and R. Krishnan. Continuation techniques for a penalty approximation of the Navier-Stokes equations. *Comput. Meths. Appl. Mech. Engrg.*, vol. 48 (1985), 265–282

[CK4] G.F. Carey and R. Krishnan. Convergence of iterative methods in penalty finite element approximations of the Navier-Stokes equations. *Comput. Meths. Appl. Mech. Engrg.*, vol. 60 (1987), 1–29

[CO1] G.F. Carey and J.T. Oden. *Finite Elements: A second course.* The Texas Finite Element Series, vol. II (Prentice Hall, 1983)

[CO2] G.F. Carey and J.T. Oden. *Finite Elements: Fluid Mechanics.* The Texas Finite Element Series, vol. VI (Prentice Hall, 1986)

[Ch] A.J. Chorin. A numerical method for solving incompressible viscous flow problems. *J. Comput. Phys.*, vol. 2 (1967), 12–26

[Ci] P.G. Ciarlet. *The finite element method for elliptic problems.* (North-Holland, 1978)

[Co1] R. Codina. An iterative penalty method for the finite element solution of the stationary Navier-Stokes equations. *CIMNE Report Num. 12* (1991) (Submitted to *Comput. Meths. Appl. Mech. Engrg.*)

[Co2] R. Codina. *A finite element model for the numerical solution of the convection-diffusion equation.* (CIMNE monograph Num. 14, 1992)

[CCO] R. Codina, M. Cervera and E. Oñate. A penalty finite element method for non-Newtonian creeping flows. *CIMNE Report Num. 13* (1991) (Submitted to *Int. J. Numer. Meth. Engrg.*)

[CR] M. Crouzieux and P.A. Raviart. Conforming and non-conforming finite element methods for the stationary Stokes equations. *RAIRO Anal. Numer.*, vol. 7 (1973), 33–76

[CSS] C. Cuvelier, A. Segal and A. van Steenhoven. *Finite element methods and Navier-Stokes equations.* (Reidel, 1986)

[DJM] J. Donea, S. Giulinani, K. Morgan and L. Quartapelle. The significance of chequerboarding in a Galerkin finite element solution of the Navier-Stokes equations. *Int. J. Numer. Meth. Engrg.*, vol. 17 (1981), 790–795

[ESG] M.S. Engelman, R.L. Sani, P.M. Gresho and M. Bercovier. Consistent vs reduced integration penalty methods for incompressible media using several old and new elements. *Int. J. Numer. Meth. Fluids*, vol. 2 (1983), 25–42

[Fe] C.A. Felippa. Iterative procedures for improving penalty function solutions of algebraic systems. *Int. J. Numer. Meth. Engrg.*, vol. 12 (1978), 821–836

[Fo1] M. Fortin. Analysis of the convergence of mixed finite element methods. *RAIRO Anal. Numer.*, vol. 11 (1977), 341–354

[Fo2] M. Fortin. Old and new finite elements for incompressible flows. *Int. J. Numer. Meth. Fluids*, vol. 1 (1981), 347–364

[Fo3] M. Fortin. Two comments on: Consistent vs reduced integration penalty methods for incompressible media using several old and new elements. *Int. J. Numer. Meth. Fluids*, vol. 3 (1983), 93–98

[FB] M. Fortin and S. Boivin. Iterative stabilization of the bilinear velocity-constant pressure element. *Int. J. Numer. Meth. Fluids*, vol. 10 (1990), 125–140

[FF] M. Fortin and A. Fortin. Experiments with several elements for viscous incompressible flows. *Int. J. Numer. Meth. Fluids*, vol. 5 (1985), 911–928

[FH] L. Franca and T.J.R. Hughes. Two classes of mixed finite element methods. *Comput. Meths. Appl. Mech. Engrg.*, vol. 69 (1988), 89–129

[FS] L. Franca and R. Stenberg. Error analysis of some Galerkin least-squares methods for the elasticity equations. *INRIA, Rapports de Recherche* (1989)

[FHL] L. Franca, T.J.R. Hughes, A.F.D. Loula and I. Miranda. A new family of stable elements for nearly incompressible elasticity based on a mixed Petrov-Galerkin finite element formulation. *Numer. Math.*, vol. 53 (1988), 123–141

[Fr] I. Fried. Finite element analysis of incompressible material by residual energy balancing. *Int. J. of Solids and Struct.*, vol. 10 (1974), 993–1002

[GR] V. Girault and P.A. Raviart. *Finite element methods for Navier-Stokes equations* (Springer-Verlag, 1986).

[Gl] R. Glowinski. *Numerical methods for nonlinear variational problems.* (North-Holland, 1984)

[GP] R. Glowinski and O. Pironneau. On a mixed finite element approximation of the Stokes problem. *Numer. Math.*, vol. 33 (1979), 397–424

[GS] P.M. Gresho and R.L. Sani. On pressure boundary conditions for the incompressible Navier- Stokes equations. In: *Finite elements in fluids*, vol. 7, R.H. Gallagher, R. Glowinski, P.M. Gresho, J.T. Oden and O.C. Zienkiewicz (eds.) (John Wiley & Sons Ltd., 1987).

[Gu] M. Gunzburger. *Finite element methods for viscous incompressible flows* (Academic Press, 1989).

[HS] P. Hansbo and A. Szepessy. A velocity-pressure streamline diffusion finite element method for the incompressible Navier-Stokes equations. *Comput. Meths. Appl. Mech. Engrg.*, vol. 84 (1990), 175–192

[HD] J.C. Heinrich and B.R. Dyne. On the penalty method for incompressible fluids. In: *Finite elements in the 90's.* E. Oñate, J. Periaux and A. Samuelson (eds.) (Springer-Verlag/CIMNE, 1991).

[HO] E. Hinton and D.R.J. Owen. *Finite element programming.* (Academic Press, 1977)

[Hu1] T.J.R. Hughes. Equivalence of finite elements for nearly-incompressible elasticity. *J. Appl. Mech.*, vol. 44 (1977), 181–183

[Hu2] T.J.R. Hughes. *The finite element method. Linear static and dynamic analysis.* (Prentice-Hall, 1987)

[HA] T.J.R. Hughes and H. Allik. Finite elements for compressible and incompressible continua. In: *Proceedings of the Symposium on civil Engineering,* Vandervilt Univ., Nashville Tenn. (1969)

[HF] T.J.R. Hughes and L.P. Franca. A new finite element formulation for computational fluid dynamics: VII. Ths Stokes problem with various well-posed boundary conditions: symmetric formulations that converge for all velocity/pressure spaces. *Comput. Meths. Appl. Mech. Engrg.*, vol. 65 (1987), 85–96

[HFB] T.J.R. Hughes, L.P. Franca and M. Balestra. A new finite element formulation for computational fluid dynamics: V. Circumventing the Babuska-Brezzi condition: a stable Petrov-Galerkin formulation for the Stokes problem accommodating equal-order interpolations. *Comput. Meths. Appl. Mech. Engrg.*, vol. 59 (1986), 85–99

[HLB] T.J.R. Hughes, W.K. Liu and A. Brooks. Finite Element Analysis of Incompressible Viscous Flows by the Penalty Function Formulation. *J. Comput. Phys.*, vol. 30 (1979), 1–60

[Ir] B. Irons. A frontal solution program. *Int. J. Numer. Meth. Engrg.*, vol. 2 (1970), 5–32

[IL] B. Irons and M. Loikkanen. An engineers' defence of the patch test. *Int. J. Numer. Meth. Engrg.*, vol. 19 (1983), 1391–1401

[JP] C. Johnson and J. Pitkäranta. Analysis of some mixed finite element methods related to reduced integration. *Math. Comp.*, vol. 38 (1982), 375–400

[KOS] N. Kikuchi, J.T. Oden and Y.J. Song. Convergence of modified penalty methods and smoothing schemes of pressure for Stokes' flow problems. In: *Finite elements in fluids*, vol. 5, R.H. Gallagher, J.T. Oden, O.C. Zienkiewicz, T. Kawai and M. Kawahara (eds.) (John Wiley & Sons Ltd., 1984).

[Ki] S.W. Kim. A finite element computational method for high Reynolds number laminar flows. NASA CR-179135 (1987).

[La] O. Ladyzhenskaya. *The mathematical theory of viscous incompressible flow.* (Gordon-Breach, 1963)

[MH] D.S. Malkus and T.J.R. Hughes. Mixed finite element methods-reduced and selective integration techniques: a unification of concepts. *Comput. Meths. Appl. Mech. Engrg.*, vol. 15 (1978), 63–81

[NPR] J.C. Nagtegaal, D.M. Parks and J.R. Rice. On numerically accurate finite element solutions in the fully plastic range. *Comput. Meths. Appl. Mech. Engrg.*, vol. 4 (1974), 153–177

[Od] J.T. Oden. RIP-methods for Stokesian flows. In: *Finite elements in fluids*, vol. 4, R.H. Gallagher, D.H. Norrie, J.T. Oden and O.C. Zienkiewicz (eds.) (John Wiley & Sons Ltd., 1982)

[OC] J.T. Oden and G.F. Carey. *Finite Elements: Mathematical aspects.* The Texas Finite Element Series, vol. IV (Prentice Hall, 1983)

[OJ1] J.T. Oden and O.P. Jacquotte. Stability of some mixed finite element methods for Stokesian flows. *Comput. Meths. Appl. Mech. Engrg.*, vol. 43 (1984), 231–247

[OJ2] J.T. Oden and O.P. Jacquotte. Stable and unstable Rip/Perturbed Lagrangian methods for two-dimensional viscous flow problems. In: *Finite elements in fluids*, vol. 5, R.H. Gallagher, J.T. Oden, O.C. Zienkiewicz, T. Kawai and M. Kawahara (eds.) (John Wiley & Sons Ltd., 1984)

[OKS] J.T. Oden, N. Kikuchi and Y.J. Song. Penalty finite element methods for the analysis of Stokesian flows. *Comput. Meths. Appl. Mech. Engrg.*, vol. 31 (1982), 297–329

[Pi] O. Pironneau. *Finite element methods for fluid flow.* (John Wiley & Sons, 1989)

[RT] P.A. Raviart and J.M. Thomas. A mixed finite element method for second order elliptic problems. In: *Mathematical aspects of the finite element method*, I. Galligani, E. Magues (eds.). Lecture notes in Mathematics, 606 (Springer, 1977)

[Ra] A. Razzaque. The patch test for elements. *Int. J. Numer. Meth. Engrg.*, vol. 22 (1986), 63–71

[RTF] M.P. Robichaud, Ph. Tanguy and M. Fortin. An iterative implementation of the Uzawa algorithm for 3-D fluid flow problems. *Int. J. Numer. Meth. Fluids*, vol. 10 (1990), 429–442

[Sa] E.M. Salonen. An iterative penalty function method in structural analysis. *Int. J. Numer. Meth. Engrg.*, vol. 10 (1976), 413–421

[SG1] R.L. Sani, P.M. Gresho, R.L. Lee and D.F. Griffiths. The cause and cure (?) of the spurious pressures generated by certain FEM solutions of the incompressible Navier-Stokes equations. Part 1. *Int. J. Numer. Meth. Fluids*, vol. 1 (1981), 17–43

[SG2] R.L. Sani, P.M. Gresho, R.L. Lee and D.F. Griffiths. The cause and cure (!) of the spurious pressures generated by certain FEM solutions of the incompressible Navier-Stokes equations. Part 2. *Int. J. Numer. Meth. Fluids*, vol. 1 (1981), 171–204

[SH] J.L. Sohn and J.C. Heinrich. Pressure calculations in penalty finite element approximations to the Navier-Stokes equations. *Int. J. Numer. Meth. Engrg.*, vol. 30 (1990), 349–361

[St1] R. Stenberg. Analysis of mixed finite element methods for the Stokes problem: a unified approach. *Math. Comp.*, vol. 42 (1984), 9–23

[St2] R. Stenberg. Error analysis of some finite element methods for the Stokes problem. *Math. Comp.*, vol. 54 (1990), 495–508

[St3] R. Stenberg. A technique for analysing finite element methods for viscous incompressible flow. *Int. J. Numer. Meth. Fluids*, vol. 11 (1990), 935–948

[TR] Ph. Le Tallec and V. Ruas. On the convergence of the bilinear-velocity constant-pressure finite element method in viscous flow. *Comput. Meths. Appl. Mech. Engrg.*, vol. 54 (1986), 235–243

[TH] C. Taylor and P. Hood. A numerical solution of the Navier-Stokes equations using the finite element method. *Comp. & Fluids*, vol. 1 (1973), 73–100

[TSZ] R.L. Taylor, J.C. Simo, O.C. Zienkiewicz and C.H. Chan. The patch test – A condition for assessing FEM convergence. *Int. J. Numer. Meth. Engrg.*, vol. 22 (1986), 39–62

[Te] R. Temam. *Navier-Stokes equations.* (North-Holland, 1984)

[Ve1] R. Verfürth. Error estimates for a mixed finite element interpolations of Stokes problem. *RAIRO Anal. Numer.*, vol. 18 (1984), 175–182

[Ve2] R. Verfürth. Finite element approximation of incompressible Navier-Stokes equations with slip boundary conditions. *Numer. Math.*, vol. 50 (1987), 697–721

[ZQT] O.C. Zienkiewicz, S. Qu, R.L. Taylor and S. Nakazawa. The patch test for mixed formulations. *Int. J. Numer. Meth. Engrg.*, vol. 23 (1986), 1873–1883

[ZT] O.C. Zienkiewicz and R.L. Taylor. *The Finite Element Method*, Fourth Edition, Vol. 1 (McGraw-Hill, 1989)

[ZTT] O.C. Zienkiewicz, R.L. Taylor and J.M. Too. Reduced integration technique in general analysis of plates and shells. *Int. J. Numer. Meth. Engrg.*, vol. 3 (1971), 275–290

[ZVT] O.C. Zienkiewicz, J.P. Vilotte, S. Toyoshima and S. Nakazawa. Iterative method for constraint and mixed approximation; an inexpensive improvement of F.E.M. performance. *Comput. Meths. Appl. Mech. Engrg.*, vol. 51 (1985), 3–29

*CHAPTER 2*

# TRANSIENT NAVIER–STOKES EQUATIONS: FULLY DISCRETE ALGORITHM AND COMPUTATIONAL ASPECTS

## 2.1 Introduction

The purpose of this chapter is to present an algorithm for the numerical simulation of the transient Navier-Stokes equations using the ideas of Chapter 1, as well as the technique presented in Reference [Co] to deal with convection dominated flows. The emphasis will be mainly computational, giving in Section 2.6 a fully discrete and linearized numerical scheme adapted to the implementation on a computer.

The basic tools of the numerical model are now briefly described. The temporal derivatives are discretized using the generalized trapezoidal rule as described in [Co] for the convection-diffusion equation. The incompressibility constraint is treated by using div-stable velocity-pressure interpolations. The pressure is eliminated through penalization. Several choices are discussed, in particular the iterative penalty method introduced and analyzed in Chapter 1 (using weak penalization) and a particular version of the artificial compressibility method. Since the stabilization of the pressure is left to the finite element interpolation, only the convection of the velocity has to be stabilized when high Reynolds number flows are considered. This is done by means of a Streamline Diffusion (SD) operator added to the Galerkin variational form and properly linearized.

While the mathematical analysis of the finite element method for the convection-diffusion equation and the stationary Navier-Stokes equations using the Galerkin approach is fairly complete, there are still a lot of open questions for the full Navier-Stokes equations. The most extensive analysis of the transient problem we are aware of is that of Heywood & Rannacher [HR1–4]. Error estimates are given for the Galerkin finite element approximation of the Navier-Stokes equations with homogeneous Dirichlet boundary conditions. The time discretization using the Crank-Nicolson scheme is analysed in the last paper of this series [HR4]. Although we are interested in more general situations, the results obtained by these authors will be often referred to in this chapter. Our approach differs from the one they analyse in the use of penalty methods, the SD operator, the boundary conditions and the way the trapezoidal rule is implemented.

Based on the results of the previous chapter, the penalization of the incompressibility constraint is viewed as an iterative procedure to achieve this restriction rather than a perturbation of the initial problem. Because of this, it is not considered until Section 2.5, where the way the nonlinear system of equations is solved is treated.

Once the description of the numerical algorithm is complete, Section 2.7 presents the methods used to compute nodal pressure values as well as nodal values of the vorticity and the physical properties when they are variable. This will be used in the next chapter, where the numerical simulation of thermally coupled flows and nonlinear materials is studied. In these cases, the density depends on the temperature and the viscosity depends on the invariants of the strain rate tensor and perhaps also on the temperature. For the particular case of two-dimensional flows, an algorithm to compute the streamfunction is presented.

The numerical examples presented in the previous chapter were mainly intended to verify the theory. However, such theoretical grounds are not available for the general problem considered here and the numerical experimentation is of fundamental importance. The most common benchmark tests for the numerical simulation of incompressible flow problems are presented in Section 2.8, namely, the driven cavity flow at (relatively) high Reynolds numbers, the flow over a backward facing step and the flow past a cylinder. The meshes used in the calculations are somehow coarse, if compared with the results presented in the literature, since one of our purposes is to assess the performance of the SD operator when the Galerkin approach yields oscillatory results. Nevertheless, they have to be fine enough to capture the physical details of the flow. In complicated flow situations (the most common in reality) this is the main challenge that computational fluid dynamics has at present.

The literature on finite element methods for incompressible viscous fluids is vast. We again refer to the well-known text books [CO], [CSS] and the more recent texts [Gu], [Pi] for a general presentation of the problem. A mathematically oriented exposition can be found in the books of Temam [Te] and Girault & Raviart [GR1]. For a comprehensive engineering treatment of the problem the reader is referred to the book of Zienkiewicz & Taylor (vol. 2) [ZT].

## 2.2 The continuous problem

In this chapter we will attempt the numerical solution of the following initial and boundary value problem:

$$\begin{aligned}
\rho[\partial_t \mathbf{u} + (\mathbf{u}\cdot\nabla)\mathbf{u}] - 2\mu\nabla\cdot\boldsymbol{\varepsilon}(\mathbf{u}) + \nabla p &= \rho\mathbf{f} && \text{in } \Omega\times(0,T) && (2.1)\\
\nabla\cdot\mathbf{u} &= 0 && \text{in } \Omega\times(0,T) && (2.2)\\
\mathbf{u} &= \bar{\mathbf{u}} && \text{on } \Gamma_D\times(0,T) && (2.3)\\
\mathbf{n}\cdot\boldsymbol{\sigma} &= \bar{\mathbf{t}} && \text{on } \Gamma_N\times(0,T) && (2.4)\\
\mathbf{u}(\mathbf{x},0) &= \mathbf{u}_0(\mathbf{x}) && \text{on } \Omega\times\{0\} && (2.5)
\end{aligned}$$

Besides the notation introduced in Chapter 1, the meaning of the different symbols appearing in (2.1)–(2.5) is the following. The time interval where the problem is to be solved is $(0,T)$, with $T > 0$. The temporal derivative of the velocity has been denoted by $\partial_t\mathbf{u}$, $t$ being the time variable. The overbars in $\bar{\mathbf{u}}$ and $\bar{\mathbf{t}}$ denote prescribed values (boundary conditions). The former is the velocity given on a part $\Gamma_D$ of $\Gamma := \partial\Omega$ (Dirichlet-type prescription) and the latter is a given surface force vector on $\Gamma_N \subset \Gamma$

(Neumann-type prescription), satisfying $\Gamma = \overline{\Gamma_D \cup \Gamma_N}$, with $\Gamma_D \cap \Gamma_N = \emptyset$. The unit outward normal to $\Gamma$ has been indicated by $\mathbf{n}$. The (Eulerian) stress tensor for a generalized Newtonian fluid is

$$\boldsymbol{\sigma} = -p\mathbf{I} + 2\mu\boldsymbol{\varepsilon}, \qquad \boldsymbol{\varepsilon}(\mathbf{u}) := \frac{1}{2}\left[(\nabla\mathbf{u}) + (\nabla\mathbf{u})^T\right] \tag{2.6}$$

where $\mathbf{I}$ is the unit tensor. In this chapter, the dynamical viscosity $\mu$ and the density $\rho$ will be considered constant (Newtonian behavior).

There are two main reasons for writing the viscous term as $2\mu\nabla \cdot \boldsymbol{\varepsilon}$. The first is that the boundary condition (2.4) on $\Gamma_N$ enters naturally the variational form of problem (2.1)–(2.5). The second is that in Chapters 3 and 4 we will consider cases with variable viscosity, and the expression $2\nabla \cdot [\mu\boldsymbol{\varepsilon}(\mathbf{u})]$ will be needed (otherwise, the gradient of $\mu$ has to be calculated). Moreover, for obtaining the simplifyed form $\mu\Delta\mathbf{u}$ used in (1.1) the condition $\nabla \cdot \mathbf{u} = 0$ has to be employed. This condition will not hold exactly when using penalty methods and it seems preferable not to use it in deriving the equations.

Equation (2.5) is the initial condition. A generic point in $\Omega$ has been denoted by $\mathbf{x}$. The given vector function $\mathbf{u}_0(\mathbf{x})$ is assumed to be divergence free and to satisfy the Dirichlet boundary conditions.

A mixed type of boundary prescriptions can also be considered. For that, let $\Gamma_M \subset \Gamma$ and let $\mathbf{g}_1, \mathbf{g}_2$ (in 3D) be the local basis for the tangent space to $\Gamma_M$. In practice, it is often useful to consider the following conditions:

$$\mathbf{u} \cdot \mathbf{n} = \bar{u}_n, \qquad \mathbf{n} \cdot \boldsymbol{\sigma} \cdot \mathbf{g}_1 = \bar{t}_1, \qquad \mathbf{n} \cdot \boldsymbol{\sigma} \cdot \mathbf{g}_2 = \bar{t}_2, \qquad \text{on } \Gamma_M \tag{2.7}$$

where $\bar{u}_n$ is a given scalar and $\bar{t}_1$ and $\bar{t}_2$ are the components of the force tangent to $\Gamma_M$ in the local basis $\mathbf{g}_1, \mathbf{g}_2$. In the numerical simulation of turbulent flows, it is common to consider $\bar{u}_n = 0$ (impermeable wall condition) and to express $\bar{t}_1$ and $\bar{t}_2$ in terms of the velocity tangent to $\Gamma_M$, trying to emulate the frictional effects of turbulent boundary layers. In Chapter 4, a special type of friction law will be introduced. For the moment, and to simplify the exposition, boundary conditions of type (2.7) will not be considered. For the stationary problem and using the Galerkin approach, they have been studied by Verfürth [Ve].

In order to write the weak form of problem (2.1)–(2.5) we need to introduce some functional spaces. The test function spaces for the velocity and the pressure, $V_t$ and $Q_t$, will be

$$\begin{aligned} V_t &= \{\mathbf{v} \in H^1(\Omega)^{N_{sd}} \mid \mathbf{v}|_{\Gamma_D} = 0\} \\ Q_t &= L^2(\Omega) \end{aligned} \tag{2.8}$$

The spaces of trial solutions will consist of time dependent functions. At least when $\Gamma_N = \emptyset$, it can be shown [Te] that the minimum regularity in time that has to be required is square-integrability. Thus, let us introduce

$$V_s = \{\mathbf{v} \in L^2(0,T; H^1(\Omega)^{N_{sd}}) \mid \mathbf{v}|_{\Gamma_D} = \bar{\mathbf{u}}, \;\; t \in (0,T)\} \tag{2.9}$$

$$Q_s = \{q \in L^2(0,T; L^2(\Omega)) \mid \int_\Omega q\,d\Omega = 0, \;\; t \in (0,T), \;\; \text{if } \Gamma_N = \emptyset\} \tag{2.10}$$

as spaces of trial solutions for the velocity and the pressure. For the latter case, it has to be remarked that when $\Gamma_N \neq \emptyset$ the pressure *is not* underdetermined by a constant, since the boundary condition (2.4) involves the pressure itself, not its derivatives:

$$\mathbf{n} \cdot \boldsymbol{\sigma} = -p\mathbf{n} + 2\mu\mathbf{n} \cdot \boldsymbol{\varepsilon} = \bar{\mathbf{t}} \tag{2.11}$$

The data $\mathbf{f}$, $\bar{\mathbf{u}}$, $\bar{\mathbf{t}}$ and $\mathbf{u}_0$ is assumed to satisfy the following conditions:

$$\begin{aligned}\mathbf{f} &\in L^2(0,T;L^2(\Omega)^{N_{sd}})\\ \bar{\mathbf{u}} &\in L^2(0,T;H^{1/2}(\Gamma)^{N_{sd}})\\ \bar{\mathbf{t}} &\in L^2(0,T;H^{-1/2}(\Gamma)^{N_{sd}})\\ \mathbf{u}_0 &\in \{\mathbf{v}\in L^2(\Omega)^{N_{sd}} \mid \nabla\cdot\mathbf{v}=0\}\end{aligned} \tag{2.12}$$

Finally, as for the stationary problem we define:

$$\begin{aligned}&a(\mathbf{u},\mathbf{v}) = 2\mu\int_\Omega \boldsymbol{\varepsilon}(\mathbf{u}):\boldsymbol{\varepsilon}(\mathbf{v})d\Omega,\\ &b(q,\mathbf{v}) = \int_\Omega q\nabla\cdot\mathbf{v}d\Omega,\\ &c(\mathbf{u},\mathbf{v},\mathbf{w}) = \rho\int_\Omega[(\mathbf{u}\cdot\nabla)\mathbf{v}]\cdot\mathbf{w}d\Omega + \frac{1}{2}\rho\int_\Omega(\nabla\cdot\mathbf{u})\mathbf{v}\cdot\mathbf{w}d\Omega,\\ &l(\mathbf{v}) = \rho\int_\Omega \mathbf{f}\cdot\mathbf{v}d\Omega + \int_{\Gamma_N}\bar{\mathbf{t}}\cdot\mathbf{v}d\Gamma,\end{aligned} \tag{2.13}$$

all these functions taking values in $L^2(0,T)$. The choice of the convective term $c$ has been already discussed in Chapter 1.

The weak form of problem (2.1)–(2.5) reads now as follows: Find $\mathbf{u}\in V_s$ and $p\in Q_s$ such that

$$\begin{aligned}\rho(\partial_t\mathbf{u},\mathbf{v}) + c(\mathbf{u},\mathbf{u},\mathbf{v}) + a(\mathbf{u},\mathbf{v}) - b(p,\mathbf{v}) &= l(\mathbf{v}) && \forall\mathbf{v}\in V_t\\ b(q,\mathbf{u}) &= 0 && \forall q\in Q_t\\ (\mathbf{u}(\mathbf{x},0),\mathbf{v}) &= (\mathbf{u}_0(\mathbf{x}),\mathbf{v}) && \forall\mathbf{v}\in V_t\end{aligned} \tag{2.14}$$

For the case $\Gamma_N=\emptyset$, it is proved in [Te] that all the terms in (2.14) make sense. Moreover, the regularity of the solution is higher than *a priori* required. If $N_{sd}=2$ a unique solution to problem (2.14) exists. One of the most important open questions in the mathematical analysis of the Navier-Stokes problem is the existence and uniqueness for $N_{sd}=3$. Existence is a well known result (weak solutions), but uniqueness can only be proved in spaces of functions more regular than (2.9)–(2.10) (classical solutions), in which case only local existence can be proved, i.e., for sufficiently small $T$ (see, e.g., [CF], [La], [Li], [Te]).

The coercivity condition (1.9) and the BB condition (1.10) are also needed for the transient equations, both for the continuous and the discrete problems. Condition (1.12) is not assumed.

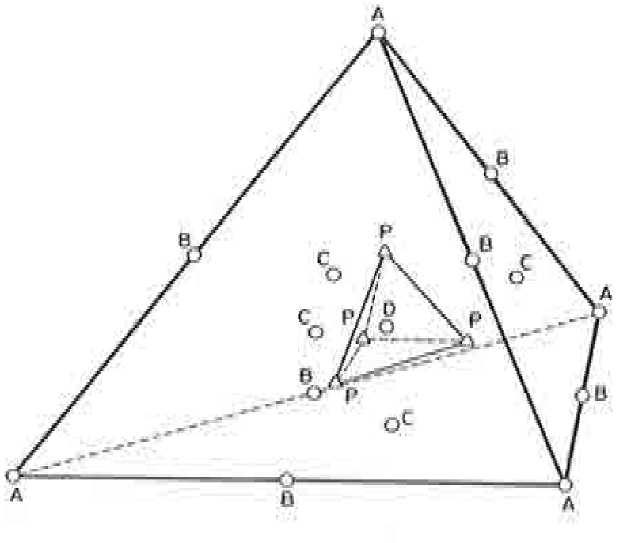

## 2.3 Discretization in time

Consider a nonlinear system of ordinary differential equations of the form

$$\dot{x} = F(x,t) \tag{2.15}$$

where $x = x(t)$ is a vector function. Let us define, for $\theta \in [0,1]$,

$$\begin{aligned} x_\theta^n &:= \theta x^n + (1-\theta)x^{n-1}, \qquad t_\theta^n := \theta t^n + (1-\theta)t^{n-1} \\ F^n(x,t) &:= F(x^n, t^n) \end{aligned}$$

where $t^n := n\Delta t$, $x^n$ is an approximation to $x(t^n)$ and $\Delta t$ is the time step size of a uniform partition of $[0,T]$. The generalized trapezoidal rule used in [Co] for the *linear* convection-diffusion equation can be extended in two different ways to *nonlinear* problems. These two forms are:

$$\frac{1}{\Delta t}(x^n - x^{n-1}) = \theta F^n(x,t) + (1-\theta)F^{n-1}(x,t) \tag{2.16}$$

$$\frac{1}{\Delta t}(x^n - x^{n-1}) = F(x_\theta^n, t_\theta^n) \tag{2.17}$$

The first choice has a clear geometrical interpretation: the time derivative in the interval $(t^{n-1}, t^n)$ has been approximated by a combination of the derivatives at $t^{n-1}$ and $t^n$. The interpretation of the second method is not so clear. If $x(t)$ were linear, then $x_\theta^n = x(t_\theta^n)$ and (2.17) would mean that the time derivative has been calculated at a point within the interval $(t^{n-1}, t^n)$.

Here we will discuss the implementation of both approaches for the Navier-Stokes problem. In the literature, the most common approach is (2.17) [Gu], [HR4], although (2.16) is also used [CSS].

Consider first (2.16). When it is applied to the strong form of the Navier-Stokes equations (2.1)–(2.2) one has to find $\mathbf{u}^n(\mathbf{x})$ and $p^n(\mathbf{x})$, aproximations to $\mathbf{u}(\mathbf{x},t^n)$ and $p(\mathbf{x},t^n)$, such that

$$\begin{aligned} \rho[(\mathbf{u}^n - \mathbf{u}^{n-1})/\Delta t + \theta(\mathbf{u}^n\cdot\nabla)\mathbf{u}^n + (1-\theta)(\mathbf{u}^{n-1}\cdot\nabla)\mathbf{u}^{n-1}] \\ -2\mu\theta\nabla\cdot\boldsymbol{\varepsilon}(\mathbf{u}^n) - 2\mu(1-\theta)\nabla\cdot\boldsymbol{\varepsilon}(\mathbf{u}^{n-1}) \\ +\theta\nabla p^n + (1-\theta)\nabla p^{n-1} = \theta\rho\mathbf{f}^n + (1-\theta)\rho\mathbf{f}^{n-1} \\ \nabla\cdot\mathbf{u}^n = 0 \end{aligned} \tag{2.18}$$

for $n = 1,2,...,$ with $\mathbf{u}^0(\mathbf{x}) = \mathbf{u}_0(\mathbf{x})$. The initial pressure $p^0(\mathbf{x})$ will be the solution of the boundary value problem

$$\begin{aligned} \Delta p^0 &= \nabla\cdot[\rho\mathbf{f}^0 - \rho(\mathbf{u}^0\cdot\nabla)\mathbf{u}^0] && \text{in } \Omega \\ \frac{\partial p^0}{\partial n} &= \mathbf{n}\cdot[\rho\mathbf{f}^0 - \rho(\mathbf{u}^0\cdot\nabla)\mathbf{u}^0 - \rho\partial_t\bar{\mathbf{u}} + 2\mu\nabla\cdot\boldsymbol{\varepsilon}(\mathbf{u}^0)] && \text{on } \Gamma_D \\ p^0 &= 2\mu\mathbf{n}\cdot\boldsymbol{\varepsilon}(\mathbf{u}^0)\cdot\mathbf{n} - \bar{\mathbf{t}}\cdot\mathbf{n} && \text{on } \Gamma_N \end{aligned} \tag{2.19}$$

In [HR1] it is proved for the case $\Gamma_N = \emptyset$ that a unique solution (modulo constants) exists for this problem.

The velocity $\mathbf{u}^n$ and the pressure $p^n$ solution of problem (2.18) have to satisfy the boundary conditions (2.3) and (2.4).

The weak form of problem (2.18) will be:

$$\begin{aligned}\rho\frac{1}{\Delta t}(\mathbf{u}^n-\mathbf{u}^{n-1},\mathbf{v})+\theta c(\mathbf{u}^n,\mathbf{u}^n,\mathbf{v})+(1-\theta)c(\mathbf{u}^{n-1},\mathbf{u}^{n-1},\mathbf{v})&\\ +\theta a(\mathbf{u}^n,\mathbf{v})+(1-\theta)a(\mathbf{u}^{n-1},\mathbf{v})&\\ -\theta b(p^n,\mathbf{v})-(1-\theta)b(p^{n-1},\mathbf{v})=\theta l^n(\mathbf{v})+(1-\theta)l^{n-1}(\mathbf{v})&\\ b(q,\mathbf{u}^n)=0&\end{aligned}\tag{2.20}$$

for all $\mathbf{v}\in V_t$ and $q\in Q_t$. Observe that $l$ is a linear function and hence $l^n(\mathbf{v})$ is the value of $l(\mathbf{v})$ evaluated with $\mathbf{f}^n$ and $\bar{\mathbf{t}}^n$.

It is easy to see that (2.20) is also obtained from the time discretization of the continuous variational form (2.14). Symbolically, we have the following commutative diagram:

$$\begin{tikzcd}\text{Eqns. (2.1) - (2.5)} \arrow[r, "\text{Time discretrization}"] \arrow[d, "\text{Weak form}"] & \text{Eqn. (2.18)} \arrow[d, "\text{Weak form}"] \\ \text{Eqn. (2.14)} \arrow[r, "\text{Time discretrization}"] & \text{Eqn. (2.20)}\end{tikzcd}$$

This remark might seem obvious in this case. However, the definition of the SD operator will depend on the order of the space and time discretizations.

Let us consider now (2.17) applied to the time discretization of the weak form of the continuous problem (2.14). Instead of (2.20) we will find:

$$\begin{aligned}\rho\frac{1}{\Delta t}(\mathbf{u}^n-\mathbf{u}^{n-1},\mathbf{v})+c(\mathbf{u}^n_\theta,\mathbf{u}^n_\theta,\mathbf{v})+a(\mathbf{u}^n_\theta,\mathbf{v})-b(p^n_\theta,\mathbf{v})=l^n_\theta(\mathbf{v})&\\ b(q,\mathbf{u}^n_\theta)=0&\end{aligned}\tag{2.21}$$

where $\mathbf{u}^n_\theta:=\theta\mathbf{u}^n+(1-\theta)\mathbf{u}^{n-1}$, $p^n_\theta:=\theta p^n+(1-\theta)p^{n-1}$ and $l^n_\theta(\mathbf{v})$ is calculated with $\mathbf{f}^n_\theta:=\theta\mathbf{f}^n+(1-\theta)\mathbf{f}^{n-1}$ and $\bar{\mathbf{t}}^n_\theta:=\theta\bar{\mathbf{t}}^n+(1-\theta)\bar{\mathbf{t}}^{n-1}$. Since $c$, $a$, $b$ and $l$ are linear in each argument, the only difference between (2.20) and (2.21) will be the convective term. For (2.21) we will have that

$$\begin{aligned}c(\mathbf{u}^n_\theta,\mathbf{u}^n_\theta,\mathbf{v})&=c(\theta\mathbf{u}^n+(1-\theta)\mathbf{u}^{n-1},\theta\mathbf{u}^n+(1-\theta)\mathbf{u}^{n-1},\mathbf{v})\\ &=\theta^2c(\mathbf{u}^n,\mathbf{u}^n,\mathbf{v})+\theta(1-\theta)c(\mathbf{u}^n,\mathbf{u}^{n-1},\mathbf{v})\\ &\quad+\theta(1-\theta)c(\mathbf{u}^{n-1},\mathbf{u}^n,\mathbf{v})+(1-\theta)^2c(\mathbf{u}^{n-1},\mathbf{u}^{n-1},\mathbf{v})\end{aligned}$$

If we denote by $c^n_\theta(\mathbf{u},\mathbf{u},\mathbf{v}):=\theta c(\mathbf{u}^n,\mathbf{u}^n,\mathbf{v})+(1-\theta)c(\mathbf{u}^{n-1},\mathbf{u}^{n-1},\mathbf{v})$ the convective term in (2.20), it is easy to show that

$$c(\mathbf{u}^n_\theta,\mathbf{u}^n_\theta,\mathbf{v})-c^n_\theta(\mathbf{u},\mathbf{u},\mathbf{v})=\theta(\theta-1)c(\mathbf{u}^n-\mathbf{u}^{n-1},\mathbf{u}^n-\mathbf{u}^{n-1},\mathbf{v})$$

and therefore the difference between (2.20) and (2.21) will be a term of order $O(\Delta t^2)$ (in the $H^1(\Omega)^{N_{sd}}$–norm). Since this is the best consistency error we can hope for (using $\theta=1/2$, i.e., the Crank-Nicolson scheme), the accuracy will not be affected if (2.20) or (2.21) are used.

Without any further information about the difference between (2.20) and (2.21) concerning their convergence properties (nonlinear stability), the decision for choosing one scheme or another will be based on computational criteria. First observe that

$$\mathbf{u}^n - \mathbf{u}^{n-1} = \frac{1}{\theta}\mathbf{u}_\theta^n - \frac{1}{\theta}\mathbf{u}^{n-1}$$

and thus (2.21) may be rewritten as

$$\begin{aligned} \rho\frac{1}{\theta\Delta t}(\mathbf{u}_\theta^n,\mathbf{v}) + c(\mathbf{u}_\theta^n,\mathbf{u}_\theta^n,\mathbf{v}) + a(\mathbf{u}_\theta^n,\mathbf{v}) - b(p_\theta^n,\mathbf{v}) &= l_\theta^n(\mathbf{v}) + \rho\frac{1}{\theta\Delta t}(\mathbf{u}^{n-1},\mathbf{v}) \\ b(q,\mathbf{u}_\theta^n) &= 0 \end{aligned} \tag{2.22}$$

This expression involves only the unknown $\mathbf{u}_\theta^n$. The computational effort of (2.20) is higher than that of (2.22), since there are more right-hand-side terms to calculate per time step. These additional terms are

$$-(1-\theta)c(\mathbf{u}^{n-1},\mathbf{u}^{n-1},\mathbf{v}) - (1-\theta)a(\mathbf{u}^{n-1},\mathbf{v}) + (1-\theta)b(p^{n-1},\mathbf{v})$$

In spite of this higher computational effort, we have chosen (2.20) and not (2.22) for the numerical implementation. There are several reasons for this. The first is the definition of the SD operator to be introduced later. It is conceptually simpler if the unknown is the velocity $\mathbf{u}^n$ and not an intermediate value $\mathbf{u}_\theta^n$ between $\mathbf{u}^{n-1}$ and $\mathbf{u}^n$. Also, the penalty methods we will discuss will be based on the fact that the pressure $p^n$, and not $p_\theta^n$, has to be calculated. The most important reason, however, is the following. Both (2.20) and (2.22) are nonlinear problems and have to be solved iteratively. In Chapters 3 and 4 we will attempt the solution of thermally coupled flows of (possibly) nonlinear materials and perhaps with a free surface. Both for the constitutive laws and for the tracking of the free surfaces the velocity $\mathbf{u}^n$ is needed. Since the iterative procedure due to this new nonlinearity will be coupled to that of the Navier-Stokes equations, the use of (2.22) would require the calculation of $\mathbf{u}^n$ from $\mathbf{u}_\theta^n$ and $\mathbf{u}^{n-1}$ *for each iteration*. We would have to deal with $\mathbf{u}^{n-1}$, $\mathbf{u}_\theta^n$ and $\mathbf{u}^n$ and this means either more computer memory (if $\mathbf{u}^n$ is stored) or more calculations (if $\mathbf{u}^n$ is computed when needed). For all these reasons, scheme (2.20) will be used in what follows.

To conclude this section, let us discuss the choice of the parameter $\theta$. The only interesting cases are $\theta = 0$ (forward Euler), $\theta = 1/2$ (Crank-Nicolson) and $\theta = 1$ (backward Euler). The first value yields a conditionally stable scheme and the other two values an unconditionally stable algorithm [Te]. However, due to the implicit nature of the pressure, the case $\theta = 0$ is unconditionally unstable using the $\mathbf{u}-p$ formulation. If the incompressibility constraint is penalized, $\epsilon$ being the penalty parameter, the critical time step $\Delta t_c$ will behave as $\epsilon$ when $\epsilon \to 0$ (incompressible limit). To see this, one can argue as follows. Once the pressure is eliminated from the penalized incompressibility condition and it is substituted in the momentum equations, the effective viscosity that will multiply some second derivatives of the velocity will be $\mu + 1/\epsilon$ (see Eqn. (1.22)). Since $\Delta t_c$ will be proportional to the inverse of this viscosity (see [Co]), $\Delta t_c \sim \epsilon$ for $\epsilon \to 0$.

The Crank-Nicolson algorithm will be useful when the accuracy in time be fundamental, since a second order approximation can be expected [HR4]. However, if the transient evolution is not very important, $\theta = 1$ should be preferred, since the resulting scheme is computationally cheaper (several terms in (2.20) vanish). Also, either if $\theta = 1$ or $\theta = 1/2$ is to be employed, the former value is recommended for the first few time steps (usually one or two). This was also valid for the transient convection-diffusion equation discussed in [Co]. The explanation we gave there was the difficulty in reproducing the rapidly oscillating harmonics associated to the series expansion of the solution of parabolic equations. Now there are two more reasons. The first is that if $\theta \neq 1$, the use of (2.20) necessitates the initial pressure $p^0$ for $n = 1$ and hence problem (2.19) has to be solved. The other reason is the singularity for $t \to 0$ that will be discussed later.

## 2.4 Space discretization and Streamline Diffusion operator

The particular version of the SD method we will consider will be based on the idea of stabilizing the convective term of the Navier-Stokes equations, with the same motivation as in Reference [Co] (Chapter 1) for the convection-diffusion problem. The role of stabilizing the pressure is assigned to the finite element interpolation, that is, the velocity-pressure spaces will have to be div-stable. It is important to emphasize this fact because this is the main difference between the formulation presented here and the least-squares techniques, to which much attention is currently being paid in the literature.

### 2.4.1 Galerkin approach and finite element spaces

*The semidiscrete problem*

The finite element approximation we will consider is *conforming*, both for the Galerkin approach and adding the SD operator [Hu1], that is, the discrete spaces of test functions and of trial solutions will be linear subspaces of the corresponding spaces for the continuous problem. We will denote them by $V_{h,t} \subset V_t$ and $V_{h,s} \subset V_s$ for the velocity and $Q_{h,t} \subset Q_t$ and $Q_{h,s} \subset Q_s$ for the pressure. They will be constructed from a finite element partition $\{\Omega^e\}$, $e = 1, ..., N_{el}$, of the spatial domain $\Omega$.

The Galerkin semidiscrete problem consists in seeking $\mathbf{u}_h \in V_{h,s}$ and $p_h \in Q_{h,s}$ such that

$$\begin{aligned} \rho(\partial_t \mathbf{u}_h, \mathbf{v}_h) + c(\mathbf{u}_h, \mathbf{u}_h, \mathbf{v}_h) + a(\mathbf{u}_h, \mathbf{v}_h) - b(p_h, \mathbf{v}_h) &= l(\mathbf{v}_h) \qquad && \forall \mathbf{v}_h \in V_{h,t} \\ b(q_h, \mathbf{u}_h) &= 0 && \forall q_h \in Q_{h,t} \qquad (2.23) \\ (\mathbf{u}_h(\mathbf{x}, 0), \mathbf{v}_h) &= (\mathbf{u}_0(\mathbf{x}), \mathbf{v}_h) && \forall \mathbf{v}_h \in V_{h,t} \end{aligned}$$

This problem is nothing but the space-discretized version of the continuous variational equations (2.14).

*Finite element spaces*

As in Chapter 1, we will use penalty methods. It is therefore desirable to employ a discontinuous pressure interpolation, since this allows to eliminate the pressure nodal unknowns at the element level as already explained. Moreover, the velocity-pressure pairs will have to satisfy the Babuška-Brezzi stability condition (div-stability).

Some of the elements we have implemented in the computer code with which the problems of this and the following two chapters have been solved are collected in Box 2.1. There, $N_{nv}$ is the number of nodes of each element with velocity unknowns (standard $C^0$ interpolation) and $N_{qp}$ the number of pressure nodes within each element ($C^{-1}$ interpolation). Concerning the schematic for the 2D case, nodes with velocity unknowns have been represented by a circle and nodes with pressure unknowns by a triangle.

**Box 2.1 Some finite elements with discontinuous pressure**

| Element | $N_{nv}$-$N_{qp}$ $(2D/3D)$ | Description | Schematic (2D) |
|---|---|---|---|
| $Q_1/P_0$ | $4/8\ -\ 1/1$ | -Continuous bi- or tri-linear velocity.<br>Piecewise constant pressure. | 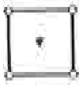 |
| $Q_2^-/P_0$ | $8/20\ -\ 1/1$ | -Serendipid velocity interpolation.<br>Piecewise constant pressure. | 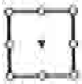 |
| $Q_2/P_1$ | $9/27\ -\ 3/4$ | -Continuous bi- or tri-quadratic velocity.<br>Piecewise linear pressure. | 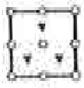 |
| $P_2/P_0$ | $6/10\ -\ 1/1$ | -Continuous quadratic velocity.<br>Piecewise constant pressure. | 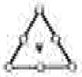 |
| $P_2^+/P_1$ | $7/15\ -\ 3/4$ | -Continuous quadratic velocity<br>enriched with bubble functions.<br>Piecewise linear pressure. | 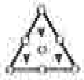 |

Let us comment now some properties of the elements in Box 2.1 concerning their convergence for stationary flows. It will be discussed thereafter what happens for the transient Navier-Stokes equations.

- *Element* $Q_1/P_0$

This is the bilinear (in 2D) or trilinear (in 3D) velocity-constant pressure element already discussed in Chapter 1. It does not satisfy the BB condition, although there are ways to stabilize it, as it has already been explained in the previous chapter. There is a simple way to see that it may work without any particular stabilization procedure. For simplicity, consider the two-dimensional case. Figure 2.1 shows how a quadratic triangular element enriched with a node placed at the barycenter of the triangle can be split into three bilinear elements. If we consider a pressure unknown for each quadrilateral, we see that the velocity and pressure spaces will be isomorphic to those of the $P_2^+/P_1$ element discussed thereafter. The velocity-pressure interpolation for this element satisfies the BB condition. Therefore, the macroelement depicted in Figure 2.1 composed of $Q_1/P_0$ elements *will also be div-stable.*

Clearly, the main problem with this approach is the distorsion of the triangular patch of three quadrilaterals. This patch has to be regular enough (i.e., the angles sufficiently close to $\pi/3$) to ensure that the isoparametric mapping to the parent domain

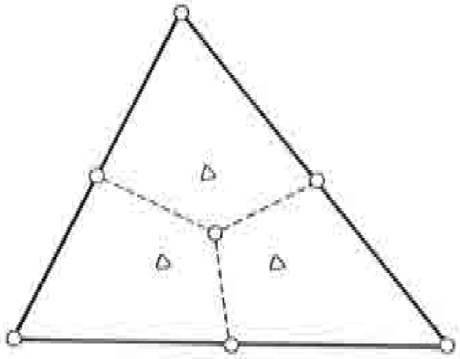

Figure 2.1 A div-stable macroelement composed of $Q_1/P_0$ elements.

(usually $[-1,1] \times [-1,1]$) is invertible. See Reference [Ci] for the regularity conditions that a finite element partition has to satisfy.

The macroelement of Figure 2.1 is homeomorphic to the macroelement of Le Tallec & Ruas [TR].

In the three-dimensional case, the $P_2^+/P_1$ element has to be split into four $Q_1/P_0$ subelements. Apparently, this connexion between the $P_2^+/P_1$ and the $Q_1/P_0$ elements has never been exploited.

Concerning the convergence properties of the $Q_1/P_0$ pair, the best we can expect is an error estimate of the form

$$\|\mathbf{u}-\mathbf{u}_h\|_k \leq Ch^{2-k}, \qquad \|p-p_h\|_0 \leq Ch \tag{2.24}$$

for $k = 0,1$ in stationary problems, since this is the interpolation error. In Reference [TR] it is proved that this is true for the Stokes problem using the macroelement introduced in this paper. In (2.24) and below, $\mathbf{u}$, $p$ denotes the solution of the continuous problem and $\mathbf{u}_h$, $p_h$ the solution of the problem discretized in space. Also, it is understood that the $L^2$ estimate for the pressure holds modulo constants if $\Gamma_N = \emptyset$.

- *Element $Q_2^-/P_0$*

This and the following elements are div-stable (see, e.g., Reference [GR3] for the proofs). The velocity interpolation uses the serendipid shape functions [Hu2], [ZT] and there is a single pressure unknown for each element. Its convergence will be driven by the pressure interpolation. Again, only an estimate of the form (2.24) can be expected.

Although several researchers actually favor the use of this element (cf. [Hu2]) because of its 'robustness', we have found from numerical experiments that it usually yields overdiffusive results, similar to those of the $Q_2/P_0$ pair emulated via reduced integration of the volumetric term (RIP method) presented in Chapter 1. The slightly higher computational effort needed for the $Q_2/P_1$ element is certainly worth affording.

- *Element $Q_2/P_1$*

For this element, both the velocity and the pressure converge at an optimal rate, i.e.,

$$\|\mathbf{u}-\mathbf{u}_h\|_k \leq Ch^{3-k}, \qquad \|p-p_h\|_0 \leq Ch^2 \tag{2.25}$$

for $k = 0,1$ (see [GR3]).

For the engineering applications, it is not only important to know that the asymptotic estimates (2.25) are optimal, but also to know how accurate the element is for a given mesh diameter $h$ (loosely speaking, this means how large the constants in (2.25) are). This knowledge is only acquired by numerical experiments. We have found the $Q_2/P_1$ pair an excellent choice for viscous incompressible flow calculations, in accordance with the results reported in the literature. This element combines several interesting features: it is quadratic in velocities, it is a quadrilateral and pressures are discontinuous. Experience shows that quadratic elements in velocities are an equilibrated compromise between accuracy and complexity (and hence, cost) [Gu]. Moreover, one can hardly expect more regularity for the continuous solution $\mathbf{u}$ and $p$ than the one needed for obtaining (2.25), that is $\mathbf{u} \in H^3(\Omega)^{N_{sd}}$, $p \in H^2(\Omega)$ for $t \in (0,T)$. On the other hand, quadrilateral elements are known to be more accurate, for a fixed $h$, than triangular ones, especially for structured meshes. Finally, elements with discontinuous pressures are superior to continuous pressure elements in capturing the details of the flow, especially in recirculation zones and boundary layers. A vast amount of numerical experiments support these facts.

Concerning the implementation of piecewise linear pressures, two options are possible. If $\mathbf{s} = (s_1, s_2, s_3)$ (in 3D) are the coordinates of the parent domain of the elements, the first choice is to place $N_{sd} + 1 = 4$ nodes within the elements, with coordinates $\mathbf{s}_j$, $j = 1,2,3,4$, and construct shape functions $N_i(\mathbf{s})$, $i = 1,2,3,4$, such that $N_i(\mathbf{s}_j) = \delta_{ij}$ (the Kronecker symbol) for $i,j = 1,2,3,4$. Then, if the pressure is interpolated as $p(\mathbf{s}) = \sum_{i=1}^{4} N_i(\mathbf{s})p_i$, the coefficients $p_i$, $i = 1,2,3,4$, have the meaning of being the nodal values of the pressure. A simpler option is to interpolate $p$ as $p(\mathbf{s}) = p_0 + s_1p_1 + s_2p_2 + s_3p_3$. Now, $p_0$ is the value of the pressure for $s_1 = s_2 = s_3 = 0$ and $p_1, p_2$ and $p_3$ are its first derivatives. In our computations, we have found no difference in the numerical results using both approaches.

The $Q_2/P_1$ element for the 3D case is represented in Figure 2.2. The pressure nodes are located at the vertices of a tetrahedron placed in the interior of the brick with the velocity nodes.

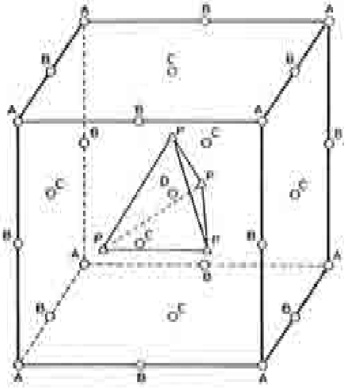

Figure 2.2 Three-dimensional $Q_2/P_1$ element.

• *Element $P_2/P_0$*

This element suffers from the same problems that the $Q_2^-/P_0$ element, perhaps to a lesser extend. Although the velocity is quadratic, the fact that the pressure is piecewise constant controls the error of the approximation. Only the estimate (2.24) can be obtained.

- *Element $P_2^+/P_1$*

This element is sometimes referred to as the Crouzieux-Raviart pair [CR]. The triangular quadratic element in velocities is enriched with bubble functions. For the 2D case, a single node is added at the barycenter of the element, whereas for the 3D case nodes have to be added also on the faces of the tetrahedron. The pressure is piecewise linear and discontinuous. The same remarks as for the $Q_2/P_1$ element regarding the implementation of the pressure interpolation apply. The 3D $P_2^+/P_1$ element is shown in Figure 2.3.

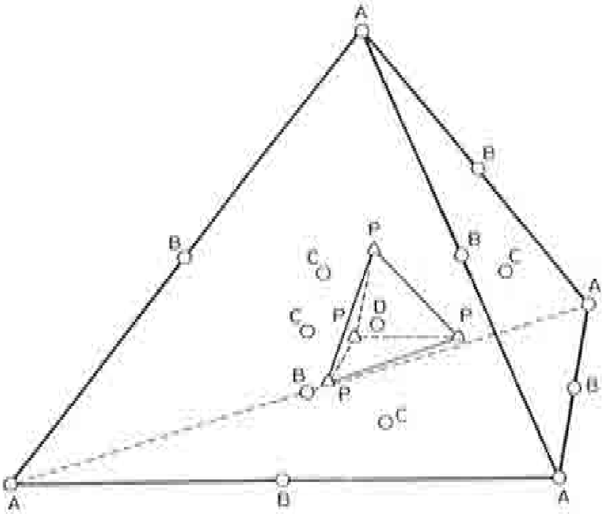

Figure 2.3 Three-dimensional $P_2^+/P_1$ element.

This element also converges at an optimal rate, i.e., estimates (2.25) hold true.

Although we prefer the $Q_2/P_1$ element for simple geometries, triangular elements have the important attribute that automatic mesh generation and thus adaptivity are easier to implement using triangles, since they are well suited for designing unstructured meshes. Therefore, the $P_2^+/P_1$ pair should be considered as a good alternative to the $Q_2/P_1$ element in complicated geometries or when adaptive procedures have to be used to obtain an error below a prescribed threshold in the computation.

For two-dimensional problems, there is a heuristic index that gives an idea of the accuracy of the element and of how can it reproduce the incompressibility constraint. It is the so called *constraint ratio*, that is the number of velocity unknowns over the number of pressure unknowns in the asymptotic limit $h \to 0$ [Hu2]. For the $P_2^+/P_1$ element it is 2, thus reproducing what happens in the continuous problem. In this sense, 2 is the optimal value. For the $Q_2/P_1$ it is 8/3, showing that this element is somehow underconstraint.

*Fully discrete problem*

When the generalized trapezoidal rule is applied to problem (2.23) one is led to the following algorithm:

*For $n = 1, 2, ..., N$, given $\mathbf{u}_h^{n-1}(\mathbf{x})$ and $p_h^{n-1}(\mathbf{x})$ find $\mathbf{u}_h^n(\mathbf{x})$ and $p_h^n(\mathbf{x})$ such that*

$$\begin{aligned}
\rho\frac{1}{\Delta t}(\mathbf{u}_h^n - \mathbf{u}_h^{n-1}, \mathbf{v}_h) + \theta c(\mathbf{u}_h^n, \mathbf{u}_h^n, \mathbf{v}_h) + (1-\theta)c(\mathbf{u}_h^{n-1}, \mathbf{u}_h^{n-1}, \mathbf{v}_h)& \\
+\theta a(\mathbf{u}_h^n, \mathbf{v}_h) + (1-\theta)a(\mathbf{u}_h^{n-1}, \mathbf{v}_h)& \\
-\theta b(p_h^n, \mathbf{v}_h) - (1-\theta)b(p_h^{n-1}, \mathbf{v}_h) = \theta l^n(\mathbf{v}_h) + (1-\theta)l^{n-1}(\mathbf{v}_h)& \\
b(q_h, \mathbf{u}_h^n) = 0&
\end{aligned} \tag{2.26}$$

where $N$ is the number of time steps of size $\Delta t$ in which the interval $[0, T]$ has been divided. Clearly, we could also have started from (2.20) and discretize this problem in space using the Galerkin method. The following diagram shows how the different problems are related:

$$\begin{tikzcd}
\text{Eqn. (2.14)} \arrow[r, "\text{Space discret.}"] \arrow[d, "\text{Time discret.}"] & \text{Eqn. (2.23)} \arrow[d, "\text{Time discret.}"] \\
\text{Eqn. (2.20)} \arrow[r, "\text{Space discret.}"] & \text{Eqn. (2.26)}
\end{tikzcd}$$

This is a commutative diagram.

*Convergence results*

Our purpose now is to quote some of the results obtained by Heywood & Rannacher [HR1–4] for the semidiscrete problem (2.23) and for the fully discrete problem (2.26) in the case $\Gamma_N = \emptyset$, i.e., when the velocity is prescribed on the whole boundary $\Gamma$ (see also [BR] for a similar analysis). For (2.26), $\theta = 1/2$ is considered. In fact, in the above quoted references the trapezoidal rule is implemented using the discrete version of (2.22). For the reasons explained earlier, we believe that these results will also hold for (2.26).

Consider first the semidiscrete problem (2.23) and assume that the finite element spaces satisfy the following interpolation properties:

$$\|(\mathbf{u} - \tilde{\mathbf{u}}_h)(t)\|_0 \leq Ch^m, \qquad \|(p - \tilde{p}_h)(t)\|_0 \leq Ch^{m-1} \tag{2.27}$$

where $\tilde{\mathbf{u}}_h$ and $\tilde{p}_h$ are the finite element interpolants for the velocity and the pressure, respectively, $m \in \{2, 3, 4, 5\}$ and $C$ is a constant independent of $t$. Then, for the solution $\mathbf{u}_h(\mathbf{x}, t)$, $p_h(\mathbf{x}, t)$ of problem (2.23) the following error bounds can be proved [HR2]:

$$\|(\mathbf{u} - \mathbf{u}_h)(t)\|_0 \leq E_1(t)h^m, \qquad \|(p - p_h)(t)\|_0 \leq E_2(t)h^{m-1} \tag{2.28}$$

where the error constants $E_1(t)$ and $E_2(t)$ become singular when $t \to 0^+$. If $\mathbf{u}_0(\mathbf{x}) = \bar{\mathbf{u}}(\mathbf{x}, 0)$ on $\Gamma$ and $\nabla \cdot \mathbf{u}_0 = 0$, it can be shown that

$$\|\mathbf{u}(t)\|_m + \|\partial_t \mathbf{u}(t)\|_{m-2} \leq Kt^{1-m/2}, \qquad \text{as } t \to 0^+ \tag{2.29}$$

where $K$ is a constant independent of $t$. A similar 'smoothing estimate' is found for parabolic equations [LR]. Since the function $E_1(t)$ involves $\|\mathbf{u}\|_m$, it will behave as

$t^{1-m/2}$ for $t \to 0^+$. A similar bound can be proved for $E_2(t)$. Roughly speaking, $E_1(t)$ and $E_2(t)$ will behave as follows:

$$E_1(t) \sim t^{1-m/2}, \qquad E_2(t) \sim t^{1/2-m/2}, \qquad \text{as } t \to 0^+ \tag{2.30}$$

For the particular case $m = 3$, the function $E_1(t)$ can be bounded above by a constant independent of $t$ if the data $\mathbf{f}$, $\mathbf{u}_0(\mathbf{x})$ and $\bar{\mathbf{u}}(\mathbf{x}, t)$ satisfy the following compatibility condition:

$$\begin{aligned} &\text{There exists } p_0 \in H^1(\Omega)/\mathbb{R} \text{ such that} && \\ &\Delta p_0 = \nabla \cdot [\mathbf{f} - (\mathbf{u}_0 \cdot \nabla)\mathbf{u}_0] && \text{in } \Omega \\ &\nabla p_0 = \rho[\mathbf{f} - (\mathbf{u}_0 \cdot \nabla)\mathbf{u}_0 - \partial_t \bar{\mathbf{u}}] + \mu \Delta \mathbf{u}_0 && \text{on } \Gamma \end{aligned} \tag{2.31}$$

This an overdetermined Neumann problem, with boundary conditions on $\nabla p_0$ and not only on $\partial p_0/\partial n$. If (2.31) holds true, then $\|\mathbf{u}(t)\|_3 < \infty$ and $\|\partial_t \mathbf{u}(t)\|_1 < \infty$ for all $t \in (0, T)$ and therefore $E_1(t) \leq E \; \forall t \in (0, T)$, with $E < \infty$ independent of $t$.

The main conclusion of these results for someone interested in computational aspects is that for $t$ small it is not possible in general to achieve the accuracy that the finite element interpolation might provide. For $m = 3$, i.e., when elements quadratic in velocities are used, both $E_1(t) \to \infty$ and $E_2(t) \to \infty$ as $t \to 0^+$. The best one can hope for is one degree of convergence less, i.e., $m = 2$. In this case, $E_1(t)$ remains bounded for $t \to 0^+$, but still $E_2(t) \to \infty$. These facts give another convincing argument for choosing a dissipative time stepping algorithm for the first few time steps. Using the generalized trapezoidal rule, $\theta = 1$ is a wise option.

Estimates (2.28) are *local*, i.e., they hold for sufficiently small $t$. Similarly to what happens for the continuous problem, $E_1(t)$ and $E_2(t)$ grow exponentially in time if $N_{sd} = 3$. Nevertheless, if the solution of the continuous problem is stable, one can hope that upper bounds for $E_1(t)$ and $E_2(t)$ exist as $t \to \infty$. Results concerning these facts are proved in [HR2] and [HR3].

Let us go now to the fully discrete problem (2.26). In Reference [HR4] the following estimates are derived for the Crank-Nicolson scheme:

$$\|\mathbf{u}_h^n - \mathbf{u}_h(t^n)\|_0 \leq F_1(t^n)\Delta t^2, \qquad \|p_h^n - p_h(t^n)\|_0 \leq F_2(t^n)\Delta t \tag{2.32}$$

In general situations, the functions $F_1(t)$ and $F_2(t)$ behave as follows:

$$F_1(t) \sim t^{-1}, \qquad F_2(t) \sim t^{-3/2}, \qquad \text{as } t \to 0^+ \tag{2.33}$$

But an upper bound for $F_1(t)$ and $F_2(t)$ is obtained if $\|\partial_{tt}^2 \mathbf{u}(t)\|_0 < \infty$, and this holds if the compatibility condition (2.31) does.

If the continuous solution $\mathbf{u}$ is exponentially stable [Jos], [Ge], then (2.32) are also valid as global estimates in time, that is, the functions $F_1(t)$ and $F_2(t)$ are bounded above as $t \to \infty$. But this is only true if the time step size is such that

$$\Delta t \leq C h^{3/2} \tag{2.34}$$

for $\theta = 1/2$. Restriction (2.34) is not needed if the Crank-Nicolson scheme is combined with the implicit Euler method in the way explained in Reference [HR4]. In any case, this analysis shows that the exponential stability of the continuous problem implies exponential stability of its discrete counterpart. A comforting result, actually.

### 2.4.2 Streamline Diffusion operator

The Galerkin aproach discussed so far has a hidden difficulty not apparent in the error estimates (2.24), (2.25) and (2.28): the stability constants are proportional to the Reynolds number of the problem, $Re$. Therefore, for $Re^{-1} < h$, these estimates are misleading, they are not as optimal as they appear at first glance.

As for the convection-diffusion equation, the suboptimal rate of convergence of the Galerkin approach is not only reflected by a more or less small loss of accuracy, but it is found in practice that important numerical oscillations occur. The parameter that now plays the role of the Péclet number is the *cell* (or *element*) *Reynolds number*, already introduced in Chapter 1:

$$(Re)^e := \rho \frac{|\mathbf{u}^e| h^e}{2\mu} \tag{2.35}$$

Linear elements are expected to yield oscillatory results for $(Re)^e > 1$ and quadratic elements for $(Re)^e > 2$.

The use of upwind techniques is absolutely necessary for convection-diffusion problems. However, this is often questioned for the Navier-Stokes equations and in fact these methods (as a family) are blamed to be inaccurate in some well known text books [CSS], [Gu]. We firmly believe that they are also necessary in this case. The problem is that high Reynolds numbers are associated to complex flow features, such as small recirculation zones, boundary layers, flow detachment, periodic oscillating flow patterns, instabilities and, finally, turbulence. There is no way to capture all these flow details but using small element sizes and therefore small cell Reynolds numbers.

*Semidiscrete problem*

Let us start considering problem (2.23). In order to stabilize the convective term $c(\mathbf{u}_h, \mathbf{u}_h, \mathbf{v}_h)$, the same procedure as for the convection-diffusion equation will be applied. The test function $\mathbf{v}_h$ will be perturbed by adding a term only affecting the element interiors. This term will be proportional to *the convection operator* applied to the test function.

The variational problem to be solved is the following: Find $\mathbf{u}_h(\mathbf{x}, t) \in V_{h,s}$ and $p_h(\mathbf{x}, t) \in Q_{h,s}$ such that

$$\begin{aligned} \rho(\partial_t \mathbf{u}_h, \mathbf{v}_h) + c(\mathbf{u}_h, \mathbf{u}_h, \mathbf{v}_h) + a(\mathbf{u}_h, \mathbf{v}_h) - b(p_h, \mathbf{v}_h) & \\ + \sum_{e=1}^{N_{el}} \mathcal{S}^e(\mathbf{u}_h, p_h; \mathbf{v}_h) = l(\mathbf{v}_h) & \qquad \forall \mathbf{v}_h \in V_{h,t} \\ b(q_h, \mathbf{u}_h) = 0 & \qquad \forall q_h \in Q_{h,t} \\ (\mathbf{u}_h(\mathbf{x}, 0), \mathbf{v}_h) = (\mathbf{u}_0(\mathbf{x}), \mathbf{v}_h) & \qquad \forall \mathbf{v}_h \in V_{h,t} \end{aligned} \tag{2.36}$$

where $\mathcal{S}^e(\mathbf{u}_h, p_h; \mathbf{v}_h)$ is the nonlinear functional

$$\mathcal{S}^e(\mathbf{u}_h, p_h; \mathbf{v}_h) := \int_{\Omega^e} \boldsymbol{\zeta}(\mathbf{u}_h, \mathbf{v}_h) \cdot [\mathcal{N}(\mathbf{u}_h, p_h) - \rho \mathbf{f}] \, d\Omega \tag{2.37}$$

The perturbation $\boldsymbol{\zeta}$ of the test function is defined as

$$\boldsymbol{\zeta}(\mathbf{u}_h, \mathbf{v}_h) := \tau^e (\mathbf{u}_h \cdot \nabla) \mathbf{v}_h \tag{2.38}$$

where $\tau^e$ is the intrinsic time to be specified later. In (2.37), the Navier-Stokes operator $\mathcal{N}$ is

$$\mathcal{N}(\mathbf{u}_h, p_h) := \rho[\partial_t \mathbf{u}_h + (\mathbf{u}_h \cdot \nabla)\mathbf{u}_h] - \mu\Delta\mathbf{u}_h + \nabla p_h \tag{2.39}$$

**Remarks 2.1**

(1) We have employed the simplified version $\mu\Delta\mathbf{u}_h$ instead of $2\mu\nabla \cdot \boldsymbol{\varepsilon}(\mathbf{u}_h)$ for the viscous term. Observe that second derivatives of the shape functions will be needed for calculating this term. The main problem with this simplification will be found in the case of nonconstant viscosities. Implicitly, in (2.37) it is assumed that the viscosity is constant for each element. In practice, this situation will be rarely found: fluids with variable viscosity usually flow at a very low Reynolds numbers, in which case adding the SD operator to the Galerkin equations is unnecessary.

(2) The functional $\mathcal{S}^e(\mathbf{u}_h, p_h; \mathbf{v}_h)$, defined on $V_{h,s} \times Q_{h,s} \times V_{h,t}$, is linear in the last two arguments, but highly nonlinear in the first. Besides the quadratic dependence on $\mathbf{u}_h$ of $\mathcal{N}(\mathbf{u}_h, p_h)$ and the linear dependence of the term $(\mathbf{u}_h \cdot \nabla)\mathbf{v}_h$, the intrinsic time $\tau^e$ will be a function of $|\mathbf{u}_h|$ and the cell Reynolds number $(Re)^e$ given by (2.35).

(3) The perturbation $\boldsymbol{\zeta}(\mathbf{u}_h, \mathbf{v}_h)$ will be in practice calculated not with a variable velocity $\mathbf{u}_h(\mathbf{x}, t)$, but with a characteristic value for each element, $\mathbf{u}^e(t)$, usually taken as the mean velocity in the element. □

The definition of the SD method (2.36) has the important drawback that it is not clear how to discretize it in time. Once the spatial discretization has been done, a system of nonlinear ordinary differential equations of the form

$$\dot{x} + F_1(x, t) + F_2(x, \dot{x}, t) = 0$$

is found, with $F_2(x, \dot{x}, t)$ coming from the SD term and $F_1(x, t)$ from the Galerkin terms.

*Fully discrete problem*

The conceptual problem found above is due to the fact that we are mixing a variational method for the spatial discretization and a finite difference method to discretize in time. In order to have a problem where only the space has to be discretized, we may assume given the time discretization (problem (2.20)) and then to discretize in space. Following this approach, a SD term will have to be added to the Galerkin equations (2.26), and not to (2.23). The residual method we will end up with is the following:

*For $n = 1, 2, ..., N$, given $\mathbf{u}_h^{n-1}(\mathbf{x})$ and $p_h^{n-1}(\mathbf{x})$ find $\mathbf{u}_h^n(\mathbf{x})$ and $p_h^n(\mathbf{x})$ such that*

$$\begin{aligned}\rho\frac{1}{\Delta t}(\mathbf{u}_h^n - \mathbf{u}_h^{n-1}, \mathbf{v}_h) + \theta c(\mathbf{u}_h^n, \mathbf{u}_h^n, \mathbf{v}_h) + (1-\theta)c(\mathbf{u}_h^{n-1}, \mathbf{u}_h^{n-1}, \mathbf{v}_h)\\ +\theta a(\mathbf{u}_h^n, \mathbf{v}_h) + (1-\theta)a(\mathbf{u}_h^{n-1}, \mathbf{v}_h) - \theta b(p_h^n, \mathbf{v}_h) - (1-\theta)b(p_h^{n-1}, \mathbf{v}_h)\\ + \sum_{e=1}^{N_{el}} \mathcal{S}^{n,e}(\mathbf{u}_h, p_h; \mathbf{v}_h) = \theta l^n(\mathbf{v}_h) + (1-\theta)l^{n-1}(\mathbf{v}_h)\\ b(q_h, \mathbf{u}_h^n) = 0\end{aligned} \tag{2.40}$$

where $\mathcal{S}^{n,e}(\mathbf{u}_h, p_h; \mathbf{v}_h)$ is defined as

$$\mathcal{S}^{n,e}(\mathbf{u}_h, p_h; \mathbf{v}_h) := \int_{\Omega^e} \boldsymbol{\zeta}(\mathbf{u}_h^n, \mathbf{v}_h) \cdot [\mathcal{N}_\theta^n(\mathbf{u}_h, p_h) - \rho\mathbf{f}_\theta^n]\, d\Omega \tag{2.41}$$

Here, $\boldsymbol{\zeta}$ is again given by (2.38) (but evaluated with $\mathbf{u}_h^n$) and

$$\begin{aligned}\mathcal{N}_\theta^n(\mathbf{u}_h, p_h) :=\ & \rho\frac{1}{\Delta t}(\mathbf{u}_h^n - \mathbf{u}_h^{n-1}) + \rho\theta(\mathbf{u}_h^n\cdot\nabla)\mathbf{u}_h^n + \rho(1-\theta)(\mathbf{u}_h^{n-1}\cdot\nabla)\mathbf{u}_h^{n-1} \\ & - \mu\theta\Delta\mathbf{u}_h^n - \mu(1-\theta)\Delta\mathbf{u}_h^{n-1} + \theta\nabla p_h^n + (1-\theta)\nabla p_h^{n-1}\end{aligned} \tag{2.42}$$

**Remarks 2.2**

(1) Observe that the perturbation $\boldsymbol{\zeta}$ given by (2.38) has to be calculated using the velocity $\mathbf{u}_h^n$, since what is pretended using (2.40) is to balance the convective term $\rho\theta(\mathbf{u}_h^n\cdot\nabla)\mathbf{u}_h^n$ with the viscous term $2\mu\theta\nabla\cdot\boldsymbol{\varepsilon}(\mathbf{u}_h^n)$ (written in weak form).

(2) Clearly, (2.40) is a residual method, i.e., the continuous functions in the space variable $\mathbf{u}^n(\mathbf{x})$ and $p^n(\mathbf{x})$ solution of problem (2.20) satisfy (2.40) for all $n$.

(3) The following diagram represents the relation between the semidiscrete and the fully discrete problems using the Galerkin approach and adding the SD operator. Problem (2.40) is *not* obtained from (2.36) using the generalized trapezoidal rule for the time discretization in its standard form. □

$$\begin{tikzcd}\text{Eqn. (2.23)} \arrow[r, "\text{SD operator}"] \arrow[d, "\text{Time discret.}"] & \text{Eqn. (2.36)} \\ \text{Eqn. (2.26)} \arrow[r, "\text{SD operator}"] & \text{Eqn. (2.40)}\end{tikzcd}$$

The SD method we will consider in all what follows is (2.40). It only remains to apply the ideas of Reference [Co] (Chapter 1) to compute the intrinsic time $\tau^e$.

*Definition of the intrinsic time*

The parameter $\tau^e$ will be calculated for each element using the results in [Co], collected in Section 1.6 of this reference. The only remarkable aspect is that for quadractic elements a single upwind function will be used (see Box 1.1 of Reference [Co]). Moreover, both for linear and quadratic elements, the upwind functions will be approximated by their asymptotic expressions. From the numerical results of Reference [Co] it was concluded that this procedure results in a certain loss of accuracy, but the numerical implementation is much easier and cheaper. In particular, the calculations to be carried out are exactly the same for linear and for quadratic elements.

The steps to be followed to compute $\tau^e$ for element $e$, $e = 1, ..., N_{el}$, are:

- Compute $\mathbf{u}^e$ as the mean velocity over the element.
- Compute $\mathbf{u}_0^e = \mathbf{J}^{-1}\mathbf{u}^e$, where $\mathbf{J}$ is the Jacobian matrix of the isoparametric mapping to the parent domain evaluated at the center of gravity of the element (assumed to be the point with velocity $\mathbf{u}^e$).
- Compute the characteristic length as (formula (1.118) in Reference [Co]):

$$h^e = h_0\frac{|\mathbf{u}^e|}{|\mathbf{u}_0^e|}$$

The values $h_0 = 2$ and $h_0 = 0.7$ are recommended for the standard parent domains [ZT] of quadrilaterals and triangles, respectively.

- Calculate the cell Reynolds number $(Re)^e$ given by (2.35) using the values just obtained.
- Set the upwind function equal to

$$\alpha^e = \alpha_0 \min\left(\frac{(Re)^e}{3}, 1\right)$$

where $\alpha_0 = 1$ for linear elements and $\alpha_0 = 1/2$ for quadratics.

- Finally, compute

$$\tau^e = \frac{\alpha^e h^e}{2|\mathbf{u}^e|} \tag{2.43}$$

*Some remarks about least-squares techniques*

The SD method described above is close to the original SUPG technique of Brooks & Hughes [BH] and used by many authors. Reference [ADP] is sometimes considered as the first to make a systematic use of this formulation.

Already before the first paper of Hughes *et al.* [HFB] about the Galerkin/least-squares method, Johnson & Saranen proposed in Reference [JS] a velocity-pressure formulation for the Navier-Stokes equations introducing a perturbation of the test funtions of the form

$$\tau\left[(\mathbf{u}_h \cdot \nabla)\mathbf{v}_h + \nabla q_h\right] \tag{2.44}$$

i.e., *including the gradient of the pressure test function* (see also [Joh]). Although the method was not analyzed in the quoted reference, the analysis of Hughes *et al.* for the Stokes problem revealed that this was the key for circumventing the BB condition. The least-squares techniques followed as a natural consequence of these results (see the references of Chapter 1), both for the Stokes problem and the Navier-Stokes equations. Several partial results concerning the convergence of this method are already available [HS], [TLu].

A very interesting fact is that sometimes the introduction of $\nabla q_h$ in (2.44) *is equivalent to a mixed velocity-pressure formulation* using div-stable interpolations. In particular, Bank & Welfert [BW] proved that this is indeed the case for the Stokes problem if the minielement of Arnold *et al.* [ABF] is used for the Galerkin approach and the linear simplicial element is used for the least-squares formulation. Of course the finite element interpolation is simpler in the latter case, but the construction and assembly of the element matrices is more complicated. It is not known which method is finally more efficient. Probably, this will depend on the problem. The use of mixed interpolations to stabilize the pressure has the important advantage that discontinuous pressure spaces are easily accomodated and therefore penalty methods fit nicely in this approach.

Let us finally mention other approaches to least-squares methods such as methods based on other variables [HG], [JS] or the interpretation of the least-squares procedure using certain time stepping algorithms [Sa], [Zi]. For another upwind technique different from the SD method and fully analyzed, see [GR2].

## 2.5 Linearized equations and penalty methods

### 2.5.1 Linearization of the convective term and the Streamline Diffusion operator

The algorithm we will use for the computations is (2.40). It only remains to describe how is it linearized in order to implement it in a computer code.

There are two sources of nonlinearity: the convective term and the SD operator. The first has a quadratic dependence on the velocity $\mathbf{u}_h^n$. We will consider the two iterative methods analyzed in Chapter 1 in the context of iterative penalization, namely, the Picard and the Newton-Raphson algorithms. Both methods may be written in the same unified expression. Assume that the velocity at time step $n$ and iteration $i-1$ ($i \geq 1$) is known. This velocity will be denoted by $\mathbf{u}_h^{n,(i-1)}$. Then, the convective term evaluated at $\mathbf{u}_h^{n,(i)}$ will be approximated by:

$$\begin{aligned} c(\mathbf{u}_h^{n,(i)}, \mathbf{u}_h^{n,(i)}, \mathbf{v}_h) \approx {} & c(\mathbf{u}_h^{n,(i-1)}, \mathbf{u}_h^{n,(i)}, \mathbf{v}_h) + \beta c(\mathbf{u}_h^{n,(i)}, \mathbf{u}_h^{n,(i-1)}, \mathbf{v}_h) \\ & - \beta c(\mathbf{u}_h^{n,(i-1)}, \mathbf{u}_h^{n,(i-1)}, \mathbf{v}_h) \end{aligned} \tag{2.45}$$

For $\beta = 0$ this is the Picard approximation and for $\beta = 1$ the Newton-Raphson method. If $\delta\mathbf{u} := \mathbf{u}_h^{n,(i)} - \mathbf{u}_h^{n,(i-1)}$, the linearization error in the first case is $O(\|\delta\mathbf{u}\|_1)$ and in the second case it is $O(\|\delta\mathbf{u}\|_1^2)$.

The convective term in the Navier-Stokes operator $\mathcal{N}_\theta^n$ given by (2.42) will be linearized in a similar way:

$$\begin{aligned} \rho\theta(\mathbf{u}_h^{n,(i)} \cdot \nabla)\mathbf{u}_h^{n,(i)} \approx {} & \rho\theta(\mathbf{u}_h^{n,(i-1)} \cdot \nabla)\mathbf{u}_h^{n,(i)} + \rho\theta\beta(\mathbf{u}_h^{n,(i)} \cdot \nabla)\mathbf{u}_h^{n,(i-1)} \\ & - \rho\theta\beta(\mathbf{u}_h^{n,(i-1)} \cdot \nabla)\mathbf{u}_h^{n,(i-1)} \end{aligned} \tag{2.46}$$

Concerning the perturbation of the test function (2.38) that defines the SD method, the velocity with which it is calculated should only affect the accuracy of the numerical method, not the convergence of the iterative procedure. In other words, this source of nonlinearity appears only because the accuracy will be improved evaluating $\boldsymbol{\zeta}$ with $\mathbf{u}_h^n$, one of the unknowns of the problem. In order to simplify the calculations per iteration, $\boldsymbol{\zeta}$ has been calculated using the velocity of the previous iteration, $\mathbf{u}_h^{n,(i-1)}$. This leads to the following linearized expression of the SD operator:

$$\mathcal{S}^{n,(i),e}(\mathbf{u}_h, p_h, \mathbf{v}_h) \approx \int_{\Omega^e} \boldsymbol{\zeta}(\mathbf{u}_h^{n,(i-1)}, \mathbf{v}_h) \cdot \left[\mathcal{N}_{\theta,\beta}^{n,(i)}(\mathbf{u}_h, p_h) - \rho\mathbf{f}_\theta^n\right] d\Omega \tag{2.47}$$

where

$$\begin{aligned} \mathcal{N}_{\theta,\beta}^{n,(i)}(\mathbf{u}_h, \mathbf{v}_h) := {} & \rho\frac{1}{\Delta t}(\mathbf{u}_h^{n,(i)} - \mathbf{u}_h^{n-1}) + \rho\theta(\mathbf{u}_h^{n,(i-1)} \cdot \nabla)\mathbf{u}_h^{n,(i)} \\ & + \rho\theta\beta(\mathbf{u}_h^{n,(i)} \cdot \nabla)\mathbf{u}_h^{n,(i-1)} - \rho\theta\beta(\mathbf{u}_h^{n,(i-1)} \cdot \nabla)\mathbf{u}_h^{n,(i-1)} \\ & + \rho(1-\theta)(\mathbf{u}_h^{n-1} \cdot \nabla)\mathbf{u}_h^{n-1} - \mu\theta\Delta\mathbf{u}_h^{n,(i)} \\ & - \mu(1-\theta)\Delta\mathbf{u}_h^{n-1} + \theta\nabla p_h^{n,(i)} + (1-\theta)\nabla p_h^{n-1} \end{aligned} \tag{2.48}$$

is the linearized expression for the Navier-Stokes operator at time step number $n$ and iteration number $i$.

**Remarks 2.3**

(1) The fact that $\zeta$ is evaluated with $\mathbf{u}_h^{n,(i-1)}$ could hinder to achieve quadratic convergence of the Newton-Raphson scheme. Numerical experiments indicate that this happens sometimes, but in general the difference in the test functions from one iteration to another keeps the quadratic rate of convergence.

(2) The values at time step $n-1$ are considered converged. This is why no iteration superscript has been introduced for them.

(3) In practice, the initial guess for each time step has been taken as the converged unknown from the previous step, that is,

$$\mathbf{u}_h^{n,(0)} = \mathbf{u}_h^{n-1} \tag{2.49}$$

(4) In Chapter 1 it has already been said that the Picard scheme converges for the steady-state problem whenever condition (1.12) holds and that the Newton-Raphson algorithm is convergent if the initial guess is close enough to the final solution. For transient problems condition (1.12) does not make sense: the solution is unique for both the continuous and the discrete problems in 2D. For 3D problems, a unique solution also exists for the discrete problem (it is not known whether this is true or not in the continuum). This can be proved using a discrete Gronwall inequality as in References [GR1], [JS] (the stability of this discrete solution is another matter). The only requirement is that the time step size $\Delta t$ be sufficiently small. This provides a natural way for obtaining stable stationary solutions of the Navier-Stokes equations, whenever they exist: to advance in time until the steady-state is reached. This avoids the need for using continuation techniques for the stationary equations. The situation in completely different in solid mechanics, where the differential equations of motion involve second time derivatives. □

### 2.5.2 Penalty methods

Similarly to what was done for the stationary equations, the incompressibility constraint in problem (2.40) will be penalized. In view of the results of Chapter 1, the iterative penalization is considered as a way to satisfy this condition. Once again, the iterations due to the nonlinearity of the problem and the penalization will be dealt with in a single iterative loop.

From the algorithmic standpoint, it is possible to place three different penalty methods within the same coding structure. For that, consider that the incompressibility condition in (2.40) is replaced by the penalized equation

$$\epsilon(p_h^{n,\epsilon(i)}, q_h) + b(q_h, \mathbf{u}_h^{n,\epsilon(i)}) = \epsilon(p_h^*, q_h) \tag{2.50}$$

for all $q_h \in Q_{h,t}$. The superscript $\epsilon$ has been added to indicate that the solution comes from a penalized problem. According to the pressure $p_h^*$ to be introduced in (2.50) we obtain the following penalty methods:

- $p_h^* \equiv 0$: *Classical penalty method*

This approach should be viewed as a perturbation of the initial problem. The incompressibility constraint will be satisfied up to an error of order $\epsilon$ that will not improve as the iterative procedure goes on.

- $p_h^* = p_h^{n-1}$: *Artificial compressibility*

  From (2.50) we will have that

$$\epsilon(p_h^{n,\epsilon(i)} - p_h^{n-1}, q_h) + b(q_h, \mathbf{u}_h^{n,\epsilon(i)}) = 0 \tag{2.51}$$

This is the discrete version of the continuous equation

$$\frac{1}{c^2}\partial_t p + \nabla \cdot \mathbf{u} = 0, \qquad \text{in } \Omega \times (0,T)$$

provided that the backward Euler scheme is used to discretize in time and $\epsilon$ is taken as

$$\epsilon = 1/c^2 \Delta t$$

the constant $c$ being the speed of sound of a slightly compressible fluid. Thus, setting $p_h^* = p_h^{n-1}$ a particular version of the artificial compressibility method of Chorin [Ch] is obtained. Clearly, if the steady-state is reached, $\partial p/\partial t \to 0$ as $t \to \infty$ and $p_h^n - p_h^{n-1} \to 0$ as $n \to \infty$ for the discrete problem. Therefore, $b(q_h, \mathbf{u}_h^{n,\epsilon(i)}) \to 0$ as $n \to \infty$. But when we are far from the steady-state or it simply does not exist, an error of order $\epsilon$ will again remain for the incompressibility constraint.

- $p_h^* = p_h^{n,\epsilon(i-1)}$: *Iterative penalization*

  This method is the extension of the one analyzed in the previous chapter for the stationary equations to the transient problem. For each time step $n$, the incompressibility condition is expected to be iteratively approximated. Although the convergence analysis of this method has not been attempted, numerical experiments show that the norm of the discrete divergence of the velocity field in fact decreases similarly to what was observed for the stationary problem. Some of these numerical results will be presented in Section 2.8.

### 2.5.3 Fully discrete and linearized algorithm

The final problem will be (2.40) with the approximations (2.45), (2.46) and (2.47) for the linearization of the nonlinear terms and (2.50) for the penalty method to be used. In the equations below, we assume that the iterative penalization is employed, that is, the pressure $p_h^*$ is set equal to $p_h^{n,\epsilon(i-1)}$. It is understood that the other possibilities described earlier can be also considered.

The perturbation of the test funtion for the SD term is computed using the characteristic element velocity $\mathbf{u}^e$, computed as the mean value of the velocity $\mathbf{u}_h^{n,\epsilon(i-1)}$ over element $e$. The calculation of the intrinsic time $\tau^e$ has already been described in detail.

Concerning the way convergence is checked, we have used the following criterion:

$$\|\mathbf{u}_h^{n,\epsilon(i)} - \mathbf{u}_h^{n,\epsilon(i-1)}\|_{L^q} \leq TOL \|\mathbf{u}_h^{n,\epsilon(i)}\|_{L^q} \tag{2.52}$$

where $TOL$ is a given tolerance and $\|\cdot\|_{L^q}$ denotes the discrete $L^q$ norm. A selected choice for $q$ controls the convergence, although the norms for $q=1$, $q=2$ and $q=\infty$ (i.e., maximum norm) are always computed. There is also a check to decide whether the steady-state has been reached or not. Since the difference between $\mathbf{u}_h^n$ and $\mathbf{u}_h^{n-1}$ will be of order $\Delta t$, the stationarity criterion that has been chosen is

$$||\mathbf{u}_h^n - \mathbf{u}_h^{n-1}||_{L^q} \leq TOL\ \Delta t\ ||\mathbf{u}_h^n||_{L^q} \tag{2.53}$$

All the terms that are known for a given iteration within a time step have been written in the right-hand-side of the equations. These equations are

- *Momentum equation:*

$$\begin{aligned}
&\rho(\mathbf{u}_h^{n,\epsilon(i)}, \mathbf{v}_h) + \theta\Delta t c(\mathbf{u}_h^{n,\epsilon(i-1)}, \mathbf{u}_h^{n,\epsilon(i)}, \mathbf{v}_h) + \theta\Delta t\beta c(\mathbf{u}_h^{n,\epsilon(i)}, \mathbf{u}_h^{n,\epsilon(i-1)}, \mathbf{v}_h)\\
&+ \theta\Delta t a(\mathbf{u}_h^{n,\epsilon(i)}, \mathbf{v}_h) - \theta\Delta t b(p_h^{n,\epsilon(i)}, \mathbf{v}_h)\\
&+ \sum_{e=1}^{N_{el}} \int_{\Omega^e} [\tau^e(\mathbf{u}^e \cdot \nabla)\mathbf{v}_h] \cdot \Big[\rho\mathbf{u}_h^{n,\epsilon(i)} + \rho\theta\Delta t(\mathbf{u}_h^{n,\epsilon(i-1)} \cdot \nabla)\mathbf{u}_h^{n,\epsilon(i)}\\
&\qquad + \rho\theta\Delta t\beta(\mathbf{u}_h^{n,\epsilon(i)} \cdot \nabla)\mathbf{u}_h^{n,\epsilon(i-1)} - \mu\theta\Delta t\Delta\mathbf{u}_h^{n,\epsilon(i)} + \theta\Delta t\nabla p_h^{n,\epsilon(i)}\Big]\\
&= l_\theta^n(\mathbf{v}_h) + \rho(\mathbf{u}_h^{n-1}, \mathbf{v}_h)\\
&- (1-\theta)\Delta t c(\mathbf{u}_h^{n-1}, \mathbf{u}_h^{n-1}, \mathbf{v}_h) + \theta\Delta t\beta c(\mathbf{u}_h^{n,\epsilon(i-1)}, \mathbf{u}_h^{n,\epsilon(i-1)}, \mathbf{v}_h)\\
&- (1-\theta)\Delta t a(\mathbf{u}_h^{n-1}, \mathbf{v}_h) + (1-\theta)\Delta t b(p_h^{n-1}, \mathbf{v}_h)\\
&+ \sum_{e=1}^{N_{el}} \int_{\Omega^e} [\tau^e(\mathbf{u}^e \cdot \nabla)\mathbf{v}_h] \cdot [\rho\mathbf{u}_h^{n-1} - \rho(1-\theta)\Delta t(\mathbf{u}_h^{n-1} \cdot \nabla)\mathbf{u}_h^{n-1}\\
&\qquad + \rho\theta\Delta t\beta(\mathbf{u}_h^{n,\epsilon(i-1)} \cdot \nabla)\mathbf{u}_h^{n,\epsilon(i-1)} + \mu(1-\theta)\Delta t\Delta\mathbf{u}_h^{n-1} - (1-\theta)\Delta t\nabla p_h^{n-1}\\
&\qquad + \theta\Delta t\mathbf{f}^n + (1-\theta)\mathbf{f}^{n-1}]
\end{aligned} \tag{2.54}$$

- *Penalized incompressibility equation:*

$$\epsilon(p_h^{n,\epsilon(i)}, q_h) + b(q_h, \mathbf{u}_h^{n,\epsilon(i)}) = \epsilon(p_h^{n,\epsilon(i-1)}, q_h) \tag{2.55}$$

## 2.6 Matrix formulation

The different problems considered so far will be written now in matrix form. This will allow us to present the basic flow chart of the algorithm implemented in a computer code that collects the numerical techniques that have been discussed in this chapter.

Let us introduce the vector

$$\mathbf{s} := \tau^e\mathbf{u}^e \tag{2.56}$$

defined for each element $e$ with characteristic velocity $\mathbf{u}^e$ and intrinsic time $\tau^e$, computed as described earlier. If s is calculated using the velocity obtained for the $i$-th iteration of the $n$-th time step, we will indicate it by $\mathbf{s}^{n,i}$.

Once the finite element interpolation has been chosen, every element of the spaces of test functions and of trial solutions will be represented by a vector containing the nodal values of this element. This vector will be denoted by the boldface capital letter corresponding to the lower case function. For example, $\mathbf{V}$ will be the vector of nodal values of a generic velocity test function and $\mathbf{U}$ the vector of nodal values of the unknown velocity. Superscripts will be used to indicate the time step and the iteration counter.

The definitions of the matrices that will be needed are collected in Box 2.2. The $L^2$ inner product in the pressure space has been denoted by $(\cdot,\cdot)_Q$ and in the velocity space by $(\cdot,\cdot)_V$.

**Box 2.2 Matrix form of the discrete equations**

| Matrix version | Terms from where it comes |
|---|---|
| $\mathbf{V}^T\cdot\mathbf{M}_{v,s}\cdot\mathbf{U}$ | $\rho(\mathbf{u}_h,\mathbf{v}_h)_V+\sum_{e=1}^{N_{el}}\int_{\Omega^e}[(\mathbf{s}\cdot\nabla)\mathbf{v}_h]\cdot(\rho\mathbf{u}_h)d\Omega$ |
| $\mathbf{V}^T\cdot\mathbf{K}_{c,s}(\mathbf{U}_1)\cdot\mathbf{U}_2$ | $c(\mathbf{u}_{h,1},\mathbf{u}_{h,2},\mathbf{v}_h)+\sum_{e=1}^{N_{el}}\int_{\Omega^e}[(\mathbf{s}\cdot\nabla)\mathbf{v}_h]\cdot[\rho(\mathbf{u}_{h,1}\cdot\nabla)\mathbf{u}_{h,2}]\,d\Omega$ |
| $\mathbf{V}^T\cdot\mathbf{K}^*_{c,s}(\mathbf{U}_1)\cdot\mathbf{U}_2$ | $c(\mathbf{u}_{h,2},\mathbf{u}_{h,1},\mathbf{v}_h)+\sum_{e=1}^{N_{el}}\int_{\Omega^e}[(\mathbf{s}\cdot\nabla)\mathbf{v}_h]\cdot[\rho(\mathbf{u}_{h,2}\cdot\nabla)\mathbf{u}_{h,1}]\,d\Omega$ |
| $\mathbf{V}^T\cdot\mathbf{K}_{d,s}\cdot\mathbf{U}$ | $a(\mathbf{u}_h,\mathbf{v}_h)+\sum_{e=1}^{N_{el}}\int_{\Omega^e}[(\mathbf{s}\cdot\nabla)\mathbf{v}_h]\cdot(-\mu\Delta\mathbf{u}_h)d\Omega$ |
| $\mathbf{V}^T\cdot\mathbf{G}_s\cdot\mathbf{P}$ | $b(p_h,\mathbf{v}_h)-\sum_{e=1}^{N_{el}}\int_{\Omega^e}[(\mathbf{s}\cdot\nabla)\mathbf{v}_h]\cdot\nabla p d\Omega$ |
| $\mathbf{V}^T\cdot\mathbf{F}_{v,s}$ | $l(\mathbf{v}_h)+\sum_{e=1}^{N_{el}}\int_{\Omega^e}[(\mathbf{s}\cdot\nabla)\mathbf{v}_h]\cdot(\rho\mathbf{f})d\Omega$ |
| $\mathbf{Q}^T\cdot\mathbf{M}_p\cdot\mathbf{P}$ | $(p_h,q_h)_Q$ |

Having introduced all these matrices and vectors, some of the problems considered heretofore can be written as follows:

- *Problem (2.23), semidiscrete Galerkin:*

*Find $\mathbf{U}=\mathbf{U}(t)$ and $\mathbf{P}=\mathbf{P}(t)$ such that, for $t\in(0,T)$,*

$$\begin{aligned}\mathbf{M}_{v,0}\cdot\frac{d}{dt}\mathbf{U}+\mathbf{K}_{c,0}(\mathbf{U})\cdot\mathbf{U}+\mathbf{K}_{d,0}\cdot\mathbf{U}-\mathbf{G}_0\cdot\mathbf{P}&=\mathbf{F}_{v,0}\\ \mathbf{G}_0^T\cdot\mathbf{U}&=\mathbf{0}\\ \mathbf{M}_{v,0}\cdot\mathbf{U}(0)&=\mathbf{U}_0\end{aligned}\tag{2.57}$$

*where $\mathbf{U}_0$ comes from the right-hand-side in the initial condition of problem (2.23).*

Neither in (2.57) nor in what follows Dirichlet boundary conditions have been introduced. They will lead to a force term in the discrete continuity equation. Subscript naught in Eqns. (2.57) indicates that the matrices are calculated with $\mathbf{s}=\mathbf{0}$.

- *Problem (2.26), fully discrete Galerkin:*

*For $n = 1, 2, \dots, N$, given $\mathbf{U}^{n-1}$ and $\mathbf{P}^{n-1}$, find $\mathbf{U}^n$ and $\mathbf{P}^n$, approximations to $\mathbf{U}(t^n)$ and $\mathbf{P}(t^n)$, such that*

$$\begin{aligned}
\mathbf{M}_{v,0} \cdot \mathbf{U}^n + \theta\Delta t\mathbf{K}_{c,0}(\mathbf{U}^n) \cdot \mathbf{U}^n + \theta\Delta t\mathbf{K}_{d,0} \cdot \mathbf{U}^n - \theta\Delta t\mathbf{G}_0 \cdot \mathbf{P}^n &\\
= \theta\Delta t\mathbf{F}^n_{v,0} + (1-\theta)\Delta t\mathbf{F}^{n-1}_{v,0} + \mathbf{M}_{v,0} \cdot \mathbf{U}^{n-1} &\\
- (1-\theta)\Delta t\mathbf{K}_{c,0}(\mathbf{U}^{n-1}) \cdot \mathbf{U}^{n-1} - (1-\theta)\Delta t\mathbf{K}_{d,0} \cdot \mathbf{U}^{n-1} &\qquad (2.58)\\
+ (1-\theta)\Delta t\mathbf{G}_0 \cdot \mathbf{P}^{n-1} &\\
\mathbf{G}_0^T \cdot \mathbf{U}^n = \mathbf{0} &
\end{aligned}$$

- *Problem (2.40), fully discrete SD method:*

*For $n = 1, 2, \dots, N$, given $\mathbf{U}^{n-1}$ and $\mathbf{P}^{n-1}$, find $\mathbf{U}^n$ and $\mathbf{P}^n$, approximations to $\mathbf{U}(t^n)$ and $\mathbf{P}(t^n)$, such that*

$$\begin{aligned}
\mathbf{M}_{v,s^n} \cdot \mathbf{U}^n + \theta\Delta t\mathbf{K}_{c,s^n}(\mathbf{U}^n) \cdot \mathbf{U}^n + \theta\Delta t\mathbf{K}_{d,s^n} \cdot \mathbf{U}^n - \theta\Delta t\mathbf{G}_{s^n} \cdot \mathbf{P}^n &\\
= \theta\Delta t\mathbf{F}^n_{v,s^n} + (1-\theta)\Delta t\mathbf{F}^{n-1}_{v,s^n} + \mathbf{M}_{v,s^n} \cdot \mathbf{U}^{n-1} &\\
- (1-\theta)\Delta t\mathbf{K}_{c,s^n}(\mathbf{U}^{n-1}) \cdot \mathbf{U}^{n-1} - (1-\theta)\Delta t\mathbf{K}_{d,s^n} \cdot \mathbf{U}^{n-1} &\qquad (2.59)\\
+ (1-\theta)\Delta t\mathbf{G}_{s^n} \cdot \mathbf{P}^{n-1} &\\
\mathbf{G}_0^T \cdot \mathbf{U}^n = \mathbf{0} &
\end{aligned}$$

- *Problem (2.54)-(2.55), fully discrete and linearized SD method:*

*For $n = 1, 2, \dots, N$, given $\mathbf{U}^{n-1}$ and $\mathbf{P}^{n-1}$, find $\mathbf{U}^n$ and $\mathbf{P}^n$, approximations to $\mathbf{U}(t^n)$ and $\mathbf{P}(t^n)$, as the converged solutions of the following iterative algorithm:*

$$\begin{aligned}
\mathbf{M}_{v,s^{n,i-1}} \cdot \mathbf{U}^{n,\epsilon(i)} + \theta\Delta t\mathbf{K}_{c,s^{n,i-1}}(\mathbf{U}^{n,\epsilon(i-1)}) \cdot \mathbf{U}^{n,\epsilon(i)} &\\
+ \theta\Delta t\beta\mathbf{K}^*_{c,s^{n,i-1}}(\mathbf{U}^{n,\epsilon(i-1)}) \cdot \mathbf{U}^{n,\epsilon(i)} &\\
+ \theta\Delta t\mathbf{K}_{d,s^{n,i-1}} \cdot \mathbf{U}^{n,\epsilon(i)} - \theta\Delta t\mathbf{G}_{s^{n,i-1}} \cdot \mathbf{P}^{n,\epsilon(i)} &\\
= \theta\Delta t\mathbf{F}^n_{v,s^{n,i-1}} + (1-\theta)\Delta t\mathbf{F}^{n-1}_{v,s^{n,i-1}} + \mathbf{M}_{v,s^{n,i-1}} \cdot \mathbf{U}^{n-1} &\qquad (2.60)\\
- (1-\theta)\Delta t\mathbf{K}_{c,s^{n,i-1}}(\mathbf{U}^{n-1}) \cdot \mathbf{U}^{n-1} &\\
+ \theta\Delta t\beta\mathbf{K}^*_{c,s^{n,i-1}}(\mathbf{U}^{n,\epsilon(i-1)}) \cdot \mathbf{U}^{n,\epsilon(i-1)} &\\
- (1-\theta)\Delta t\mathbf{K}_{d,s^{n,i-1}} \cdot \mathbf{U}^{n-1} + (1-\theta)\Delta t\mathbf{G}_{s^{n,i-1}} \cdot \mathbf{P}^{n-1} &\\
\epsilon\mathbf{M}_p\mathbf{P}^{n,\epsilon(i)} + \mathbf{G}_0^T \cdot \mathbf{U}^{n,\epsilon(i)} = \epsilon\mathbf{M}_p\mathbf{P}^{n,\epsilon(i-1)} &
\end{aligned}$$

We are now in a position to present the basic flow chart of the algorithm to be implemented on the computer. This has been schematically represented in Box 2.3, where the following integers have been introduced: $n_{eu}$ is the number of time steps in which the Euler scheme ($\theta = 1$) is to be used and $i_{pi}$ is the number of iterations to be carried out using the Picard scheme ($\beta = 0$). For $\Delta t$ small enough, $i_{pi}$ may be set to zero, since the solution of the previous time step will be a good initial guess for the solution of the current step and the Newton-Raphson method ($\beta = 1$) will converge.

For steady flow calculations, the convergence tolerance within each time step may be larger than the tolerance to check if the steady-state has been reached, in order to perform only one iteration per time step.

In Box 2.3 we have taken into account the fact that the pressure is discontinuous between elements. This allows to eliminate the pressure in the momentum equation as explained in Chapter 1. Expressions (1.48)–(1.50) have been used for the problem now considered to form the element matrices of the final algebraic system.

**Box 2.3 Algorithm for the transient Navier–Stokes equations**

```
• Set the initial condition $\mathbf{U}^0$ and $\mathbf{P}^0 = \mathbf{0}$
• $n := 0$
• WHILE $n < N$ and (non-stationary) DO:
    • $n \leftarrow n + 1$
    • IF $n < n_{eu}$ then $\theta = 1$
      ELSE select $\theta$, $\theta \geq 1/2$
    • $i := 0$
    • Set $\mathbf{U}^{n,\epsilon(0)} = \mathbf{U}^{n-1}$ and $\mathbf{P}^{n,\epsilon(0)} = \mathbf{P}^{n-1}$
    • WHILE (not converged) DO:
        • $i \leftarrow i + 1$
        • IF $i < i_{pi}$ then $\beta = 0$
          ELSE $\beta = 1$
        • IF (classical penalization) then $\mathbf{P}^* = \mathbf{0}$
          ELSE if (artificial compressibility) then $\mathbf{P}^* = \mathbf{P}^{n-1}$
          ELSE if (iterative penalization) then $\mathbf{P}^* = \mathbf{P}^{n,\epsilon(i-1)}$
        • For each element, compute $\mathbf{s}^{n,i-1}$ and
          $\mathbf{A}^{(e)} := \mathbf{M}^{(e)}_{v,s^{n,i-1}} + \theta\Delta t\mathbf{K}^{(e)}_{c,s^{n,i-1}}(\mathbf{U}^{(e),n,\epsilon(i-1)})$
              $+ \theta\Delta t\beta\mathbf{K}^{(e),*}_{c,s^{n,i-1}}(\mathbf{U}^{(e),n,\epsilon(i-1)}) + \theta\Delta t\mathbf{K}^{(e)}_{d,s^{n,i-1}}$
              $+ \theta\Delta t\frac{1}{\epsilon}\mathbf{G}^{(e)}_{s^{n,i-1}}\mathbf{M}^{(e)^{-1}}_{p}\mathbf{G}^{(e)^{T}}_{0}$
          $\mathbf{B}^{(e)} := \theta\Delta t\mathbf{F}^{(e),n}_{v,s^{n,i-1}} + (1-\theta)\Delta t\mathbf{F}^{(e),n-1}_{v,s^{n,i-1}} + \mathbf{M}^{(e)}_{v,s^{n,i-1}}\mathbf{U}^{(e),n-1}$
              $- (1-\theta)\Delta t\mathbf{K}^{(e)}_{c,s^{n,i-1}}(\mathbf{U}^{(e),n-1})\mathbf{U}^{(e),n-1}$
              $+ \theta\Delta t\beta\mathbf{K}^{(e),*}_{c,s^{n,i-1}}(\mathbf{U}^{(e),n,\epsilon(i-1)})\mathbf{U}^{(e),n,\epsilon(i-1)}$
              $- (1-\theta)\Delta t\mathbf{K}^{(e)}_{d,s^{n,i-1}}\mathbf{U}^{(e),n-1}$
              $+ (1-\theta)\Delta t\mathbf{G}^{(e)}_{s^{n,i-1}}\mathbf{P}^{(e),n-1} + \theta\Delta t\mathbf{G}^{(e)}_{s^{n,i-1}}\mathbf{P}^{(e),*}$
        • Assemble $\mathbf{A}^{(e)}$ and $\mathbf{B}^{(e)}$ and solve $\mathbf{A}\mathbf{U}^{n,\epsilon(i)} = \mathbf{B}$
        • Compute $\mathbf{P}^{n,\epsilon(i)} = \mathbf{P}^* - \frac{1}{\epsilon}\mathbf{M}_p^{-1}\mathbf{G}_0^T\mathbf{U}^{n,\epsilon(i)}$
        • IF $\|\mathbf{U}^{n,\epsilon(i)} - \mathbf{U}^{n,\epsilon(i-1)}\|_{L^q} \leq TOL\|\mathbf{U}^{n,\epsilon(i)}\|_{L^q}$ then (converged)
      END while (not converged)
    • $\mathbf{U}^n \leftarrow \mathbf{U}^{n,\epsilon(i)}$
    • $\mathbf{P}^n \leftarrow \mathbf{P}^{n,\epsilon(i)}$
    • IF $\|\mathbf{U}^n - \mathbf{U}^{n-1}\|_{L^q} \leq TOL\ \Delta t\ \|\mathbf{U}^n\|_{L^q}$ then (stationary)
  END while $n < N$ and (non-stationary)
  END
```

## 2.7 Computing secondary variables

Once the velocity and pressure are calculated, one may be interested in other physical unknowns of the problem. Moreover, for visualizing the flow it is interesting to obtain a continuous pressure field and, for two dimensional flows, the streamfunction. Here we will describe some numerical procedures to obtain nodal values of the pressure, the vorticity and the physical properties of the fluid whenever they be variable. An algorithm to compute the streamfunction will also be described.

### 2.7.1 Least-squares smoothing

In the numerical procedure described in the preceeding sections, the pressure nodal values are located within each element. Also, when the physical properties of the fluid are variable (Chapters 3 and 4) they have to be stored at the integration points in order to perform the numerical quadrature. All these scalar fields will be discontinuous across interelement boundaries. For plotting purposes, it is interesting to obtain a continuous function that approximates a discontinuous one. Here, the least-squares technique employed in our calculations will be briefly described.

Let $\phi_c$ be a computed function, discontinuous across elements. A continuous function $\phi_s$ is then calculated by minimizing:

$$\|\phi_c - \phi_s\|^2_{L^2} = \int_\Omega (\phi_c - \phi_s)^2 \, d\Omega \tag{2.61}$$

The function $\phi_s$ is interpolated like the components of the velocity field. If $N_{tp}$ is the total number of nodal points of the mesh, $N^{(i)}$ denotes the shape function associated to node $i$ and $\phi_s^{(i)}$ is the nodal value of $\phi_s$ at this point, the minimization of the functional (2.61) leads to the system:

$$\mathbf{M}^c \mathbf{\Phi} = \mathbf{R} \tag{2.62}$$

where the components of the matrix $\mathbf{M}^c$ and the vectors $\mathbf{\Phi}$ and $\mathbf{R}$ are:

$$M^c_{ij} = \int_\Omega N^{(i)} N^{(j)} d\Omega, \quad i,j = 1, ..., N_{tp} \tag{2.63}$$

$$\Phi_j = \phi_s^{(j)}, \quad j = 1, ..., N_{tp} \tag{2.64}$$

$$R_i = \int_\Omega N^{(i)} \phi_c d\Omega, \quad i = 1, ..., N_{tp} \tag{2.65}$$

This smoothing technique is standard [Hu2], [ZT]. In order to avoid the solution of the system (2.62), it is usual to approximate the matrix $\mathbf{M}^c$ by a diagonal matrix $\mathbf{M}^l$. This matrix can be obtained either by the row-sum lumping technique or by using a nodal quadrature rule to evaluate the integrals in (2.63) and (2.65). In this case, the quadrature points are placed on the nodes of the element and the shape functions are assumed to be such that

$$N^{(i)}(\mathbf{x}_j) = \delta_{ij} \tag{2.66}$$

when evaluated at the $j$-th node of the finite element mesh, with coordinates $\mathbf{x}_j$. An estimate of how well $\phi_s$ approximates $\phi_c$ can be easily obtained using standard results from interpolation theory and numerical quadrature theory [SF].

### 2.7.2 Nodal quadrature rules

We present in Box 2.4 some nodal quadrature rules for the most common finite elements used in practice. Some of these rules are well known (rules 1–3, 6–11, 17 in Box 2.4). Our interest in obtaining the others is not their accuracy but the fact that they allow to approximate the matrix $\mathbf{M}^e$ in Eqn. (2.62) by a diagonal matrix, as explained above.

In Box 2.4, $R_n$ indicates the rule number and $N_{ne}$ the number of nodes of the element. This is followed by a schematic description of the element that has to be precised. For both 2D and 3D elements, the bubble function is associated with a node placed at the center of the element. It is understood that the original shape functions (without the addition of the new node) have to be modified in order to have zero value at the center. Otherwise, the nodal unknown at this point would not have the meaning of being the value of the interpolated function and the matrix $\mathbf{M}^e$ would not be diagonal, since condition (2.66) would not hold. For the element considered in rule number 15, bubble functions are also added in the center of the faces of the element. Elements corresponding to rules number 1, 2, 5 and 6 are triangular, tetrahedral for rules number 9, 10, 13, 14 and 15, quadrilateral for rules number 3, 4, 7 and 8 and hexahedral for rules number 11, 12, 16 and 17.

The quadrature rule is defined by the weights of the nodes. All the nodes placed at the corners of the element have the same weight, as well as the nodes placed in the middle of the edges and in the center of the faces (in 3D elements). The values given have been normalized in such a way that their sum is 1. In the final entry of Box 2.4, the accuracy of the quadrature rule is given by the polynomial that can be exactly integrated. The set of polynomials of degree $n$ is denoted by $P_n$, whereas $Q_n$ denotes the set of tensor-product polynomials of degree $n$ in each Cartesian direction $x, y, z$.

All the rules except rule number 5 are the best that can be obtained with the given number of quadrature points. In fact, for the 2D quadratic (simplicial) element, a second order quadrature rule is obtained if the weights are taken as 0 for the corner nodes and $\frac{1}{3}$ for the mid-side nodes. However, this rule yields a matrix $\mathbf{M}^l$, approximation of $\mathbf{M}^e$, with some zero diagonal values (those corresponding to the corner nodes). The weights given for rule number 5 have been obtained splitting the triangle into four subtriangles and applying rule number 1. It is interesting to remark that if the Richardson extrapolation is applied to rules number 1 and 5, the mentioned second order rule is recovered.

In general, these quadrature rules cannot be used for the numerical integration of the matrices of the discrete Navier-Stokes equations, since their accuracy is not enough to preserve the order of convergence of the finite element discretization. Open quadrature rules have to be employed in these cases, i.e., with the nodes placed in the interior of the elements. The product Gauss-Legendre rule is the common option for quadrilateral and hexahedral elements. Open quadrature rules for triangles can be found in Reference [LG] and for tetrahedra in Reference [GeH].

### 2.7.3 Pressure, vorticity and physical properties smoothing

The least-squares technique combined with the nodal quadrature rules to compute the integrals will be applied now to approximate several discontinuous fields by continuous functions. The number of integration points used for the calculation of the element matrices of the Navier-Stokes equations will be denoted by $N_{gp}$. A point in the parent domain $\Omega_0$ will be indicated by $\boldsymbol{\xi}$.

**Box 2.4 Nodal quadrature rules for linear and quadratic elements**

*Two-dimensional elements*

| $R_n$ | $N_{no}$ | Description | Weights | | | Polynomial |
|---|---|---|---|---|---|---|
| | | | Corners | Edges | Center | |
| 1 | 3 | Linear | 1/3 | | | $P_1$ |
| 2 | 4 | Linear + bubble | 1/12 | | 3/4 | $P_2$ |
| 3 | 4 | Bilinear | 1/4 | | | $Q_1$ |
| 4 | 5 | Bilinear + bubble | 1/12 | | 2/3 | $P_2$ |
| 5 | 6 | Quadratic | 1/12 | 1/4 | | $P_1$ |
| 6 | 7 | Quad. + bubble | 1/20 | 2/15 | 9/20 | $P_3$ |
| 7 | 8 | Serendipid | −1/12 | 1/3 | | $P_2$ |
| 8 | 9 | Biquadratic | 1/36 | 1/9 | 4/9 | $Q_3$ |

*Three-dimensional elements*

| $R_n$ | $N_{no}$ | Description | Weights | | | | Polynomial |
|---|---|---|---|---|---|---|---|
| | | | Corners | Edges | Faces | Center | |
| 9 | 4 | Linear | 1/4 | | | | $P_1$ |
| 10 | 5 | Linear + bubble | 1/20 | | | 4/5 | $P_2$ |
| 11 | 8 | Trilinear | 1/8 | | | | $Q_1$ |
| 12 | 9 | Trilinear + bubble | 1/24 | | | 2/3 | $P_2$ |
| 13 | 10 | Quadratic | −1/120 | 1/5 | | | $P_2$ |
| 14 | 11 | Quad. + bubble | 1/160 | 1/15 | | 8/15 | $P_3$ |
| 15 | 15 | Quad. + bubble<br>+ face bubbles | 17/840 | 4/105 | 27/280 | 32/105 | $P_3$ and terms<br>$x^2yz, xy^2z, xyz^2$ |
| 16 | 20 | Serendipid | −1/8 | 1/6 | | | $P_2$ |
| 17 | 27 | Triquadratic | 1/216 | 1/54 | 2/27 | 8/27 | $Q_3$ |

Since all the matrices and vectors are obtained from the assembly of their element contributions, we will only concentrate on these elemental expressions.

The Gramm matrix appearing in Eqn. (2.62) can be approximated in all the cases by the diagonal matrix resulting from the nodal quadrature rule. The right-hand-side term in this equation, $\mathbf{R}$, can be computed either using this nodal rule or the same numerical integration employed for the Navier-Stokes equations. For the smoothing of the pressure and the vorticity, both options are equally easy to implement. However, when the physical properties of the fluid are considered, we will see that the second procedure is much easier than the former.

Let $J(\boldsymbol{\xi})$ be the Jacobian determinant of the isoparametric mapping and $w_k$, $k = 1, ..., N_{no}$, the weights given in Box 2.4 multiplied by $\text{meas}(\Omega_0)$. The components of the element contributions to the matrix $\mathbf{M}^c$ and the approximated matrix $\mathbf{M}^l$ are:

$$\begin{aligned} M_{ij}^{(e),c} &= \int_{\Omega^e} N^{(e,i)} N^{(e,j)} d\Omega = \int_{\Omega_0} N^{(e,i)}(\boldsymbol{\xi}) N^{(e,j)}(\boldsymbol{\xi}) |J^{(e)}(\boldsymbol{\xi})| d\Omega_0 \\ &\approx M_{ij}^{(e),l} = \sum_{k=1}^{N_{no}} w_k |J^{(e)}(\boldsymbol{\xi}_k)| N^{(e,i)}(\boldsymbol{\xi}_k) N^{(e,j)}(\boldsymbol{\xi}_k) \\ &= \sum_{k=1}^{N_{no}} w_k |J^{(e)}(\boldsymbol{\xi}_k)| \delta_{ik} \delta_{jk} \\ &= \left[ w_i |J^{(e)}(\boldsymbol{\xi}_i)| \right] \delta_{ij} \qquad \text{(no sum)} \end{aligned} \tag{2.67}$$

Let $N_p^{(e,j)}$ be the pressure shape function associated to the $j$-th node of element $e$ and $p^{(e,j)}$ the corresponding pressure nodal value. The components of the force term $\mathbf{R}$ for the pressure smoothing approximated by the nodal quadrature rule will be

$$\begin{aligned} R_{p,i}^{(e)} &= \int_{\Omega^e} N^{(e,i)}\, p\, d\Omega = \int_{\Omega^e} N^{(e,i)} \left( \sum_{j=1}^{N_{qp}} N_p^{(e,j)} p^{(e,j)} \right) d\Omega \\ &= \int_{\Omega_0} N^{(e,i)}(\boldsymbol{\xi}) \left( \sum_{j=1}^{N_{qp}} N_p^{(e,j)}(\boldsymbol{\xi}) p^{(e,j)} \right) |J^{(e)}(\boldsymbol{\xi})| d\Omega_0 \\ &\approx \sum_{k=1}^{N_{no}} w_k |J^{(e)}(\boldsymbol{\xi}_k)| \delta_{ik} \left( \sum_{j=1}^{N_{qp}} N_p^{(e,j)}(\boldsymbol{\xi}_k) p^{(e,j)} \right) \\ &= w_i |J^{(e)}(\boldsymbol{\xi}_i)| \left( \sum_{j=1}^{N_{qp}} N_p^{(e,j)}(\boldsymbol{\xi}_i) p^{(e,j)} \right) \end{aligned} \tag{2.68}$$

It is observed from (2.68) that all the shape functions (those associated to the continuous approximation and the discontinuous pressure interpolation) and their derivatives have to be evaluated at the nodes of the elements.

The smoothing of the vorticity $\boldsymbol{\omega}_h := \nabla \times \mathbf{u}_h$ can be performed in a similar way. For two dimensional flows, this vector has only one non-zero component, $\omega_3 = \partial_1 u_2 - \partial_2 u_1$, the subscripts referring to the Cartesian coordinates now denoted $x_i$, $i = 1, 2, 3$. For simplicity, assume that $N_{sd} = 2$. The components for the right-hand-side term $\mathbf{R}$ are now

$$\begin{aligned} R_{\omega,i}^{(e)} &= \int_{\Omega^e} N^{(e,i)}\, \omega_3\, d\Omega = \int_{\Omega^e} N^{(e,i)} (\partial_1 u_2 - \partial_2 u_1) d\Omega \\ &= \int_{\Omega^e} N^{(e,i)} \sum_{j=1}^{N_{no}} \left( \partial_1 N^{(e,j)} U_2^{(e,j)} - \partial_2 N^{(e,j)} U_1^{(e,j)} \right) d\Omega \\ &= \int_{\Omega_0} N^{(e,i)}(\boldsymbol{\xi}) \sum_{j=1}^{N_{no}} \left( \partial_1 N^{(e,j)}(\boldsymbol{\xi}) U_2^{(e,j)} - \partial_2 N^{(e,j)}(\boldsymbol{\xi}) U_1^{(e,j)} \right) |J^{(e)}(\boldsymbol{\xi})| d\Omega \\ &\approx w_i |J^{(e)}(\boldsymbol{\xi}_i)| \sum_{j=1}^{N_{no}} \left( \partial_1 N^{(e,j)}(\boldsymbol{\xi}_i) U_2^{(e,j)} - \partial_2 N^{(e,j)}(\boldsymbol{\xi}_i) U_1^{(e,j)} \right) \end{aligned} \tag{2.69}$$

Consider now a variable physical property $\varphi(\mathbf{x})$. Examples of this situation will be found in the next two chapters. In order to compute the matrices for the Navier-Stokes equations (or for the temperature equation, as it will be seen in the following chapter) the values of $\varphi$ have to be stored for each element and for each quadrature point within the element. Let us denote them by $\varphi_j^{(e)}$, $j = 1, ..., N_{gp}$. If $\varphi$ is interpolated within the element and this interpolation is used to compute the values at the nodes, the resulting function will be discontinuous and the smoothing is again needed. Observe that the interpolation functions are not the standard shape functions of the element. Therefore, it is easier to compute the integrals in Eqn. (2.65) in this case *using the same numerical integration as for the Navier-Stokes equations*. Otherwise, a new set of interpolation functions should be defined. The right-hand-side term of the smoothing equations will be

$$\begin{aligned} R_{\varphi,i}^{(e)} &= \int_{\Omega^e} N^{(e,i)}\, \varphi^{(e)}\, d\Omega = \int_{\Omega_0} N^{(e,i)}(\boldsymbol{\xi})\varphi^{(e)}(\boldsymbol{\xi})|J^{(e)}(\boldsymbol{\xi})|d\Omega \\ &\approx \sum_{k=1}^{N_{gp}} w_k^* |J^{(e)}(\boldsymbol{\xi}_k)| N^{(e,i)}(\boldsymbol{\xi}_k)\varphi_k^{(e)} \end{aligned} \tag{2.70}$$

where $w_k^*$ are the weights for the quadrature rule of $N_{gp}$ points, with coordinates in the parent domain $\boldsymbol{\xi}_k$.

### 2.7.4 An algorithm for the calculation of the streamfunction

For incompressible bidimensional flows, the streamfunction provides a simple way for plotting streamlines (its contours) and also gives a measure of the quantity of fluid that crosses a segment of a curve per unit of time, i.e., the flux of the velocity field multiplied by the density. Here we will present an algorithm for the calculation of the nodal values of this function (see Reference [Ja] for a different method).

For exactly divergence free velocities ($\nabla \cdot \mathbf{u}_h = 0$) there exists a streamfunction $\psi_h$ such that $\mathbf{u}_h = \nabla \times \psi_h := (\partial_2\psi_h, -\partial_1\psi_h)$. Consider a segment of curve defined by the initial point $A$ and the end point $B$. Let $\mathbf{t}$ be the tangent to this curve and $\mathbf{n}$ normal to it, $\{\mathbf{n}, \mathbf{t}\}$ having the same orientation as the canonical basis. We will have that

$$\mathbf{n} = (n_1, n_2) = (t_2, -t_1)$$

and hence

$$\begin{aligned} \int_A^B \mathbf{u}_h \cdot \mathbf{n} ds &= \int_A^B (\partial_2\psi_h, -\partial_1\psi_h) \cdot (t_2, -t_1) ds \\ &= \int_A^B \nabla\psi_h \cdot \mathbf{t} ds = \psi_h(B) - \psi_h(A) \end{aligned}$$

that is,

$$\psi_h(B) = \psi_h(A) + \int_A^B \mathbf{u}_h \cdot \mathbf{n} ds \tag{2.71}$$

If $AB$ is a straight segment of length $|AB|$ and we define

$$\begin{aligned} \vec{AB} &:= (B_1 - A_1, B_2 - A_2) \\ \vec{AB}^{\perp} &:= (B_2 - A_2, A_1 - B_1) \end{aligned}$$

we will have that $\mathbf{n} = \vec{AB}^{\perp}/|AB|$. Assuming that the variation of $\mathbf{u}_h \cdot \mathbf{n}$ along $AB$ is linear, Eqn. (2.71) reduces to

$$\begin{aligned}\psi_h(B) &= \psi_h(A) + \frac{1}{2}\left[(\mathbf{u}_h \cdot \mathbf{n})(A) + (\mathbf{u}_h \cdot \mathbf{n})(B)\right]|AB| \\ &= \psi_h(A) + \frac{1}{2}\left[\mathbf{u}_h(A) + \mathbf{u}_h(B)\right] \cdot \vec{AB}^{\perp}\end{aligned} \tag{2.72}$$

Equation (2.72) provides a method to calculate the streamfunction values at the nodes of the finite element mesh. Recall that the two approximations inherent to (2.72) are that $AB$ has been considered a straight segment and the variation of $\mathbf{u}_h \cdot \mathbf{n}$ linear along it.

The velocity $\mathbf{u}_h$ that will be obtained from the finite element solution of the Navier-Stokes equations is not pointwise divergence free. All we can expect is that $\int_{\Omega^e} \nabla \cdot \mathbf{u}_h d\Omega = 0$ for all the elements. In fact, this equation will not hold exactly, since the continuity condition has been penalized. Nevertheless, our method will be based on this equality.

The idea is the following. Once $\psi_h$ is known for a certain node of an element, the value of this function can be computed for the next node using (2.72). In this way, we can go through all the nodes of the element placed on its boundary. What is not possible is to compute $\psi_h$ for the interior nodes of the elements, whenever they exist. What we do in these cases is to interpolate $\psi_h$ for this node using the values calculated for the others and the shape functions corresponding to the interpolation without the interior node. For example, for the seven-noded quadratic triangle enriched with a bubble function, $\psi_h$ for the central node is computed from the quadratic interpolation based on the six-noded triangle.

Once we come back following this process to the first node of the element where the streamfunction was known, the new value may be slightly different from the original one. What we do is to compute $\psi_h$ several times for each node (as many as the algorithm presented thereafter yields) and take the final result as the average of the calculated values.

The final algorithm is presented in Box 2.5, where the following variables and arrays have been introduced:

$\psi(i)$ : Value of $\psi_h$ for node $i$.
$NT(i)$ : Number of times that $\psi_h$ has been calculated for the node $i$.
$N_{cp}$ : Number of points where $\psi_h$ is known.
$N_{cp}^{(e)}$ : Number of points of element $e$ where $\psi_h$ is known.
$I_{cp}^{(e)}$ : First node of element $e$ where $\psi_h$ is known.
$\bar{w}_j$ : Weights coming from the interpolation of $\psi_h$ for the interior nodes.

Since the streamfunction is determined up to a constant, its value for the first node of the mesh has been set equal to zero. Thus, the algorithm starts with one known value of $\psi_h$.

The fact that node number $N_{no}$ of the element be interior or not has been indicated by the statement *($N_{no}$ interior)*. No distinction has been made between the global and the local numbering of a node. In Box 2.5, $i_{no}$ stands for the node where $\psi_h$ is to be calculated and $i_{pr}$ for the 'previous' node, where the streamfunction is already known. Finally, recall that $N_{tp}$ is the total number of nodes of the finite element mesh.

This algorithm has proved to work very well for the problems we have considered, even though the velocity is not exactly weakly solenoidal.

**Box 2.5 Algorithm for the calculation of the streamfunction**

```
• Set $e = 0$, $NT(1) = 1$, $\psi(1) = 0$, $N_{cp} = 1$
• WHILE $N_{cp} < N_{tp}$ DO:
    • $e \leftarrow \mathrm{mod}(e+1, N_{el})$
    • IF $e = 0$ then $e \leftarrow N_{el}$
    • Compute $N_{cp}^{(e)}$
    • IF $0 < N_{cp}^{(e)} < N_{no}$ then
        • Determine $I_{cp}^{(e)}$
        • FOR $i = 1, N_{no}$ DO:
            • $i_{no} = I_{cp}^{(e)} + i$
            • IF $i_{no} = N_{no}$ and $(N_{no}$ interior) then $i_{no} \leftarrow i_{no} + 1$
            • IF $i_{no} > N_{no}$ then $i_{no} \leftarrow \mathrm{mod}(i_{no}, N_{no})$
            • IF $i_{no} > 1$ then $i_{pr} = i_{no} - 1$
              ELSE if $(N_{no}$ interior) then $i_{pr} = N_{no} - 1$
              ELSE $i_{pr} = N_{no}$
            • Compute
              $\psi(i_{no}) \leftarrow \psi(i_{no}) + \psi(i_{pr})$
                      $+ 0.5\,[u_1(i_{no}) + u_1(i_{pr})]\,[Y(i_{no}) - Y(i_{pr})]$
                      $+ 0.5\,[u_2(i_{no}) + u_2(i_{pr})]\,[X(i_{pr}) - X(i_{no})]$
            • IF $NT(i_{no}) = 0$ then $N_{cp} \leftarrow N_{cp} + 1$
            • $NT(i_{no}) \leftarrow NT(i_{no}) + 1$
          END
        • IF $(N_{no}$ interior) then
            • $\psi(N_{no}) = \sum_{j=1}^{N_{no}-1} \bar{w}_j \psi(j)$
            • $N_{cp} \leftarrow N_{cp} + 1$
            • $NT(i_{no}) \leftarrow NT(i_{no}) + 1$
          END
      END
  END
• FOR $i = 1, N_{tp}$ DO:
    • $\psi(i) \leftarrow \psi(i)/NT(i)$
  END
  END
```

## 2.8 Numerical examples

In this section, some classical benchmark problems for incompressible viscous flows will be solved. The first is the driven cavity flow, for which detailed numerical results can be found, e.g., in References [GGS], [GC2], [GuH], [Ki], [KM], [Sh], [SK], [So], among many others. The second problem is the flow over a backward facing step. Numerical experiments for this problem are reported in References [ADS], [Ga], [GC2], [HRS], [Ki], [KM], [So]. Both for this problem and for the first one the stationary solution is sought. The next example is the flow past a cylinder, for wich the steady-state solution is not stable and a periodic flow pattern develops behind the cylinder if a uniform initial condition is slightly perturbed. Numerical experiments for this problem can be found in References [EJ], [GC2], [TGL], [TLi], [TMS].

All the above quoted references have been selected because of the details they give about how the numerical simulation has been carried out, but many other works dealing with numerical models for the Navier-Stokes equations present similar experiments.

Our calculations have been performed on a CONVEX-C120 computer using double arithmetic precision.

**Example 2.1** *Flow inside a wall-driven cavity*

The Stokes solution for this problem has been considered in detail in the previous chapter. The essential feature of this benchmark test case when the Navier-Stokes equations are solved is the prediction of various vortices inside the cavity. The notation we will use for them is shown in Figure 2.4.

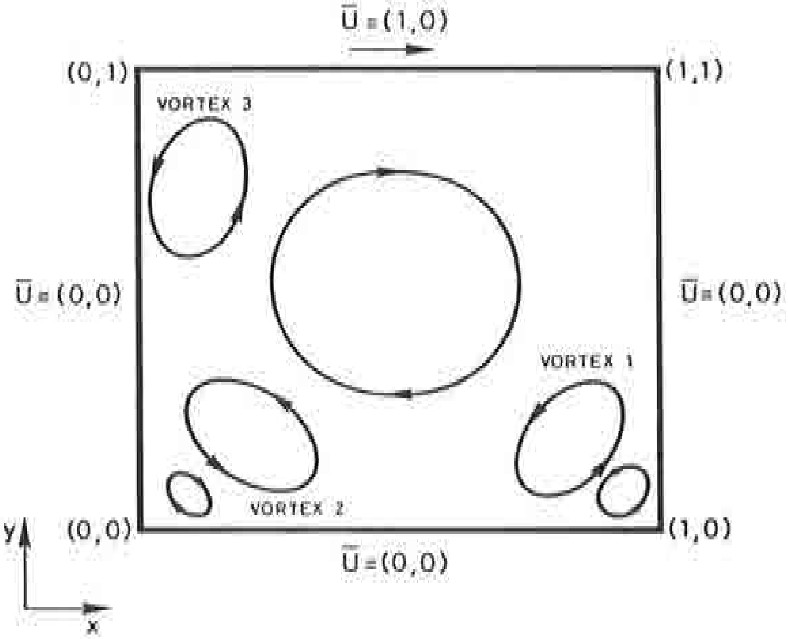

Figure 2.4 Geometry, boundary conditions and nomenclature of cavity flow

Numerical results will be presented for values of the Reynolds number $Re = 1000$, 4000 and 8000, computed using the length of the cavity and the velocity prescribed on the top edge. In References [GGS], [GC2], [Ki] and [So] results are presented for other values of $Re$, so our results are complementary to theirs. In particular, the case $Re = 10000$ is solved in these references. This value can be considered as a limit for steady calculations, since Shen has shown through detailed numerical experiments that above this bound the stationary solution ceases to be stable and a Hopf bifurcation occurs [Sh].

The computational domain has been discretized using a mesh composed of 676 $Q_2/P_1$ elements and 2809 nodal points for all the Reynolds numbers. This mesh has been designed to capture the details of the flow in the corners and boundary layers (see Figure 2.5). The smallest element size is $h_{min} = 0.01$ (twice the distance between nodes).

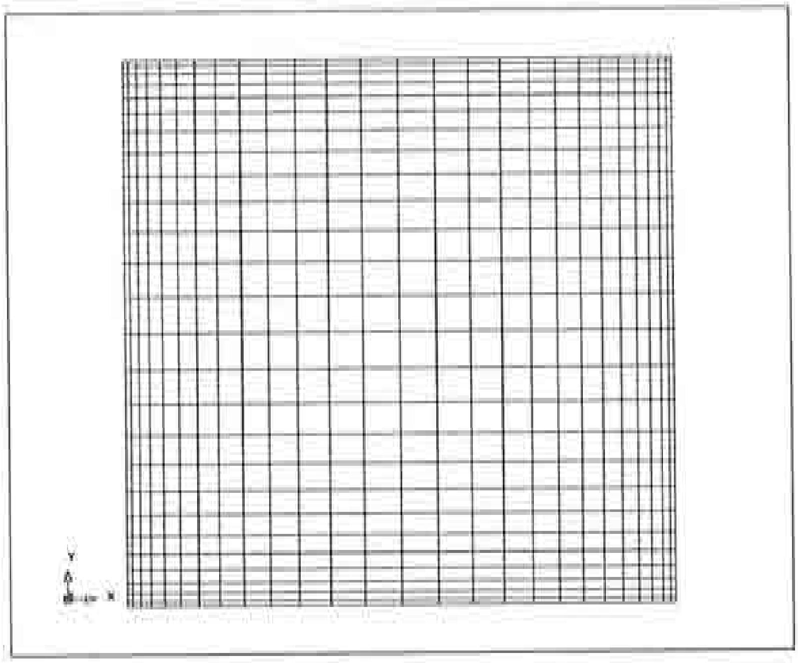

Figure 2.5 Finite element mesh for the cavity flow problem (676 $Q_2/P_1$ elements, 2809 nodal points).

This mesh is similar to the one used by Gresho *et al.* [GC2], which consists of $50 \times 50$ $Q_1/P_0$ elements and $51 \times 51 = 2601$ nodal points. They also used an upwind technique [GC1]. For $Re > 4000$, the Galerkin method yields oscillatory results and it is only possible to use this method on much finer meshes, as those used by Kim [Ki] (1024 $Q_2/P_1$ elements, 4225 nodal points), Sohn [So] (1600 $Q_2/P_1$ elements, 6561 nodal points, $h_{min} = 0.00326$) or Ghia *et al.* [GGS] (uniform mesh of $257 \times 257 = 66049$ nodal points, with $h = 0.0039$). In this last reference, a finite-difference multigrid method based on the streamfunction-vorticity formulation is used.

In all our computations we have taken $\epsilon = 10^{-3}$ (penalty parameter). The iterative penalty method has been employed. Concerning the parameters of the SD method, $h_0 = 2$ has been chosen (element length for the parent domain) and $\alpha_0 = 0.5$ (upwind factor).

For $Re = 1000$, the Galerkin solution yields very good answers, without any oscillations. Results are shown in Figures 2.6 to 2.9.

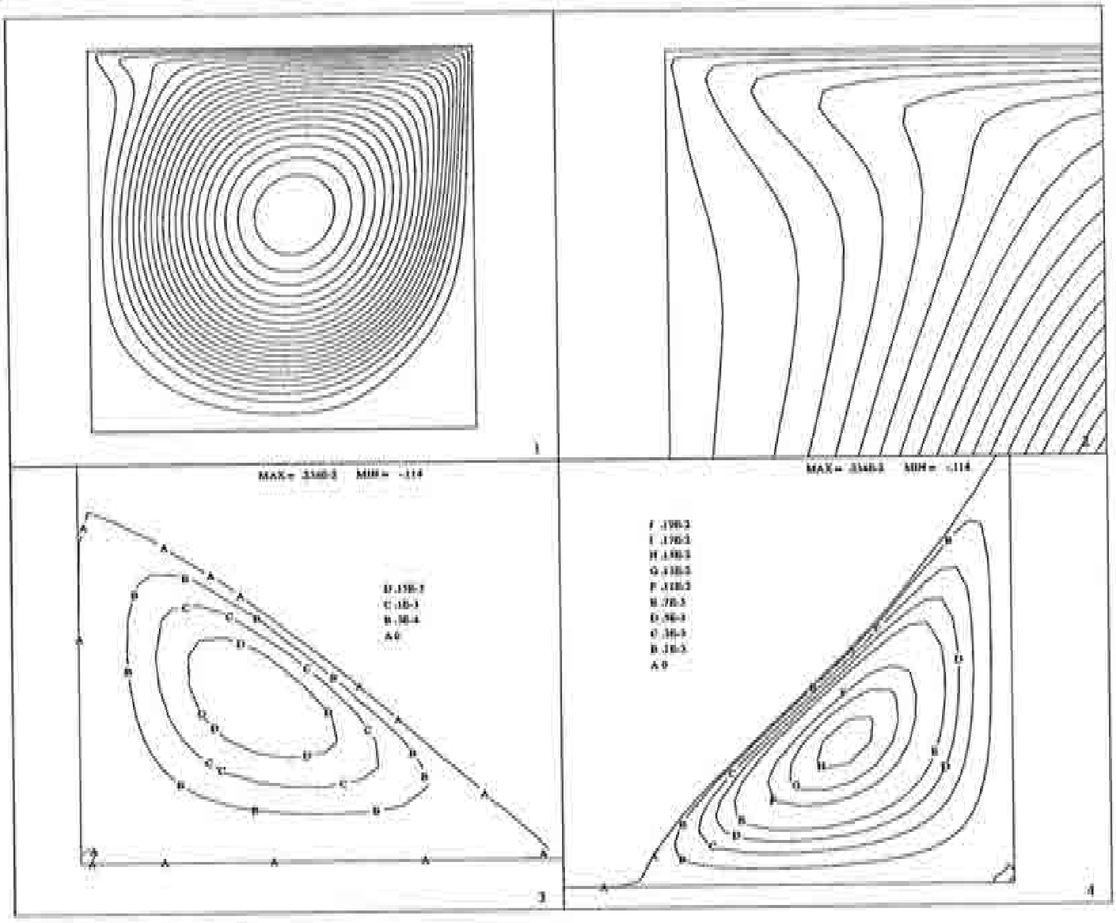

Figure 2.6 Numerical solution of the cavity flow problem at $Re = 1000$ (Galerkin method), streamlines. (1): General pattern; (2): Detail of the top left corner; (3): Detail of bottom left corner; (4): Detail of bottom right corner.

Since the computation has started with zero velocities everywhere, the first effective initial guess is the Stokes solution. If the Newton-Raphson method is then used, the algorithm does not converge. The strategy we have followed is to use the Picard method ($\beta = 0$) for the first three iterations and then move to the Newton-Raphson scheme ($\beta = 1$). For a convergence tolerance in the relative $L^2$ norm of 0.1 %, i.e., $TOL = 10^{-3}$ in (2.52), eight iterations have been required. The final value of the norm of the discrete divergence of the velocity has been approximately $10^{-11}$, starting from an inital value of order $10^{-4}$.

The streamlines are shown in Figure 2.6. For this value of the Reynolds number, vortex 3 in Figure 2.4 does not appear. The extreme values of the streamfunction in vortices 1 and 2 will be compared with the results presented in References [GGS], [GC2], [So] and [Ki]. Recall that our results have been obtained using the Galerkin formulation. Results of Reference [So] have been obtained using the FIDAP code, which allows to use a version of the streamline upwind (STU) technique employed also in [GC2] and described in [GC1], but now applied to quadratic elements (in particular, to the $Q_2/P_1$ pair). This consists basically in adding an anisotropic viscosity following

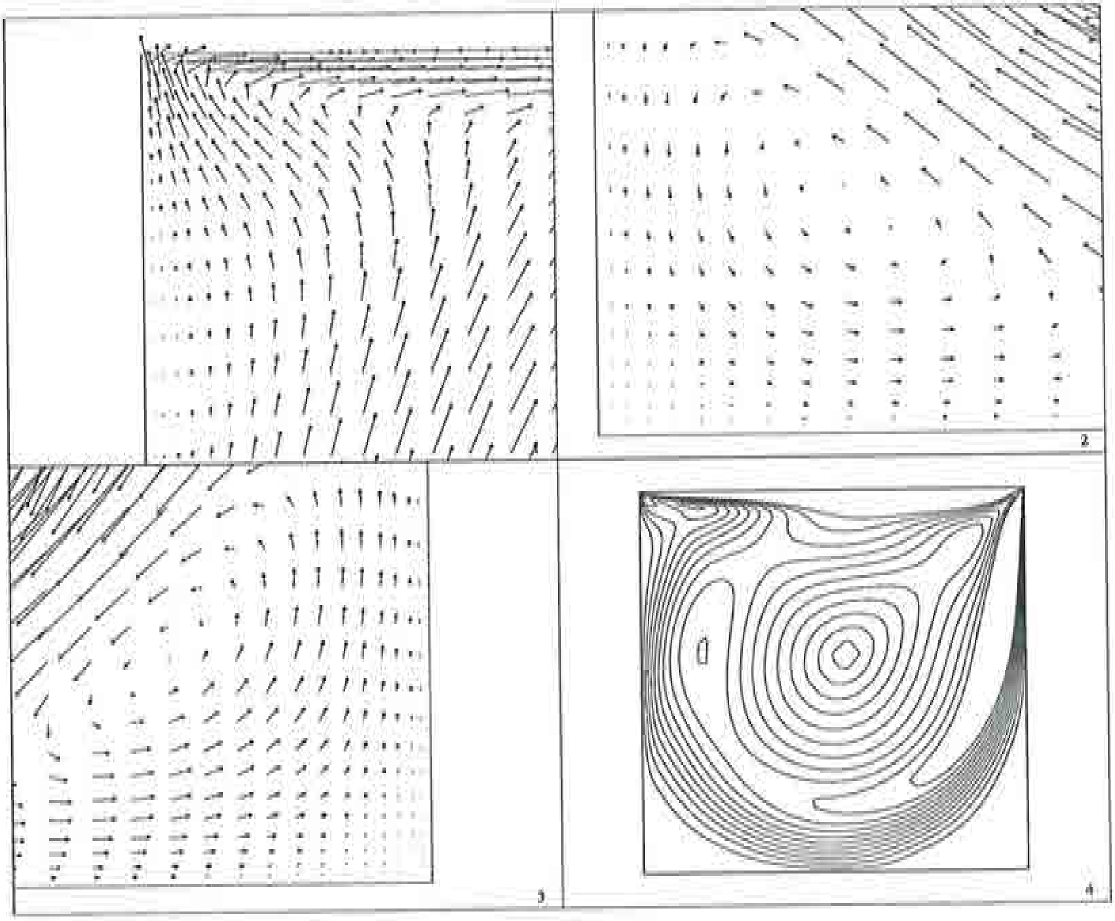

Figure 2.7 Numerical solution of the cavity flow problem at $Re = 1000$, velocities. (1): Detail of the top left corner; (2): Detail of bottom left corner; (3): Detail of bottom right corner; (4): Contours of the velocity norm.

the streamlines, something very similar to what the Taylor-Galerkin method yields. Therefore, the final scheme is not a consistent weighted residual method, in the sense that the exact solution does not satisfy exactly the discrete variational equations.

The extreme values of the streamfunction to be compared are the following:

| Reference | Vortex 1 | Vortex 2 |
|---|---|---|
| [GGS] | $1.75 \times 10^{-3}$ | $2.31 \times 10^{-4}$ |
| [GC2] | $1.76 \times 10^{-3}$ | $2.00 \times 10^{-4}$ |
| [Ki] | $1.66 \times 10^{-3}$ | $2.20 \times 10^{-4}$ |
| [So], without STU | $1.63 \times 10^{-3}$ | $2.17 \times 10^{-4}$ |
| [So], with STU | $1.10 \times 10^{-3}$ | $9.40 \times 10^{-5}$ |
| Present study | $1.61 \times 10^{-3}$ | $1.99 \times 10^{-4}$ |

It is observed that the STU technique used by Sohn yields overdiffusive results

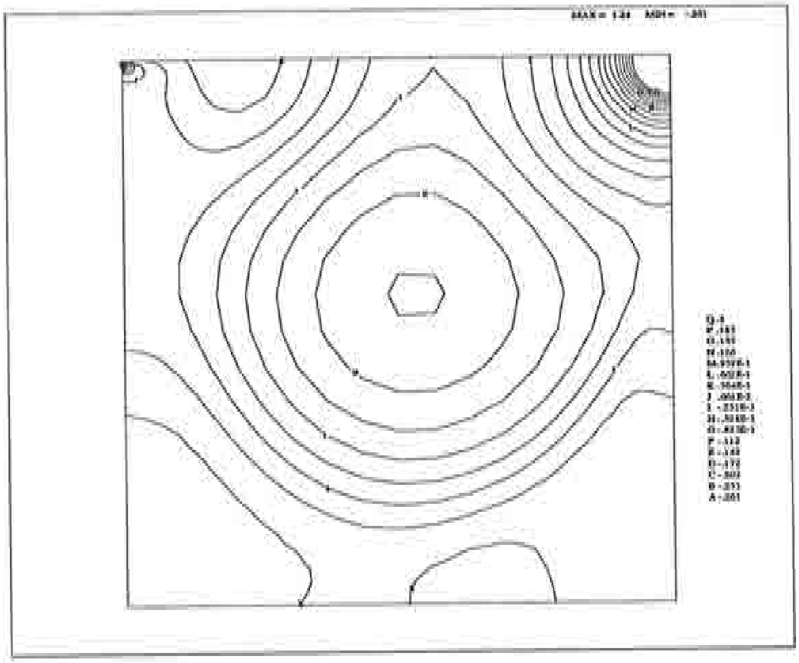

Figure 2.8 Numerical solution of the cavity flow problem at $Re = 1000$. Pressure contours.

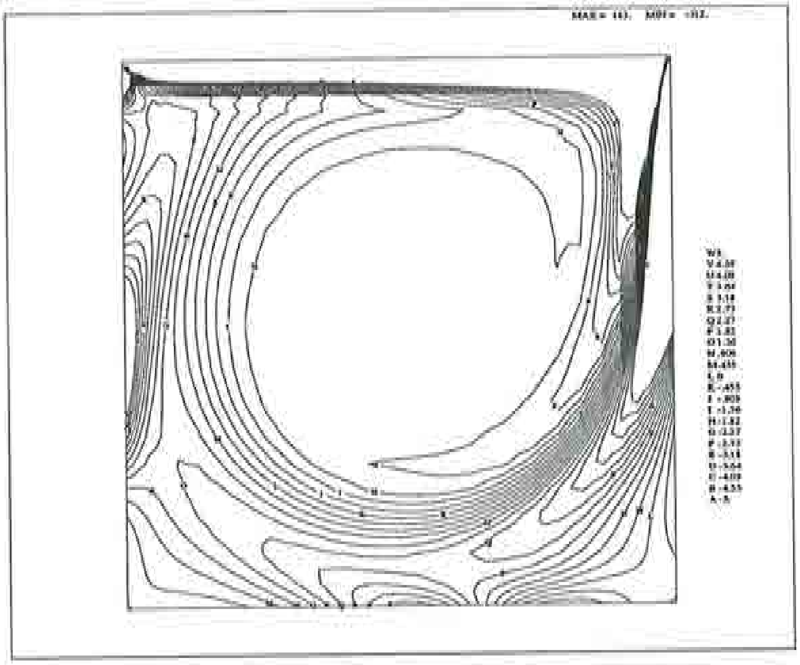

Figure 2.9 Numerical solution of the cavity flow problem at $Re = 1000$. Vorticity contours.

and that the extreme values of $\psi_h$ are higher using linear elements ($Q_1/P_0$ in [GC2], a difference scheme in [GGS]) than the $Q_2/P_1$ pair (results of Kim, Sohn and ours). It is also observed that the extreme values found in the present work are slightly smaller than those in [Ki] and [So]. It is very important to keep this fact in mind because the same behavior will be observed for higher Reynolds numbers using the SD method described in this chapter. Since, apart from the iterative penalty method, our formulation is very close to that employed in [Ki] and [So], we believe that these differences are due to the fact that the mesh employed here is much coarser than theirs. Moreover, Kim has also compared the results for a coarser mesh (25 × 25 nodal points) concluding that this yields smaller absolute values for the peaks of the streamfunction.

Details of the velocity vectors in the corners of the cavity are shown in Figures 2.7.(1)–(3). The contours of the Euclidian norm of these vectors have been plotted in Figure 2.7.(4). Observe that no oscillations appear. Figures 2.8 and 2.9 show the pressure and vorticity contours, respectively. In general trends, these results are very similar to those presented in the above quoted references.

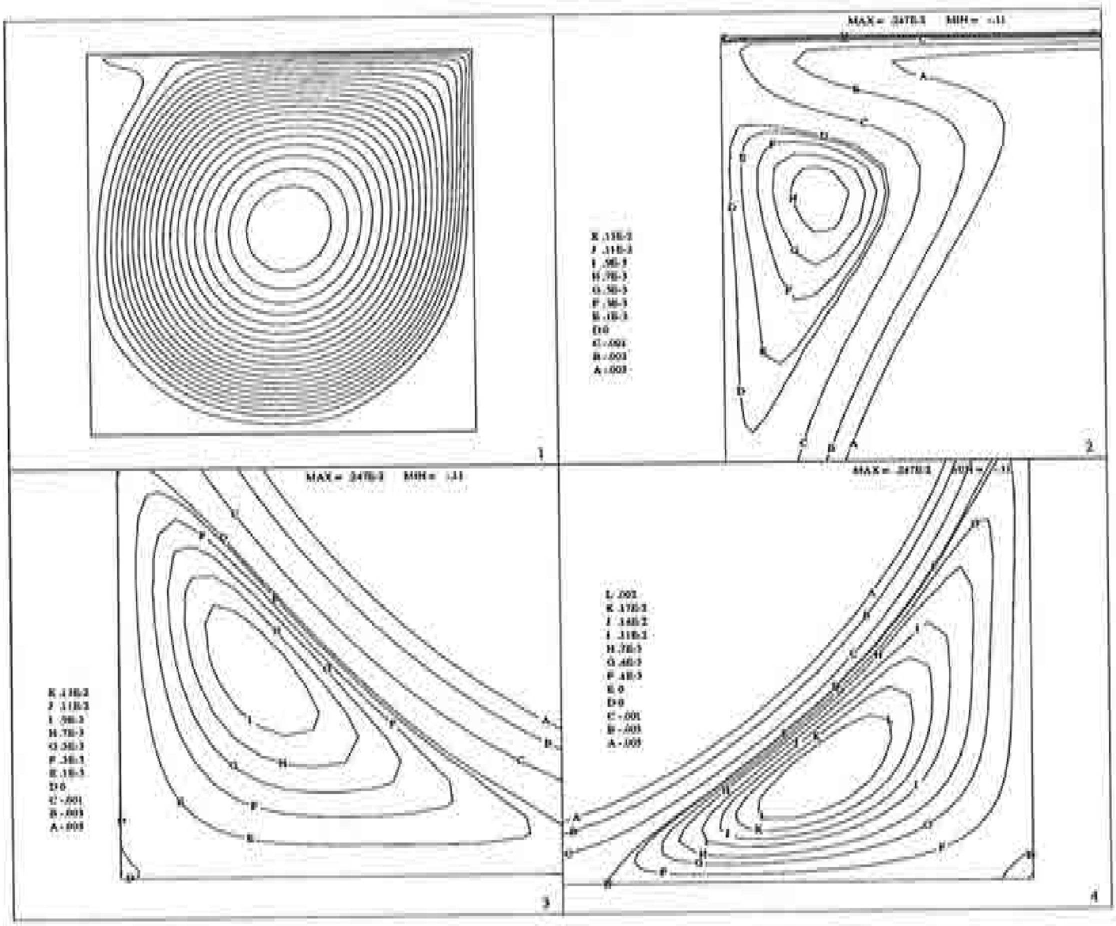

Figure 2.10 Numerical solution of the cavity flow problem at $Re = 4000$ (Galerkin method), streamlines. (1): General pattern; (2): Detail of the top left corner; (3): Detail of bottom left corner; (4): Detail of bottom right corner.

Consider now the case $Re = 4000$. The iterative strategy followed consists in using the Picard scheme for the first three iterations and the Newton-Raphson algorithm from

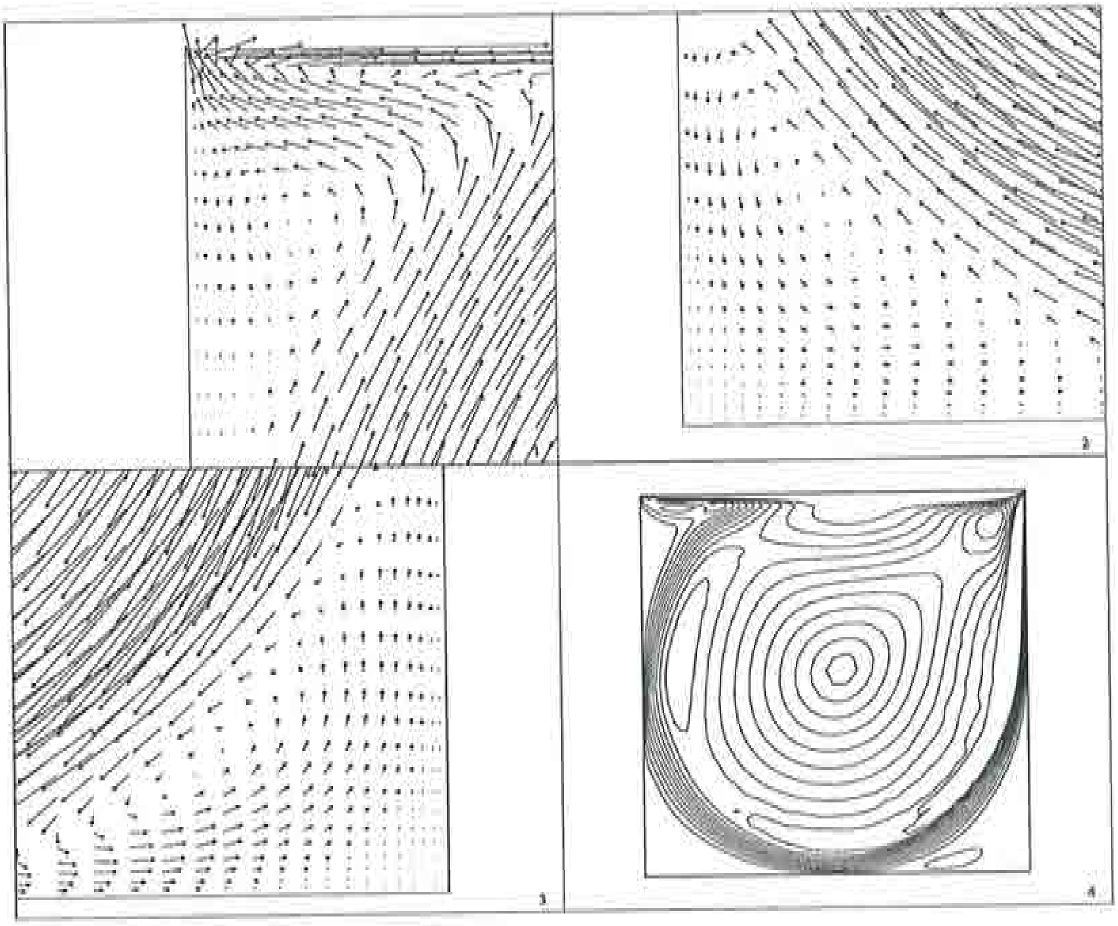

Figure 2.11 Numerical solution of the cavity flow problem at $Re = 4000$, velocities. (1): Detail of the top left corner; (2): Detail of bottom left corner; (3): Detail of bottom right corner; (4): Contours of the velocity norm.

there on. Now, twelve iterations have been needed to converge up to a convergence tolerance of 0.1%, but again the Stokes solution has been found to be a good enough initial guess for the iterative process.

Numerical results are shown in Figures 2.10 to 2.12, corresponding to the same plots as for the $Re = 1000$ case. Once again, *the Galerkin* formulation has been employed.

From Figure 2.10.(2) it is observed that now the top left vortex has appeared, with an extreme value of $0.9 \times 10^{-3}$ for the streamfunction. The other two vortices have an increased strength with respect to the results for $Re = 1000$.

The velocity vectors are shown in Figure 2.11. From the contours of their norm plotted in Figure 2.11.(4) it is seen that *small numerical oscillations begin to appear* in zones with a high velocity and a relatively large element size, that is, with a large cell Reynolds number. These oscillations appear near the bottom right corner. Nevertheless, they do not affect the quality of the solution in the rest of the domain and, in particular, the vortices are well reproduced. The effect of the small velocity oscillations on the pressure is very weak, as it may be observed from Figure 2.12.

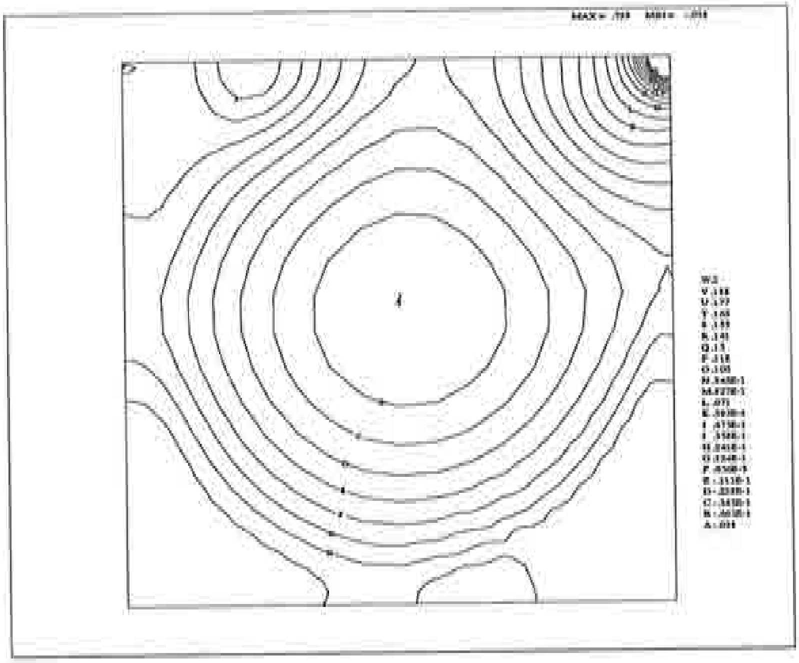

Figure 2.12 Numerical solution of the cavity flow problem at $Re = 4000$. Pressure contours.

The situation is completely different for $Re = 8000$. Concerning the iterative procedure, we have failed to obtain a converged solution by solving directly the stationary Navier-Stokes equations. The alternative to use continuation techniques as in [So] is to advance in time. We have chosen the solution obtained for $Re = 4000$ as the initial condition. In order to decrease the computational effort, the following strategies have been used:

- $\theta = 1$, i.e., the Euler scheme has been used. The steady-state is reached faster than using $\theta = 1/2$ (Crank-Nicolson) and the computational effort is smaller.
- Artificial compressibility method. Only for the steady state a good approximation to the incompressibility constraint is needed. For $\epsilon = 10^{-3}$, the final value of the norm of the discrete velocity divergence has been found to be of order $10^{-10}$.
- High convergence tolerance. In order to perform only one iteration per time step, we have taken $TOL = 0.1$ (10%) in (2.52).
- Small tolerance to check the steady-state. $TOL = 10^{-3}$ (0.1%) has been taken in (2.53).
- The time step size has been chosen as $\Delta t = 0.1$ For higher values, the solution oscillates from one time step to another.

Using all these numerical parameters, the steady-state has been found using the SD method for $t = 5.1$, i.e., after 51 time steps. The steady-state has not been found using the Galerkin method. The solution obtained at every time step is oscillatory.

Numerical results using the SD method are shown in Figures 2.13 to 2.15. In general, the flow features encountered for $Re = 4000$ are now accentuated, although nothing new appears. For $Re = 10000$ it is known that new secondary vortices develop in the left and right bottom corners.

Let us compare now the extreme values for the streamfunction at $Re = 5000$ that

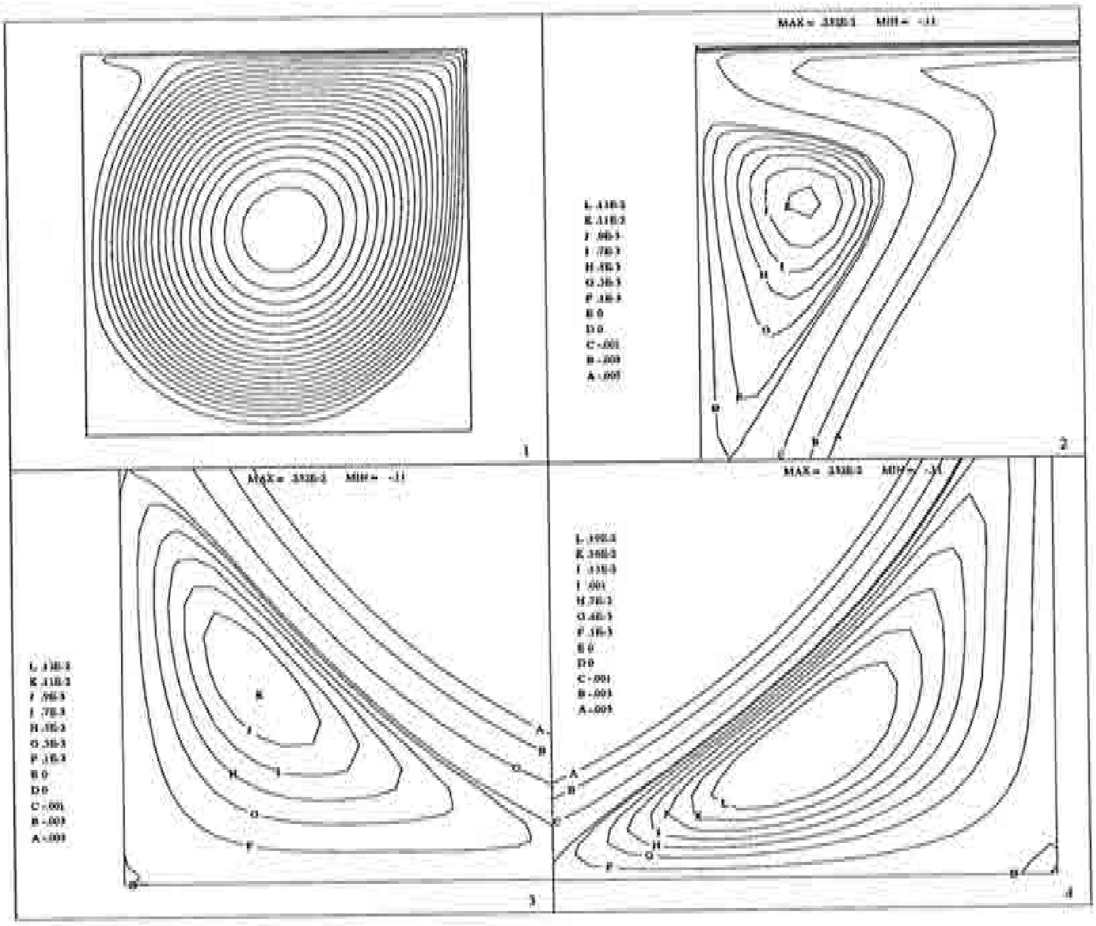

Figure 2.13 Numerical solution of the cavity flow problem at $Re = 8000$ (SD method), streamlines. (1): General pattern; (2): Detail of the top left corner; (3): Detail of bottom left corner; (4): Detail of bottom right corner.

we have obtained (plots not shown) with those given in the previous references. The results are the following:

| Reference | Vortex 1 | Vortex 3 |
|---|---|---|
| [GGS] | $3.08 \times 10^{-3}$ | $1.46 \times 10^{-3}$ |
| [GC2] | $3.87 \times 10^{-3}$ | $1.23 \times 10^{-3}$ |
| [Ki] | $2.79 \times 10^{-3}$ | $1.30 \times 10^{-3}$ |
| [So], without STU | $2.80 \times 10^{-3}$ | $1.28 \times 10^{-3}$ |
| [So], with STU | $1.71 \times 10^{-3}$ | $1.94 \times 10^{-4}$ |
| Present study | $2.49 \times 10^{-3}$ | $1.21 \times 10^{-3}$ |

The conclusions that may be drawn from these values is that the SD method we have employed is much less overdiffusive than the STU technique used by Sohn, but peaks are still smaller than in [Ki] and [So] using the Galerkin formulation. Recall

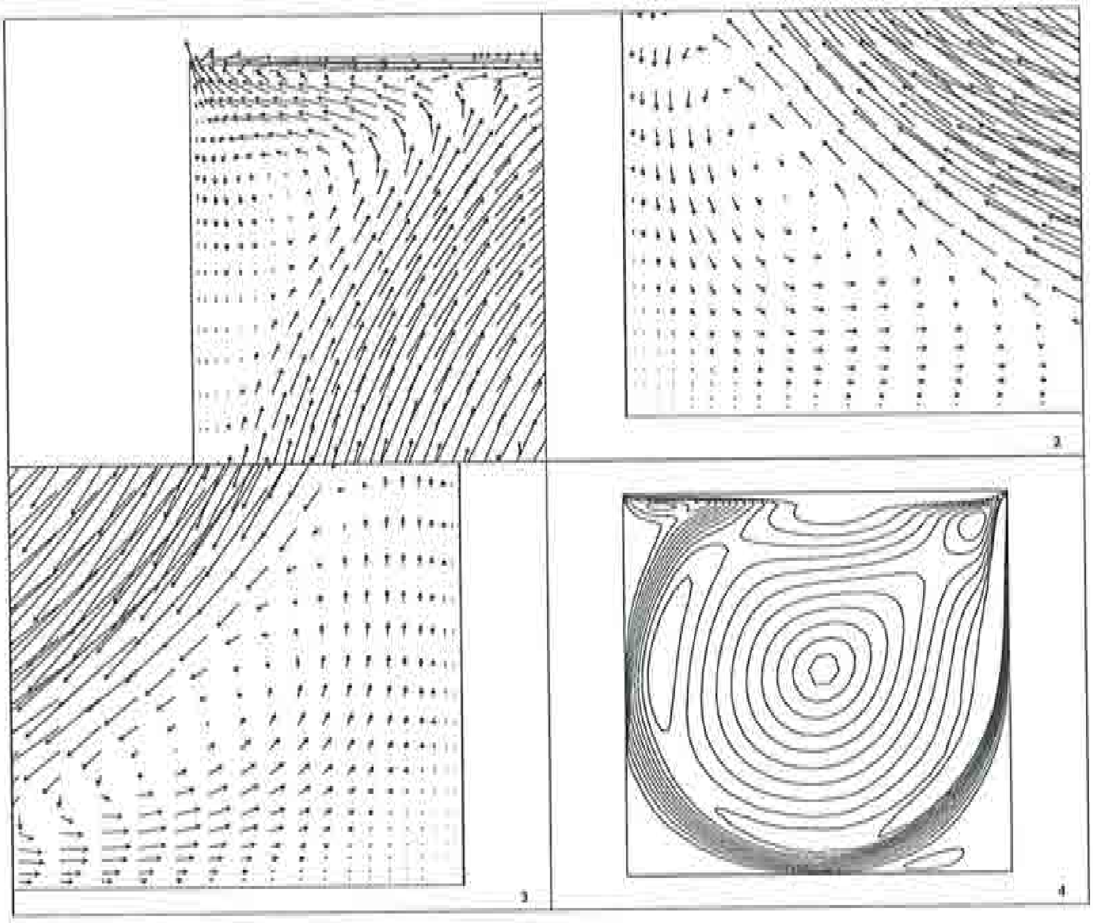

Figure 2.14 Numerical solution of the cavity flow problem at $Re = 8000$, velocities. (1): Detail of the top left corner; (2): Detail of bottom left corner; (3): Detail of bottom right corner; (4): Contours of the velocity norm.

that this also happened for $Re = 1000$ when the Galerkin method was used in our computation. The fact that our mesh is coarser than the one used in [Ki] and [So] may be responsible in part for these results. Anyway, if the SD method contributes to damp peaks out, it is clear that this effect is not very important and the numerical answers are very accurate.

We consider now the convergence of the SD method. When the Picard scheme is used, the rate of convergence is only linear and the way the SD has been linearized does not affect it. The situation is different when the Newton-Raphson algorithm is employed. The linearization of the SD operator described earlier is only linear, and therefore the rate of convergence of the scheme may be driven by this linearization, regardless of the fact that the convective terms of the equations have been linearized up to second order.

Let us see what happens when the $P_2^+/P_1$ element is used. The mesh used is shown in Figure 2.16. It is an unstructured mesh composed of 338 $P_2^+/P_1$ elements and 1063 nodal points. The iterative penalization has been used, with $\epsilon = 10^{-4}$. For the SD method we have taken $\alpha_0 = 0.5$ (upwind factor) and $h_0 = 0.7$ (element

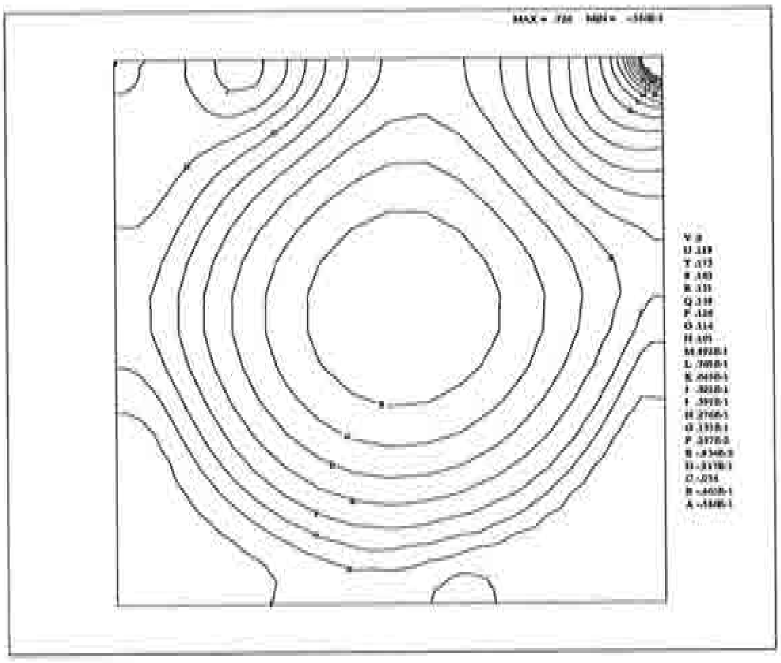

Figure 2.15 Numerical solution of the cavity flow problem at $Re = 8000$. Pressure contours.

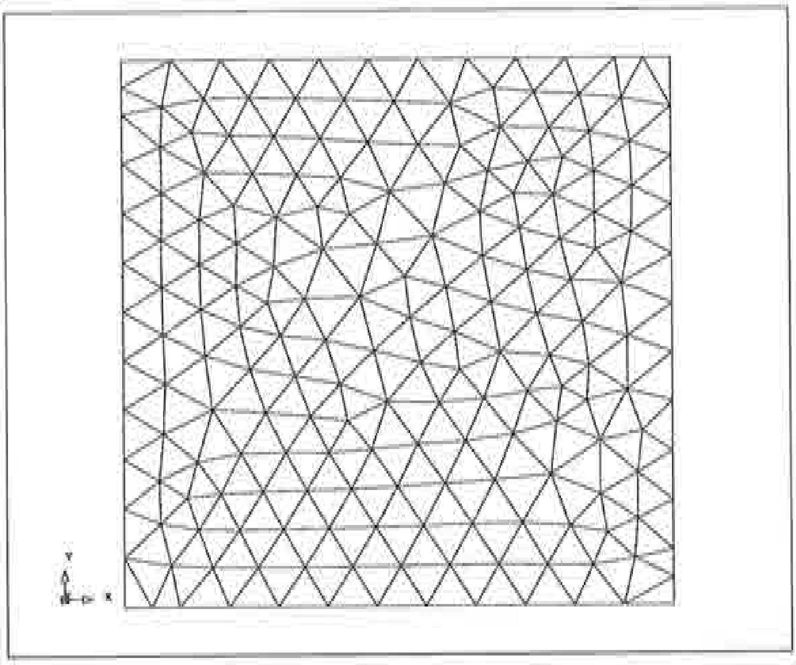

Figure 2.16 Finite element mesh for the cavity flow problem (338 $P_2^+/P_1$ elements, 1063 nodal points).

length in the parent domain). For $Re = 1000$, the velocity does not oscillate using the Galerkin method. Results are shown in Figure 2.17, both using the Galerkin and the

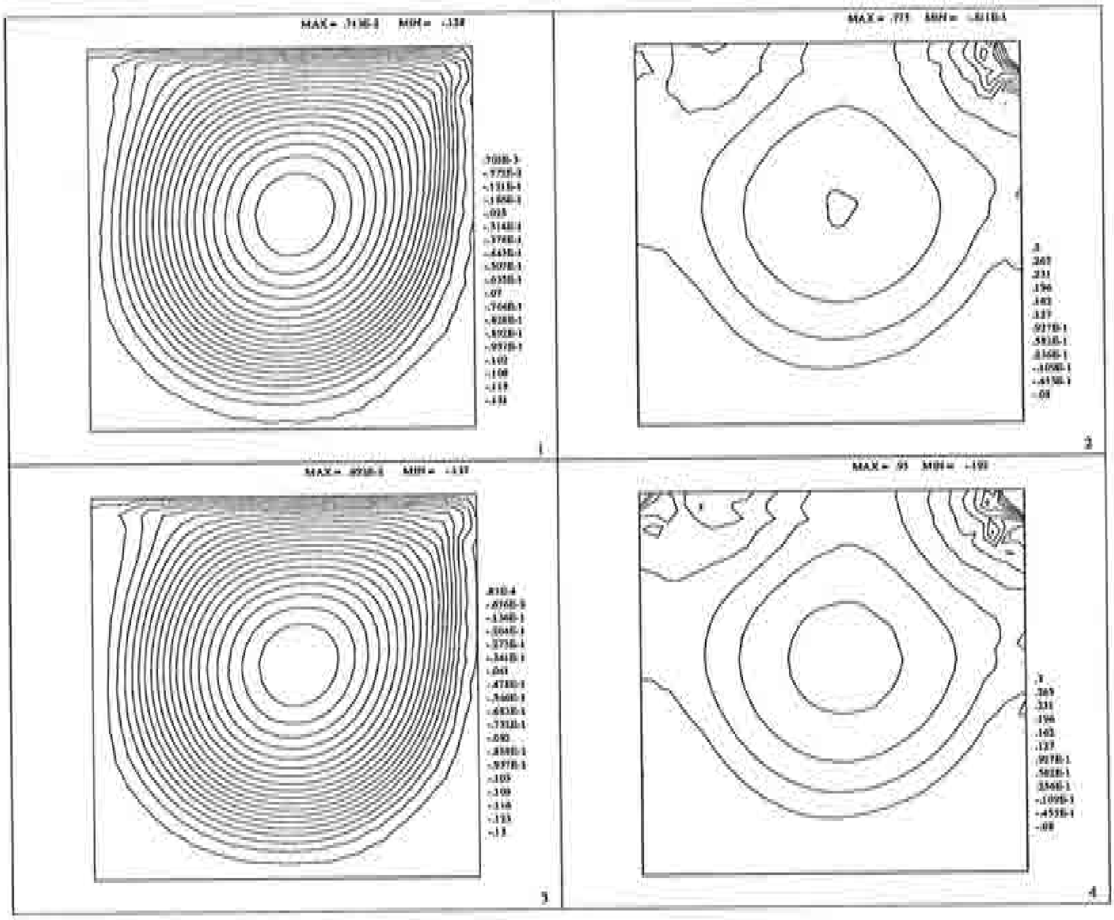

Figure 2.17 Numerical solution of the cavity flow problem at $Re = 1000$ using the $P_2^+/P_1$ element. (1): Streamlines, Galerkin formulation; (2): Pressure contours, Galerkin formulation; (3): Streamlines, SD method; (4): Pressure contours, SD method.

SD formulations.

The convergence history has been plotted in Figure 2.18.(a). The Picard method has been used for the first two iterations, after which the Newton-Raphson scheme has been employed. It is observed that the Galerkin method yields a quadratic rate of convergence. However, this rate turns from quadratic to linear at iteration number eight if the SD method is used. The evolution of the norm of the discrete divergence is quite peculiar (the same notation as in Chapter 1 has been adopted). From Figure 2.18.(b) it is seen that this norm increases during the first three iterations and then decreases with a rate similar to that of the convergence history. Of course this does not contradict the results of Chapter 1, since what we obtained there was only an error bound for the difference between the penalized solution and the solenoidal one. In Figure 2.18.(b), $||\mathbf{BU}||$ has been normalized by dividing it by $N_{tp}^{1/2}$.

The same numerical experiments have been carried out using the $Q_2/P_1$ pair for $Re = 1000$ and a uniform mesh composed of $12 \times 12$ elements (625 nodal points), with $\epsilon = 10^{-4}$. Results are again very similar using the Galerkin and the SD methods (not shown). The convergence history and the evolution of the discrete norm of the velocity

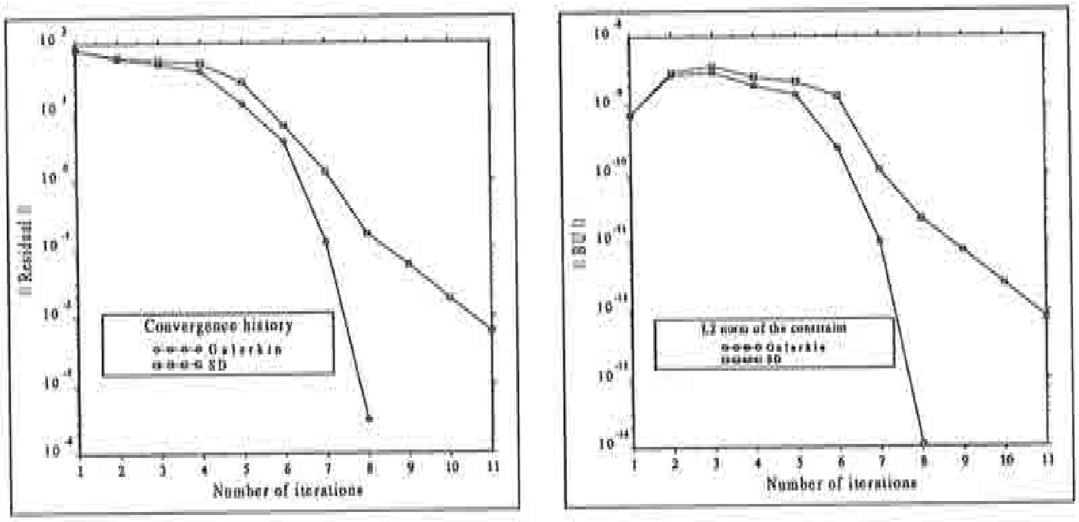

Figure 2.18 Comparison of the convergence of the Galerkin and the SD methods for $Re = 1000$ using the $P_2^+/P_1$ element, $\epsilon = 10^{-4}$. (1): Convergence history; (2): Norm of the constraint.

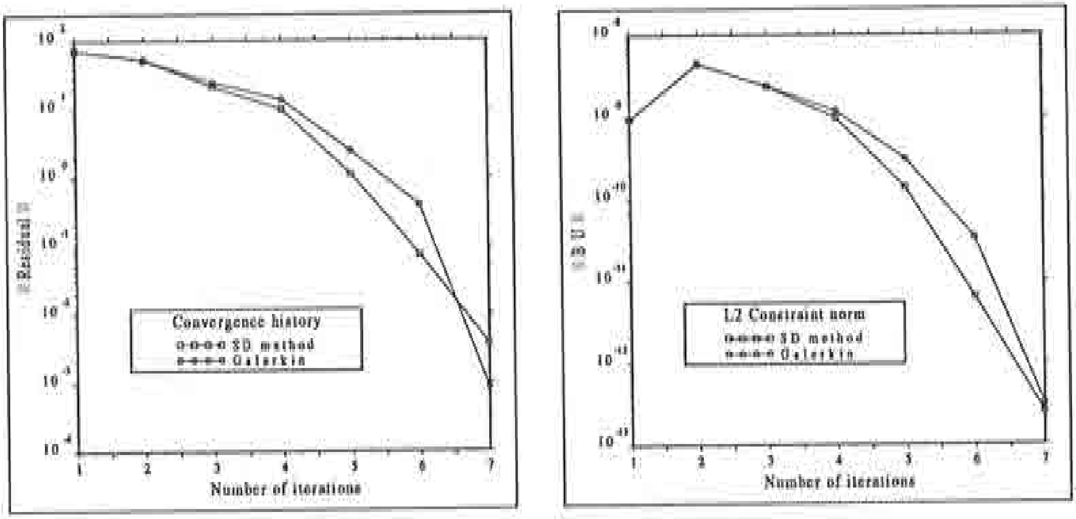

Figure 2.19 Comparison of the convergence of the Galerkin and the SD methods for $Re = 1000$ using the $Q_2/P_1$ element, $\epsilon = 10^{-4}$. (1): Convergence history; (2): Norm of the constraint.

divergence have been plotted in Figure 2.19. The same general trends as for the $P_2^+/P_1$ element are observed, although now convergence is faster and the residual using the SD method is smaller than using the Galerkin approach during the first six iterations.

From the all the results obtained for this example, it may be concluded that the SD method fulfils the requirement for which it has been designed: it produces numerical answers without oscillations at high cell Reynolds numbers. Nevertheless, there is a price for it. First, care must be taken in the computation of the intrinsic time in order to avoid overdiffusive results, which anyway will be somehow overdamped. Second, the SD operator introduces a high nonlinearity in the problem that may deteriorate the convergence rate of the Newton-Raphson algorithm.

**Example 2.2** *Flow over a backward-facing step*

The laminar backward-facing step flow is now considered. The problem description is shown in Figure 2.20. Aspect ratio of the backward-facing step ($H$) to the overall sectional width is 1:2 and the total length in the horizontal direction is $40H$. A fully developed velocity parabolic velocity profile is prescribed at the inlet boundary. Experimental data can be found in Reference [ADS]. A detail of the mesh used in the calculation is shown in Figure 2.21. This mesh is composed of 495 $Q_2/P_1$ elements and 2077 nodal points.

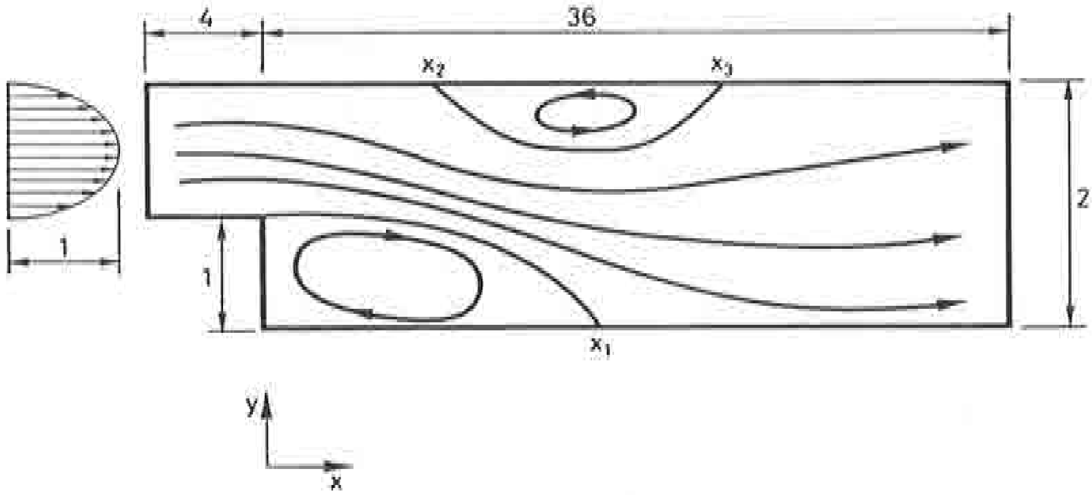

Figure 2.20 Geometry, boundary conditions and nomenclature of backward-facing step problem.

According to Arnali *et al.* [ADS], the Reynolds number will be based on the average value of the inlet velocity profile and the cross-sectional width of the whole domain. For $Re < 500$ there exists only one recirculation zone behind the step. For higher values of $Re$, another recirculation zone appears at the top wall of the channel. Experimental results indicate that a third recirculation zone appears at the bottom wall for values of $Re$ higher than approximately 1000.

The main feature of this test for the stationary Navier-Stokes equations is the prediction of the vortices as well as the position of the separation and reattachment points (coordinates $x_1$, $x_2$ and $x_3$ in Figure 2.20). For low values of $Re$, approximately up to 500, a fairly good agreement exists among the numerical and experimental results that can be found in the literature [ADS], [KM], [Ki], [So]. For $Re > 600$, three-dimensional effects in the experiments are the argued reason for the discrepancies between computational predictions and experimental results [ADS].

Our numerical results agree very well for $Re \leq 600$ with those that can be found in the above mentioned references. For brevity, they have not been included here. We will concentrate only on high values of the Reynolds number. In particular, results will be shown for $Re = 800$ and $Re = 1000$.

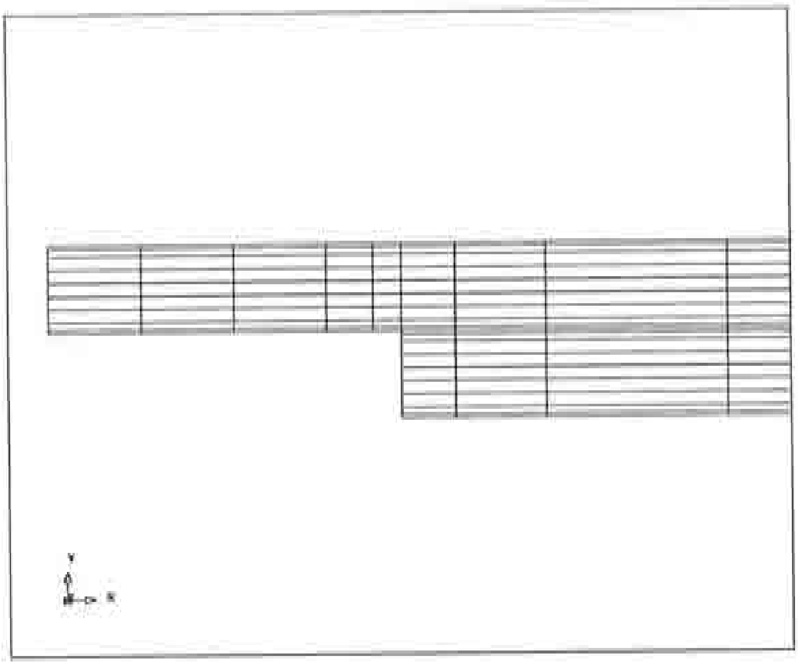

Figure 2.21 Detail of the finite element mesh for the backward-facing step problem (495 $Q_2/P_1$ elements, 2077 nodal points).

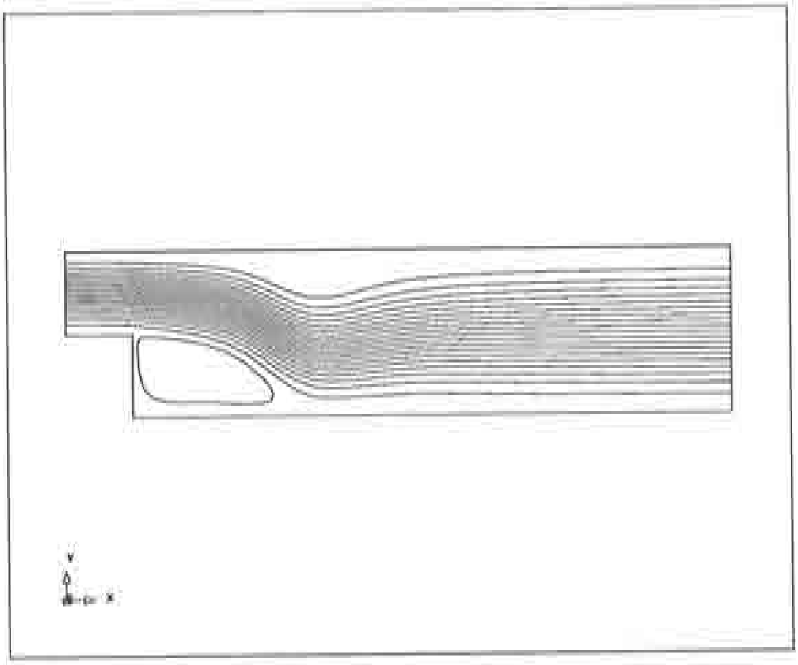

Figure 2.22 General pattern of the streamlines for the backward-facing step problem at $Re = 800$.

The SD method has been used in the calculations, with $\alpha_0 = 0.5$ and $h_0 = 2$. The penalty parameter has been taken as $\epsilon = 10^{-4}$, using the iterative penalization,

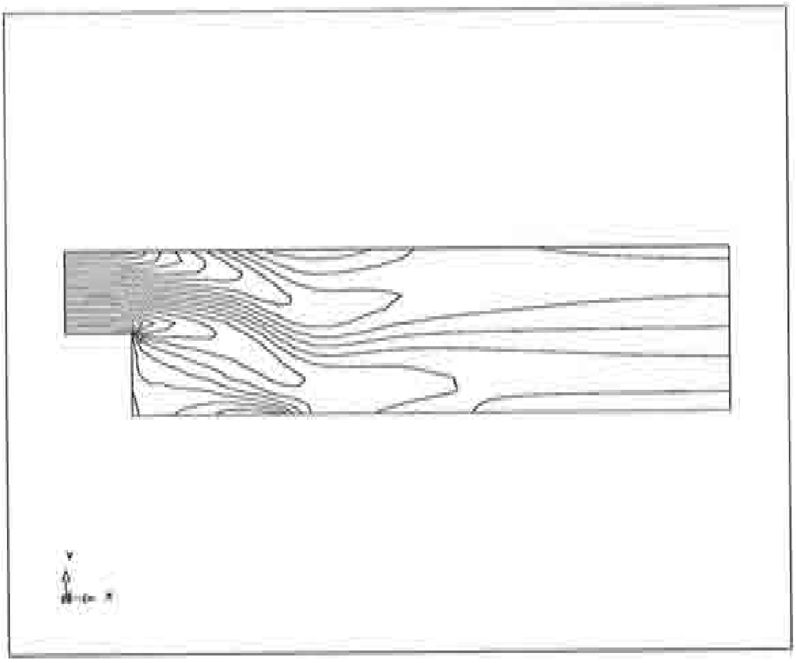

Figure 2.23 Vorticity contours for the backward-facing step problem at $Re = 800$.

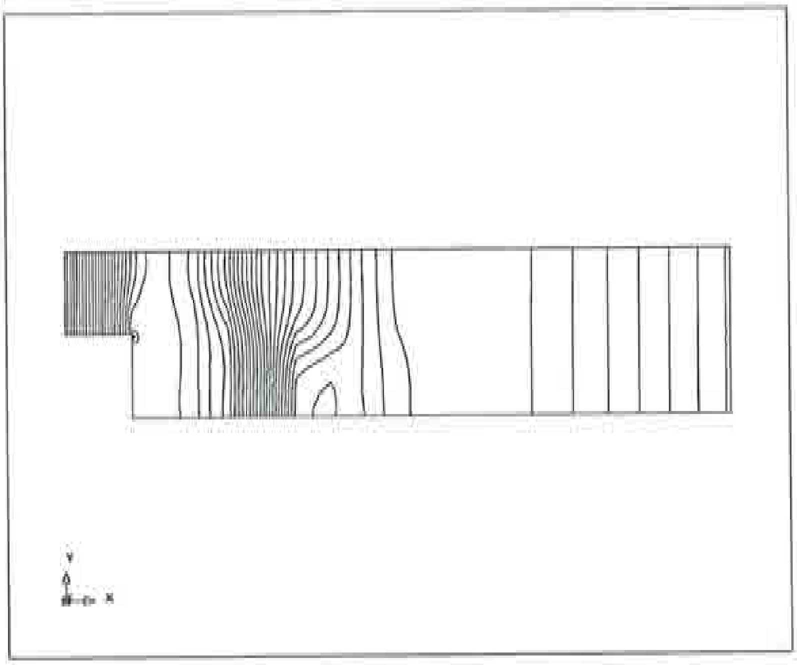

Figure 2.24 Pressure contours for the backward-facing step problem at $Re = 800$.

yielding a final value of order $10^{-14}$ for the norm of the discrete velocity divergence. For $Re = 100$, the computation has started with zero velocities everywhere. The numerical

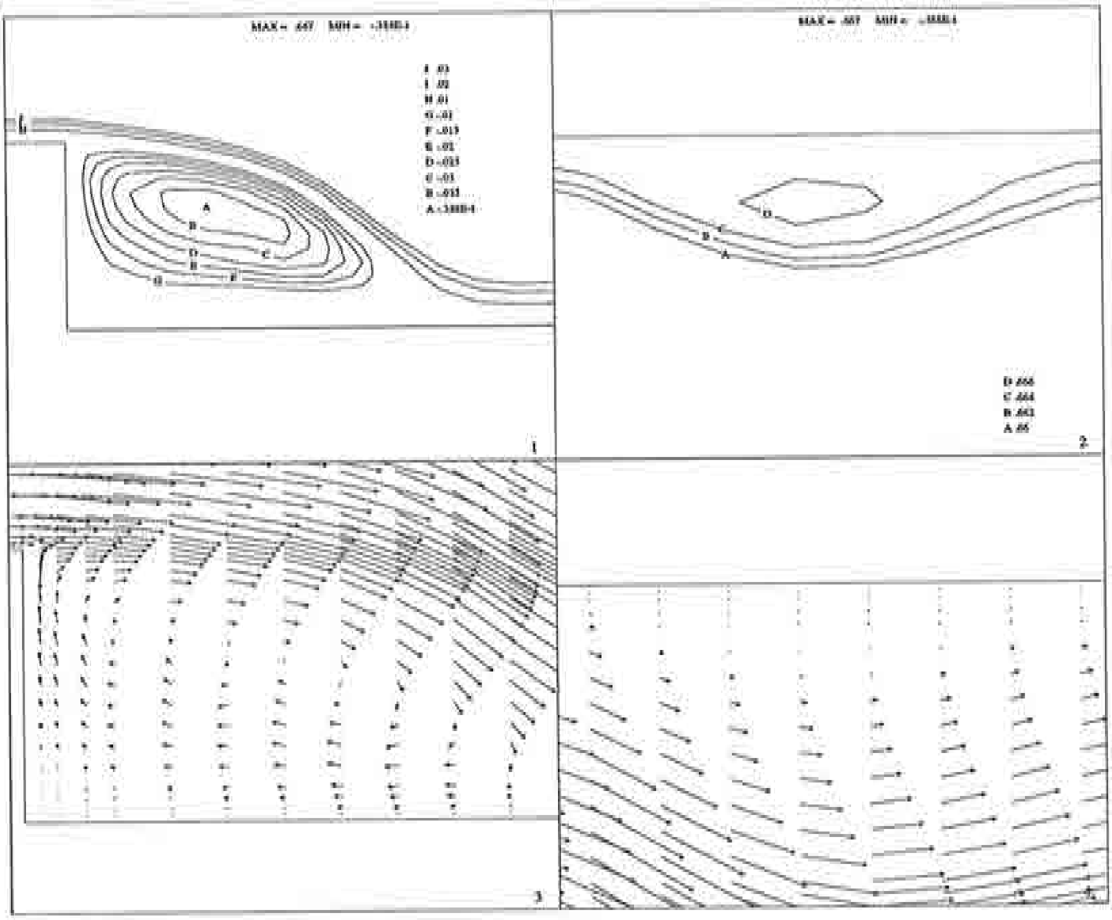

Figure 2.25 Details of the velocity and the streamlines in the recirculation zones for the backward-facing step problem at $Re = 800$. (1): Streamlines behind the step; (2): Streamlines in the recirculation zone at the top wall; (3): Velocity vectors behind the step; (4): Velocity vectors in the recirculation zone at the top wall.

results obtained for this case have been used as the initial guess for $Re = 200$, and the procedure has been repeated until $Re = 1000$. This type of continuation technique has been adopted only because the whole range of Reynolds numbers were to be solved. For $Re = 1000$ we have also tried to reach the stationary solution via the evolution in time, starting from the Stokes flow solution. The convergence towards the steady-state has been found to be extremely slow, and only after a time $t = 207$ the steady-state has been reached. We have used $\Delta t = 0.1$ and the backward Euler scheme ($\theta = 1$), with a single iteration per time step ($TOL = 0.1$ in (2.53)) and a tolerance of 0.1% to check if the steady-state has been reached. This slow evolution towards the stationary solution is due to the pressure waves that are reflected at the outflow boundary, for which the numerical boundary condition chosen is zero traction. Concerning the steady calculations, two Picard iterations and three or four Newton-Raphson iterations have been performed for each Reynolds number increment to reach a convergence tolerance of 0.1%.

Consider first the case $Re = 800$. Figure 2.22 shows the general streamline pattern (the $y-$direction has been scaled by a factor of 5 in all the plots). Vorticity and pressure contours are shown in Figures 2.23 and 2.24, respectively. From the last picture, it is observed that the zero traction outflow condition, which must be viewed as an artificial boundary condition to simulate a long channel, does not produce pressure reflexion. The pressure gradient is parallel to the $x-$direction.

A detail of the streamlines and the velocity vectors in the recirculation zones is shown is Figure 2.25. The vortex behind the step is much stronger than the one in the top wall of the channel. The extreme values of the streamfunction are $-3.88 \times 10^{-2}$ for the first vortex and $6.67 \times 10^{-1}$ for the second. The values of the coordinates $x_i$, $i = 1, 2, 3$ in Figure 2.20 are the following:

| Coordinate | Experimental | Computed |
|---|---|---|
| $x_1$ | 14.3 | 10.3 |
| $x_2$ | 10.6 | 10.8 |
| $x_3$ | 19.8 | 17.2 |

The given computed values have been obtained from the plots and therefore should be considered only as an approximation. The experimental values correspond to those given in [ADS]. As it has been already said, discrepancies should be expected due to the three-dimensionality of the experimental flow at this Reynolds number.

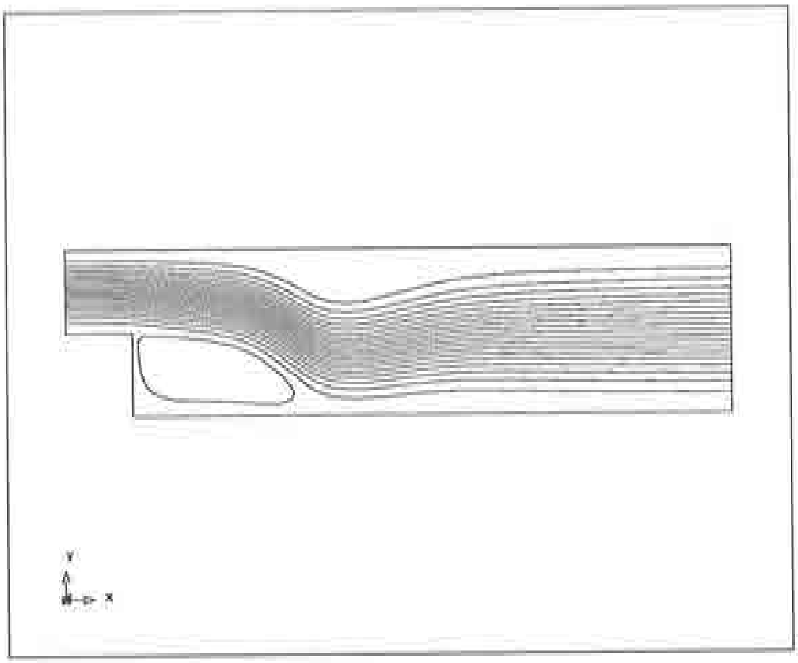

Figure 2.26 General pattern of the streamlines for the backward-facing step problem at $Re = 1000$.

Results for $Re = 1000$ are shown in Figures 2.26 to 2.29. The essential features of the flow are the same as for $Re = 800$, although now accentuated. In Figure 2.28 it is observed that higher pressure gradients develop at the reattachment point behind the cylinder. The detail of the vortices depicted in Figure 2.29 indicate that they are

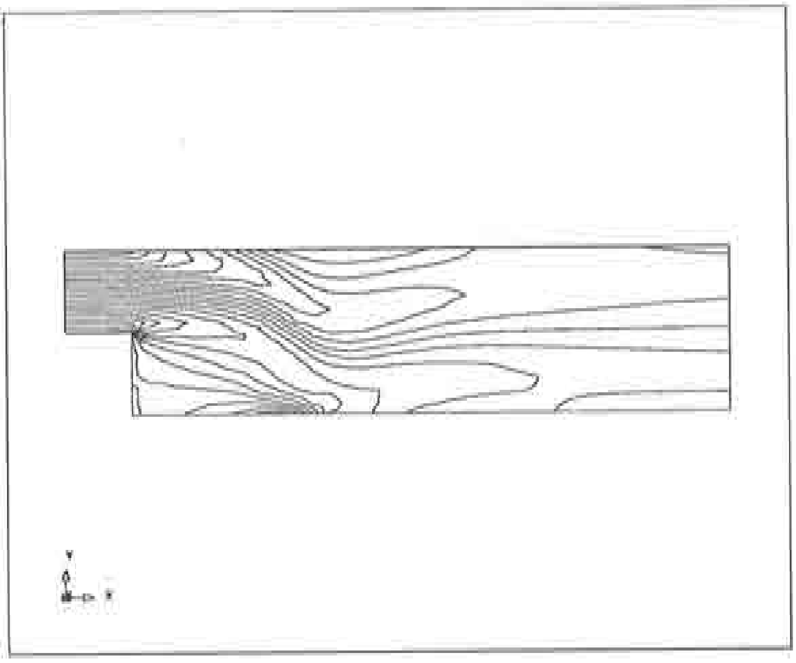

Figure 2.27 Vorticity contours for the backward-facing step problem at $Re =$ 1000.

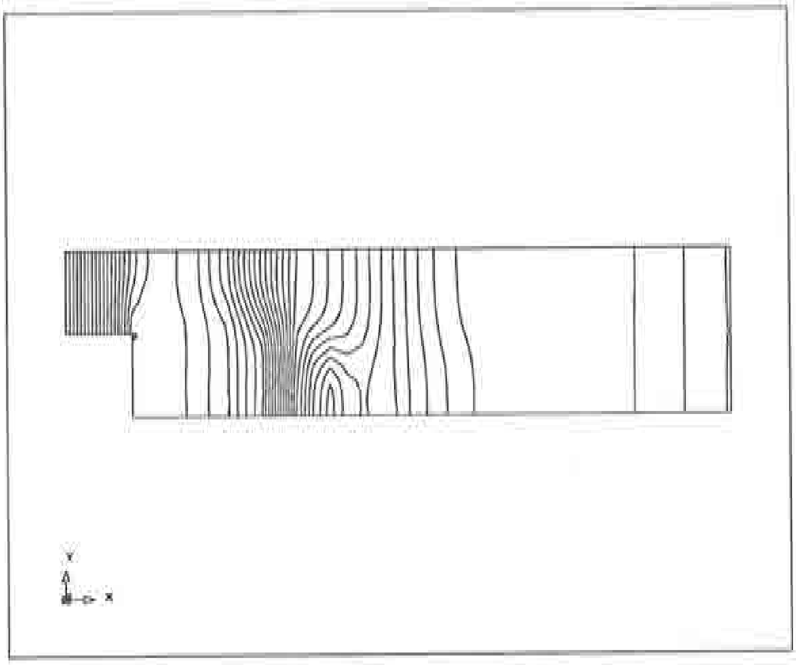

Figure 2.28 Pressure contours for the backward-facing step problem at $Re =$ 1000.

stronger now that for $Re = 800$. It is also observed that a third vortex begins to appear at the top wall (Figure 2.29.(2)).

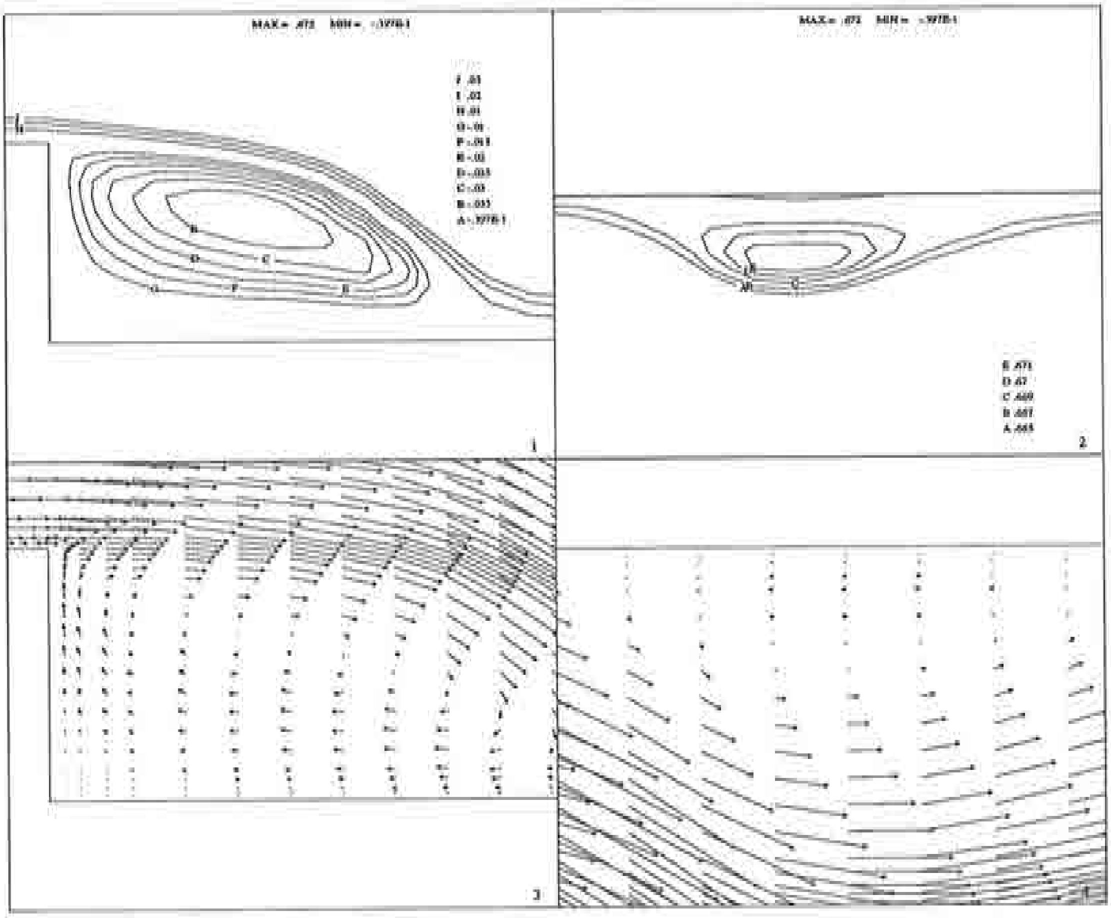

Figure 2.29 Details of the velocity and the streamlines in the recirculation zones for the backward-facing step problem at $Re = 1000$. (1): Streamlines behind the step; (2): Streamlines in the recirculation zone at the top wall; (3): Velocity vectors behind the step; (4): Velocity vectors in the recirculation zone at the top wall.

The approximate values of the coordinates $x_i$, $i = 1, 2, 3$ are found to be $x_1 = 12.8$, $x_2 = 13.0$ and $x_3 = 22.1$. Although the recirculation zones are now longer that for the $Re = 800$ case, they are still shorter than the experimental values for this Reynolds number.

**Example 2.3** *Vortex shedding behind a cylinder*

This last example involves the flow past a cylinder, another widely solved benchmark problem. A circular cylinder is immersed in a viscous fluid. The Reynolds number is based on the cylinder diameter and the prescribed uniform inflow velocity. The geometry and boundary conditions are shown in Figure 2.30.

For $Re$ approximately less than 40, two symmetrical eddies develop behind the cylinder. These eddies become unstable at higher Reynolds numbers and periodic vortex shedding occurs, leading to the so called von Karman vortex street. The case $Re = 100$ to be solved here is usually considered as the standard test.

Consider first the stationary (unstable) solution. To show the behavior of the

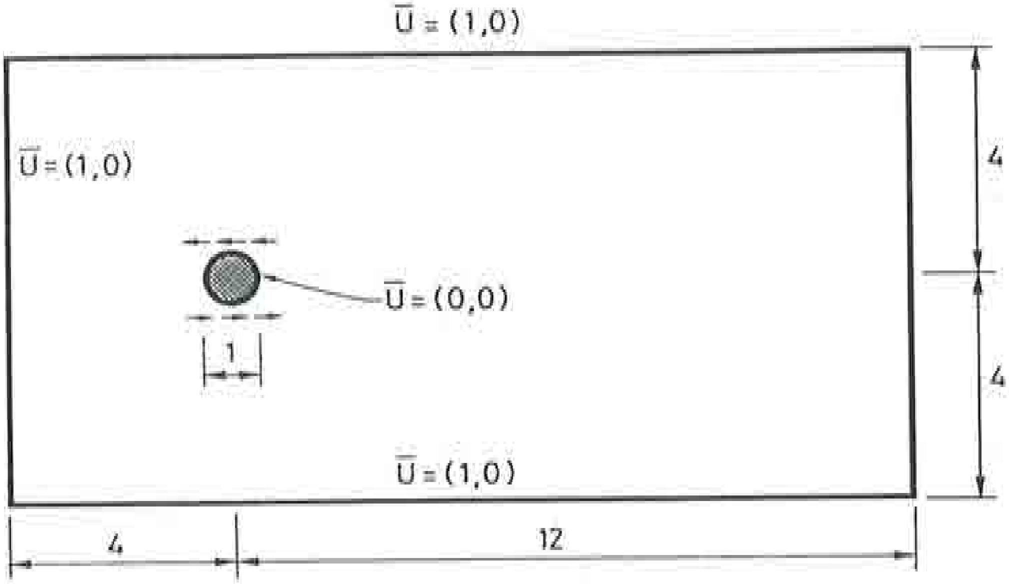

Figure 2.30 Geometry, boundary conditions and initial perturbation for the flow past a cylinder.

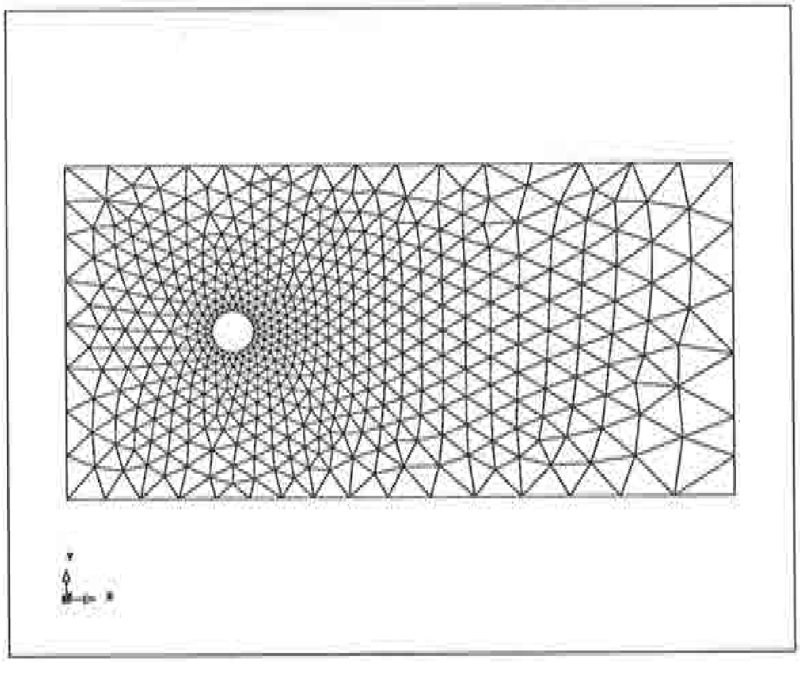

Figure 2.31 Finite element mesh for the flow past a cylinder using the $P_2^+/P_1$ element (1014 elements, 3112 nodal points).

$P_2^+/P_1$ pair, we have solved this problem using this element. The finite element mesh shown in Figure 2.31 consists of 1014 elements and 3112 nodal points. The steady calculation has started with zero velocities everywhere. First, two Picard iterations have been performed, after which four more Newton-Raphson iterations have been

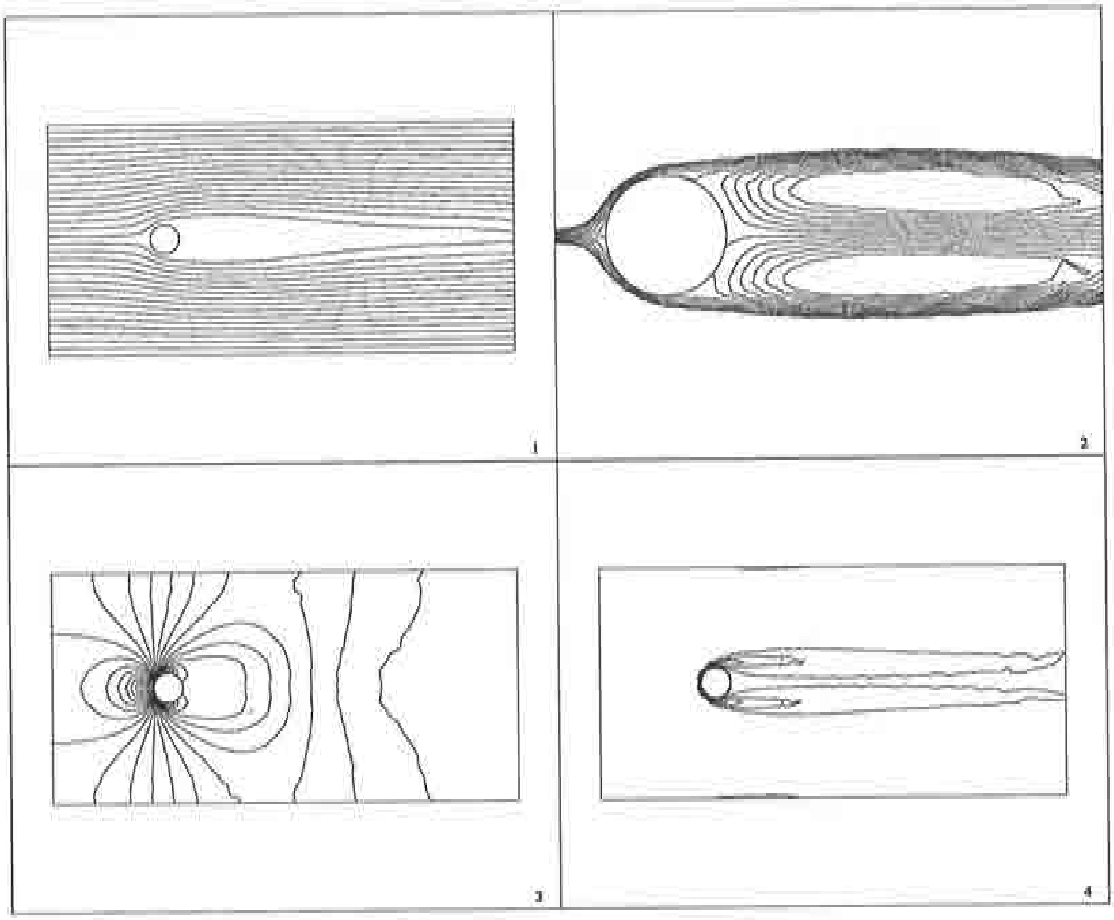

Figure 2.32 Stationary (unstable) solution using the $P_2^+/P_1$ element. (1): Streamlines; (2): Detail of the symmetrical eddies at the downstream side of the cylinder; (3): Pressure contours; (4): Vorticity contours.

needed to reach a convergence tolerance of 0.1%. The iterative penalty method has been employed, with a penalty parameter $\epsilon = 10^{-3}$. The upwind factor to calculate the intrinsic time has been chosen as $\alpha_0 = 0.5$ (quadratic elements) and the length of the parent domain $h_0 = 0.7$. Results are shown in Figure 2.32.

If the stationary solution is slightly perturbed, the two symmetric eddies disappear and vortex shedding occurs. The numerical simulation of this phenomenon has been carried out using the $Q_2/P_1$ element and the finite element mesh depicted in Figure 2.33 (500 elements, 2100 nodal points). First, the stationary solution has been obtained (results not shown), with a strategy similar to the previous case. This solution has been perturbed by introducing a small rotating flow field around the cylinder, as shown in Figure 2.30, and taking this as the initial condition for the transient computation.

In order to obtain a fully developed vortex shedding, 90 time steps have been performed with $\Delta t = 1$ (time step size) and $\theta = 0.5$ (Crank-Nicolson scheme), although $\theta = 1$ has been chosen for the first time step. The convergence tolerance within each time step has been taken as 1%. A single Picard iteration has been needed using the classical penalty method with $\epsilon = 10^{-3}$. The parameters of the SD method are

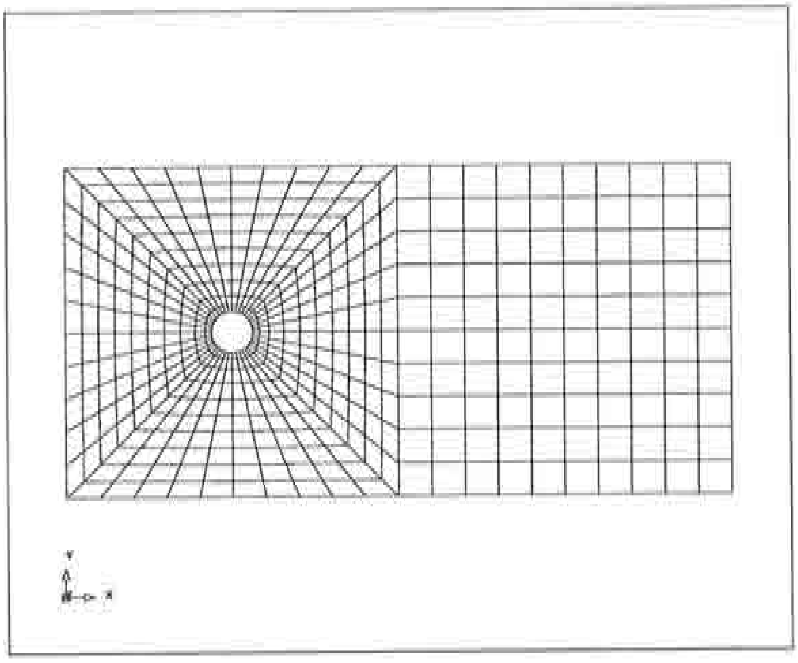

Figure 2.33 Finite element mesh for the flow past a cylinder using the $Q_2/P_1$ element (500 elements, 2100 nodal points).

$\alpha_0 = 0.5$ and $h_0 = 2$. The solution thus obtained is only a crude approximation, but the computational effort has been relatively low (56 CPU seconds per time step) and the periodic flow pattern obtained is fully developed.

The results obtained using this procedure have been taken as the initial condition for a more accurate calculation. Now, $\Delta t = 0.1$ has been chosen. Two Newton-Raphson iterations coupled with the iterative penalization have been performed for each time step. The initial guess for the first one has been the solution of the previous step. The relative $L^2$−norm of the velocity residuals found has been approximately the 2% and the normalized norm of the discrete velocity divergence of order $10^{-6}$. After the second iteration, the relative norm of the velocity residuals decreases to the 0.02% and the norm of the discrete velocity divergence to a value of order $10^{-8}$. The total CPU time required per time step has been 139 seconds.

Numerical results are shown in Figures 2.34 to 2.40. The period of the oscillations has been found to be 5.7 time units. The values given in references [BH] and [GC2] are 6.0 and 5.6, respectively. In Reference [EJ], the period obtained with a very fine mesh (3426 $Q_2/P_1$ elements, 14000 nodal points) is 5.8 time units.

The streamline snapshots shown in Figure 2.34 correspond to the times $t =$ 10, 11, 12 and 13, that is, approximately half a period ($t = 0$ corresponds to the periodic solution computed as described earlier with a higher tolerance and a higher time step size). Details of the streamlines and the velocity vectors at the downstream side of the cylinder are plotted in Figures 2.35 and 2.36, respectively. The pressure and vorticity are shown in Figures 2.37–2.38 and 2.39–2.40. In general, all these results agree very well with those that can be found in the literature. Perhaps the only point to be remarked is that the smoothing of the pressure and the vorticity we have employed does not yield very smooth contours, since both fields are highly variable in space due to the transportation of the eddies downstream.

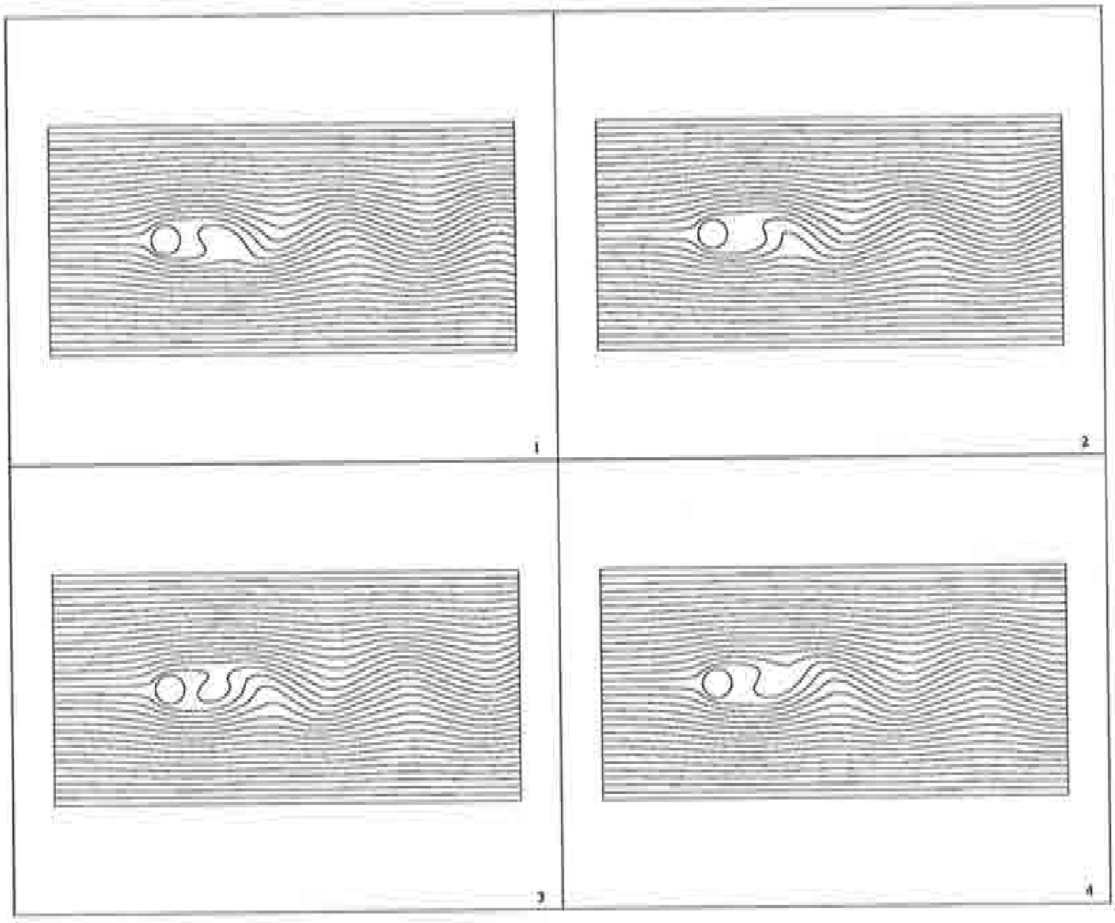

Figure 2.34 Development of vortex shedding: Streamlines. (1): $t = 10.$; (2): $t = 11.$; (3): $t = 12.$; (4): $t = 13.$.

## 2.9 Summary and conclusions

The finite element method to solve the Navier-Stokes equations proposed in this work has been fully described in this chapter. Most of the ideas developed in the previous chapter have been applied here, although now the purpose has been to present a *methodology* rather than to introduce new developments. In particular, the following items have been treated:

- *Time discretization.* The trapezoidal rule applied to the transient Navier-Stokes equations has been described in detail. Special emphasis has been given to justify, both using theoretical and computational arguments, the choice of the parameter $\theta$ of the trapezoidal rule.
- *Streamline Diffusion method.* As for the convection-diffusion equation studied in Reference [Co], a SD term is added to the Galerkin formulation of the Navier-Stokes equations. This term has been designed to avoid the numerical oscillations of the Galerkin approach, but not to stabilize the pressure interpolation. Therefore, the velocity-pressure spaces to be used have to be div-stable. The calculation of the intrinsic time is of fundamental importance, since overdiffusive answers are

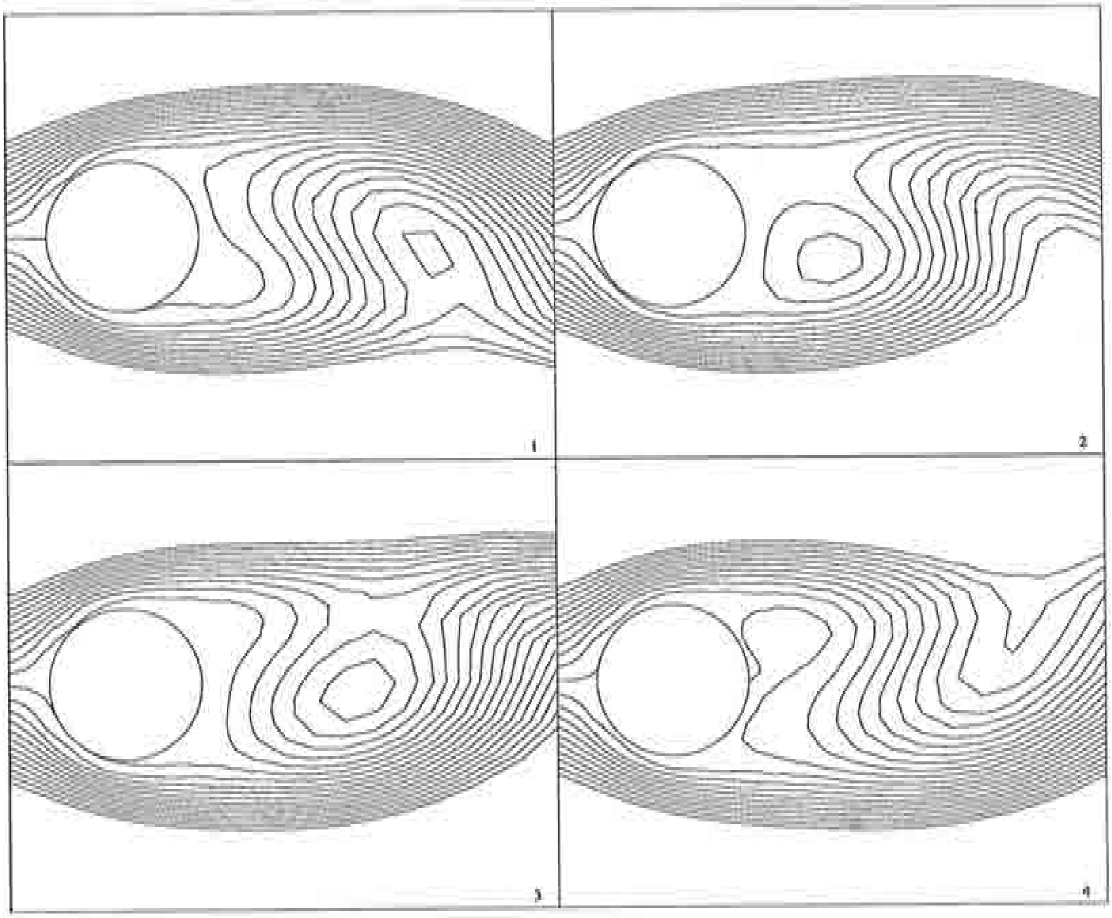

Figure 2.35 Development of vortex shedding: Detail of streamlines. (1): $t = 10.$; (2): $t = 11.$; (3): $t = 12.$; (4): $t = 13.$.

obtained if this parameter is overestimated. The simplest method of those proposed in Reference [Co] for computing the upwind function has proved to be effective. Whenever a converged solution has been obtained, no oscillations have been found and the results compare very well with reference numerical solutions selected from the available literature.

- *Linearization procedures.* The way the final nonlinear system of equations is linearized has been treated in detail. In order to avoid a high computational effort due to the SD method, terms coming form the SD operator have been linearized only up to first order. When the convective term is linearized up to second order, the quadratic rate of convergence that one finds using the Galerkin approach is in general deteriorated, although convergence is still much faster than using the Picard scheme, i.e., first order linearization for the convective term. This is a price to be paid for using the SD method.
- *Iterative penalization.* The iterative penalty method analyzed in Chapter 1 has been extended to the transient equations and used in conjunction with the SD method. We have found that this is certainly worth doing in all the cases. Although it has not been our purpose here to check its behavior, for which the numerical experiments of Chapter 1 were intended, in all the numerical examples

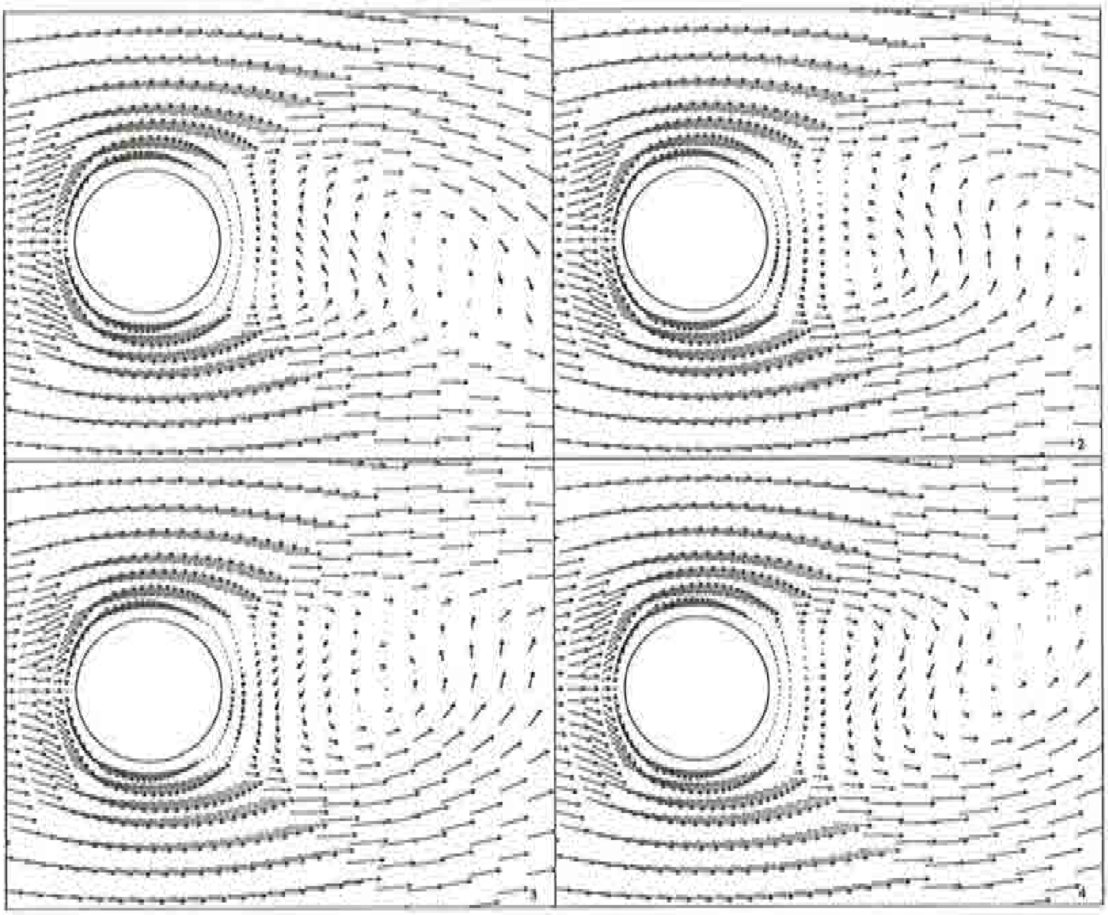

Figure 2.36 Development of vortex shedding: Detail of velocity vectors. (1): $t = 10.$; (2): $t = 11.$; (3): $t = 12.$; (4): $t = 13.$.

we have given the penalty parameter and the final value of the norm of the velocity divergence. Results have always been very good, with an approximation of the incompressibility constraint much better than what could be expected using the classical penalty method.

Some specific contributions have also been introduced here. After describing the smoothing technique employed in the calculation of the pressure and the vorticity, nodal quadrature rules have been given for the most common finite elements used in practice, not only those that have been employed here. Finally, an algorithmic procedure to calculate the streamfuction has been presented using the genuine structure of finite element programming.

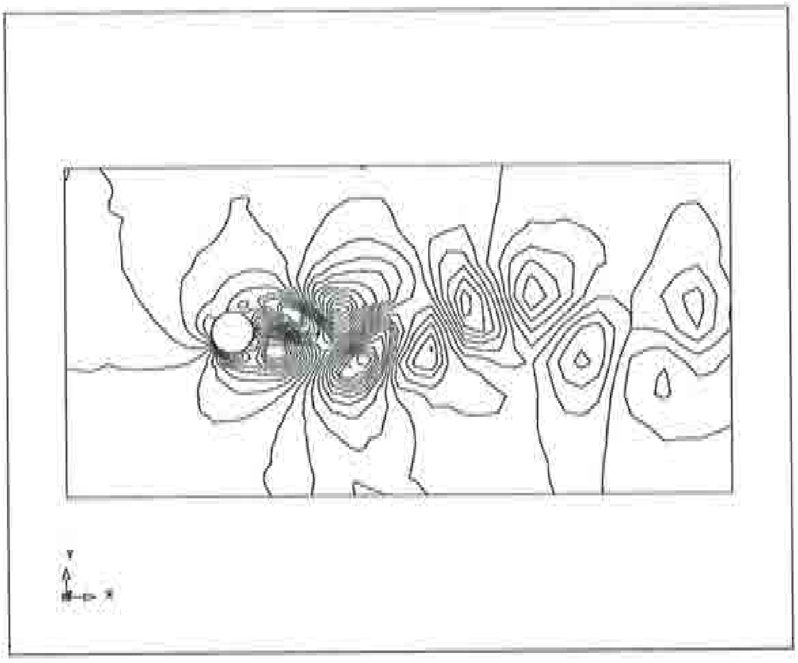

Figure 2.37 Pressure contours at $t = 15.$ time units.

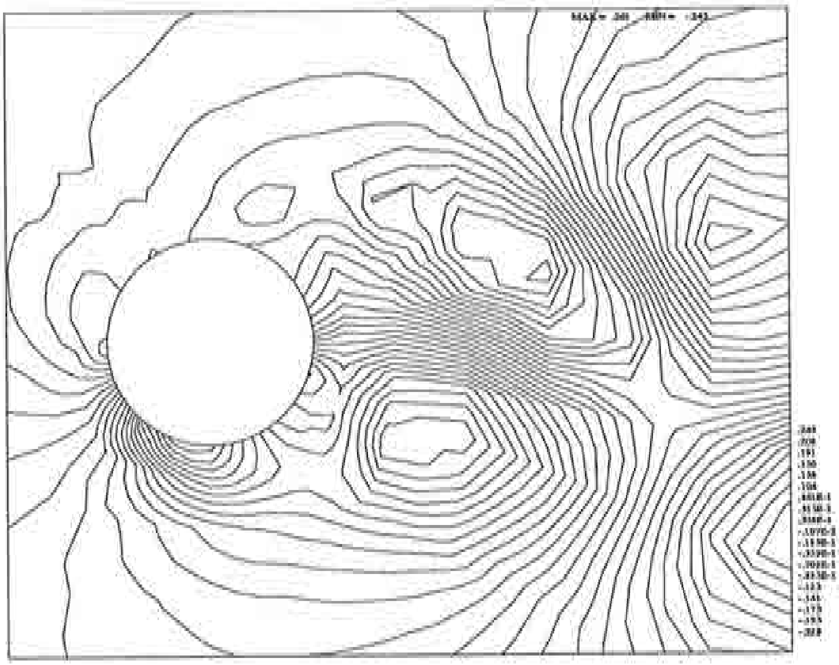

Figure 2.38 Detail of pressure contours at $t = 15.$ time units.

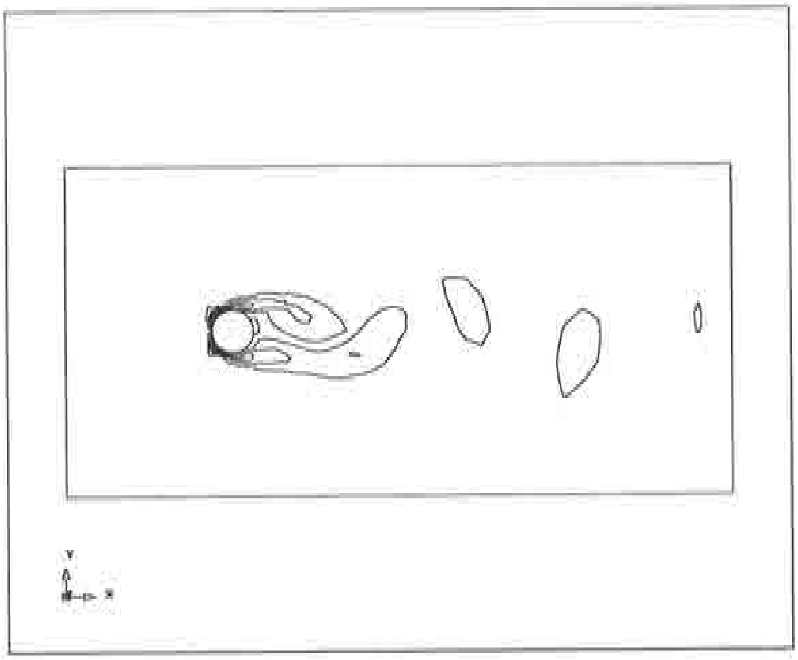

Figure 2.39 Vorticity contours at $t = 15.$ time units.

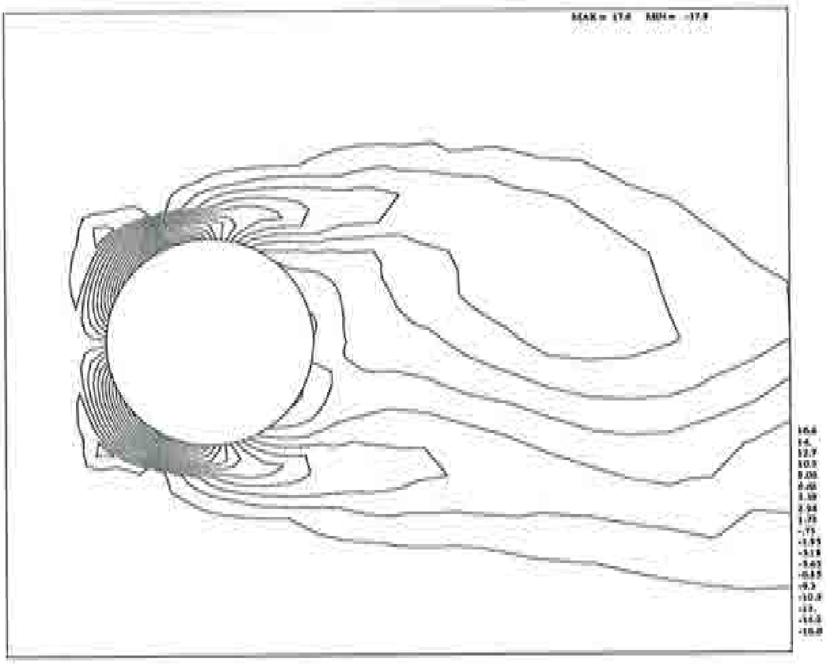

Figure 2.40 Detail of vorticity contours at $t = 15.$ time units.

## References

[ADP] J. Argyris, J. St. Doltsinis, P.M. Pimenta and H. Wustenberg. Natural finite element techniques for viscous fluid motion. *Comput. Meth. Appl. Mech. Engrg.*, vol. 45 (1984), 3–55

[ADS] B.F. Armaly, F. Durst, J.C.F. Pereira and B. Schonung. Experimental and theoretical investigation of backward-facing step flow. *J. Fluid Mech.*, vol. 127 (1983), 473–476

[ABF] D.N. Arnold., F. Brezzi and M. Fortin. A stable finite element for the Stokes equations. *Calcolo*, vol. 21 (1984), 337–344

[BW] R.E. Bank and B.D. Welfert. A comparison between the mini-element and the Petrov-Galerkin formulations for the generalized Stokes problem. *Comput. Meths. Appl. Mech. Engrg.*, vol. 83 (1990), 61–68

[BR] C. Bernardi and G. Raugel. A conforming finite element method for the time dependent Navier-Stokes equations. *SIAM J. Numer. Anal.*, vol. 22 (1985), 455–473

[BH] A.N. Brooks and T.J.R. Hughes. Streamline Upwind/Petrov-Galerkin formulations for convective dominated flows with particular emphasis on the incompressible Navier-Stokes equations. *Comput. Meths. Appl. Mech. Engrg.*, vol. 32 (1982), 199–259

[CO] G.F. Carey and J.T. Oden. *Finite Elements: Fluid Mechanics.* The Texas Finite Element Series, vol. VI (Prentice Hall, 1986)

[Ch] A.J. Chorin. A numerical method for solving incompressible viscous flow problems. *J. Comput. Phys.*, vol. 2 (1967), 12–26

[Ci] P.G. Ciarlet. *The finite element method for elliptic problems* (North-Holland, 1978).

[Co] R. Codina. *A finite element model for the numerical solution of the convection-diffusion equation.* (CIMNE Monograph Num. 14, 1992)

[CF] P. Constantin and C. Foias. *Navier-Stokes equations* (Chicago Press, 1989).

[CR] M. Crouzieux and P.A. Raviart. Conforming and non-conforming finite element methods for the stationary Stokes equations. *RAIRO Anal. Numer.*, vol. 7 (1973), 33–76

[CSS] C. Cuvelier, A. Segal and A. van Steenhoven. *Finite element methods and Navier-Stokes equations* (Reidel, 1986).

[EJ] M.S. Engelman and M.A. Jamnia. Transient flow past a circular cylinder: A benchmark solution. *Int. J. Numer. Meth. Fluids*, vol. 11 (1990), 985–1000

[Ga] D.K. Gartling. A test problem for outflow boundary conditions–Flow over a backward-facing step. *Int. J. Numer. Meth. Fluids*, vol. 11 (1990), 953–967

[GeH] M. Gellert and R. Harbord. Moderate degree cubature formulas for 3D tetrahedral finite-element approximations. *Comm. Appl. Numer. Meth.*, vol. 7 (1991), 487–495

[Ge] A. Georgescu. *Hydrodynamic stability theory* (Nijhoff, 1985).

[GGS] U. Ghia, K.N. Ghia and C.T. Shin. High-Re solutions for incompressibe flow using the Navier-Stokes equations and a multi-grid. *J. Comput. Phys.*, vol. 48 (1982), 387–411

[GR1] V. Girault and P.A. Raviart. *Finite element approximation of the Navier-Stokes equations* (Springer-Verlag, 1979).

[GR2] V. Girault and P.A. Raviart. An analysis of upwind schemes for the Navier-Stokes equations. *SIAM J. Numer. Anal.*, vol. 19 (1982), 312–333

[GR3] V. Girault and P.A. Raviart. *Finite element methods for Navier-Stokes equations* (Springer-Verlag, 1986).

[GC1] P.M. Gresho, S.T. Chan, R.L. Lee and C.D. Upson. A modified finite element method for solving the time-dependent, incompressible Navier-Stokes equations. Part 1: Theory. *Int. J. Numer. Meth. Fluids*, vol. 4 (1984), 557–598

[GC2] P.M. Gresho, S.T. Chan, R.L. Lee and C.D. Upson. A modified finite element method for solving the time-dependent, incompressible Navier-Stokes equations. Part 2: Applications. *Int. J. Numer. Meth. Fluids*, vol. 4 (1984), 619–640

[Gu] M. Gunzburger. *Finite element methods for viscous incompressible flows* (Academic Press, 1989).

[GuH] K. Gustafson and K. Halasi. Vortex dynamics of cavity flows. *J. Comput. Phys.*, vol. 64 (1986), 279–319

[HRS] L.P. Hackman, G.D. Raithby and A.B. Strong. Numerical predictions of flows over backward-facing steps. *Int. J. Numer. Meth. Fluids*, vol. 4 (1984), 711–724

[HS] P. Hansbo and A. Szepessy. A velocity-pressure streamline diffusion finite element method for the incompressible Navier-Stokes equations. *Comput. Meths. Appl. Mech. Engrg.*, vol. 84 (1990), 175–192

[HG] R. Harbord and M. Gellert. A simple least-squares method for FE analysis of the Navier-Stokes problem. *Comput. Mech.*, vol. 8 (1991), 19–24

[HR1] J.G. Heywood and R. Rannacher. Finite element approximation of the nonstationary Navier-Stokes problem. I: Regularity of solutions and second order error estimates for spatial discretization. *SIAM J. Numer. Anal.*, vol. 19 (1982), 275–311

[HR2] J.G. Heywood and R. Rannacher. Finite element approximation of the nonstationary Navier-Stokes problem. II: Stability of solutions and error estimates uniform in time. *SIAM J. Numer. Anal.*, vol. 23 (1986), 750–777

[HR3] J.G. Heywood and R. Rannacher. Finite element approximation of the nonstationary Navier-Stokes problem. III: Smoothing property and higher order estimates for spatial discretization. *SIAM J. Numer. Anal.*, vol. 25 (1988), 489–512

[HR4] J.G. Heywood and R. Rannacher. Finite element approximation of the nonstationary Navier-Stokes problem. IV: Error analysis for second-order time discretization. *SIAM J. Numer. Anal.*, vol. 27 (1990), 353–384

[Hu1] T.J.R. Hughes. Recent progress in the development and understanding of SUPG methods with special reference to the compressible Euler and Navier-Stokes equations. In: *Finite elements in Fluids*, vol. 7, R.H. Gallagher, R. Glowinski, P.M. Gresho, J.T. Oden and O.C. Zienkiewicz (eds.) (John Wiley & Sons Ltd., 1987)

[Hu2] T.J.R. Hughes. *The finite element method. Linear static and dynamic analysis* (Prentice-Hall, 1987).

[HFB] T.J.R. Hughes, L.P. Franca and M. Balestra. A new finite element formulation for computational fluid dynamics: V. Circumventing the Babuska-Brezzi condition: a stable Petrov-Galerkin formulation for the Stokes problem accommodating equal-order interpolations. *Comput. Meths. Appl. Mech. Engrg.*, vol. 59 (1986), 85–99

[Ja] Y.J. Jan. A simple program for plotting streamlines and calculating residence times. *Comm. Appl. Numer. Meth.*, vol. 4 (1988), 699–707

[Joh] C. Johnson. The Streamline Diffusion finite element method for compressible and incompressible fluid flow. Von Karman Lecture Series, IV: Computational Fluid Dynamics (March 1990)

[JS] C. Johnson and J. Saranen. Streamline Diffusion methods for the incompressible Euler and Navier-Stokes equations. *Math. Comput.*, vol. 47 (1986), 1–18

[Jos] D.D. Joseph. *Stability of fluid motions* (Springer-Verlag, 1976).

[Ki] S.W. Kim. A finite element computational method for high Reynolds number laminar flows. NASA CR-179135 (1987).

[KM] J. Kim and P. Moin. Application of a fractional-step method to incompressible Navier-Stokes equations. *J. Comput. Phys.*, vol. 59 (1985), 308–323

[LG] M.E. Laursen and M. Gellert. Some criteria for numerically integrated matrices and quadrature formulas for triangles. *Int. J. Numer. Meth. Engrg.*, vol. 12 (1978), 67–76

[La] O. Ladyzhenskaya. *The mathematical theory of viscous incompressible flow* (Gordon-Breach, 1963).

[Li] J.L. Lions. *Quelques méthodes de résolution des problèmes aux limites non lineaires* (Dunod, 1968).

[LR] M. Luskin and R. Rannacher. On the smoothing property of the Galerkin method for parabolic equations. *SIAM J. Numer. Anal.*, vol. 19 (1981), 93–113

[Pi] O. Pironneau. *Finite element methods for fluid flow* (John Wiley & Sons, 1989).

[Sa] P.A.B. de Sampaio. A Petrov-Galerkin formulation for the incompressible Navier-Stokes equations using equal order interpolations for velocity and pressure. *Int. J. Numer. Meth. Engrg.*, vol. 31 (1991), 1135–1150

[SK] R. Schreiber and H.B. Keller. Driven cavity flows by efficient numerical techniques. *J. Comput. Phys.*, vol. 49 (1983), 310–333

[Sh] J. Shen. Hopf bifurcation of the unsteady regularized driven cavity-flow. *J. Comput. Phys.*, vol. 95 (1991), 228–245

[So] J.L. Sohn. Evaluation of FIDAP on some classical laminar and turbulent benchmarks. NASA CR NAS8-35918 (1987).

[SF] G. Strang and G. Fix. *An analysis of the finite element method* (Prentice-Hall, 1973).

[TR] Ph. Le Tallec and V. Ruas. On the convergence of the bilinear-velocity constant-pressure finite element method in viscous flow. *Comput. Meths. Appl. Mech. Engrg.*, vol. 54 (1986), 235–243

[Te] R. Temam. *Navier-Stokes equations* (North-Holland, 1984).

[TGL] T.E. Tezduyar, R. Glowinski and J. Liou. Petrov-Galerkin methods on multiply connected domains for the vorticity-stream function formulation of the incompressible Navier-Stokes equations. *Int. J. Numer. Meth. Fluids*, vol. 8 (1988), 1269–1290

[TLi] T.E. Tezduyar and J. Liou. Computation of spatially periodic flows based on the vorticity-stream function formulation. *Comput. Meths. Appl. Mech. Engrg.*, vol. 83 (1990), 121–142

[TMS] T.E. Tezduyar, S. Mittal and R. Shih. Time-accurate incompressible flow computations with quadrilateral velocity-pressure elements. *Comput. Meths.*

*Appl. Mech. Engrg.*, vol. 87 (1991), 363–384

[TLu] L. Tobiska and G. Lube. A modified streamline-diffusion method for solving the stationary Navier-Stokes equations. *Numer. Math.*, vol. 59 (1991), 13–29

[Ve] R. Verfürth. Finite element approximation of incompressible Navier-Stokes equations with slip boundary conditions. *Numer. Math.*, vol. 50 (1987), 697–721

[Zi] O.C. Zienkiewicz. Explicit (or semiexplicit) general algorithm for compressible and incompressible flows with equal finite element interpolation. Department of Structural Mechanics, Chalmers University of Technology, Goteborg, Report 90:5 (1990)

[ZT] O.C. Zienkiewicz and R.L. Taylor. *The Finite Element Method.* Fourth Edition, vols. 1 and 2 (McGraw-Hill, 1989)

# *CHAPTER 3*

# THERMALLY COUPLED FLOWS AND NONLINEAR MATERIALS

## 3.1 Introduction

The numerical model developed in the previous chapters will be now applied to several problems of physical and engineering interest. In particular, this chapter will be devoted to the numerical simulation of thermally coupled flows and nonlinear materials and the following to the mould filling simulation. The technological interest of these problems will be discussed in detail in the numerical examples that will be presented.

Thermally coupled flows involve the numerical solution of the energy balance equation, together with the momentum and incompressibility equations, and a coupling algorithm between these two problems. Besides the description of the numerical solution procedure for each problem independently, a block iterative technique used to couple them will be discussed. This will be the only new ingredient of the numerical model and will be treated in some detail.

The coupling between the mechanical and the thermal behavior of a fluid may be due basically to two physical effects. First, temperature variations may lead to density gradients whose presence means that gravitational potential energy can be converted into motion through the action of bouyant forces. These density gradients may be also due to concentration differences in mixtures of one or more components, like salt water. Both effects are coupled in some practical physical situations (see [He] and references therein). Here, only density variations due to temperature will be considered. When the fluid is assumed to have a uniform density except for the body force term, one is led to the so called Boussinesq approximation (see, e.g., [LL]), a model of wide applicability in practical problems. The Boussinesq problem will be the subject of Section 3.2.

Thermally coupled flows may also arise because of the variation of some physical properties of the fluid with temperature [IOS], [ZMS], such as the viscosity, the diffusion or the specific heat. The temperature in turn changes with the velocity field due to convection and the dissipation of mechanical work into heat (Joule effect). Usually, this source term in the energy equation is negligible, although it has to be taken into account when highly viscous flows are considered. In particular, this term is fundamental when the flow of viscoplastic materials is studied.

Section 3.3 is concerned with the numerical simulation of generalized Newtonian fluids. This is a particular case of non-Newtonian behavior in which the constitutive law takes the same expression as for Newtonian materials although the viscosity is allowed to depend on the invariants of the strain rate tensor. The flow of many fluids can be accurately represented by some well known constitutive laws (power-law, Carreau model, etc.) derived from experimental results (see [Ta] for a comprehensive description of this type of fluids). Another important family of constitutive laws of this kind is the one represented by viscoplastic materials when the elastic effects are neglected (flow approach). This rheological behavior is widely used in metal forming processes (see, e.g., papers in [CO], [TWZ]).

The general problem, including material nonlinearity and thermal coupling, is considered in Section 3.4. The basic algorithm of Box 2.3 is completed with the numerical solution of the energy balance equation and the block iterative algorithm.

Some results concerning the analysis of the problems to be considered here will be referred to during the exposition. These analyses are restricted to some simplified problems, but they help to get insight into the numerical problems that may be encountered when dealing with more complicated situations.

The last part of this chapter contains the numerical results obtained for three different model problems, representative of the type of applications that may be treated with the numerical tools described here. The first problem is the simulation of the thermoconvective instability of plane Poiseuille flow heated from below, using the Boussinesq approximation. This model is also used to solve the natural convection of low-Prandtl-number fluids, such as liquid metals. A periodic oscillating flow pattern is encountered when the Grashof number exceeds a critical value. The last example is the 4:1 plane extrusion of a power-law fluid with an exponential-type thermal dependence. Numerical results will help to understand the physics of this problem. Although the simulation of all these flow problems has an inherent interest, emphasis will be placed on the numerical behavior of the finite element model proposed here, trying to demonstrate its potential applications.

## 3.2 The Boussinesq model

### 3.2.1 The continuous problem

The Boussinesq approximation is based on several thermodynamical assumptions and an analysis of the relative importance of the thermal effects (see, e.g., [Jo], [LL]). The main hypothesis, based on thermodynamical grounds, is that the density satisfies the following equation of state:

$$\rho = \rho_0[1 - \beta(\vartheta - \vartheta_0)] \tag{3.1}$$

Here and below, the temperature will be denoted by $\vartheta$ (not to be confused with the parameter $\theta$ of the genealized trapezoidal rule). The parameter $\beta$ in Eqn. (3.1) is the volume expansion coefficient and subscript naught refers to a reference state.

Once (3.1) is assumed, a dimensional analysis reveals that the density may be taken as constant and equal to $\rho_0$ for all the terms of the Navier-Stokes and temperature equations except for the body force term of the former. Neglecting the rate of dissipation of mechanical energy in the temperature equation and assuming the physical properties to be constant, the system of partial differential equations we are led to is the following:

$$\rho_0[\partial_t \mathbf{u} + (\mathbf{u}\cdot\nabla)\mathbf{u}] - 2\mu\nabla\cdot\boldsymbol{\varepsilon}(\mathbf{u}) + \nabla p = \rho_0\mathbf{g}[1-\beta(\vartheta-\vartheta_0)] \tag{3.2}$$

$$\nabla\cdot\mathbf{u} = 0 \tag{3.3}$$

$$\rho_0 c_p[\partial_t\vartheta + (\mathbf{u}\cdot\nabla)\vartheta] - k\Delta\vartheta = 0 \tag{3.4}$$

to be solved in an open bounded domain $\Omega$ of $\mathbb{R}^{N_{sd}}$ with some certain initial and boundary conditions. In (3.2)–(3.4), $\mathbf{g}$ is the gravitational acceleration, $c_p$ is the specific heat at constant pressure and $k$ is the thermal conduction coefficient. The rest of the notation has been introduced in the previous chapters. For simplicity, source terms in (3.4) have been omitted, as well as body forces in the Navier-Stokes equations other than gravitational.

Assume now that there is a length scale $L$ and a temperature scale $\delta\vartheta$ inherent to the problem. For example, $L$ may be taken as the diameter of $\Omega$ and $\delta\vartheta$ as the temperature difference between two walls of $\partial\Omega$. Given a velocity scale $U$, the following dimensionless numbers are defined:

| | |
|---|---|
| $Re := \dfrac{\rho_0 L U}{\mu},$ | Reynolds number |
| $Pe := \dfrac{\rho_0 c_p L U}{k},$ | Péclet number |
| $Gr := \dfrac{\beta\lvert\mathbf{g}\rvert\rho_0^2 L^3\delta\vartheta}{\mu^2}$ | Grashof number |
| $Pr := \dfrac{c_p\mu}{k}$ | Prandtl number |
| $Ra := \dfrac{\beta\lvert\mathbf{g}\rvert c_p\rho_0^2 L^3\delta\vartheta}{\mu k}$ | Rayleigh number |
| $Fr := \dfrac{U^2}{\rho_0\lvert\mathbf{g}\rvert\delta\vartheta L}$ | Froude number |

These numbers are related by

$$Ra = Gr\ Pr, \qquad Fr = Re^2\ Gr^{-1}, \qquad Re = Pe\ Pr^{-1} \tag{3.5}$$

If the thermal diffusivity $\kappa := k/c_p\rho_0$ and the kinematic viscosity $\nu := \mu/\rho_0$ are introduced, $Pr$ may be written as $Pr = \nu/\kappa$. Therefore, the Prandtl number is a measure for the similarity of the transport of heat and momentum. The Grashof number is a measure of the relative importance of the bouyancy forces to the viscous forces.

For the definition of the velocity scale $U$, two cases will be distinguished. First, if the velocity $\mathbf{u}$ is prescribed to a nonzero value on a part of $\partial\Omega$, a characteristic value of the boundary condition may be chosen as $U$ (e.g., the average or maximum prescribed values). This is the so called *forced convection* problem. If time is nondimensionalized using $L/U$ as time scale, equations (3.2)–(3.4) may be written in dimensionless form as follows:

$$\begin{aligned} \partial_t\mathbf{u} + (\mathbf{u}\cdot\nabla)\mathbf{u} - 2\frac{1}{Re}\nabla\cdot\boldsymbol{\varepsilon}(\mathbf{u}) + \nabla p &= -\frac{1}{Fr}\vartheta\hat{\mathbf{g}} \\ \nabla\cdot\mathbf{u} &= 0 \\ \partial_t\vartheta + (\mathbf{u}\cdot\nabla)\vartheta - \frac{1}{Pe}\Delta\vartheta &= 0 \end{aligned} \tag{3.6}$$

Here, body force terms of the form $C\mathbf{g}$, with $C$ a constant, have been introduced in $\nabla p$ and the resulting pressure nondimensionalized by $\rho_0 U^2$. The vector $\hat{\mathbf{g}}$ in the momentum equation denotes the normalized gravity acceleration vector. No distinction has been made between dimensional and dimensionless variables.

The second case of interest is found when $\mathbf{u}$ is prescribed to zero on $\partial\Omega$, part of which may be left free. In this case, there are two possibilities for choosing the velocity scale $U$. If we take $U = \mu/L\rho_0$, then $Re = 1$. On the other hand, if $U = \kappa/L$ is chosen, then $Pe = 1$ automatically. Using this last choice, the dimensionless form of equations (3.2)–(3.4) may be written as

$$\begin{aligned} \partial_t \mathbf{u} + (\mathbf{u}\cdot\nabla)\mathbf{u} - 2Pr\ \nabla\cdot\boldsymbol{\varepsilon}(\mathbf{u}) + \nabla p &= -Pr\ Ra\ \vartheta\hat{\mathbf{g}} \\ \nabla\cdot\mathbf{u} &= 0 \\ \partial_t\vartheta + (\mathbf{u}\cdot\nabla)\vartheta - \Delta\vartheta &= 0 \end{aligned} \tag{3.7}$$

This case is known as *natural convection*.

Both for the forced convection and the natural convection cases, a stationary (or motionless) solution may exist, whenever it does exist for the uncoupled Navier-Stokes equations. If the temperature field is such that $\nabla\vartheta$ is parallel to $\hat{\mathbf{g}}$ and normal to $\mathbf{u}$, the velocity and pressure solutions are independent of the temperature. Otherwise, motion is induced by the bouyancy forces. However, the stability of the stationary solution can only be ensured for low values of the Reynolds and Rayleigh numbers [Jo]. As they are increased, bifurcation phenomena occur and stable solutions are no more stationary.

Let $\Gamma$ be the boundary of the domain $\Omega$, split into two sets of disjoint components $\Gamma = \overline{\Gamma_{du} \cup \Gamma_{nu}}$ and $\Gamma = \overline{\Gamma_{dt} \cup \Gamma_{nt}}$. The type of boundary conditions that will be considered is the same as in the previous chapter for the Navier-Stokes equations, that is, (2.3) and (2.4). For the convection-diffusion equation, both Dirichlet and Neumann type boundary conditions will be taken into account. Let $\mathbf{n}$ be the unit vector normal to $\Gamma$, $\bar{\mathbf{u}}$ the velocity prescribed on $\Gamma_{du}$, $\bar{\mathbf{t}}$ the prescribed traction on $\Gamma_{nu}$, $\bar{\vartheta}$ the given temperature on $\Gamma_{dt}$ and $\bar{\varphi}$ the prescribed heat flux on $\Gamma_{nt}$. The boundary conditions to be considered are

$$\begin{aligned} \mathbf{u} &= \bar{\mathbf{u}} &\quad& \text{on } \Gamma_{du} \\ \mathbf{n}\cdot\boldsymbol{\sigma} &= \bar{\mathbf{t}} && \text{on } \Gamma_{nu} \\ \vartheta &= \bar{\vartheta} && \text{on } \Gamma_{dt} \\ -k\mathbf{n}\cdot\nabla\vartheta &= \bar{\varphi} && \text{on } \Gamma_{nt} \end{aligned} \tag{3.8}$$

where the expression of the stress tensor $\boldsymbol{\sigma}$ is given by (2.6).

The notation used heretofore to indicate the spaces of test functions and of trial solutions will be slightly modified. Subscripts $u$, $p$ and $t$ will be used to refer to velocity, pressure and temperature, respectively.

If $(0,T)$ denotes the time interval where the problem is to be solved and $\mathbf{u}(\mathbf{x},0) = \mathbf{u}_0(\mathbf{x})$, $\vartheta(\mathbf{x},0) = \vartheta_0(\mathbf{x})$ are the initial conditions ($\mathbf{x} \in \Omega$), the spaces of trial solutions that will be needed are

$$\begin{aligned} V_u &= \{\mathbf{v} \in L^2(0,T;H^1(\Omega)^{N_{sd}}) \mid \mathbf{v}|_{\Gamma_{du}} = \bar{\mathbf{u}},\ \ t \in (0,T)\} \\ V_p &= \{q \in L^2(0,T;L^2(\Omega)) \mid \int_\Omega q\,d\Omega = 0,\ \ t \in (0,T),\ \text{ if } \Gamma_{nu} = \emptyset\} \\ V_t &= \{\eta \in L^2(0,T;H^1(\Omega)) \mid \eta|_{\Gamma_{dt}} = \bar{\vartheta},\ \ t \in (0,T)\} \end{aligned} \tag{3.9}$$

The corresponding spaces of test functions are

$$\begin{aligned} W_u &= \{\mathbf{v} \in H^1(\Omega)^{N_{sd}} \mid \mathbf{v}|_{\Gamma_{du}} = 0\} \\ W_p &= L^2(\Omega) \\ W_t &= \{\eta \in H^1(\Omega) \mid \eta|_{\Gamma_{dt}} = 0\} \end{aligned} \tag{3.10}$$

The reason for choosing these spaces has already been explained in Chapter 2.

In order to write the weak form of problem (3.6) with the dimensionless form of the boundary conditions (3.8), let us introduce the multilinear forms

$$\begin{aligned} a(\mathbf{u},\mathbf{v}) &= \frac{2}{Re}\int_\Omega \boldsymbol{\varepsilon}(\mathbf{u}) : \boldsymbol{\varepsilon}(\mathbf{v}) d\Omega, \\ b(q,\mathbf{v}) &= \int_\Omega q\nabla\cdot\mathbf{v} d\Omega, \\ c(\mathbf{u},\mathbf{v},\mathbf{w}) &= \int_\Omega [(\mathbf{u}\cdot\nabla)\mathbf{v}]\cdot\mathbf{w} d\Omega + \frac{1}{2}\int_\Omega (\nabla\cdot\mathbf{u})\mathbf{v}\cdot\mathbf{w} d\Omega, \\ d(\eta,\mathbf{v}) &= \frac{1}{Fr}\int_\Omega \eta\bar{\mathbf{g}}\cdot\mathbf{v} d\Omega, \\ e(\vartheta,\eta) &= \frac{1}{Pe}\int_\Omega \nabla\vartheta\cdot\nabla\eta d\Omega, \\ f(\mathbf{u},\vartheta,\eta) &= \int_\Omega \eta\mathbf{u}\cdot\nabla\vartheta d\Omega, \\ l_u(\mathbf{v}) &= \int_{\Gamma_{nu}} \bar{\mathbf{t}}\cdot\mathbf{v} d\Gamma, \\ l_t(\eta) &= \int_{\Gamma_{nt}} \bar{\varphi}\eta d\Gamma, \end{aligned} \tag{3.11}$$

where $\mathbf{u}$, $\mathbf{v}$, $\mathbf{w} \in V_u$ or $W_u$, $q \in V_p$ or $W_p$ and $\vartheta$, $\eta \in V_t$ or $W_t$. The weak formulation of the problem is now given as follows: Find $\mathbf{u} \in V_u$, $p \in V_p$ and $\vartheta \in V_t$ such that

$$(\partial_t\mathbf{u},\mathbf{v}) + c(\mathbf{u},\mathbf{u},\mathbf{v}) + a(\mathbf{u},\mathbf{v}) - b(p,\mathbf{v}) + d(\vartheta,\mathbf{v}) = l_u(\mathbf{v}) \tag{3.12}$$

$$b(q,\mathbf{u}) = 0 \tag{3.13}$$

$$(\partial_t\vartheta,\eta) + f(\mathbf{u},\vartheta,\eta) + e(\vartheta,\eta) = l_t(\eta) \tag{3.14}$$

$$(\mathbf{u}(\mathbf{x},0),\mathbf{v}) = (\mathbf{u}_0(\mathbf{x}),\mathbf{v}) \tag{3.15}$$

$$(\vartheta(\mathbf{x},0),\eta) = (\vartheta_0(\mathbf{x}),\eta) \tag{3.16}$$

for all $\mathbf{v} \in W_u$, $q \in W_p$ and $\eta \in W_t$ and for $t \in (0,T)$.

Some partial results concerning the existence, uniqueness and regularity of solutions for problem (3.12)–(3.16) are known. For the stationary problem and natural convection, uniqueness of solution can only be proved for sufficiently small values of the Rayleigh number [Li], [Cu] (the changes to be introduced in the dimensionless parameters of (3.11) to consider the natural convection problem (3.7) are obvious).

### 3.2.2 Discretization in space and time

The numerical solution of problem (3.12)–(3.16) will be carried out using the same techniques as in Chapter 2 for the transient Navier-Stokes equations. The space discretization will be performed using div-stable velocity-pressure finite element interpolations and the Streamline Diffusion (SD) method to stabilize high-Reynolds-number flows. The finite element space for the temperature will consist of piecewise polynomials of the same degree and with respect to the same finite element partition $\{\Omega^e\}$ as for the velocity components. In doing so, the same convergence rate for the temperature as for the velocity can be expected, at least for the Galerkin approach (cf. [Gu]). The SD method will also be used for the energy equation.

Once space has been discretized, the resulting initial-value problem will be solved using the generalized trapezoidal rule.

As usual, subscript $h$ will be used to denote the discrete finite element spaces and the functions belonging to them.

Using the same notation and arguments that led us to problem (2.40), the fully discrete version of problem (3.12)–(3.16) that will be used reads as follows:

*For $n = 1, 2, ..., N$, given $\mathbf{u}_h^{n-1}(\mathbf{x})$, $p_h^{n-1}(\mathbf{x})$ and $\vartheta_h^{n-1}(\mathbf{x})$, find $\mathbf{u}_h^n(\mathbf{x})$, $p_h^n(\mathbf{x})$ and $\vartheta_h^n(\mathbf{x})$ such that*

$$\begin{aligned}\frac{1}{\Delta t}(\mathbf{u}_h^n - \mathbf{u}_h^{n-1}, \mathbf{v}_h) + \theta c(\mathbf{u}_h^n, \mathbf{u}_h^n, \mathbf{v}_h) + (1-\theta)c(\mathbf{u}_h^{n-1}, \mathbf{u}_h^{n-1}, \mathbf{v}_h)&\\ + \theta a(\mathbf{u}_h^n, \mathbf{v}_h) + (1-\theta)a(\mathbf{u}_h^{n-1}, \mathbf{v}_h)&\\ - \theta b(p_h^n, \mathbf{v}_h) - (1-\theta)b(p_h^{n-1}, \mathbf{v}_h)&\\ + \theta d(\vartheta_h^n, \mathbf{v}_h) + (1-\theta)d(\vartheta_h^{n-1}, \mathbf{v}_h)&\\ + \sum_{e=1}^{N_{el}} \mathcal{S}_{\mathbf{u}}^{n,e}(\mathbf{u}_h, p_h, \vartheta_h; \mathbf{v}_h)&\\ = \theta l_{\mathbf{u}}^n(\mathbf{v}_h) + (1-\theta)l_{\mathbf{u}}^{n-1}(\mathbf{v}_h)&\end{aligned} \tag{3.17}$$

$$b(q_h, \mathbf{u}_h^n) = 0 \tag{3.18}$$

$$\begin{aligned}\frac{1}{\Delta t}(\vartheta_h^n - \vartheta_h^{n-1}, \eta_h) + \theta f(\mathbf{u}_h^n, \vartheta_h^n, \eta_h) + (1-\theta)f(\mathbf{u}_h^{n-1}, \vartheta_h^{n-1}, \eta_h)&\\ + \theta e(\vartheta_h^n, \eta_h) + (1-\theta)e(\vartheta_h^{n-1}, \eta_h)&\\ + \sum_{e=1}^{N_{el}} \mathcal{S}_t^{n,e}(\mathbf{u}_h, \vartheta_h; \eta_h)&\\ = \theta l_t^n(\eta_h) + (1-\theta)l_t^{n-1}(\eta_h)&\end{aligned} \tag{3.19}$$

*for all $\mathbf{v}_h \in W_{u,h}$, $q_h \in W_{p,h}$ and $\eta_h \in W_{t,h}$.*

The Streamline Diffusion term $\mathcal{S}_{\mathbf{u}}^{n,e}(\mathbf{u}_h, p_h, \vartheta_h; \mathbf{v}_h)$ for the momentum equations is defined as

$$\begin{aligned}\mathcal{S}_{\mathbf{u}}^{n,e}(\mathbf{u}_h, p_h, \vartheta_h; \mathbf{v}_h) := \int_{\Omega^e} \zeta_u(\mathbf{u}_h^n, \mathbf{v}_h) \cdot [&\mathcal{N}_\theta^n(\mathbf{u}_h, p_h)\\ &+ \frac{1}{Fr}\hat{\mathbf{g}}\ \left(\theta\vartheta_h^n + (1-\theta)\vartheta_h^{n-1}\right)]\, d\Omega\end{aligned} \tag{3.20}$$

where

$$\begin{aligned}\mathcal{N}_\theta^n(\mathbf{u}_h, p_h) :&= \frac{1}{\Delta t}(\mathbf{u}_h^n - \mathbf{u}_h^{n-1}) + \rho\theta(\mathbf{u}_h^n \cdot \nabla)\mathbf{u}_h^n + \rho(1-\theta)(\mathbf{u}_h^{n-1} \cdot \nabla)\mathbf{u}_h^{n-1}\\ &- \frac{1}{Re}\theta\Delta\mathbf{u}_h^n - \frac{1}{Re}(1-\theta)\Delta\mathbf{u}_h^{n-1} + \theta\nabla p_h^n + (1-\theta)\nabla p_h^{n-1}\end{aligned} \tag{3.21}$$

$$\zeta_{\mathbf{u}}(\mathbf{u}_h, \mathbf{v}_h) := \tau_{\mathbf{u}}^e(\mathbf{u}_h \cdot \nabla)\mathbf{v}_h \tag{3.22}$$

The intrinsic time $\tau_{\mathbf{u}}^e$ is computed as in Chapter 2 (Eqn. (2.43)) using the cell Reynolds number, now given by $(Re)^e = |\mathbf{u}^e| h^e Re/2$ (recall that $\mathbf{u}^e$ and $h^e$ are assumed to be dimensionless).

For the energy equation, the SD term is

$$S_t^{n,e}(\mathbf{u}_h, \vartheta_h; \eta_h) := \int_{\Omega^e} \zeta_t(\mathbf{u}_h^n, \eta_h)\mathcal{E}_\theta^n(\mathbf{u}_h, \vartheta_h)d\Omega \tag{3.23}$$

where

$$\begin{aligned}\mathcal{E}_\theta^n(\mathbf{u}_h, \vartheta_h) :&= \frac{1}{\Delta t}(\vartheta_h^n - \vartheta_h^{n-1}) + \theta(\mathbf{u}_h^n \cdot \nabla)\vartheta_h^n + (1-\theta)(\mathbf{u}_h^{n-1} \cdot \nabla)\vartheta_h^{n-1} \\ &- \frac{1}{Pe}\theta\Delta\vartheta_h^n - \frac{1}{Pe}(1-\theta)\Delta\vartheta_h^{n-1}\end{aligned} \tag{3.24}$$

$$\zeta_t(\mathbf{u}_h, \eta_h) := \tau_t^e(\mathbf{u}_h \cdot \nabla)\eta_h \tag{3.25}$$

and the intrinsic time $\tau_t^e$ is computed as explained in Reference [Co] for the convection-diffusion equation using the cell Péclet number $\gamma := |\mathbf{u}^e| h^e Pe/2$.

**Remarks 3.1**

(1) The observations pointed out in Remarks 2.1 and 2.2 also apply to the problem now considered.

(2) In Reference [He], it is concluded that the consistent Streamline Diffusion method does not work for a problem very similar to the present one using the $Q_1/P_0$ element. The misbehavior found was overcome dropping the bouyancy forces in (3.20) and the discretized version of the velocity time derivative in (3.21) (the viscous and pressure terms vanish for the $Q_1/P_0$ element). As explained in Reference [Co] this is equivalent to introduce an artificial diffusion along the streamlines. We have not encountered these problems. The answer we give is that the $Q_1/P_0$ element is not div-stable. Pressure gradients in (3.21) do have an important role and for the $Q_1/P_0$ element they do not approximate the gradients of the continuous pressure field.

(3) An analysis of the Galerkin finite element solution of the natural convection problem can be found in Reference [BL], where a slightly different formulation of the physical problem is considered. The fluid-filled domain is linked through an interface with heat conduction in the solid enclosing the fluid. Optimal rates of convergence are proved when the velocity-pressure interpolation consists of nonconforming $P_1/P_0$ elements and $V_{t,h}$ is built up using $P_1$ elements with respect to the same triangulation as for the velocity. □

Before going any further, let us introduce the matrix version of problem (3.17)–(3.19). The matrices defined in Box 2.2 for the Navier-Stokes equations will also be used now (taking $\rho = 1$, $\mu = 1/Re$, $l = l_u$, $\mathbf{f} = 0$ and replacing the vector $\mathbf{s}$ by $\mathbf{s}_u := \tau_u^e \mathbf{u}^e$, $\mathbf{u}^e$ being the characteristic velocity for element $e$). The new matrices that will be needed to account for the thermal coupling are defined in Box 3.1, where $\mathbf{s}_t := \tau_t^e \mathbf{u}^e$, $\mathbf{\Theta}$ denotes the vector of nodal values of a generic function in $V_t$ and $\tilde{\mathbf{\Theta}}$ the vector of nodal values of an element in $W_t$. The vector of nodal values of an element in the velocity test function space $W_{\mathbf{u}}$ has been represented by $\mathbf{V}$. The $L^2$ inner product in the temperature space has been indicated by $(\cdot,\cdot)_t$. In order to avoid the introduction of more subscripts in the matrices, the convection and diffusion matrices for the temperature have been denoted by $\mathbf{H}$, instead of the traditional notation $\mathbf{K}$, already used for the matrices of the Navier-Stokes equations.

**Box 3.1 Matrix form of the discrete equations**

| Matrix version | Terms from where it comes |
|---|---|
| $\mathbf{V}^T \cdot \mathbf{C}_{s_u} \cdot \boldsymbol{\Theta}$ | $d(\vartheta_h, \mathbf{v}_h) + \sum_{e=1}^{N_{el}} \int_{\Omega^e} [(\mathbf{s}_u \cdot \nabla)\mathbf{v}_h] \cdot \hat{\mathbf{g}} \frac{1}{Fr} \vartheta_h d\Omega$ |
| $\bar{\boldsymbol{\Theta}}^T \cdot \mathbf{M}_{t,s_t} \cdot \boldsymbol{\Theta}$ | $(\vartheta_h, \eta_h)_t + \sum_{e=1}^{N_{el}} \int_{\Omega^e} [(\mathbf{s}_t \cdot \nabla)\eta_h] \vartheta_h d\Omega$ |
| $\bar{\boldsymbol{\Theta}}^T \cdot \mathbf{H}_{c,s_t}(\mathbf{U}) \cdot \boldsymbol{\Theta}$ | $f(\mathbf{u}_h, \vartheta_h, \eta_h) + \sum_{e=1}^{N_{el}} \int_{\Omega^e} [(\mathbf{s}_t \cdot \nabla)\eta_h] (\mathbf{u}_h \cdot \nabla)\vartheta_h d\Omega$ |
| $\bar{\boldsymbol{\Theta}}^T \cdot \mathbf{H}_{d,s_t} \cdot \boldsymbol{\Theta}$ | $e(\vartheta_h, \eta_h) + \sum_{e=1}^{N_{el}} \int_{\Omega^e} [(\mathbf{s}_t \cdot \nabla)\eta_h] \left( -\frac{1}{Pe} \Delta \vartheta_h \right) d\Omega$ |
| $\bar{\boldsymbol{\Theta}}^T \cdot \mathbf{F}_t$ | $l_t(\eta_h)$ |

Having introduced these matrices and vectors, problem (3.17)–(3.19) may be written as follows:

*For $n = 1, 2, ..., N$, given $\mathbf{U}^{n-1}$, $\mathbf{P}^{n-1}$ and $\boldsymbol{\Theta}^{n-1}$, find $\mathbf{U}^n$, $\mathbf{P}^n$ and $\boldsymbol{\Theta}^n$, approximations to $\mathbf{U}(t^n)$, $\mathbf{P}(t^n)$ and $\boldsymbol{\Theta}(t^n)$, such that*

$$\begin{aligned}
\mathbf{M}_{v,s_u^n} \cdot \mathbf{U}^n &+ \theta \Delta t \mathbf{K}_{c,s_u^n}(\mathbf{U}^n) \cdot \mathbf{U}^n + \theta \Delta t \mathbf{K}_{d,s_u^n} \cdot \mathbf{U}^n \\
&- \theta \Delta t \mathbf{G}_{s_u^n} \cdot \mathbf{P}^n + \theta \Delta t \mathbf{C}_{s_u^n} \cdot \boldsymbol{\Theta}^n \\
&= \theta \Delta t \mathbf{F}^n_{v,s_u^n} + (1-\theta)\Delta t \mathbf{F}^{n-1}_{v,s_u^n} + \mathbf{M}_{v,s_u^n} \cdot \mathbf{U}^{n-1} \\
&- (1-\theta)\Delta t \mathbf{K}_{c,s_u^n}(\mathbf{U}^{n-1}) \cdot \mathbf{U}^{n-1} - (1-\theta)\Delta t \mathbf{K}_{d,s_u^n} \cdot \mathbf{U}^{n-1} \\
&+ (1-\theta)\Delta t \mathbf{G}_{s_u^n} \cdot \mathbf{P}^{n-1} - (1-\theta)\Delta t \mathbf{C}_{s_u^n} \cdot \boldsymbol{\Theta}^{n-1}
\end{aligned} \tag{3.26}$$

$$\mathbf{G}_0^T \cdot \mathbf{U}^n = \mathbf{0} \tag{3.27}$$

$$\begin{aligned}
\mathbf{M}_{t,s_t^n} \cdot \boldsymbol{\Theta}^n &+ \theta \Delta t \mathbf{H}_{c,s_t^n}(\mathbf{U}^n) \cdot \boldsymbol{\Theta}^n + \theta \Delta t \mathbf{H}_{d,s_t^n} \cdot \boldsymbol{\Theta}^n \\
&= \theta \Delta t \mathbf{F}_t^n + (1-\theta)\Delta t \mathbf{F}_t^{n-1} + \mathbf{M}_{t,s_t^n} \cdot \boldsymbol{\Theta}^{n-1} \\
&- (1-\theta)\Delta t \mathbf{H}_{c,s_t^n}(\mathbf{U}^{n-1}) \cdot \boldsymbol{\Theta}^{n-1} - (1-\theta)\Delta t \mathbf{H}_{d,s_t^n} \cdot \boldsymbol{\Theta}^{n-1}
\end{aligned} \tag{3.28}$$

### 3.2.3 Block iterative algorithm

Now we will consider an iterative solution procedure for problem (3.26)–(3.28). In particular, the block iterative technique used to uncouple the calculation of the temperature and the velocity and pressure will be discussed in detail.

Equations (3.26)–(3.28) may be written together in a unified matrix expression. Let us denote by $\mathbf{R}_u$ and $\mathbf{R}_t$ the right-hand-side terms in Eqns. (3.26) and (3.28), respectively, and define the following matrices:

$$\begin{aligned}
\mathbf{A}_{11}(\mathbf{U}^n) &:= \mathbf{M}_{v,s_u^n} + \theta\Delta t\mathbf{K}_{c,s_u^n}(\mathbf{U}^n) + \theta\Delta t\mathbf{K}_{d,s_u^n} \\
\mathbf{A}_{12} &:= -\theta\Delta t\mathbf{G}_{s_u^n} \\
\mathbf{A}_{13} &:= \theta\Delta t\mathbf{C}_{s_u^n} \\
\mathbf{A}_{21} &:= \mathbf{G}_0^T \\
\mathbf{A}_{33}(\mathbf{U}^n) &:= \mathbf{M}_{t,s_t^n} + \theta\Delta t\mathbf{H}_{c,s_t^n}(\mathbf{U}^n) + \theta\Delta t\mathbf{H}_{d,s_t^n}
\end{aligned} \tag{3.29}$$

Having introduced this notation, Eqns. (3.26)–(3.28) are rewritten as:

$$\begin{pmatrix} \mathbf{A}_{11}(\mathbf{U}^n) & \mathbf{A}_{12} & \mathbf{A}_{13} \\ \mathbf{A}_{21} & \mathbf{0} & \mathbf{0} \\ \mathbf{0} & \mathbf{0} & \mathbf{A}_{33}(\mathbf{U}^n) \end{pmatrix} \begin{pmatrix} \mathbf{U}^n \\ \mathbf{P}^n \\ \mathbf{\Theta}^n \end{pmatrix} = \begin{pmatrix} \mathbf{R}_u \\ \mathbf{0} \\ \mathbf{R}_t \end{pmatrix} \tag{3.30}$$

In fact, $\mathbf{A}_{12}$ and $\mathbf{A}_{13}$ also depend on $\mathbf{U}^n$ through the SD term, although such dependence has not been explicitly indicated. Assume for a moment that the Galerkin formulation is used and therefore $\mathbf{A}_{12}$ and $\mathbf{A}_{13}$ are constant. Suppose that the convective terms in the Navier-Stokes and the energy equations are linearized as follows:

$$\begin{aligned}
c(\mathbf{u}_h^{n,i}, \mathbf{u}_h^{n,i}, \mathbf{v}_h) &\approx c(\mathbf{u}_h^{n,i-1}, \mathbf{u}_h^{n,i}, \mathbf{v}_h) + \beta_u c(\mathbf{u}_h^{n,i}, \mathbf{u}_h^{n,i-1}, \mathbf{v}_h) - \beta_u c(\mathbf{u}_h^{n,i-1}, \mathbf{u}_h^{n,i-1}, \mathbf{v}_h) \\
f(\mathbf{u}_h^{n,i}, \vartheta_h^{n,i}, \eta_h) &\approx f(\mathbf{u}_h^{n,i-1}, \vartheta_h^{n,i}, \eta_h) + \beta_t f(\mathbf{u}_h^{n,i}, \vartheta_h^{n,i-1}, \eta_h) - \beta_t f(\mathbf{u}_h^{n,i-1}, \vartheta_h^{n,i-1}, \eta_h)
\end{aligned} \tag{3.31}$$

where superscript $i$ denotes the iteration counter. For $\beta_u = \beta_t = 1$, (3.31) is the Newton-Raphson linearization and for $\beta_u = \beta_t = 0$ the Picard scheme. The resulting matrix version of the linearized equations will have the following aspect:

$$\begin{pmatrix} \mathbf{A}_{11}(\mathbf{U}^{n,i-1}) + \beta_u \mathbf{A}_{11}^*(\mathbf{U}^{n,i-1}) & \mathbf{A}_{12} & \mathbf{A}_{13} \\ \mathbf{A}_{21} & \mathbf{0} & \mathbf{0} \\ \beta_t \mathbf{A}_{31}^*(\mathbf{\Theta}^{n,i-1}) & \mathbf{0} & \mathbf{A}_{33}(\mathbf{U}^{n,i-1}) \end{pmatrix} \begin{pmatrix} \mathbf{U}^{n,i} \\ \mathbf{P}^{n,i} \\ \mathbf{\Theta}^{n,i} \end{pmatrix} = \begin{pmatrix} \mathbf{R}_u^* \\ \mathbf{0} \\ \mathbf{R}_t^* \end{pmatrix} \tag{3.32}$$

where

$$\begin{aligned}
\mathbf{R}_u^* &:= \mathbf{R}_u + \beta_u \mathbf{A}_{11}^*(\mathbf{U}^{n,i-1}) \cdot \mathbf{U}^{n,i-1} \\
\mathbf{R}_t^* &:= \mathbf{R}_t + \beta_t \mathbf{A}_{31}^*(\mathbf{\Theta}^{n,i-1}) \cdot \mathbf{U}^{n,i-1}
\end{aligned} \tag{3.33}$$

and $\mathbf{A}_{11}^*$, $\mathbf{A}_{31}^*$ are the matrices coming respectively from the terms $c(\mathbf{u}_h^{n,i}, \mathbf{u}_h^{n,i-1}, \mathbf{v}_h)$ and $f(\mathbf{u}_h^{n,i}, \vartheta_h^{n,i-1}, \eta_h)$. Let us define now

$$\begin{aligned}
&\mathbf{B}_{11} := \begin{pmatrix} \mathbf{A}_{11}(\mathbf{U}^{n,i-1}) + \beta_u \mathbf{A}_{11}^*(\mathbf{U}^{n,i-1}) & \mathbf{A}_{12} \\ \mathbf{A}_{21} & \mathbf{0} \end{pmatrix} \\
&\mathbf{B}_{12} := \begin{pmatrix} \mathbf{A}_{13} \\ \mathbf{0} \end{pmatrix}, \qquad \mathbf{B}_{21} := \begin{pmatrix} \beta_t \mathbf{A}_{31}^*(\mathbf{\Theta}^{n,i-1}) & \mathbf{0} \end{pmatrix} \\
&\mathbf{B}_{22} := \mathbf{A}_{33}(\mathbf{U}^{n,i-1}) \\
&\mathbf{X} := \begin{pmatrix} \mathbf{U}^{n,i} \\ \mathbf{P}^{n,i} \end{pmatrix}, \qquad \mathbf{F}_x := \begin{pmatrix} \mathbf{R}_u^* \\ \mathbf{0} \end{pmatrix} \\
&\mathbf{Y} := \mathbf{\Theta}^{n,i}, \qquad \mathbf{F}_y := \mathbf{R}_t^*
\end{aligned} \tag{3.34}$$

The linear system (3.32) may be written as

$$\begin{pmatrix} \mathbf{B}_{11} & \mathbf{B}_{12} \\ \mathbf{B}_{21} & \mathbf{B}_{22} \end{pmatrix} \begin{pmatrix} \mathbf{X} \\ \mathbf{Y} \end{pmatrix} = \begin{pmatrix} \mathbf{F}_x \\ \mathbf{F}_y \end{pmatrix} \tag{3.35}$$

A block iterative algorithm may be employed to solve (3.35). The main advantatge of this method is that smaller linear systems will have to be solved, although iterations will be required. For the particular case of (3.35), two options are equally easy to implement [SB]:

- *Block Jacobi method (or block total-step method):*

$$\begin{aligned} \mathbf{B}_{11}\mathbf{X}^j &= \mathbf{F}_x - \mathbf{B}_{12}\mathbf{Y}^{j-1} \\ \mathbf{B}_{22}\mathbf{Y}^j &= \mathbf{F}_y - \mathbf{B}_{21}\mathbf{X}^{j-1} \end{aligned} \tag{3.36}$$

- *Block Gauss-Seidel method (or block single-step method):*

$$\begin{aligned} \mathbf{B}_{11}\mathbf{X}^j &= \mathbf{F}_x - \mathbf{B}_{12}\mathbf{Y}^{j-1} \\ \mathbf{B}_{22}\mathbf{Y}^j &= \mathbf{F}_y - \mathbf{B}_{21}\mathbf{X}^{j} \end{aligned} \tag{3.37}$$

or

$$\begin{aligned} \mathbf{B}_{22}\mathbf{Y}^j &= \mathbf{F}_y - \mathbf{B}_{21}\mathbf{X}^{j-1} \\ \mathbf{B}_{11}\mathbf{X}^j &= \mathbf{F}_x - \mathbf{B}_{12}\mathbf{Y}^{j} \end{aligned} \tag{3.38}$$

**Remarks 3.2**

(1) It is understood that a convergence criterion has to be chosen to stop the iterative algorithms (3.36)–(3.38).

(2) Physically, the distinction between (3.37) and (3.38) relies on which equation (mechanical or thermal) is solved first. Depending on the physics of the problem, one option may be more efficient than the other, although the improvement will be in no more than one iteration. In what follows, we will assume that the Navier-Stokes equations are solved first, being clear that the following discussion carries out verbatim if the order of block iterations is swapped. □

The convergence of any of the algorithms (3.36)–(3.38) depends on the spectral radius of the square matrices contained in the off-diagonal matrices $\mathbf{B}_{12}$ and $\mathbf{B}_{21}$ [SB]. Matrix $\mathbf{B}_{21}$ may be set to zero by selecting $\beta_t = 0$ (Picard method for the energy equation). However, from (3.34) and (3.29) it is seen that $\mathbf{B}_{12}$ contains the coupling matrix $\mathbf{C}_{s_{\mathbf{u}}^{n}}$. For a given time step size and a mesh diameter $h$, this matrix is proportional to $1/Fr$ (see Box 3.1) or, equivalently, to $Gr/Re^2$ (cf. Eqns. (3.5)). Therefore, *algorithms (3.36)–(3.38) will only converge for sufficiently small values of the Grashof number.* Although this fact might seem an important drawback for using a block iterative algorithm, this is not the case: when $Gr$ (or $Ra$) are very high, even the linearization of the initial problem (3.30) leads to diverging schemes. Relaxation procedures are needed for these extreme cases to compute converged solutions.

The computational efficiency of a block iterative scheme is not clear for the linear problem (3.35). However, this linear system arises from the linearization of (3.30), i.e., from (3.32). The natural idea is to deal with the iterations due to the problem nonlinearity and the block iterations in a single iterative loop. This leads to the following scheme:

$$\begin{pmatrix} \mathbf{A}_{11}(\mathbf{U}^{n,i-1}) + \beta_u \mathbf{A}_{11}^*(\mathbf{U}^{n,i-1}) & \mathbf{A}_{12} \\ \mathbf{A}_{21} & \mathbf{0} \end{pmatrix} \begin{pmatrix} \mathbf{U}^{n,i} \\ \mathbf{P}^{n,i} \end{pmatrix} = \begin{pmatrix} \mathbf{R}_u^* - \mathbf{A}_{13}\Theta^{n,i-1} \\ \mathbf{0} \end{pmatrix} \tag{3.39}$$

$$\mathbf{A}_{33}(\mathbf{U}^{n,i-1})\Theta^{n,i} = \mathbf{R}_t^* - \beta_t \mathbf{A}_{31}^*(\Theta^{n,i-1})\mathbf{U}^{n,k} \tag{3.40}$$

where for $k = i - 1$ this is a Jacobi-type method and for $k = i$ a Gauss-Seidel-type algorithm. Using the expression for $\mathbf{R}_t^*$ given by (3.33), from Eqn. (3.40) we have that

$$\mathbf{A}_{33}(\mathbf{U}^{n,i-1}) \cdot \mathbf{\Theta}^{n,i} + \beta_t \mathbf{A}_{31}^*(\mathbf{\Theta}^{n,i-1}) \cdot \mathbf{U}^{n,k} - \beta_t \mathbf{A}_{31}^*(\mathbf{\Theta}^{n,i-1}) \cdot \mathbf{U}^{n,i-1} = \mathbf{R}_t \tag{3.41}$$

For $\beta_t = 0$ (Picard linearization for the energy equation) or $k = i - 1$ (block Jacobi algorithm), this last expression reduces to

$$\mathbf{A}_{33}(\mathbf{U}^{n,i-1}) \cdot \mathbf{\Theta}^{n,i} = \mathbf{R}_t$$

Assume that $\beta_t = 1$ and $k = i$. Since

$$\mathbf{A}_{33}(\mathbf{U}^{n,i-1}) \cdot \mathbf{\Theta}^{n,i} + \mathbf{A}_{31}^*(\mathbf{\Theta}^{n,i-1}) \cdot \mathbf{U}^{n,i} - \mathbf{A}_{31}^*(\mathbf{\Theta}^{n,i-1}) \cdot \mathbf{U}^{n,i-1}$$

is precisely the linearized expression of $\mathbf{A}_{33}(\mathbf{U}^{n,i}) \cdot \mathbf{\Theta}^{n,i}$ and $\mathbf{U}^{n,i}$ is already known from (3.39), Eqn. (3.41) reduces to

$$\mathbf{A}_{33}(\mathbf{U}^{n,i}) \cdot \mathbf{\Theta}^{n,i} = \mathbf{R}_t$$

Summarizing, Eqn. (3.40) may be replaced by

$$\mathbf{A}_{33}(\mathbf{U}^{n,k}) \cdot \mathbf{\Theta}^{n,i} = \mathbf{R}_t \tag{3.42}$$

where

*a)* $k = i - 1$ if the convective term in the energy equation is linearized up to first order (Picard method) or the block Jacobi method is used to couple the mechanical and thermal problems,

*b)* $k = i$ otherwise, that is, second order linearization is used for the convective term in the energy equation and the block Gauss-Seidel method is employed as block iterative scheme.

Let us go back now to the original matrix notation for (3.39) and (3.40). There are two sources of nonlinearity reflected in these equations, the first coming from the nonlinear character of the physical problem and the second due to the block iterative method. As in Chapter 2, we will add two more sources: the SD method and the iterative penalization. Altogether, there are four reasons to iterate (nonlinear terms, block iterative coupling, SD method and iterative penalization) and they will be dealt with in a single iterative loop.

The final algorithm is the following (compare with (2.60)):

*For $n = 1, 2, ..., N$, given $\mathbf{U}^{n-1}$, $\mathbf{P}^{n-1}$ and $\mathbf{\Theta}^{n-1}$, find $\mathbf{U}^n$, $\mathbf{P}^n$ and $\mathbf{\Theta}^n$, approximations to $\mathbf{U}(t^n)$, $\mathbf{P}(t^n)$ and $\mathbf{\Theta}(t^n)$, as the converged solutions of the following iterative algorithm:*

$$\begin{aligned}
\mathbf{M}_{v,s_u^{n,i-1}} \cdot \mathbf{U}^{n,\epsilon(i)} + \theta \Delta t \mathbf{K}_{c,s_u^{n,i-1}}(\mathbf{U}^{n,\epsilon(i-1)}) \cdot \mathbf{U}^{n,\epsilon(i)}& \\
+ \theta \Delta t \beta_u \mathbf{K}^*_{c,s_u^{n,i-1}}(\mathbf{U}^{n,\epsilon(i-1)}) \cdot \mathbf{U}^{n,\epsilon(i)}& \\
+ \theta \Delta t \mathbf{K}_{d,s_u^{n,i-1}} \cdot \mathbf{U}^{n,\epsilon(i)} - \theta \Delta t \mathbf{G}_{s_u^{n,i-1}} \cdot \mathbf{P}^{n,\epsilon(i)}& \\
= \theta \Delta t \mathbf{F}^n_{v,s_u^{n,i-1}} + (1-\theta)\Delta t \mathbf{F}^{n-1}_{v,s_u^{n,i-1}} + \mathbf{M}_{v,s_u^{n,i-1}} \cdot \mathbf{U}^{n-1}& \\
- (1-\theta)\Delta t \mathbf{K}_{c,s_u^{n,i-1}}(\mathbf{U}^{n-1}) \cdot \mathbf{U}^{n-1}& \\
+ \theta \Delta t \beta_u \mathbf{K}^*_{c,s_u^{n,i-1}}(\mathbf{U}^{n,\epsilon(i-1)}) \cdot \mathbf{U}^{n,\epsilon(i-1)}& \\
- (1-\theta)\Delta t \mathbf{K}_{d,s_u^{n,i-1}} \cdot \mathbf{U}^{n-1} + (1-\theta)\Delta t \mathbf{G}_{s_u^{n,i-1}} \cdot \mathbf{P}^{n-1}& \\
- \Delta t \mathbf{C}_{s_u^{n,i-1}} \cdot \left(\theta \mathbf{\Theta}^{n,\epsilon(i-1)} + (1-\theta)\mathbf{\Theta}^{n-1}\right)&
\end{aligned} \tag{3.43}$$

$$\epsilon \mathbf{M}_p \mathbf{P}^{n,c(i)} + \mathbf{G}_0^T \cdot \mathbf{U}^{n,c(i)} = \epsilon \mathbf{M}_p \mathbf{P}^{n,c(i-1)} \tag{3.44}$$

$$\begin{aligned} \mathbf{M}_{t,s_t^{n,k}} \cdot \boldsymbol{\Theta}^{n,c(i)} &+ \theta \Delta t \mathbf{H}_{c,s_t^{n,k}}(\mathbf{U}^{n,c(k)}) \cdot \boldsymbol{\Theta}^{n,c(i)} + \theta \Delta t \mathbf{H}_{d,s_t^{n,k}} \cdot \boldsymbol{\Theta}^{n,c(i)} \\ &= \theta \Delta t \mathbf{F}_t^n + (1-\theta)\Delta t \mathbf{F}_t^{n-1} + \mathbf{M}_{t,s_t^{n,k}} \cdot \boldsymbol{\Theta}^{n-1} \\ &\quad - (1-\theta)\Delta t \mathbf{H}_{c,s_t^{n,k}}(\mathbf{U}^{n-1}) \cdot \boldsymbol{\Theta}^{n-1} \\ &\quad - (1-\theta)\Delta t \mathbf{H}_{d,s_t^{n,k}} \cdot \boldsymbol{\Theta}^{n-1} \end{aligned} \tag{3.45}$$

*where $k = i - 1$ or $k = i$, according to the options a) and b) indicated above.*

It is assumed in (3.44) that the iterative penalty method is used.

**Remarks 3.3**

(1) The linearization of the SD term, the iterative penalization and the block Jacobi or block Gauss-Seidel methods can only yield a linear convergence rate, with a more or less steep slope in a plot iterations vs logarithm of the residual. Sooner or later, convergence will be driven by the slowest of these rates as the iterative procedure goes on, even though $\beta_u = 1$ be selected to linearize the Navier-Stokes equations. We have found from numerical experiments that the Newton-Raphson method is only useful when the Reynolds and the Rayleigh numbers are small. Otherwise, it only contributes to increase the computational cost, without reducing the number of iterations needed to reach a prescribed convergence tolerance.

(2) If instead of using $\boldsymbol{\Theta}^{n,c(i-1)}$ in (3.44) and $\mathbf{U}^{n,c(k)}$ in (3.45) ($k = i-1$ or $k = i$) they are replaced by the temperature and velocity nodal values of the previous time step, $\boldsymbol{\Theta}^{n-1}$ and $\mathbf{U}^{n-1}$, one is led to the so called 'staggered algorithms', in which the coupling between the Navier-Stokes and the energy equations is accomplished by means of the time stepping. The algorithm in time in this case is block explicit, regardless of the value of the parameter $\theta$. Therefore, a critical time step exists above which the algorithm becomes unstable. See, e.g., References [PF], [WTS], [Zi] for related methods.

(3) Referring again to the stability in time, if a fully converged solution is obtained for (3.43)–(3.45) then stability should be ensured provided that $\theta \geq 1/2$. Obviously, the block iterative method will not give exactly the same solution as the full nonlinear system. An error will remain that may affect the stability of the algorithm in time. Numerical experiments indicate that this in fact happens. We have found that $\theta = 1/2$ (Crank-Nicolson) is very sensitive to the convergence tolerance adopted for each time step. The higher it is, the sooner instabilities begin to appear, leading to the numerical blow-up after a few time steps. In this sense, the backward Euler scheme ($\theta = 1$) has been found to be much more robust. We have never found instability problems using this method. □

## 3.3 Creeping flow of nonlinear materials

### 3.3.1 Generalized Newtonian fluids

The constitutive equation for a Newtonian fluid relates the stress tensor $\boldsymbol{\sigma}$ with the strain rate tensor $\boldsymbol{\varepsilon}$ through a linear equation, viz.,

$$\boldsymbol{\sigma} = -p\mathbf{I} + 2\mu\boldsymbol{\varepsilon}(\mathbf{u}) \tag{3.46}$$

For a number of important materials, it is not possible to describe their rheological behavior with Eqn. (3.46) and using a constant value for the dynamical viscosity $\mu$.

A very simple extension of the Newtonian constitutive law is to consider a variable viscosity $\mu$ in Eqn. (3.46) (this is still a particular case of the Reiner-Rivlin constitutive model). This allows to model several non-Newtonian flow phenomena observed in practice.

According to Tanner [Ta], the non-Newtonian fluid behavior in shear may be classified into three different types: time independent fluids, time dependent fluids and viscoelastic materials. The constitutive law for the first two types can be written as (3.46), with $\mu$ variable. Elastic effects have to be taken into account for viscoelastic materials.

Here, only time independent non-Newtonian fluids will be considered. Sometimes they are just called non-Newtonian viscous fluids or generalized Newtonian fluids. Time dependent materials could also be easily accomodated within the following formulation. For these materials, the viscosity increases in time (rheopectic fluids) or decreases (thixotropic fluids) for a constant shear rate. For simplicity, we shall assume that $\mu$ is time independent.

Generalized Newtonian fluids may be classified in turn into Bingham, pseudo-plastic and dilatant materials. Bingham materials only flow after the stress exceeds a certain threshold (yield stress). For pseudo-plastic fluids the viscosity falls progressively as the shear rate increases. Only for very high rates of shear, it ceases to decrease and remains constant. Dilatant materials exhibit the opposite response.

Pseudo-plastic and dilatant fluids have very important technological applications. High polymers, polymer solutions and many suspensions exhibit a pseudo-plastic behavior. Dilatant fluids are much less common in industrial applications. Some concentrated solutions of solids are an example of this type of materials.

One of the most extensively used constitutive laws for generalized Newtonian fluids is the so called *power law*. For a simple shear flow, its expression is

$$\mu = K_0|\dot{\gamma}|^{n-1}, \quad n > 0, \quad K_0 > 0 \tag{3.47}$$

where $K_0$ is the *material consistency* and $n$ the *rate sensitivity*. Both $K_0$ and $n$ are physical parameters to be determined from experimental data. In Eqn. (3.47), $\dot{\gamma}$ is the shear rate. For $0 < n < 1$, this equation represents a pseudo-plastic fluid (presenting the shear thinning effect near the walls) and for $n > 1$ a dilatant material (showing shear thickening near the walls). Observe that when $|\dot{\gamma}| = 0$ Eqn. (3.47) is meaningless. Another constitutive law that has a wider range of applicability is the Carreau model, whose expression for a simple shear flow is

$$\mu = \mu_0 \left[1 + (\lambda\dot{\gamma})^2\right]^{(n-1)/2} \tag{3.48}$$

where $\mu_0 > 0$ and $\lambda > 0$ are physical parameters and now $0 < n < 1$.

In general, $\mu$ can be considered as a function of the principle invariants of the strain rate tensor $\boldsymbol{\varepsilon}$, defined as

$$\begin{aligned} I_1(\boldsymbol{\varepsilon}) &:= \mathrm{Tr}(\boldsymbol{\varepsilon}) = \nabla \cdot \mathbf{u}, \\ I_2(\boldsymbol{\varepsilon}) &:= \frac{1}{2}\boldsymbol{\varepsilon} : \boldsymbol{\varepsilon}, \\ I_3(\boldsymbol{\varepsilon}) &:= \det(\boldsymbol{\varepsilon}) \end{aligned} \tag{3.49}$$

For incompressible fluids, $\nabla \cdot \mathbf{u} = 0$ and thus $I_1(\boldsymbol{\varepsilon}) = 0$. In most situations of physical interest, $\mu$ is independent of $I_3(\boldsymbol{\varepsilon})$.

Let us see how Eqns. (3.47) and (3.48) can be generalized. For a simple plane shear flow with $\mathbf{u} = (u_1(x_2), 0)$ (in Cartesian coordinates $x_1$ and $x_2$) we have that

$$|\dot{\gamma}| = |\frac{\partial u_1}{\partial x_2}| = |2\boldsymbol{\varepsilon} : \boldsymbol{\varepsilon}|^{1/2} = |4I_2(\boldsymbol{\varepsilon})|^{1/2}$$

and therefore the generalized expressions for (3.47) and (3.48) are

$$\mu = K_0\,[4I_2(\boldsymbol{\varepsilon})]^{(n-1)/2} \qquad \text{(Power law)} \tag{3.50}$$

$$\mu = \mu_0\,\left[1 + 4\lambda^2 I_2(\boldsymbol{\varepsilon})\right]^{(n-1)/2} \qquad \text{(Carreau)} \tag{3.51}$$

Another very important type of constitutive law is the one representing viscoplastic materials. This rheological behavior is particularly well suited to model the flow of metals in metal forming processes. When plastic deformations are much more important than elastic deformations, elastic effects may be simply neglected. This is the so called *flow approach*.

Here we will briefly describe a particular type of viscoplastic model, namely, Perzyna's model (see, e.g., References [Oñ], [OH], [ZG], [ZJO], [ZOH] for more information). The basic assumption is that the viscoplastic strain rate is related to the stress through the following equation:

$$\varepsilon_{ij} = \gamma < \phi(F) > \frac{\partial Q}{\partial \sigma_{ij}} \tag{3.52}$$

where $F$ is the yield function for the material, $Q$ the plastic potential, $\phi$ a certain function that defines the model and $< \cdot >$ is the Macauley bracket, defined by $< f >= f$ if $f \geq 0$ and $< f >= 0$ if $f < 0$. The constant $\gamma$ in Eqn. (3.52) has the physical meaning of being the fluidity parameter.

Assume now associate plasticity ($F = Q$) and take for $F$ the von Mises yield surface,

$$F = Q = \sqrt{3I_2(\boldsymbol{\sigma}')} - \sigma_y \tag{3.53}$$

where $\sigma_y$ is the uniaxial yield stress of the material and $I_2(\boldsymbol{\sigma}')$ is the second principle invariant of the tensor $\boldsymbol{\sigma}' := \boldsymbol{\sigma} + p\mathbf{I}$. For the function $\phi$, the following power law is adopted:

$$\phi(F) = F^m \tag{3.54}$$

After some calculations, from (3.53) it is found that

$$\frac{\partial Q}{\partial \sigma_{ij}} = \frac{\sqrt{3}}{2\sqrt{I_2(\boldsymbol{\sigma}')}}\sigma'_{ij} \tag{3.55}$$

Using Eqns. (3.53)–(3.55) in (3.52) we obtain that

$$\varepsilon_{ij} = \gamma < \left(\sqrt{3I_2(\boldsymbol{\sigma}')} - \sigma_y\right)^m > \frac{\sqrt{3}}{2\sqrt{I_2(\boldsymbol{\sigma}')}}\sigma'_{ij} \tag{3.56}$$

This equation (3.56) represents a generalized Newtonian material, the viscosity $\mu$ being one half of the inverse of the coefficient multiplying $\sigma'_{ij}$

Assume that $\sqrt{3I_2(\boldsymbol{\sigma}')} - \sigma_y > 0$ and define

$$\hat{\varepsilon} := \left(\frac{2}{3}\varepsilon_{ij}\varepsilon_{ij}\right)^{1/2} = \left(\frac{4}{3}I_2(\boldsymbol{\varepsilon})\right)^{1/2} \tag{3.57}$$

We will have that

$$\begin{aligned} I_2(\boldsymbol{\sigma}') &= \frac{1}{2}\boldsymbol{\sigma}' : \boldsymbol{\sigma}' = \frac{1}{2}(2\mu)^2\boldsymbol{\varepsilon} : \boldsymbol{\varepsilon} = 3\mu^2\hat{\varepsilon}^2, \\ \hat{\varepsilon} &= \frac{1}{\sqrt{3}\mu}\sqrt{I_2(\boldsymbol{\sigma}')} = \gamma\left(\sqrt{3I_2(\boldsymbol{\sigma}')} - \sigma_y\right)^m \\ &= \gamma(3\mu\hat{\varepsilon} - \sigma_y)^m \end{aligned}$$

and hence

$$\mu = \frac{\sigma_y + (\hat{\varepsilon}/\gamma)^{1/m}}{3\hat{\varepsilon}} \tag{3.58}$$

This expression will only be valid for high values of $\hat{\varepsilon}$. Observe that for $\sigma_y = 0$ it reduces to the power-law model given by (3.50) and with a certain identification of the physical parameters.

In Section 3.5.3 we will present a numerical simulation of a fluid whose viscosity obeys the power-law (3.50) and in next chapter the problem of lamination of a metal flat plate using the constitutive equation (3.58).

Besides the nonlinear dependence of the viscosity on the invariant $I_2(\boldsymbol{\varepsilon})$ expressed by Eqns. (3.50), (3.51) and (3.58), it may also depend on the temperature and the pressure. The physical parameters in these equations depend on the temperature [ZJO], [ZOH]. But even for Newtonian fluids, the viscosity depends on the temperature and the pressure. Using reaction-rate concepts [Ta], the viscosity may be expressed in terms of the (absolute) temperature $\vartheta$ as

$$\mu = \mu_0 \exp\left(\frac{E}{R\vartheta}\right) \tag{3.59}$$

where $E$ is the activation energy, $R$ the gas constant (8.314 J $\mathrm{K}^{-1}\mathrm{mol}^{-1}$) and $\mu_0$ is the viscosity for $E = 0$. For small temperature changes around a reference value $\vartheta_0$, Eqn. (3.59) may be replaced by

$$\mu = \mu_0 \exp\left[-\alpha(\vartheta - \vartheta_0)\right]$$

where now $\mu_0$ is the viscosity for $\vartheta = \vartheta_0$.

Concerning the dependence of $\mu$ on a pressure variation $p$, an expression of the form

$$\mu = \mu_0 \exp\left(\frac{p}{B}\right) \tag{3.60}$$

is often adopted. This equation can be derived from thermodynamical bases using the free volume concept [Ta]. In general, the physical parameter $B$ is very large and pressure variations do not affect much the value of the viscosity.

In what follows, we will assume that an expression of $\mu$ in terms of $I_2(\boldsymbol{\varepsilon})$ and $\vartheta$ is given. Since $I_2(\boldsymbol{\varepsilon})$ is really a function of the velocity field $\mathbf{u}$, we will write, symbolically,

$$\mu = \mu(\vartheta, \mathbf{u}) \tag{3.61}$$

The only way to solve fluid flow problems involving nonlinear viscosities is numerically. For Newtonian flows, analytical solutions in some simple cases allow to understand which could be the flow behavior in more general situations. However, for non-Newtonian flows even for simple problems numerical techniques are needed. For the numerical simulation of some simple flow cases of non-Newtonian fluids, see, e.g., References [BLL], [BP], [CC], [DK], [DR], [SY], [TTK], among many others.

### 3.3.2 Stationary problem and finite element discretization

The rheological behavior described above is usually valid for highly viscous materials. Therefore, inertial terms in the Navier-Stokes equations will have a very little influence, i.e., the Reynolds number will be very small. In order to simplify the exposition, the convective term in the momentum equations will be dropped, that is, only creeping flows will be considered. Moreover, since the transient evolution will not introduce anything new, the stationary problem will be treated.

Under the assumptions just stated, the problem to be solved is to find a velocity field $\mathbf{u}$, a pressure $p$ and a temperature $\vartheta$ such that

$$\begin{aligned} -2\nabla \cdot [\mu\boldsymbol{\varepsilon}(\mathbf{u})] + \nabla p = \rho\mathbf{f} \qquad & \text{in } \Omega \\ \nabla \cdot \mathbf{u} = 0 \qquad & \text{in } \Omega \\ \rho c_p \mathbf{u} \cdot \nabla\vartheta - k\Delta\vartheta = Q \qquad & \text{in } \Omega \end{aligned} \tag{3.62}$$

In the energy equation, $Q$ is the source term. Only the source coming from the mechanical dissipation into heat will be taken into account:

$$\begin{aligned} Q &= \boldsymbol{\sigma} : \boldsymbol{\varepsilon} = -p\mathbf{I} : \boldsymbol{\varepsilon}(\mathbf{u}) + 2\mu\boldsymbol{\varepsilon}(\mathbf{u}) : \boldsymbol{\varepsilon}(\mathbf{u}) \\ &= 2\mu\boldsymbol{\varepsilon}(\mathbf{u}) : \boldsymbol{\varepsilon}(\mathbf{u}) \end{aligned} \tag{3.63}$$

where the fact that $\mathbf{I} : \boldsymbol{\varepsilon}(\mathbf{u}) = \nabla \cdot \mathbf{u} = 0$ has been used.

The same boundary conditions as in Section 3.2 will be considered (Eqns. (3.8)). Sometimes, the Neumann-type prescription for the temperature has to be generalized to a Robbins boundary condition to include the surface heat convection, although this is immaterial for what follows.

The spaces of trial solutions needed for the stationary problem are:

$$\begin{aligned} V_u &= \{\mathbf{v} \in H^1(\Omega)^{N_{sd}} \mid \mathbf{v}|_{\Gamma_{du}} = \bar{\mathbf{u}}\} \\ V_p &= \{q \in L^2(\Omega) | \int_\Omega q d\Omega = 0 \ \text{ if } \ \Gamma_{nu} = \emptyset\} \\ V_t &= \{\eta \in H^1(\Omega) \mid \eta|_{\Gamma_{dt}} = \bar{\vartheta}\} \end{aligned} \tag{3.64}$$

The spaces of test functions are again given by (3.10). Introducing the forms

$$
\begin{aligned}
a(\mu;\mathbf{u},\mathbf{v}) &= 2\int_\Omega \mu\boldsymbol{\varepsilon}(\mathbf{u}):\boldsymbol{\varepsilon}(\mathbf{v})d\Omega,\\
b(q,\mathbf{v}) &= \int_\Omega q\nabla\cdot\mathbf{v}d\Omega,\\
l_u(\mathbf{v}) &= \int_\Omega \rho\mathbf{f}\cdot\mathbf{v}d\Omega + \int_{\Gamma_{nu}} \bar{\mathbf{t}}\cdot\mathbf{v}d\Gamma,\\
e(\vartheta,\eta) &= \int_\Omega k\nabla\vartheta\cdot\nabla\eta d\Omega,\\
f(\mathbf{u},\vartheta,\eta) &= \int_\Omega \rho c_p\eta\mathbf{u}\cdot\nabla\vartheta d\Omega,\\
l_t(\mu,\mathbf{u};\eta) &= 2\int_\Omega \mu\boldsymbol{\varepsilon}(\mathbf{u}):\boldsymbol{\varepsilon}(\mathbf{u})\eta d\Omega + \int_{\Gamma_{nt}} \bar{\varphi}\eta d\Gamma,
\end{aligned}
\tag{3.65}
$$

the weak form of problem (3.62) with the boundary conditions (3.8) is: Find $\mathbf{u}\in V_u$, $p\in V_p$ and $\vartheta\in V_t$ such that

$$
\begin{aligned}
a(\mu;\mathbf{u},\mathbf{v}) - b(p,\mathbf{v}) = l_u(\mathbf{v}) \qquad & \forall\mathbf{v}\in W_u\\
b(q,\mathbf{u}) = 0 \qquad & \forall q\in W_p\\
f(\mathbf{u},\vartheta,\eta) + e(\vartheta,\eta) = l_t(\mu,\mathbf{u};\eta) \qquad & \forall\eta\in W_t
\end{aligned}
\tag{3.66}
$$

We now consider the finite element discretization of problem (3.66). For simplicity, the Galerkin approach will be used, although the SD formulation might be needed to stabilize the convective term in the energy equation.

The discrete version of problem (3.66) leads to the following algebraic system:

$$\mathbf{K}(\mu)\cdot\mathbf{U} - \mathbf{G}\cdot\mathbf{P} = \mathbf{F}_u \tag{3.67}$$

$$\mathbf{G}^T\cdot\mathbf{U} = \mathbf{0} \tag{3.68}$$

$$\mathbf{H}(\mathbf{u})\cdot\boldsymbol{\Theta} = \mathbf{F}_t(\mu,\mathbf{u}) \tag{3.69}$$

The notation used for the matrices and the vectors is the same as before, although subscripts have been omitted. Matrix $\mathbf{H}(\mathbf{u})$ for the temperature equation (3.69) accounts for both the diffusive and convective terms. We have explicitly indicated the dependence of the matrices and vectors in the above equations on the viscosity and the velocity.

Let us discuss now the construction of the finite element spaces $V_{u,h}$, $V_{p,h}$ and $V_{t,h}$. Consider first the case in which the viscosity $\mu$ does not depend on the temperature $\vartheta$. Under this assumption, Eqns. (3.67) and (3.68) are uncoupled with Eqn. (3.69), that can be solved once $\mathbf{U}$ is known. If the viscosity $\mu$ is constant (Newtonian fluid), we know that the discrete velocity space $V_{u,h}$ and pressure space $V_{p,h}$ must satisfy the discrete Babuška-Brezzi (BB) stability condition. When the viscosity depends on the invariants of the strain-rate tensor $\boldsymbol{\varepsilon}(\mathbf{u})$, the question is whether this condition will be sufficient for assessing stability and convergence of the finite element scheme. In Reference [BN], it is proved that for the case in which the viscosity obeys the power law or the Carreau model, stable and convergent velocity-pressure pairs for the Stokes problem with $\mu$ constant are also stable for the nonlinear case. Concerning the convergence of the method, let $h$ be the diameter of $\{\Omega^e\}$ and suppose that the rate of convergence for the velocity is of order $h^m$ for Newtonian flows. Assume now that $\mu$ satisfies the power law with rate of sensitivity $n$, with $0 < n < 1$. Then, the rate of convergence for the velocity will be of order $h^{mn}$. For the Carreau model, the same rate of convergence as for the constant viscosity case can be obtained. See Reference [BN] for details.

Based on these results, finite element interpolations for the velocity and the pressure that are known to satisfy the discrete Babuška-Brezzi condition have been employed also for this problem. As in Section 3.2, the temperature will be interpolated like the velocity components.

### 3.3.3 Iterative techniques

*Iterative penalty method*

Let us consider first the case in which $\mu$ is constant. The iterative penalty method applied to problem (3.67)–(3.69) is:

*Given* $\mathbf{P}^{\epsilon(0)}$, *for* $i = 1, 2, ...$ *find* $\mathbf{U}^{\epsilon(i)}$ *and* $\mathbf{P}^{\epsilon(i)}$ *such that*

$$\begin{aligned} \mathbf{K}(\mu) \cdot \mathbf{U}^{\epsilon(i)} - \mathbf{G} \cdot \mathbf{P}^{\epsilon(i)} &= \mathbf{F}_u \\ \mathbf{G}^T \cdot \mathbf{U}^{\epsilon(i)} + \epsilon \mathbf{M}_p \cdot \mathbf{P}^{\epsilon(i)} &= \epsilon \mathbf{M}_p \cdot \mathbf{P}^{\epsilon(i-1)} \end{aligned} \tag{3.70}$$

This is the discrete version of problem (3.73). It should be remarked that the initial guess $\mathbf{P}^{\epsilon(0)}$ must be such that the associated pressure (interpolated from these nodal values) have zero mean value.

The analysis of Section 1.4.1 revealed that the convergence of (3.70) relies on the value of the parameter

$$\bar{\epsilon} := \epsilon \frac{N_a^2}{K_a K_b^2}$$

where $N_a$ is the norm of $a(\mu; \cdot, \cdot)$, $K_a$ its coercivity constant and $K_b$ the constant in the Babuška-Brezzi condition. Since now both $N_a$ and $K_a$ will be proportional to $\mu$, we will have that

$$\bar{\epsilon} = \epsilon \mu C \tag{3.71}$$

for a certain constant $C$. In fact, using the same arguments as in Section 1.4.1 one obtains (see Reference [CCO] for details):

$$\begin{aligned} \|\mathbf{U} - \mathbf{U}^{\epsilon(i)}\| &\leq (\epsilon \mu C)^i \frac{C'}{\mu} \|\mathbf{P} - \mathbf{P}^{\epsilon(0)}\| \\ \|\mathbf{P} - \mathbf{P}^{\epsilon(i)}\| &\leq (\epsilon \mu C)^i \|\mathbf{P} - \mathbf{P}^{\epsilon(0)}\| \end{aligned} \tag{3.72}$$

where $C'$ is a constant and $\| \cdot \|$ denotes the discrete $L^2$ norm.

It is important to observe that convergence is governed by the parameter $\bar{\epsilon}$, which is proportional to the viscosity $\mu$. This explains why $\epsilon$ must be taken proportional to $\mu^{-1}$, since what provides an idea of how well the incompressibility constraint will be approximated is $\bar{\epsilon}$, and not $\epsilon$ itself. Of course, this comment can also be applied to the classical penalty method (observe that the first pass in (3.70) is nothing but the standard penalty method), and must be kept in mind when one deals with non-constant viscosities.

In practical problems, we have encountered two cases in which the the standard penalty method cannot be applied and the iterative penalization is mandatory. The first is the one discussed now, concerning non-Newtonian flows with variable viscosity. In the numerical examples presented below, it will be seen that the viscosity varies several orders of magnitude in the fluid domain. Recall that the practical rule for choosing the penalty parameter for the classical penalty method is to take it in the range $10^{-6}\mu^{-1}$ to $10^{-9}\mu^{-1}$. If a reference viscosity $\mu_0$ is chosen *a priori* for determining a suitable value of $\epsilon$, it is not known whether this penalty parameter will yield a sufficiently accurate satisfaction of the incompressibility constraint or to ill-conditioning of the final stiffness matrix. We will insist on this point later. Let us just mention that this ill-conditioning for non-Newtonian flows precludes the use of iterative solvers for the resulting algebraic system, in which case the behavior of the standard penalty method is certainly disappointing [CWJ]. For an application of the Augmented Lagrangian method to non-Newtonian fluids, see Reference [HTB].

Perhaps another case in which the importance of the variable viscosity is more clear is when the pseudo-concentration method is used to follow free surfaces. This will be the subject of Chapter 4.

*Iterative algorithm for thermally coupled non-Newtonian flows*

In order to solve the coupled nonlinear system of equations (3.67)–(3.69) we will use a block iterative algorithm, as in Section 3.2. Once again, the nonlinearity of the problem and the iterative penalization will be dealt with within the same iterative loop.

Let $\mu^{(k,l)}$ denote the viscosity function when the temperature is known at iteration $k$ and the velocity at iteration $l$. Let $TOL$ be a given convergence tolerance. As in the previous chapter, we check convergence using the criterion $\|\mathbf{U}^{\epsilon(i)} - \mathbf{U}^{\epsilon(i-1)}\| < TOL\|\mathbf{U}^{\epsilon(i)}\|$. The iterative scheme used is the following:

**Box 3.2 Algorithm for thermally coupled non-Newtonian flows**

```
• Initialise $\mu^{(0,0)}$, $\mathbf{P}^{(0)}$, $\boldsymbol{\Theta}^{(0)}$
• $i := 0$
• WHILE (not converged) DO:
    • $i \leftarrow i + 1$
    • Solve:
        $\mathbf{K}\left(\mu^{(i-1,i-1)}\right) \cdot \mathbf{U}^{\epsilon(i)} - \mathbf{G} \cdot \mathbf{P}^{\epsilon(i)} = \mathbf{F}_u$
        $\mathbf{G}^T \cdot \mathbf{U}^{\epsilon(i)} + \epsilon \mathbf{M}_p \cdot \mathbf{P}^{\epsilon(i)} = \epsilon \mathbf{M}_p \mathbf{P}^{\epsilon(i-1)}$
    • Update:
        $\mu^{(i-1,i)} = \mu(\vartheta^{\epsilon(i-1)}, \mathbf{u}^{\epsilon(i)})$
    • Solve:
        $\mathbf{H}(\mathbf{u}^{\epsilon(i)}) \cdot \boldsymbol{\Theta}^{\epsilon(i)} = \mathbf{F}_t(\mu^{(i-1,i)}, \mathbf{u}^{\epsilon(i)})$
    • Update:
        $\mu^{(i,i)} = \mu(\vartheta^{\epsilon(i)}, \mathbf{u}^{\epsilon(i)})$
    • Check convergence:
        If $\|\mathbf{U}^{\epsilon(i)} - \mathbf{U}^{\epsilon(i-1)}\| < TOL\|\mathbf{U}^{\epsilon(i)}\|$ then (converged)
  END while
  END
```

**Remarks 3.4**

(1) Observe that the thermal problem is solved once the mechanical variables **U** and **P** are known for a certain iteration. There is also the possibility of swapping the order of block iterations. However, for the problems we have considered so far we have found the described option (slightly) more efficient.

(2) The iterative penalization in the above algorithm is coupled with the iterative loop used to deal with the nonlinearity of the problem. It will be seen in the numerical experiments presented below that this does not deteriorate the convergence rate of the scheme.

(3) If the viscosity does not depend on the temperature, the algorithm presented is a Picard (or successive substitution) type scheme. This is the most common option in practice [CWJ], [HTB], [LLH], [ZJO], [ZOH]. In fact, convergence problems have been observed when a Newton-Raphson scheme has been employed in the type of problems we consider (see Reference [CSS] for further discussion and references therein). The Picard method has been found to be faster than the Newton-Raphson algorithm. Anyway, convergence is slow for small values of the rate sensitivity $n$ when the Power-law model is adopted for the viscosity. In Reference [TNB], it is proposed to redefine $\mu^{(k,i)}$ as

$$\mu^{(k,i)} \leftarrow \mu^{(k,i)} + \omega(1-n)\left(\mu^{(k,i)} - \mu^{(k,i-1)}\right)$$

The value $\omega = 0.4$ was found to be a good choice.

(4) From the results of the previous section, it is clear that the algorithm of Box 3.2 can be thought of as a Gauss-Seidel iterative scheme with a Newton-Raphson linearization of the energy equation, since the velocity used in this equation is the actual iterate, both for the convective term and the source term. □

## 3.4 General problem—Iterative procedure

### 3.4.1 Motivation

In Sections 3.2 and 3.3 we have described the numerical techniques used for two particular problems of practical interest. Both problems can be placed in the general setting to be considered now, defined by the following system of partial differential equations:

$$\begin{aligned}
\rho[\partial_t \mathbf{u} + (\mathbf{u}\cdot\nabla)\mathbf{u}] - 2\nabla\cdot[\mu\boldsymbol{\varepsilon}(\mathbf{u})] + \nabla p &= \rho\mathbf{f} && \text{in } \Omega,\ t\in(0,T)\\
\nabla\cdot\mathbf{u} &= 0 && \text{in } \Omega,\ t\in(0,T)\\
\rho c_p[\partial_t\vartheta + (\mathbf{u}\cdot\nabla)\vartheta] - \nabla\cdot(k\nabla\vartheta) &= Q && \text{in } \Omega,\ t\in(0,T)
\end{aligned} \tag{3.73}$$

where the physical properties and the forcing terms may be variable. Particular cases of interest are:

- $\rho$ and $c_p$ depend on the temperature. This in fact is observed experimentally [IOS], [ZMS]. However, the Eulerian derivatives of $\rho$ and $c_p$ have to be small enough to ensure that the simplifications that lead from the general conservation equations of continuum mechanics (momentum, mass and energy) to (3.73) are still valid.
- $\mu$ is a function of $\vartheta$ and the invariants of $\boldsymbol{\varepsilon}(\mathbf{u})$. This is the problem considered in Section 3.3.

- $k$ is a function of $\vartheta$. No assumption on the magnitude of the spatial and temporal derivatives of the diffusion is now required. This situation is found when the Fourier law of heat conduction, $\mathbf{q} = -k\nabla\vartheta$, $\mathbf{q}$ being the flux of heat, has to be generalized to $\mathbf{q} = -\nabla g(\vartheta)$, where $g$ is a nonlinear function of the temperature. The effective conduction coefficient is now $g'(\vartheta)$. Nonlinear diffusion problems are often found in practice.
- $\mathbf{f}$ depends on the temperature. The Boussinesq approximation is an example of this situation.
- $Q$ depends on the velocity and the temperature. This happens when the Joule effect is not neglected (Section 3.3). Internal heat sources may be also introduced, due for example to chemical reactions or electromagnetic effects.
- In Chapter 4, $\rho$, $\mu$, $c_p$ and $k$ will be considered variable in space due to the presence of two different fluids in the domain $\Omega$.

Other nonlinearities in the problem may arise because of the boundary conditions. For example, typical surface radiation models lead to the boundary condition

$$-k\mathbf{n}\cdot\nabla\vartheta = \bar{\varphi} + \alpha(\vartheta^r - \vartheta^r_\infty)$$

for the temperature, $\alpha$ and $r$ being physical parameters and $\vartheta_\infty$ the ambient temperature outside the domain $\Omega$. Surface convection and surface conduction laws have similar expressions.

### 3.4.2 Time discretization

The fact that the density $\rho$ and the specific heat $c_p$ be variable introduce an additional difficulty in the time discretization of Eqns. (3.73). To see this, let us neglect the convective term in the momentum equation and let us write it as

$$\rho\partial_t\mathbf{u} + \mathcal{G}(\mathbf{u}, p) = \rho\mathbf{f} \tag{3.74}$$

where $\mathcal{G}(\mathbf{u}, p) = -2\nabla\cdot[\mu\boldsymbol{\varepsilon}(\mathbf{u})] + \nabla p$. Dividing Eqn. (3.74) by $\rho$ and using the generalized trapezoidal rule to discretize in time leads to

$$\begin{aligned}\frac{1}{\Delta t}\left(\mathbf{u}^n - \mathbf{u}^{n-1}\right) + \frac{\theta}{\rho^n}\mathcal{G}(\mathbf{u}^n, p^n) + \frac{1-\theta}{\rho^{n-1}}\mathcal{G}(\mathbf{u}^{n-1}, p^{n-1})\\ = \theta\mathbf{f}^n + (1-\theta)\mathbf{f}^{n-1}\end{aligned} \tag{3.75}$$

If $\mu$ is constant, the terms in $\mathcal{G}(\mathbf{u}, p)$ will lead to constant matrices once the spatial discretization has been performed, and one needs to compute them only once. However, if $\mathcal{G}(\mathbf{u}, p)$ is multiplied by $1/\rho$, these matrices have to be computed for each time step. In order to avoid this additional computational cost, let us multiply Eqn. (3.75) by $\rho^n$:

$$\begin{aligned}\frac{\rho^n}{\Delta t}\left(\mathbf{u}^n - \mathbf{u}^{n-1}\right) + \theta\mathcal{G}(\mathbf{u}^n, p^n) + (1-\theta)\frac{\rho^n}{\rho^{n-1}}\mathcal{G}(\mathbf{u}^{n-1}, p^{n-1})\\ = \rho^n\theta\mathbf{f}^n + \rho^n(1-\theta)\mathbf{f}^{n-1}\end{aligned} \tag{3.76}$$

Since the temporal derivative of $\rho$ must be small, we can approximate

$$\frac{\rho^n}{\rho^{n-1}} \approx 1 \tag{3.77}$$

Using the approximation (3.77), the variation of $\rho$ only affects the terms where it appears explicitly in Eqn. (3.74), that is, the approximation of the velocity time derivative and the body force term.

Observe from Eqn. (3.76) that the approximation given by (3.76) is unnecessary when $\theta = 1$. A similar situation is found when the specific heat varies in time.

The approximation just described will be used in Chapter 4, where the temporal variation of $\rho$ and $c_p$ will be due to the advance of a fluid in an air-filled domain.

### 3.4.3 Fully discrete and linearized problem

We proceed now to present the algorithm that combines all the ideas developed up to now. The basic scheme for the numerical solution of the Navier-Stokes equations was presented in Box 2.3. This scheme will be completed now with the inclusion of the temperature equation and the block iterative method to couple the mechanical and thermal problems.

The notation used before will be kept in what follows. In particular, the forms that define the problem will be those given by (2.13) and (3.65), now with all the physical properties within the integral symbol, since they may be variable. The dependence on these physical properties of the matrices and vectors resulting after the finite element discretization has been performed will be explicitly indicated. The source term $Q$ in the energy equation will be considered in the force vector $\mathbf{F}_t$.

The final transient and iterative algorithm using the generalized trapezoidal rule to discretize in time, the SD formulation for the space discretization, the iterative penalty method and the block iterative coupling is the following:

*For $n = 1, 2, ..., N$, given $\mathbf{U}^{n-1}$, $\mathbf{P}^{n-1}$ and $\Theta^{n-1}$, find $\mathbf{U}^n$, $\mathbf{P}^n$ and $\Theta^n$, approximations to $\mathbf{U}(t^n)$, $\mathbf{P}(t^n)$ and $\Theta(t^n)$, as the converged solutions of the following iterative algorithm:*

$$\begin{aligned}
&\mathbf{M}_{v,s_u^{n,i-1}}(\rho^n)\cdot\mathbf{U}^{n,\epsilon(i)} + \theta\Delta t\mathbf{K}_{c,s_u^{n,i-1}}(\rho^n;\mathbf{U}^{n,\epsilon(i-1)})\cdot\mathbf{U}^{n,\epsilon(i)}\\
&\quad + \theta\Delta t\beta_u\mathbf{K}^*_{c,s_u^{n,i-1}}(\rho^n;\mathbf{U}^{n,\epsilon(i-1)})\cdot\mathbf{U}^{n,\epsilon(i)}\\
&\quad + \theta\Delta t\mathbf{K}_{d,s_u^{n,i-1}}(\mu^n)\cdot\mathbf{U}^{n,\epsilon(i)} - \theta\Delta t\mathbf{G}_{s_u^{n,i-1}}\cdot\mathbf{P}^{n,\epsilon(i)}\\
&\quad = \theta\Delta t\mathbf{F}^n_{v,s_u^{n,i-1}} + (1-\theta)\Delta t\mathbf{F}^{n-1}_{v,s_u^{n,i-1}} + \mathbf{M}_{v,s_u^{n,i-1}}(\rho^n)\cdot\mathbf{U}^{n-1}\\
&\quad - (1-\theta)\Delta t\mathbf{K}_{c,s_u^{n,i-1}}(\rho^n;\mathbf{U}^{n-1})\cdot\mathbf{U}^{n-1}\\
&\quad + \theta\Delta t\beta_u\mathbf{K}^*_{c,s_u^{n,i-1}}(\rho^n;\mathbf{U}^{n,\epsilon(i-1)})\cdot\mathbf{U}^{n,\epsilon(i-1)}\\
&\quad - (1-\theta)\Delta t\mathbf{K}_{d,s_u^{n,i-1}}(\mu^{n-1})\cdot\mathbf{U}^{n-1} + (1-\theta)\Delta t\mathbf{G}_{s_u^{n,i-1}}\cdot\mathbf{P}^{n-1}
\end{aligned}\tag{3.78}$$

$$\epsilon\mathbf{M}_p\mathbf{P}^{n,\epsilon(i)} + \mathbf{G}_0^T\cdot\mathbf{U}^{n,\epsilon(i)} = \epsilon\mathbf{M}_p\mathbf{P}^{n,\epsilon(i-1)}\tag{3.79}$$

$$\begin{aligned}
&\mathbf{M}_{t,s_t^{n,i}}(\rho^n,c_p^n)\cdot\Theta^{n,\epsilon(i)} + \theta\Delta t\mathbf{H}_{c,s_t^{n,i}}(\rho^n,c_p^n;\mathbf{U}^{n,\epsilon(i)})\cdot\Theta^{n,\epsilon(i)}\\
&\quad + \theta\Delta t\mathbf{H}_{d,s_t^{n,i}}(k^n)\cdot\Theta^{n,\epsilon(i)}\\
&\quad = \theta\Delta t\mathbf{F}^n_{t,s_t^{n,i}} + (1-\theta)\Delta t\mathbf{F}^{n-1}_{t,s_t^{n,i}} + \mathbf{M}_{t,s_t^{n,i}}(\rho^n,c_p^n)\cdot\Theta^{n-1}\\
&\quad - (1-\theta)\Delta t\mathbf{H}_{c,s_t^{n,i}}(\rho^n,c_p^n;\mathbf{U}^{n-1})\cdot\Theta^{n-1}\\
&\quad - (1-\theta)\Delta t\mathbf{H}_{d,s_t^{n,i}}(k^{n-1})\cdot\Theta^{n-1}
\end{aligned}\tag{3.80}$$

Observe that the approximation given by (3.77) has been employed for the terms involving the density (and also for the specific heat).

**Box 3.3 General algorithm for thermally coupled flows**

```
• Set the initial condition $\mathbf{U}^0$, $\Theta^0$ and $\mathbf{P}^0 = 0$
• $n := 0$
• WHILE $n < N$ and *(non-stationary)* DO:
    • $n \leftarrow n + 1$
    • IF $n < n_{eu}$ then $\theta = 1$
      ELSE select $\theta$, $\theta \geq 1/2$
    • $i := 0$
    • Set $\mathbf{U}^{n,\epsilon(0)} = \mathbf{U}^{n-1}$, $\mathbf{P}^{n,\epsilon(0)} = \mathbf{P}^{n-1}$ and $\Theta^{n,\epsilon(0)} = \Theta^{n-1}$
    • WHILE *(not converged)* DO:
        • $i \leftarrow i + 1$
        • Solve the Navier-Stokes equations (3.78)–(3.79)
        • Update:
              $\mu^n \leftarrow \mu(\vartheta^{n,\epsilon(i-1)}, \mathbf{u}^{n,\epsilon(i)})$
              $\mathbf{F}_t^n \leftarrow \mathbf{F}_t(\vartheta^{n,\epsilon(i-1)}, \mathbf{u}^{n,\epsilon(i)})$
        • Solve the temperature equation (3.80)
        • Update:
              $\rho^n \leftarrow \rho(\vartheta^{n,\epsilon(i)})$
              $\mu^n \leftarrow \mu(\vartheta^{n,\epsilon(i)}, \mathbf{u}^{n,\epsilon(i)})$
              $\mathbf{F}_v^n \leftarrow \mathbf{F}_v(\vartheta^{n,\epsilon(i)})$
              $c_p^n \leftarrow c_p(\vartheta^{n,\epsilon(i)})$
              $k^n \leftarrow k(\vartheta^{n,\epsilon(i)})$
              $\mathbf{F}_t^n \leftarrow \mathbf{F}_t(\vartheta^{n,\epsilon(i)}, \mathbf{u}^{n,\epsilon(i)})$
        • Check convergence:
              IF $\|\mathbf{U}^{n,\epsilon(i)} - \mathbf{U}^{n,\epsilon(i-1)}\|_{L^q} < TOL\|\mathbf{U}^{n,\epsilon(i)}\|_{L^q}$
              and $\|\Theta^{n,\epsilon(i)} - \Theta^{n,\epsilon(i-1)}\|_{L^q} < TOL\|\Theta^{n,\epsilon(i)}\|_{L^q}$
              then *(converged)*
      END while *(not converged)*
    • $\mathbf{U}^n \leftarrow \mathbf{U}^{n,\epsilon(i)}$
    • $\mathbf{P}^n \leftarrow \mathbf{P}^{n,\epsilon(i)}$
    • $\Theta^n \leftarrow \Theta^{n,\epsilon(i)}$
    • Check if the steady-state has been reached:
          IF $\|\mathbf{U}^n - \mathbf{U}^{n-1}\|_{L^q} < TOL\ \Delta t\ \|\mathbf{U}^n\|_{L^q}$
          and $\|\Theta^n - \Theta^{n-1}\|_{L^q} < TOL\ \Delta t\ \|\Theta^n\|_{L^q}$
          then *(stationary)*
END while $n < N$ and *(non-stationary)*
END
```

We shall assume that the physical properties $\rho$, $c_p$ and $k$ and the body force term in Eqn. (3.78) are functions of the temperature $\vartheta$ and that the viscosity and the forcing term $\mathbf{F}_t$ depend on the temperature and the velocity, the latter through the source term $Q$. The basic flow chart to solve Eqns. (3.78)–(3.79) is given in Box 3.3, where the same notation as in Box 2.3 has been employed. It is assumed that all the terms depending on the temperature and the velocity are updated as soon as possible. For the particular case of the Boussinesq problem, it has been shown in Section 3.2 that this is equivalent to use the Gauss-Seidel block iterative method and the Newton-Raphson linearization of the energy equation.

## 3.5 Some applications of the numerical method

We present thereafter the numerical simulation of three different problems involving thermally coupled flows. The Boussinesq approximation is the mathematical model for the first two examples. The last problem is the 4:1 plane extrusion of a nonlinear material, with the viscosity depending on the temperature.

The numerical calculations have been carried out on a CONVEX-C320 computer using double arithmetic precision.

### 3.5.1 Thermoconvective instability of plane Poiseuille flow

The problem definition is sketched in Figure 3.1. It consists of a two-dimensional laminar flow in a horizontal channel suddently heated from below. A parabolic inlet velocity profile is prescribed, whereas the outlet is left free, i.e., the associated natural boundary condition is zero traction.

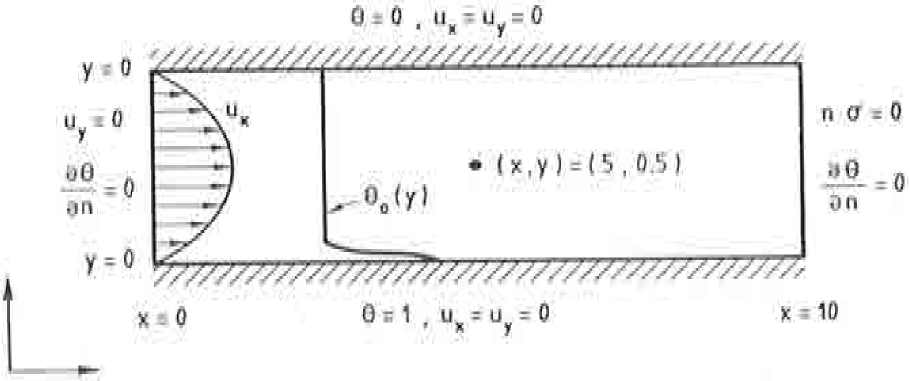
$\theta = 0$ , $u_x = u_y = 0$
$y = 0$
$u_y = 0$
$\frac{\partial\theta}{\partial n} = 0$
$y = 0$
$u_x$
$\theta_0(y)$
$(x, y) = (5, 0.5)$
$n\ \sigma = 0$
$\frac{\partial\theta}{\partial n} = 0$
$y$
$x$
$x = 0$
$\theta = 1$ , $u_x = u_y = 0$
$x = 10$

Figure 3.1 Geometry, initial and boundary conditions for the problem of thermoconvective instability of plane Poiseuille flow. Coordinates, velocity and temperature are assumed to be dimensionless.

This problem is solved in Reference [EP] as a benchmark for open boundary flows using a finite difference method and a fine grid.

This numerical test can be considered as a model for several relevant engineering problems, such as the fabrication of microelectronic circuits using the chemical vapour deposition process (cf. [EP], see references therein).

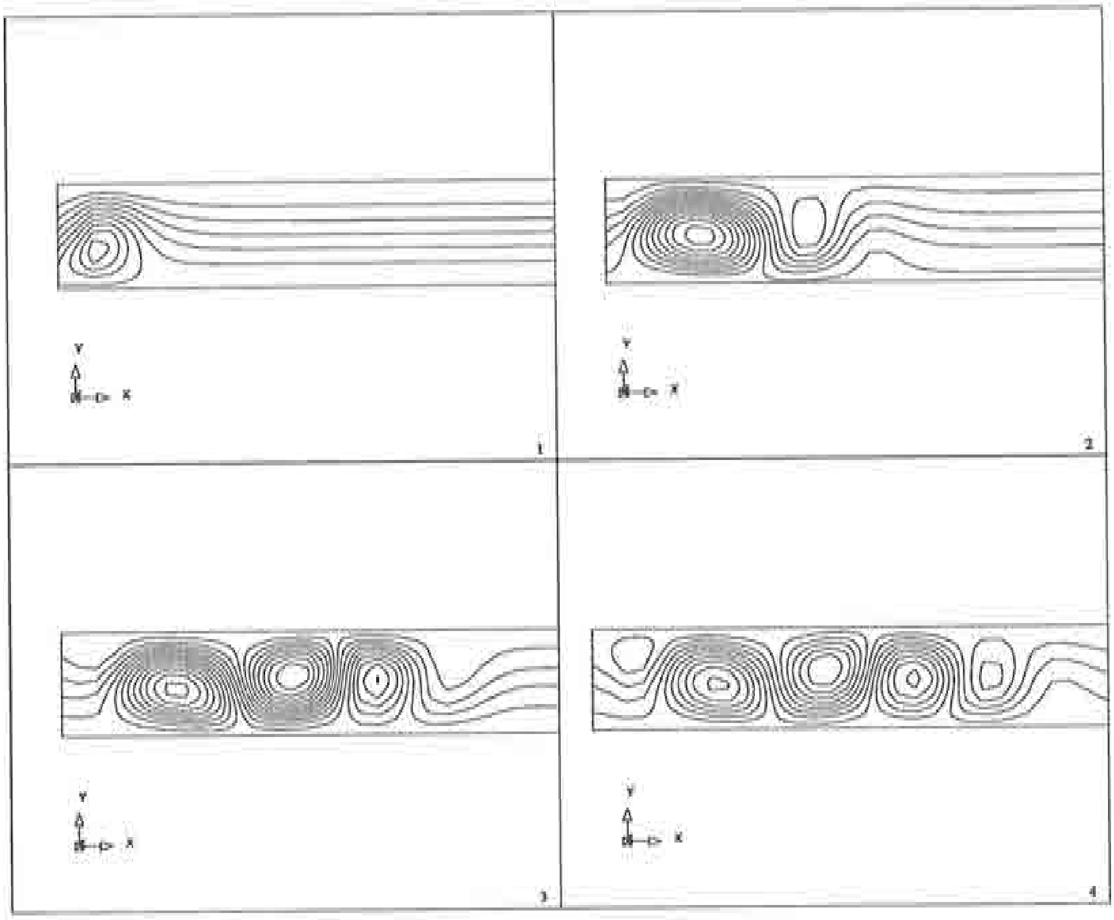

Figure 3.2 Transient evolution of the streamlines for the plane Poiseuille flow (PPF) heated from below at times: (1): $t = 0.2$; (2): $t = 0.8$; (3): $t = 1.2$; (4): $t = 1.4$.

Referring to Eqns. (3.6), the dimensionless parameters of the problem have been taken as $Re = 10$, $Fr = 1/150$ and $Pe = 40/9$ (the average inlet velocity, the height of the channel and the temperature difference between the top and bottom walls have been chosen as reference values for velocity, length and temperature, respectively). These parameters are the same as in Reference [EP] except for the Péclet number, which is slightly higher in that work ($Pe = 20/3$). In both cases, these values result in a thermoconvective instability of the basic Poiseuille flow. The linear stability analysis of unstable stratified plane Poiseuille flow in a infinite horizontal channel can be found in Reference [GR]. It is shown there that the form of the instability could vary from travelling tranverse waves to longitudinal rolls, with axes parallel to the main flow direction and thus leading to a three-dimensional flow pattern. Travelling transverse waves are found for small values of the Rayleigh number. This is the situation for the dimensionless parameters used here and therefore a two-dimensional calculation is possible. It should be remarked, however, that three-dimensional effects are in general very important for thermally coupled flows [Ke].

Let us describe now the numerical strategy followed to solve this problem. The domain $[0, 10] \times [0, 1]$ has been discretized using a uniform mesh of $30 \times 15 = 450$ $Q_2/P_1$

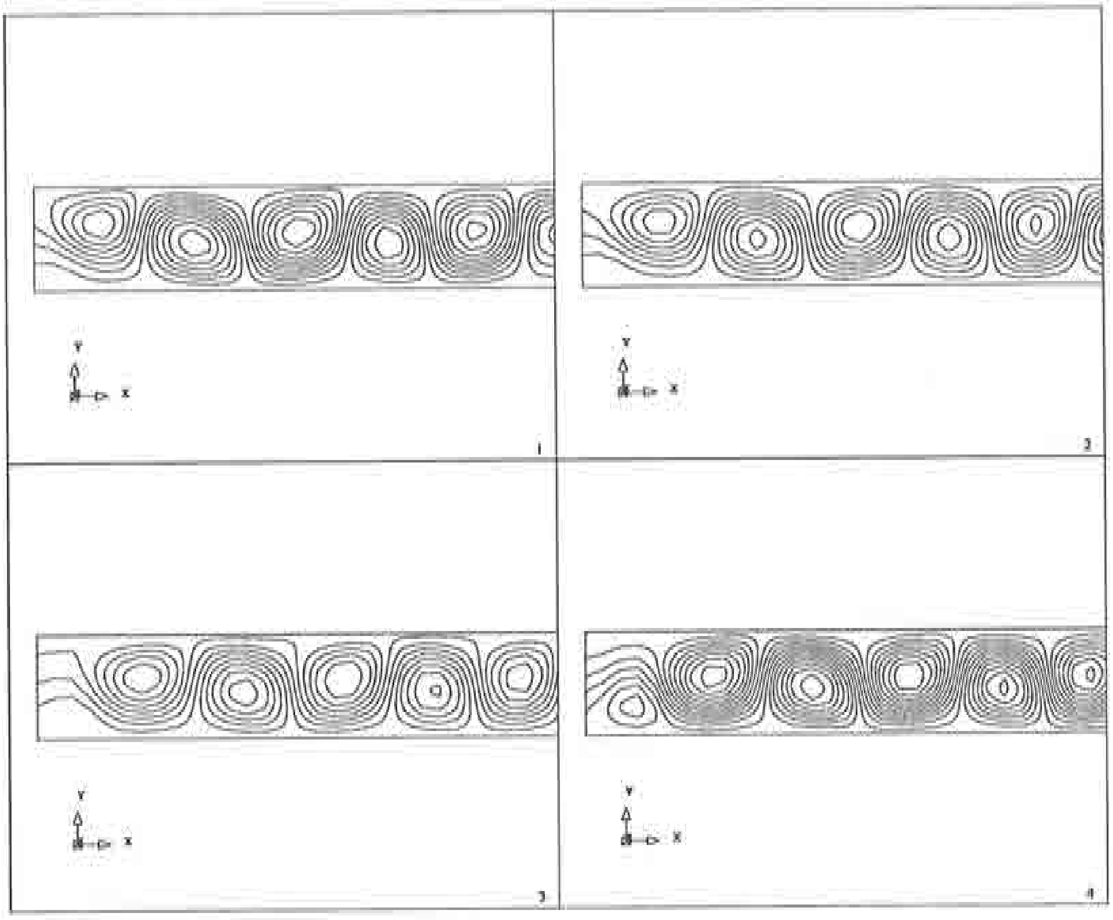

Figure 3.3 Transient evolution of the streamlines for the plane Poiseuille flow (PPF) heated from below at times: (1): $t = 1.6$; (2): $t = 1.8$; (3): $t = 2.2$; (4): $t = 2.5$.

elements, yielding 1891 nodal points. For this longitudinal length, it is concluded in Reference [EP] that the numerical solution is not affected by the artificial boundary conditions for $2 \leq x \leq 8$.

We have tested both the iterative penalty method with a parameter $\epsilon = 10^{-4}$ and the classical penalization, now with $\epsilon = 10^{-7}$. We will show later that both approaches yield a similar approximation for the incompressibility constraint and convergence history.

The SD formulation has been used for the space discretization, with and upwind parameter $\alpha_0 = 0.5$ (quadratic elements) and a natural length $h_0 = 2$ (corresponding to quadrilateral elements). The use of this method is needed to stabilize the convective terms of both the Navier-Stokes and the energy equations, since the cell Reynolds number and the cell Péclet number are higher than two. It is found that the maximum velocity norm is about 14.6 (cf. Figure 3.15) and therefore the maximum values of these parameters are $(Re)^e_{max} = |\mathbf{u}^e|_{max} h^e Re/2 \approx 14.6 \times 0.33 \times 10/2 = 24.33$ and $\gamma_{max} = |\mathbf{u}^e|_{max} h^e Pe/2 \approx 14.6 \times 0.33 \times 4.44/2 = 10.81$.

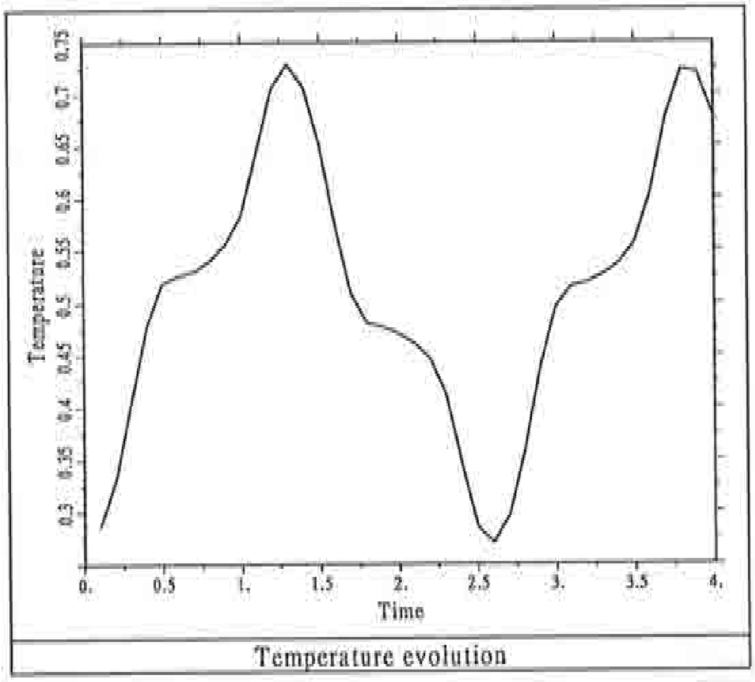

Figure 3.4 Transient evolution of the temperature at the central point ($x = 5$, $y = 0.5$). The initial time corresponds to $t = 3.3$ of the initial calculation shown in Figures 3.2 and 3.3 (PPF).

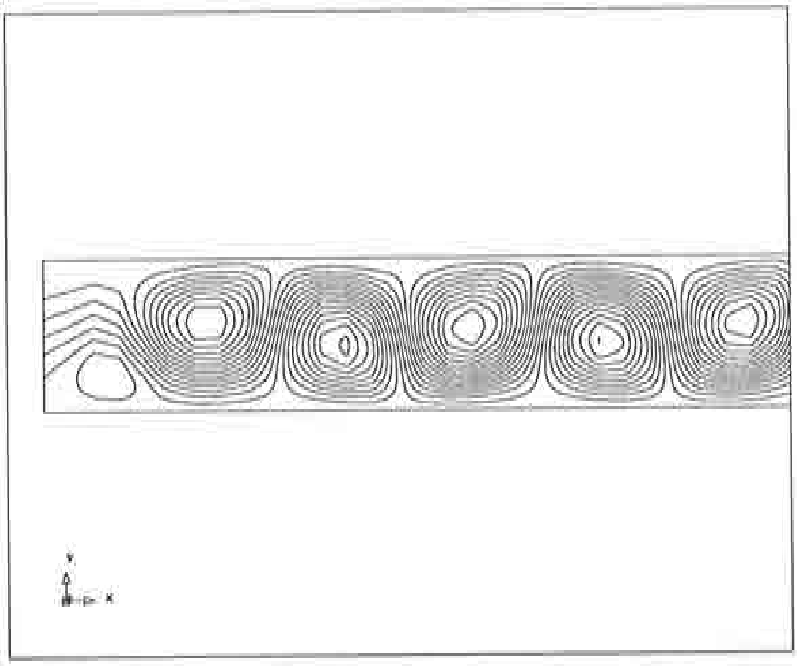

Figure 3.5 Streamlines for $t = 1.3$, corresponding approximately to the maximum value of the temperature at the central point (PPF).

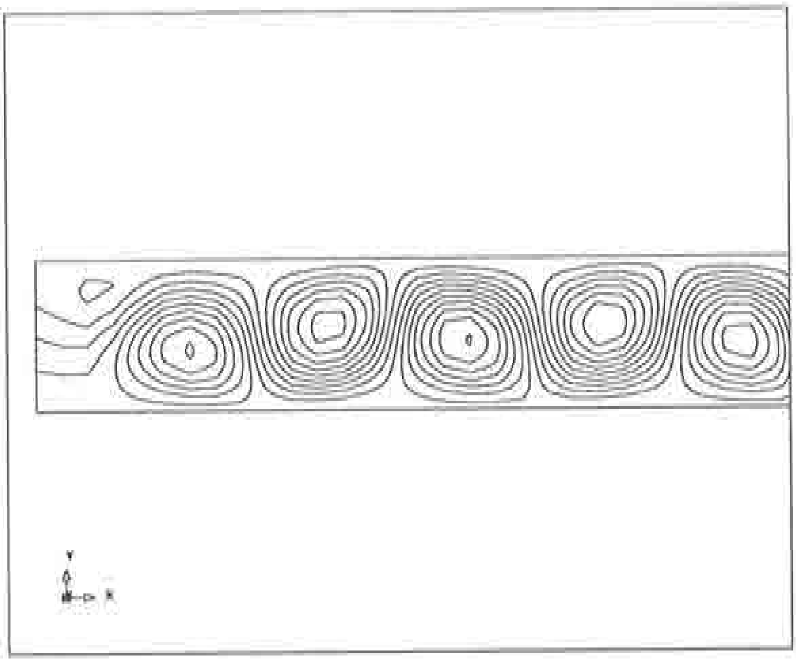

Figure 3.6 Streamlines for $t = 2.6$, corresponding approximately to the minimum value of the temperature at the central point (PPF).

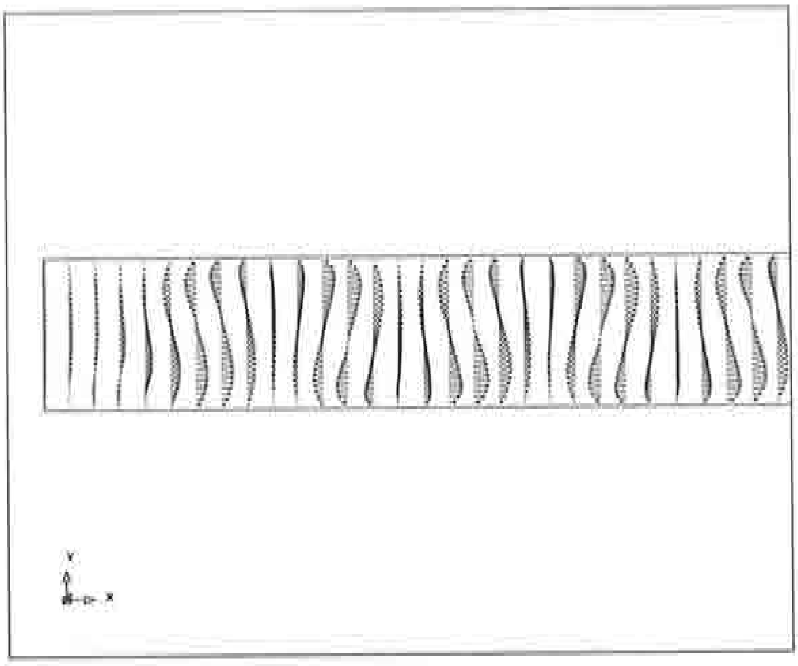

Figure 3.7 Velocity vectors for $t = 1.3$, corresponding approximately to the maximum value of the temperature at the central point (PPF).

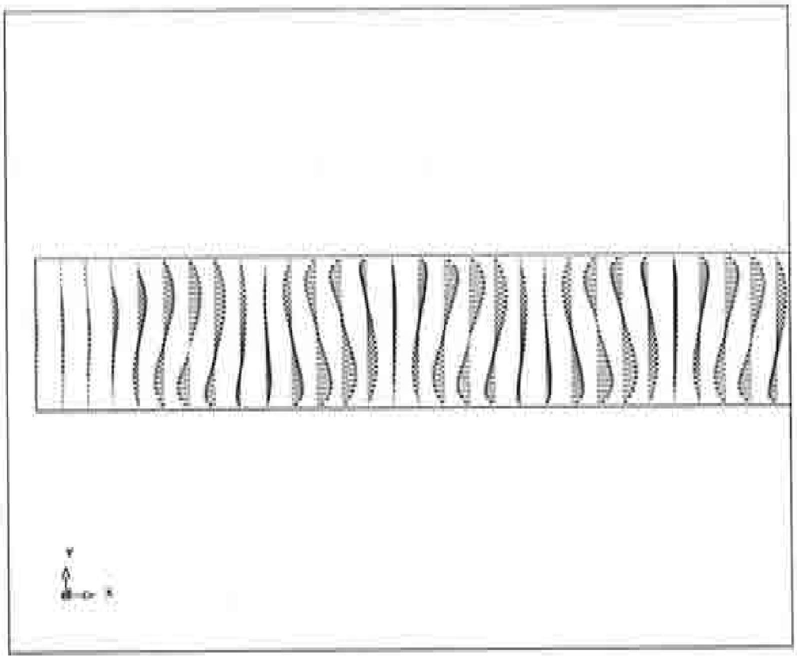

Figure 3.8 Velocity vectors for $t = 2.6$, corresponding approximately to the minimum value of the temperature at the central point (PPF).

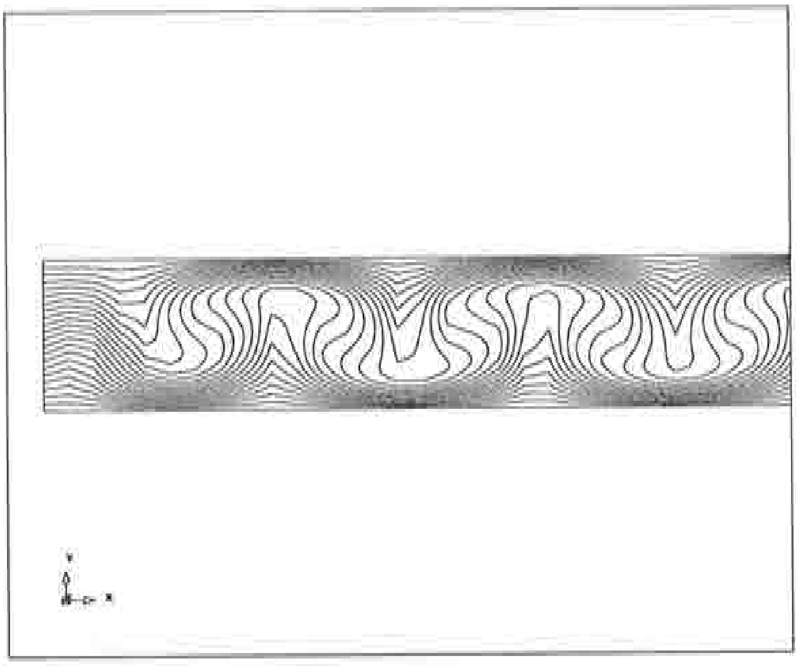

Figure 3.9 Temperature contours for $t = 1.3$, corresponding approximately to the maximum value of the temperature at the central point (PPF).

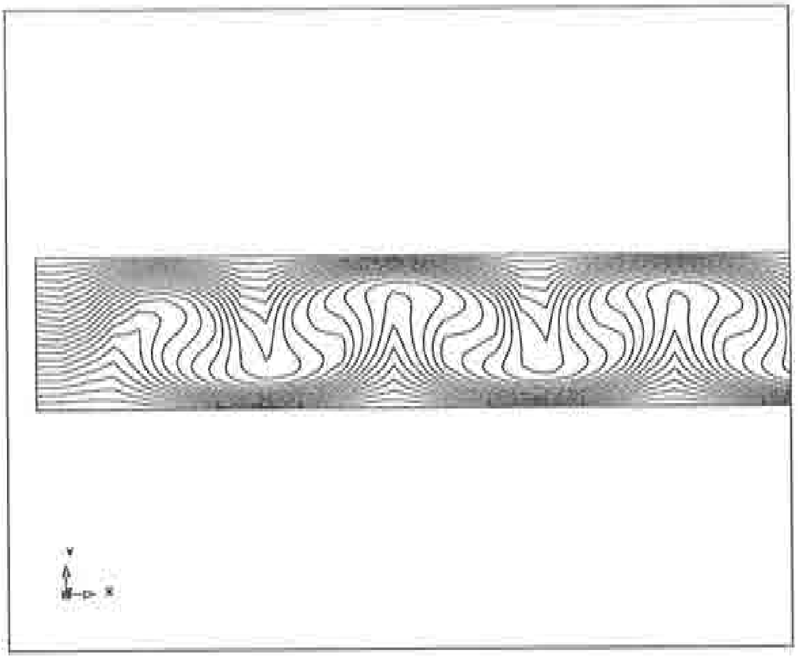

Figure 3.10 Temperature contours for $t = 2.6$, corresponding approximately to the minimum value of the temperature at the central point (PPF).

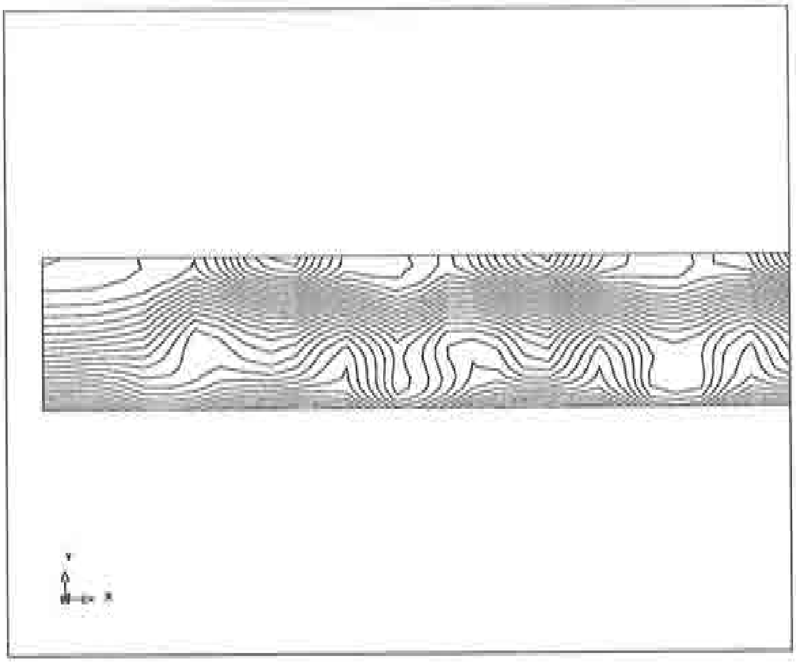

Figure 3.11 Pressure contours for $t = 1.3$, corresponding approximately to the maximum value of the temperature at the central point (PPF).

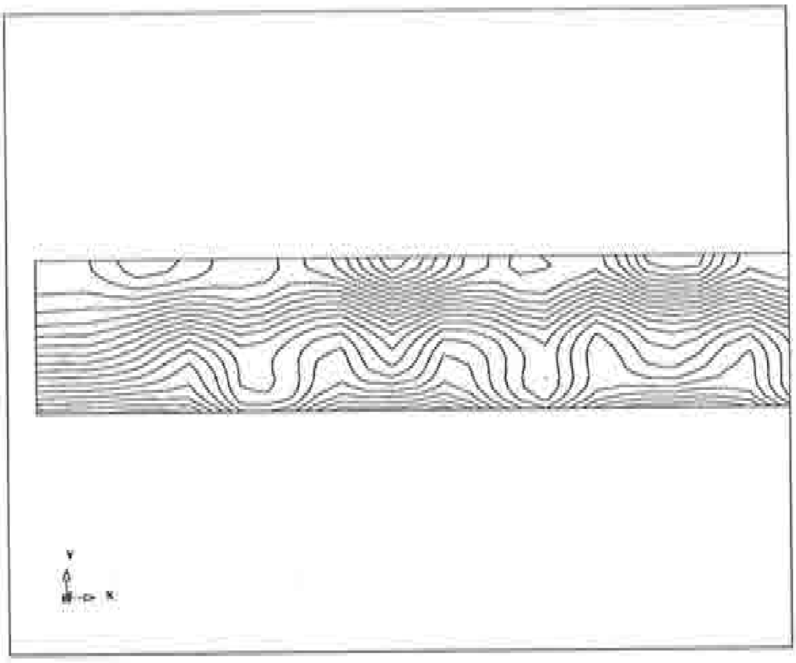

Figure 3.12 Pressure contours for $t = 2.6$, corresponding approximately to the minimum value of the temperature at the central point (PPF).

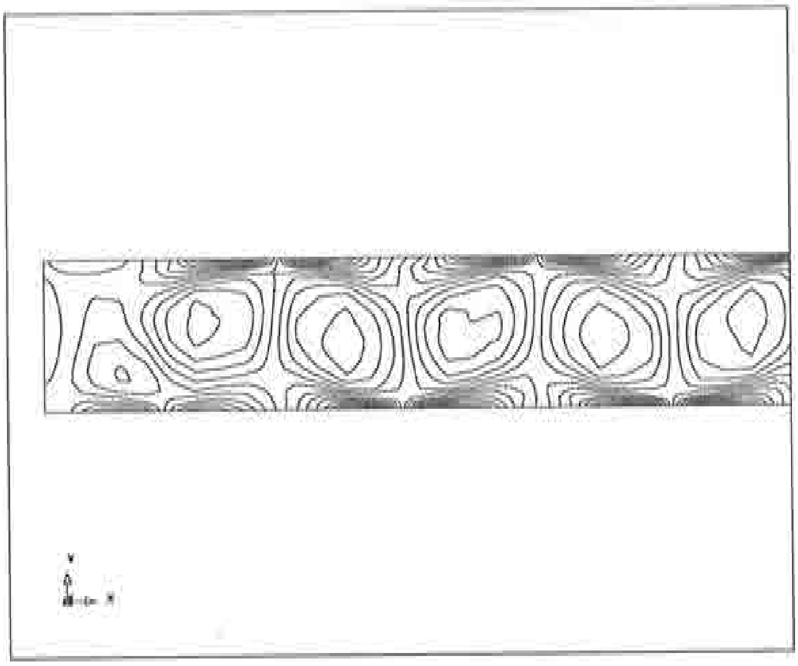

Figure 3.13 Vorticity contours for $t = 1.3$, corresponding approximately to the maximum value of the temperature at the central point (PPF).

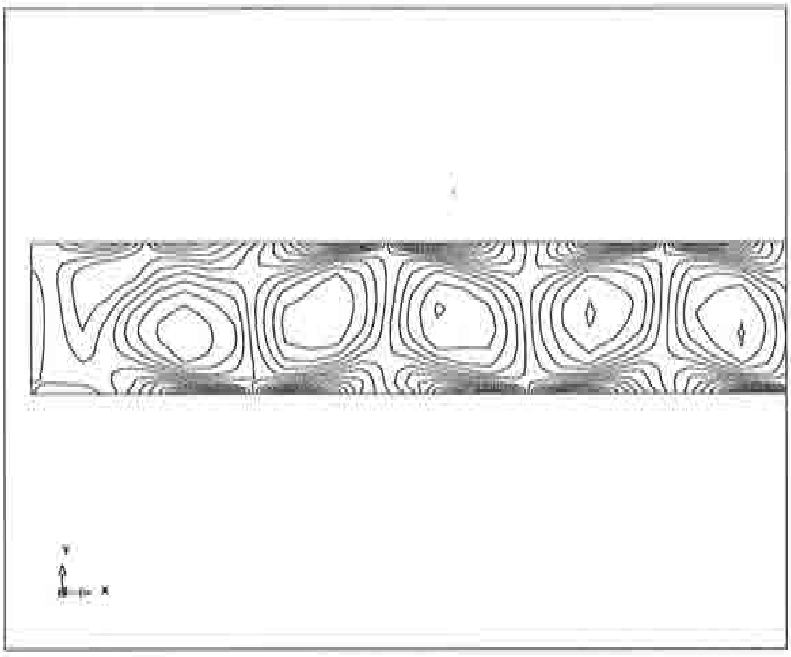

Figure 3.14 Vorticity contours for $t = 2.6$, corresponding approximately to the minimum value of the temperature at the central point (PPF).

The Gauss-Seidel block iterative procedure with a Newton-Raphson linearization of the energy equation has been used, solving first the Navier-Stokes equations and then the temperature equation. The first problem has been linearized only up to first order (Picard method). The convergence tolerance has been taken as 0.1 % in the relative $L^2$ norm.

Of special interest is the choice of the parameter $\theta$ of the generalized trapezoidal rule. As it has already been mentioned, we have found that the Crank-Nicolson method is very sensitive to the convergence tolerance (see Remark 3.3.(3)). The time step size has been taken as $\Delta t = 0.01$. For $TOL = 10\%$, instability problems have been found at time step number 5, whereas for $TOL = 1\%$ they do not appear until time step number 37 and for $TOL = 0.1\%$ until time step number 121. Using the backward Euler method ($\theta = 1$) the time stepping algorithm has been found to be stable in all the cases. The results presented here have been obtained using this method.

Numerical results are shown in Figures 3.2 to 3.18 (only one half of the computational domain is shown). The acronym 'PPF' (standing for Plane Poiseuille Flow) has been used to identify the problem to which figures correspond. The transient evolution from the basic Poiseuille flow to the periodic flow pattern finally obtained has been plotted in the eight snapshots of Figures 3.2 and 3.3 (times are given in the captions). After a time $t = 3.3$, the travelling waves are fully developed and a new run has been carried out, redefining $t = 0$ for $t = 3.3$. The period of the oscillations has been found to be approximately 2.5 time units. This can be observed from the transient evolution of the temperature at the central point ($x = 5, y = 0.5$) depicted in Figure 3.4. This value is very sensitive to the Péclet number, since in Reference [EP] and for $Pe = 20/3$ this period was found to be approximately 1.5 time units.

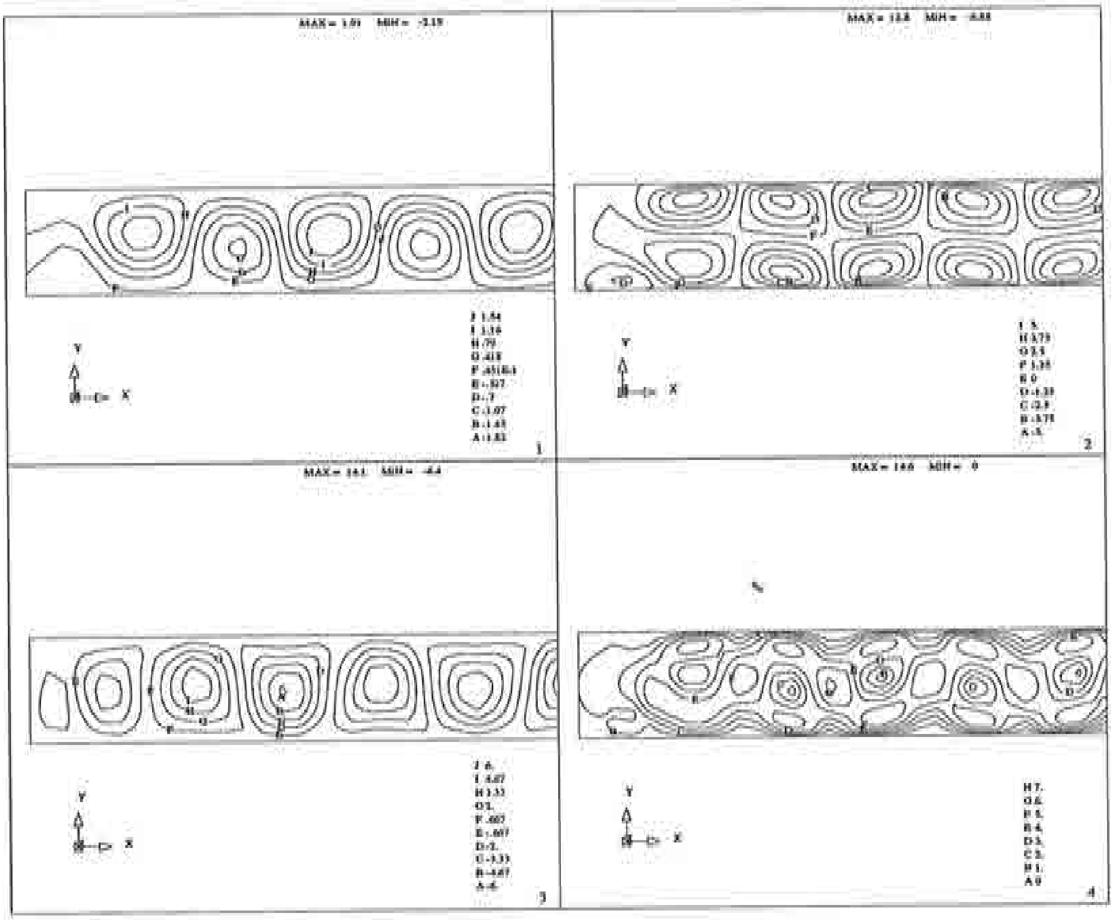

Figure 3.15 Numerical values for the velocity and streamfunction at $t = 1.3$ (PPF). (1): Streamfunction; (2): $x-$velocity component contours; (3): $y-$velocity component contours; (4): Norm of the velocity contours.

The streamlines, velocity vectors, temperature contours, isobars and vorticity contours for $t = 1.3$ and $t = 2.6$ are plotted in Figures 3.5 to 3.14. The first time corresponds to a maximum value for the temperature at the central point and the latter to a minimum. The periodicity of all these fields can be observed from the plots. Numerical values are given for $t = 1.3$ in Figures 3.15 and 3.16.

Finally, Figures 3.17 and 3.18 show the streamlines for $t = 1.3$ and $t = 2.6$ in the whole computational domain. The bad influence of the artificial boundary conditions can be observed, especially in what concerns the outlet wall. It is clear that the zero traction prescription does not reproduce the effect of an infinitely long channel. The proper evaluation of boundary conditions necessary for the numerical simulation of flows in infinite domains is an area that still deserves a lot of research.

Once the numerical strategy and the physical results have been described, let us discuss now the numerical behavior of the algorithm. The convergence history and the evolution of the incompressibility constraint for the first two time steps, starting from the Poiseuille flow, are shown in Figure 3.19. These results correspond to the iterative penalty method with $\epsilon = 10^{-4}$. The same plots for time step number 532 ($t = 5.32$)

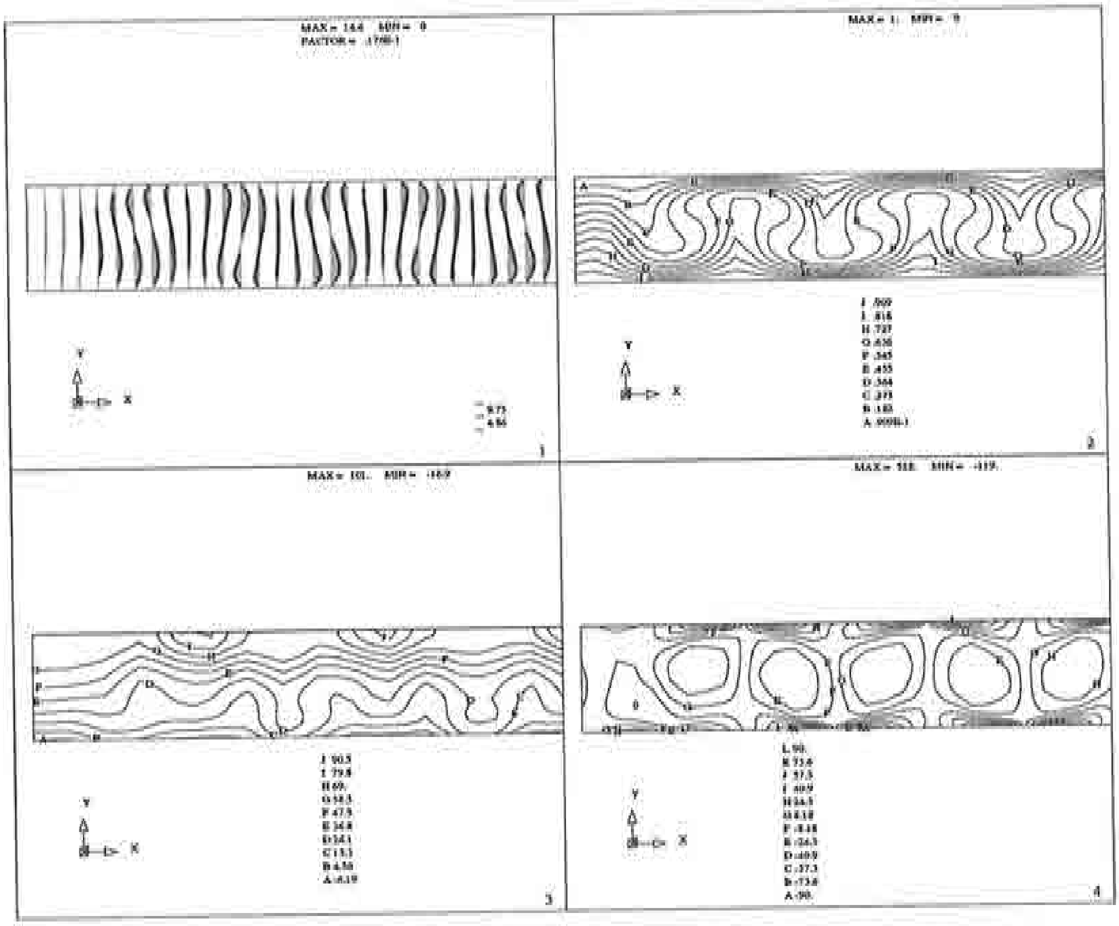

Figure 3.16 Numerical values for the velocity vectors, temperature, pressure and vorticity at $t = 1.3$ (PPF). (1): Velocity vectors; (2): Temperature; (3): Pressure; (4): Vorticity.

are shown in Figure 3.20, now for both the iterative penalty method with $\epsilon = 10^{-4}$ and the classical penalization with $\epsilon = 10^{-7}$. It is observed that the convergence history in both cases is almost the same, whereas the norm of the discrete velocity divergence decreases in the first case to $0.5 \times 10^{-7}$ and in the second case it remains constant and equal to $0.15 \times 10^{-7}$. The excellent behavior of the iterative penalty method is again observed for this type of problems.

Between three and five iterations have been required to converge for each time step. The CPU time per iteration has been 22.1 seconds. It is important to remark that the solution of the Navier-Stokes equation requires the 78.98% of CPU, whereas the temperature equation only the 15.24%. The increase of the computing time is not only due to the formation of the element matrices and assembly, more costly for the Navier-Stokes equations, but also to the solution of the final algebraic system of equations. The time required for the temperature equation is the 29% of the time needed for the Navier-Stokes equations. This gives an idea of the rapid increase of the computing time with the number of equations of the system using a direct solver, that is what we have employed. Having this in mind and observing that the iterations needed for each time step are mainly due to the nonlinearity of the Navier-Stokes equations, the block

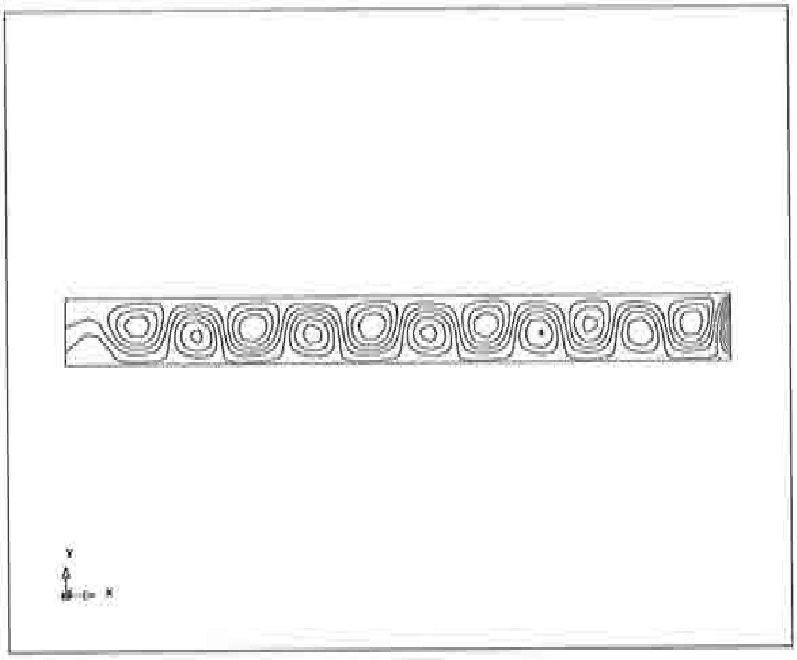

Figure 3.17 Influence of the outflow boundary condition for $t = 1.3$, corresponding approximately to the maximum value of the temperature at the central point (PPF).

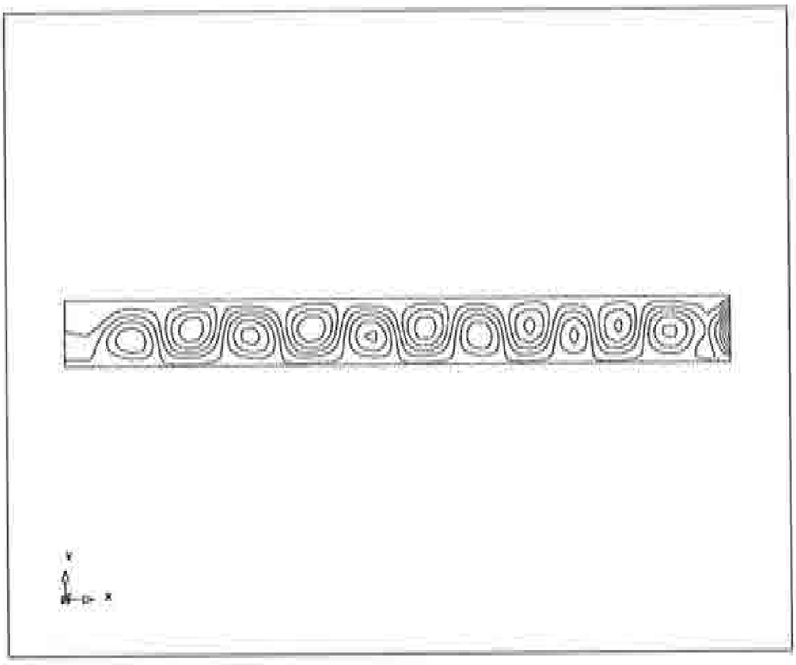

Figure 3.18 Influence of the outflow boundary condition for $t = 2.6$, corresponding approximately to the minimum value of the temperature at the central point (PPF).

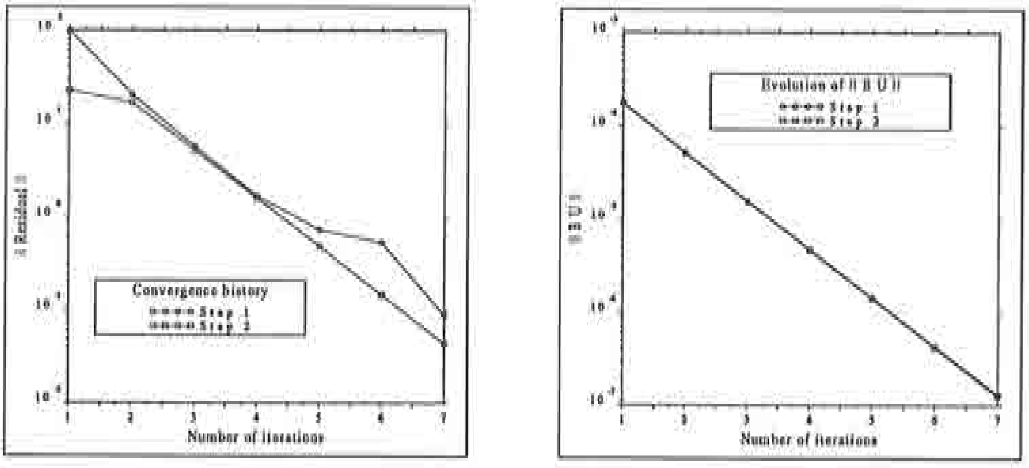

Figure 3.19 Convergence history and evolution of the norm of the incompressibility constraint for the first and second time steps (PPF).

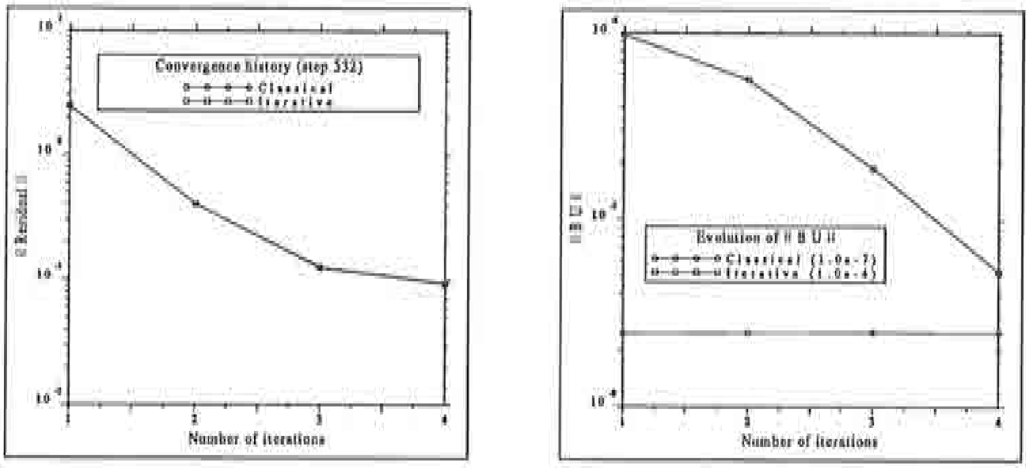

Figure 3.20 Convergence history and evolution of the norm of the incompressibility constraint using the classical penalty method with $\epsilon = 10^{-7}$ and the iterative penalization with $\epsilon = 10^{-4}$ for time step No. 532 (PPF).

iterative algorithm used to uncouple the thermal and mechanical problems seems to be a very efficient procedure.

### 3.5.2 Transient natural convection of low-Prandtl-number fluids

In this example, the transient convective motion of a fluid enclosed in a square cavity driven by a temperature gradient will be numerically analysed. The left vertical wall is suddently heated and mantained at a constant temperature, while the right vertical wall is mantained at the initial temperature. Horizontal walls are assumed to be adiabatic, i.e., the zero heat flux boundary condition is prescribed. Homogeneous Dirichlet boundary conditions are prescribed everywhere on the boundary for the velocity.

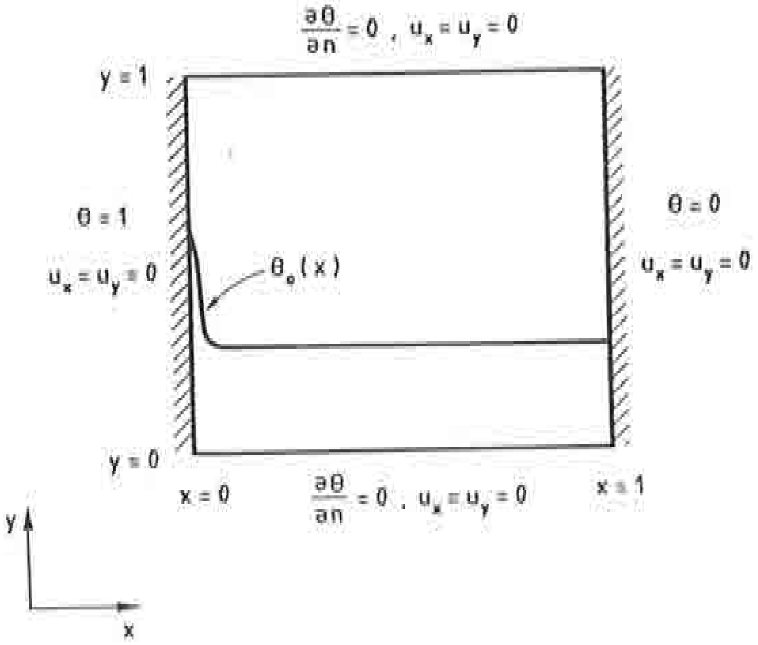
$\frac{\partial\theta}{\partial n} = 0$ , $u_x = u_y = 0$
y = 1
θ = 1
$u_x = u_y = 0$
$\theta_0(x)$
θ = 0
$u_x = u_y = 0$
y = 0
x = 0
$\frac{\partial\theta}{\partial n} = 0$ , $u_x = u_y = 0$
x = 1
y
x

Figure 3.21 Geometry, initial and boundary conditions for the problem of transient natural convection of low-Prandtl-number fluids. Coordinates, velocity and temperature are assumed to be dimensionless.

The problem definition is represented in Figure 3.21. All the variables of the problem have been nondimensionalized using the length of the cavity and the temperature difference between the two vertical walls as reference values for length and temperature, respectively. The reference velocity has been taken as $\kappa/L$, as explained in Section 3.2.1. Referring to Eqns. (3.7), the only dimensionless parameters involved in the problem are the Prandtl number $Pr$ and the Rayleigh number $Ra$ or, equivalently, the Grashof number $Gr$. Numerical results will be presented for $Pr = 0.005$ and the values $Gr = 3 \times 10^6$ and $Gr = 5 \times 10^6$.

The value $Pr = 0.005$ is very small and not often encountered in common fluids. For example, the Prandtl number is 0.71 for air, 7.03 for water and 0.0249 for mercury (at 293 K). Small values of $Pr$ are typical of liquid metals and semiconductors. The problem to be studied now is relevant to the solidification of ingots and casting, crystal growth from melts, materials processing, nuclear reactor safety and other applications (cf. [MV]).

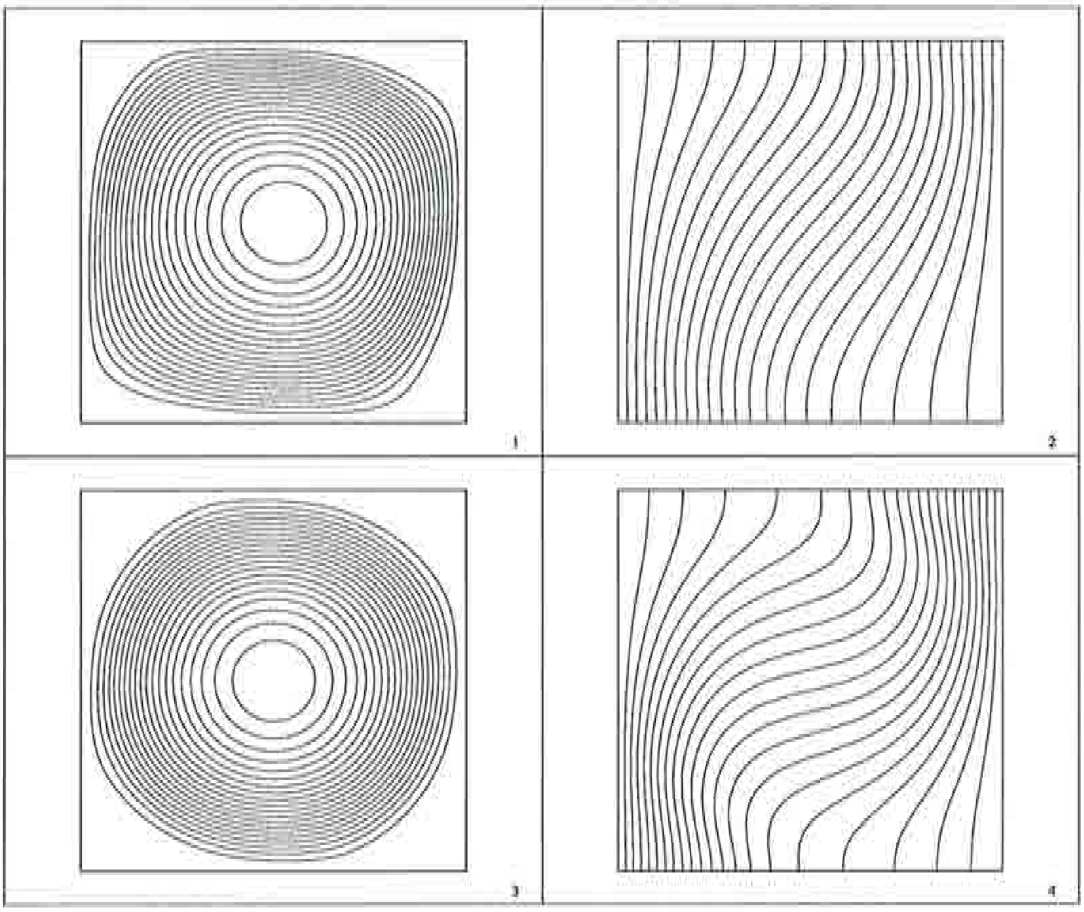

Figure 3.22 Transient evolution of the streamlines and the temperature contours for the problem of natural convection of low-Prandtl-number fluids (LPN), $Gr = 3 \times 10^6$. (1): Streamlines, $t = 0.4$; (2): Temperature contours, $t = 0.4$; (3): Streamlines, $t = 1.2$; (4): Temperature contours, $t = 1.2$.

Although the problem just described is a very popular test for thermally coupled flows when $Pr$ is high, the interest for solving low-Prandtl-number flows is that this problem is not yet well understood. It is found that the flow exhibits a periodic oscillation when the Grashof number exceeds a critical value. In particular, for $Pr = 0.005$ a steady-state solution is obtained for $Gr = 3 \times 10^6$ but the solution bifurcates and for $Gr = 5 \times 10^6$ an oscillatory flow field is found. For further information about this problem the reader is referred to the work of Mohamad & Viskanta [MP], from where this problem has been taken. Our purpose here is to demonstrate the efficiency of the numerical method proposed in this work and also to get more insight in the physics of the problem now considered. A much more detailed information about the recirculation zones at the corners of the cavity and the dynamics of the vorticity than in the above quoted reference will be given.

The numerical strategy employed is as follows. The finite element mesh used to discretize the unit square is the same as in Example 2.1 and shown in Figure 2.6. It consists of 671 $Q_2/P_1$ elements and 2809 nodal points. The SD formulation has been

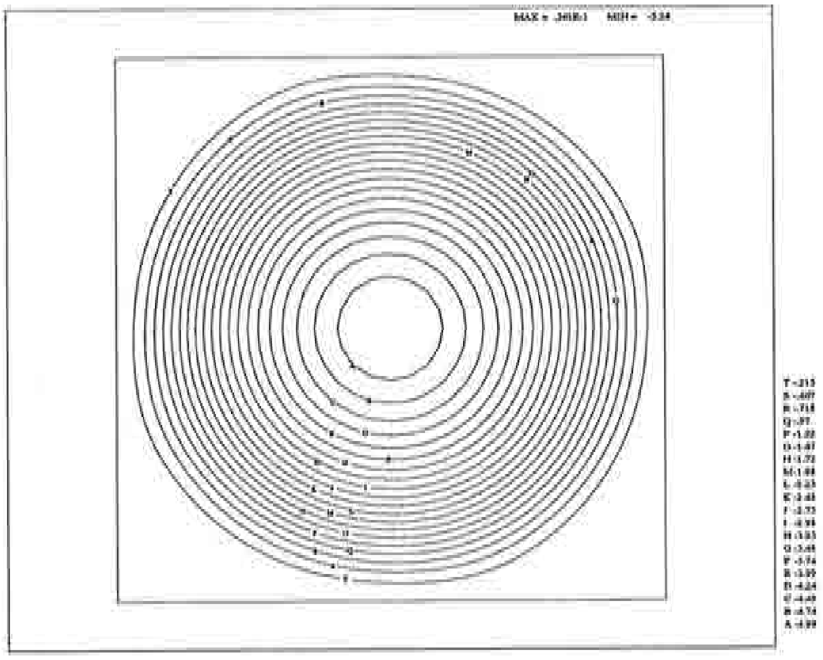

**Figure 3.23** Numerical values of the streamfunction when the steady-state has already been reached, $Gr = 3 \times 10^6$ (LPN).

used for both the Navier-Stokes and the energy equation, with $\alpha_0 = 0.5$ and $h_0 = 2$ as upwind factors and length of the parent domain, respectively. The iterative penalization with $\epsilon = 10^{-4}$ has been chosen, yielding a final value of order $10^{-12}$ for the norm of the discrete velocity divergence in all the time steps. The Navier-Stokes equations have been linearized up to first order, and the Gauss-Seidel block iterative method and Newton-Raphson linearization of the temperature equation have been adopted. The convergence tolerance has been taken as 0.1% in the relative $L^2$ norm. Based on the results and comments of the previous section, $\theta = 1$ (backward Euler) has been taken for the generalized trapezoidal rule to advance in time.

Let us first discuss the results for $Gr = 3 \times 10^6$ and shown in Figures 3.22 to 3.28 (the abbreviation 'LPN', standing for Low-Prandt-Number, has been included to identify the problem). It has already been said that in this case a stable steady-state solution is found. The time step size has been taken as $\Delta t = 0.04$, a high value, considering that it is of the same magnitude as the mesh diameter and the backward Euler scheme is only first order accurate. The steady-state solution is completely developed at $t = 6$, time for which results are presented.

Figure 3.22 shows the transient evolution from the motionless flow field to the thermally induced solution. It is observed that the streamlines are initially a little squared (for $t = 0.4$) and evolve to the almost circular shape shown in Figure 3.23 (for $t = 6$). It is also observed how the temperature contours accomodate from the initial constant temperature gradient to the final configuration of Figure 2.25. A detail of the vortices created at the corners of the cavity is shown in Figure 3.24. Two vortices appear at the top right and bottom left corners with similar strength, and only one in the other two corners. Let us remark that the maximum and minimum values for the streamfunction are *exactly* the same as those obtained in Reference [MV] using a much finer mesh ($81 \times 81 = 6561$ grid points) but a finite difference method.

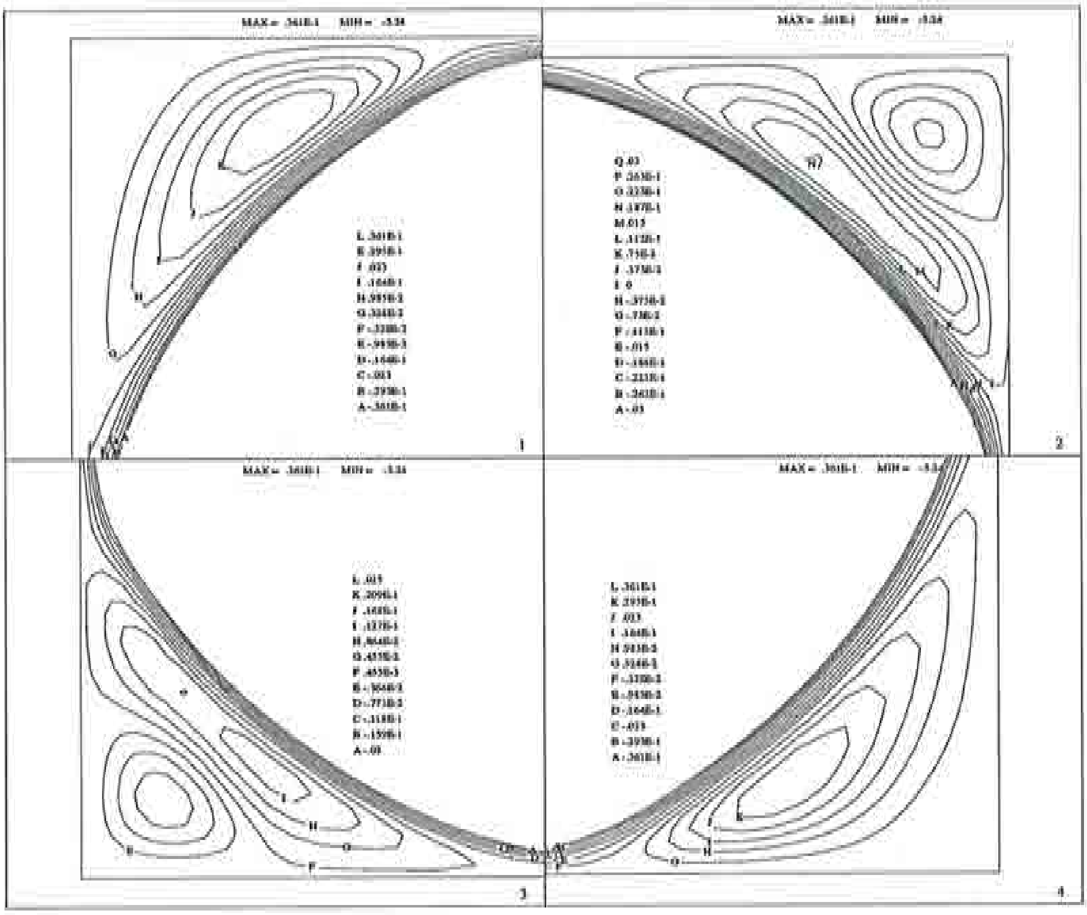

Figure 3.24 Details of the steady-state streamlines at the four corners of the cavity (LPN), $Gr = 3 \times 10^6$. (1): Top left corner; (2): Top right corner; (3): Bottom left corner; (4): Bottom right corner.

The velocity vectors, isobars and vorticiy contours are shown in Figures 3.26, 3.27 and 3.28, respectively. It is interesting to observe that pressure gradients are almost constant at the middle of the walls and that high vorticity gradients are generated there. It is argued in Reference [MV] that the instability found for higher values of $Gr$ is originated at the top right vortex. We believe that the sources of instability are these high gradients of vorticity just mentioned. They are due to the fact that the flow has to accomodate from the circular velocity field in the middle of the cavity to a zero velocity at the walls, without smooth transition. Figure 3.26 is illustrative of this situation.

The case $Gr = 5 \times 10^6$ is considered next. Now the time step size has been taken as $\Delta t = 0.004$. The computation has started with the steady-state solution found before, redefining $t = 0$ for $t = 6$. The transient evolution of the $x-$velocity component at the points of coordinates $(0.995, 0.5)$ and $(0.976, 0.5)$ is depicted in Figure 2.29. It is observed that an oscillatory flow pattern has been developed. The amplitude of the oscillations grows slowly as time goes on. Details of the streamlines, temperature contours, isobars and vorticity contours are shown for $t = 3.2$ in Figures 3.30 to 3.34. From the former it is seen that now two more secondary vortices appear at the top left

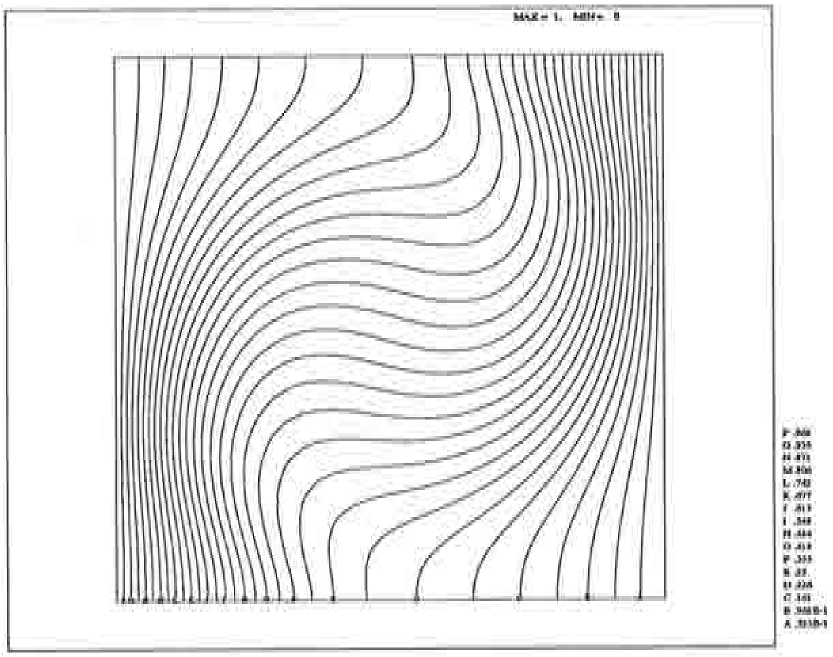

**Figure 3.25** Steady-state temperature contours, $Gr = 3 \times 10^6$ (LPN).

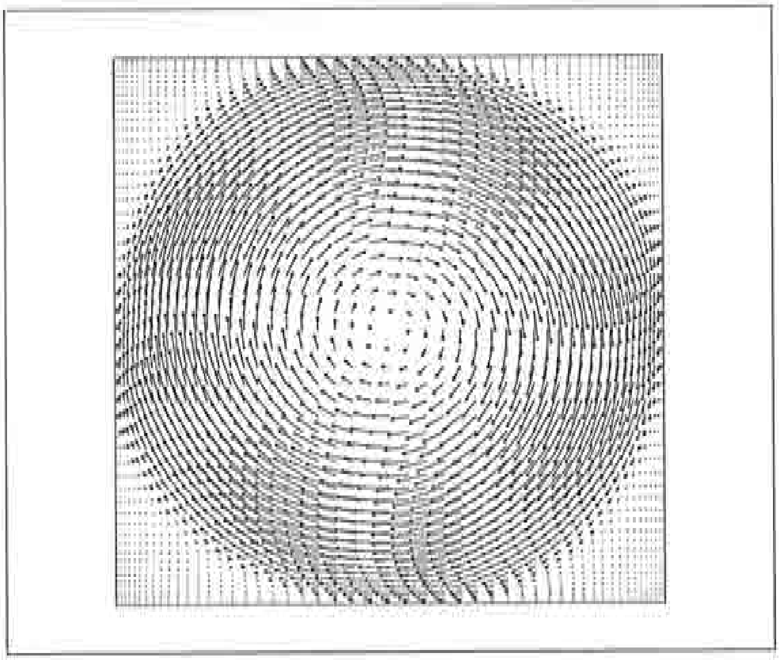

**Figure 3.26** Steady-state velocity vectors, $Gr = 3 \times 10^6$ (LPN).

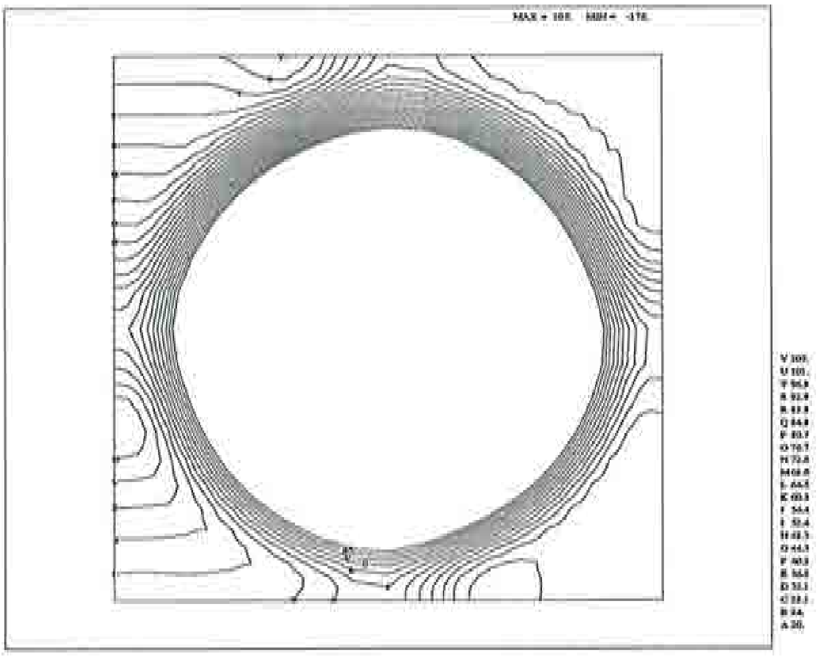

Figure 3.27 Steady-state pressure contours, $Gr = 3 \times 10^6$ (LPN).

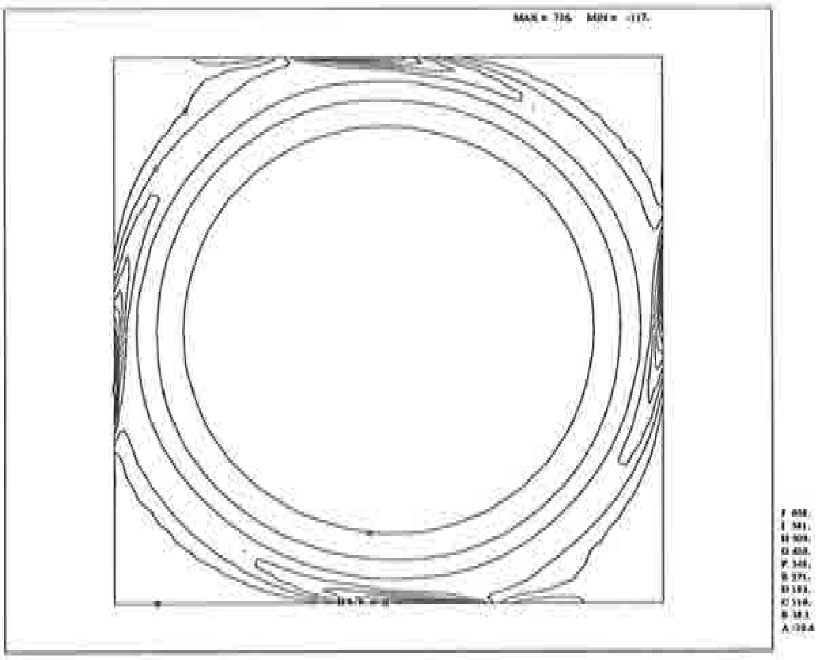

Figure 3.28 Steady-state vorticity contours, $Gr = 3 \times 10^6$ (LPN).

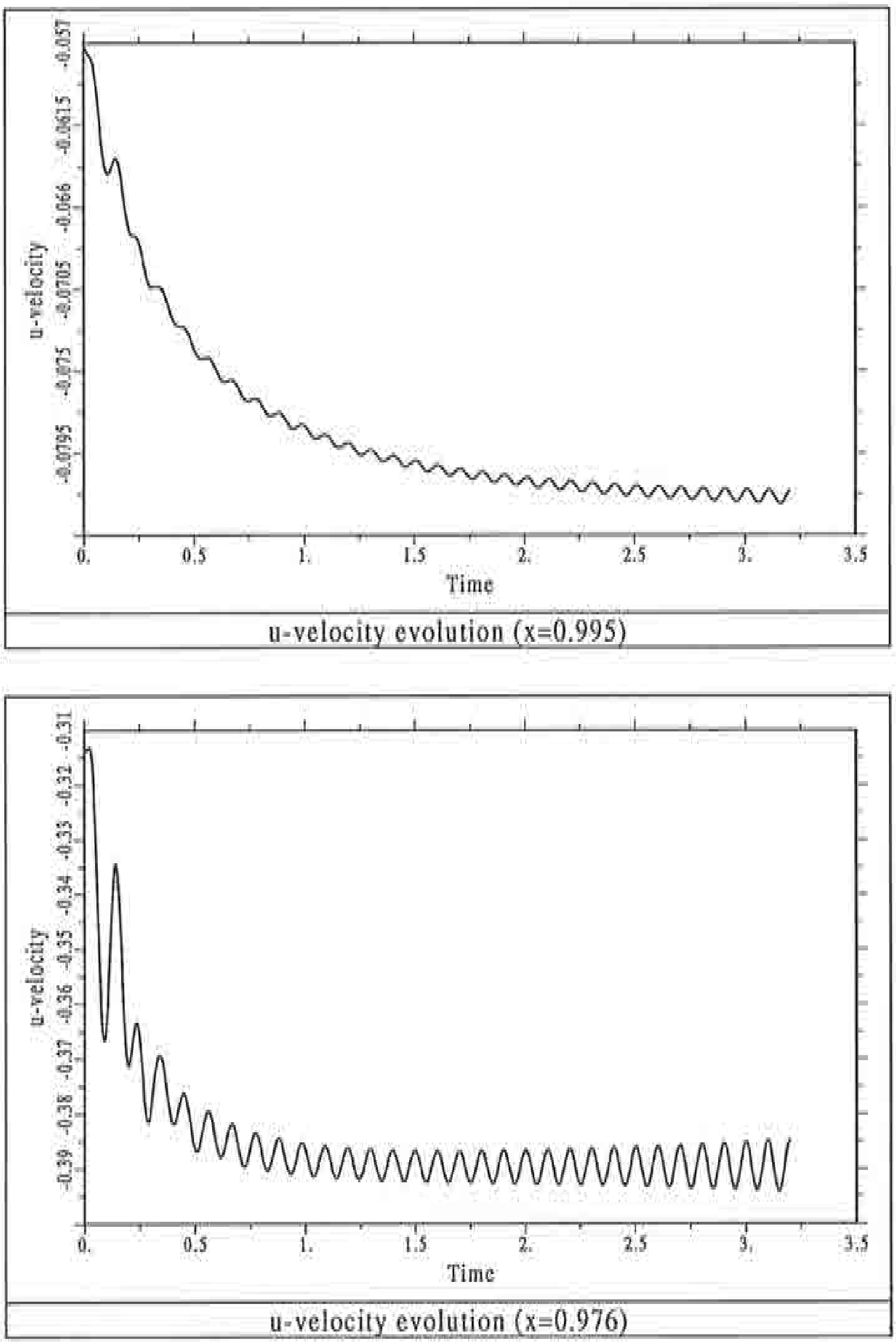

u-velocity evolution (x=0.995)

u-velocity evolution (x=0.976)

**Figure 3.29** Transient evolution of the $x-$velocity component at points $(0.995, 0.5)$ and $(0.976, 0.5)$, $Gr = 5 \times 10^6$ (LPN).

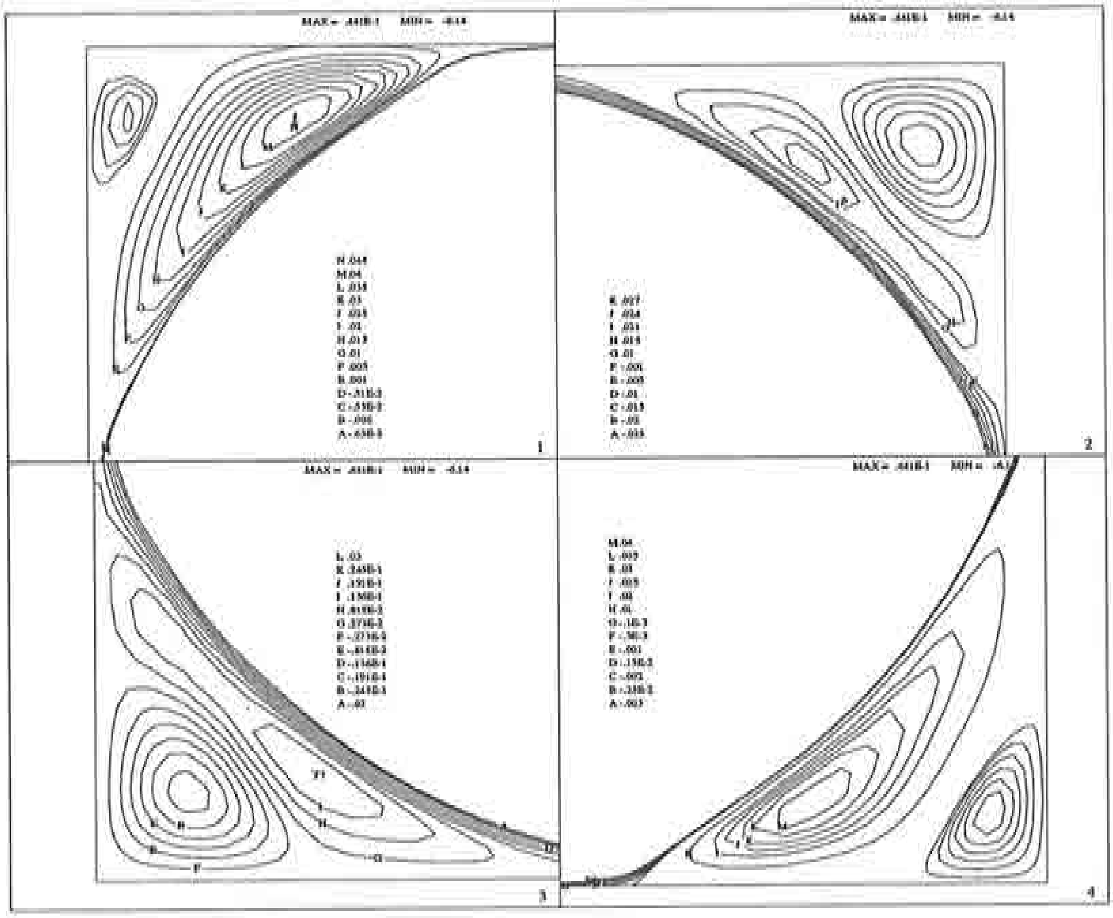

Figure 3.30 Details of the streamlines at the four corners of the cavity for $t = 3.2$, $Gr = 5 \times 10^6$ (LPN). (1): Top left corner; (2): Top right corner; (3): Bottom left corner; (4): Bottom right corner.

and bottom right corners. The center of the elongated vortex at the other two corners oscillates around the position found for $Gr = 3 \times 10^6$ (compare with Figure 3.24).

Finally, let us mention that the CPU time needed per iteration has been 45.483 seconds, of which the 83.41% are required by the Navier-Stokes solver and the 16.13% for the solution of the temperature equation. The solution of the linear algebraic system for this problem needs the 25.37% of what is needed for the Navier-Stokes equations. Between two and three iterations have been needed per time step for the case $Gr = 3 \times 10^6$ with $\Delta t = 0.04$ and only one in most of the time steps for the case $Gr = 5 \times 10^6$ with $\Delta t = 0.004$. This again indicates that using a block iterative method for thermally coupled problems is a good option.

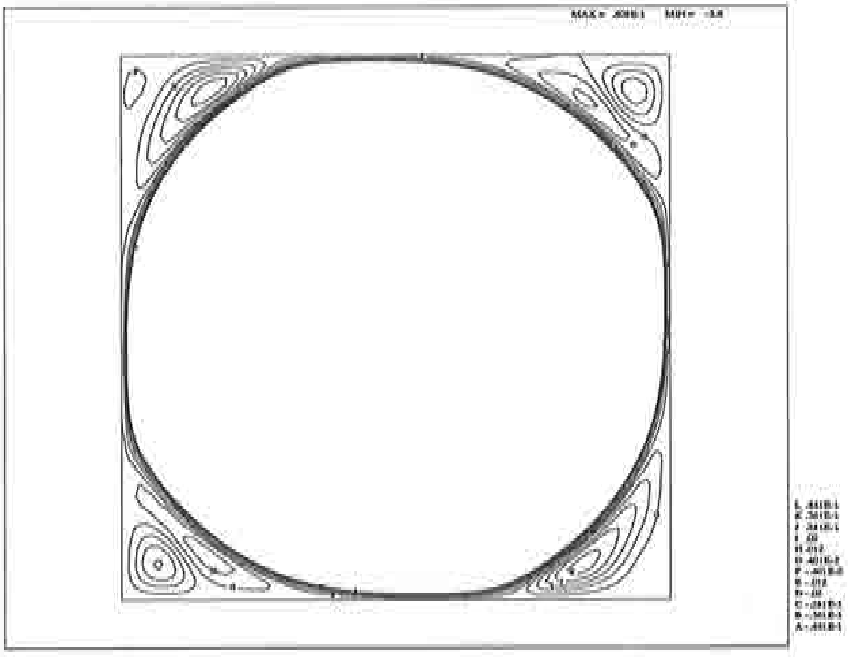

Figure 3.31 Global picture of the streamlines at the corners cavity for $t = 3.2$, $Gr = 5 \times 10^6$ (LPN).

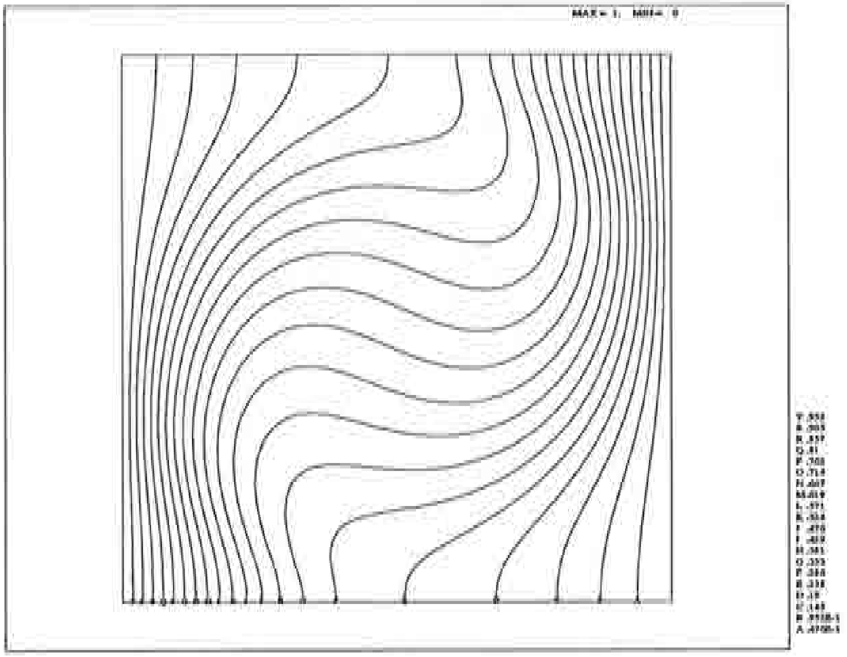

Figure 3.32 Temperature contours for $t = 3.2$, $Gr = 5 \times 10^6$ (LPN).

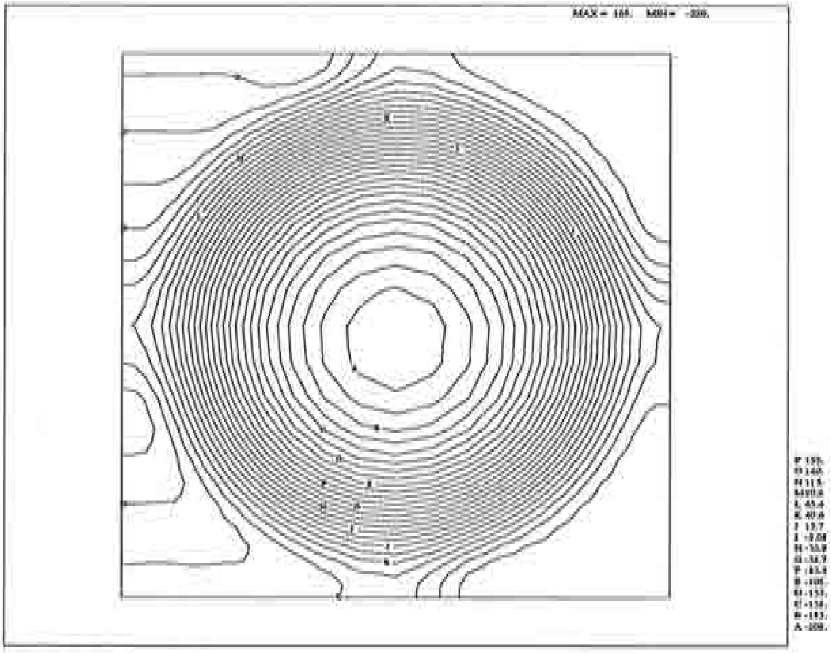

Figure 3.33 Pressure contours for $t = 3.2$, $Gr = 5 \times 10^6$ (LPN).

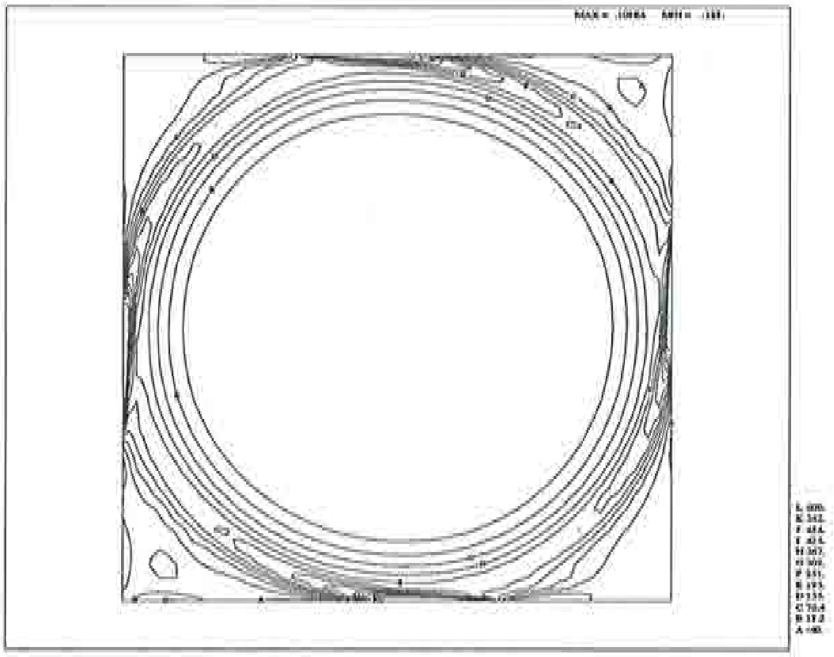

Figure 3.34 Vorticity contours for $t = 3.2$, $Gr = 5 \times 10^6$ (LPN).

### 3.5.3 The 4:1 plane extrussion of a power-law fluid

In this section we present some numerical results obtained for the well-known 4:1 plane extrusion problem. This is a very popular test for non-Newtonian flows, since all the flow features that characterize these fluids are present in this problem. It is also used as a test to check error estimators and adaptive remeshing techniques (see, e.g., Reference [DT]).

The geometry and the boundary conditions are depicted in Figure 3.35. The variation of the viscosity and the components of the velocity will be given for sections $AA$, $BB$ and $CC$ indicated in this Figure.

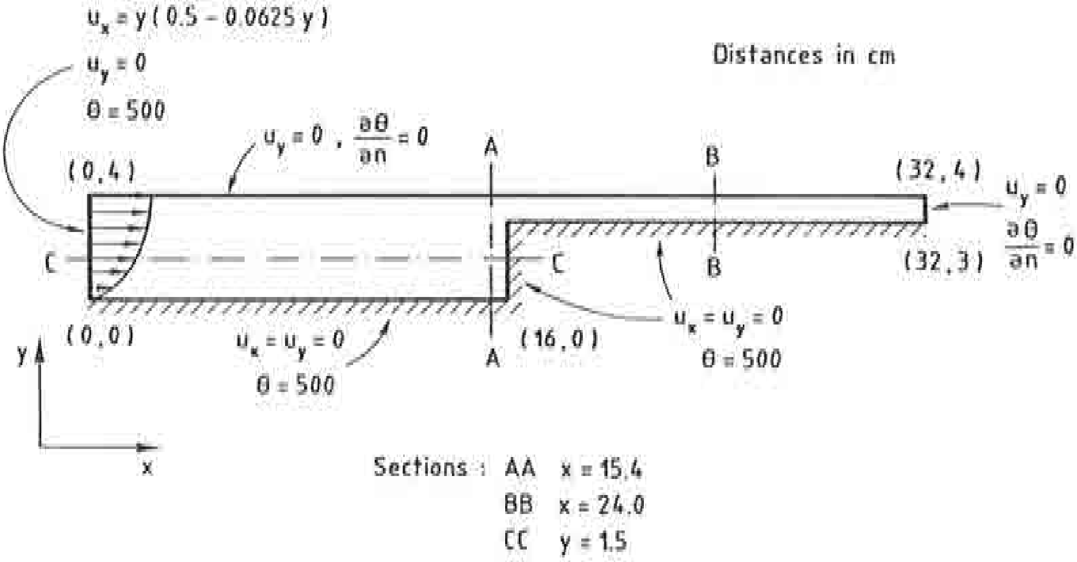

**Figure 3.35** Geometry and boundary conditions for the 4:1 plane extrusion of a power-law fluid.

Here, Eqns. (3.62) modelling the creeping flow of nonlinear materials will be solved numerically. The finite element mesh employed for the space discretization is composed of 525 $Q2/P1$ elements (biquadratic interpolation for the velocity, piecewise linear pressure), with a total of 2201 nodal points. There are 15 elements in the $y-$direction from the coordinates $y = 3$ to $y = 4$ and only 12 from $y = 0$ to $y = 3$. The concentration of elements in the former zone is needed if one wants to reproduce accurately the shear thinning effect of fluids whose viscosity obeys the power law that we shall consider now, given by

$$\mu = K_0 \left[4I_2(\varepsilon)\right]^{(n-1)/2} \exp\left(\frac{\beta}{\vartheta}\right) \tag{3.81}$$

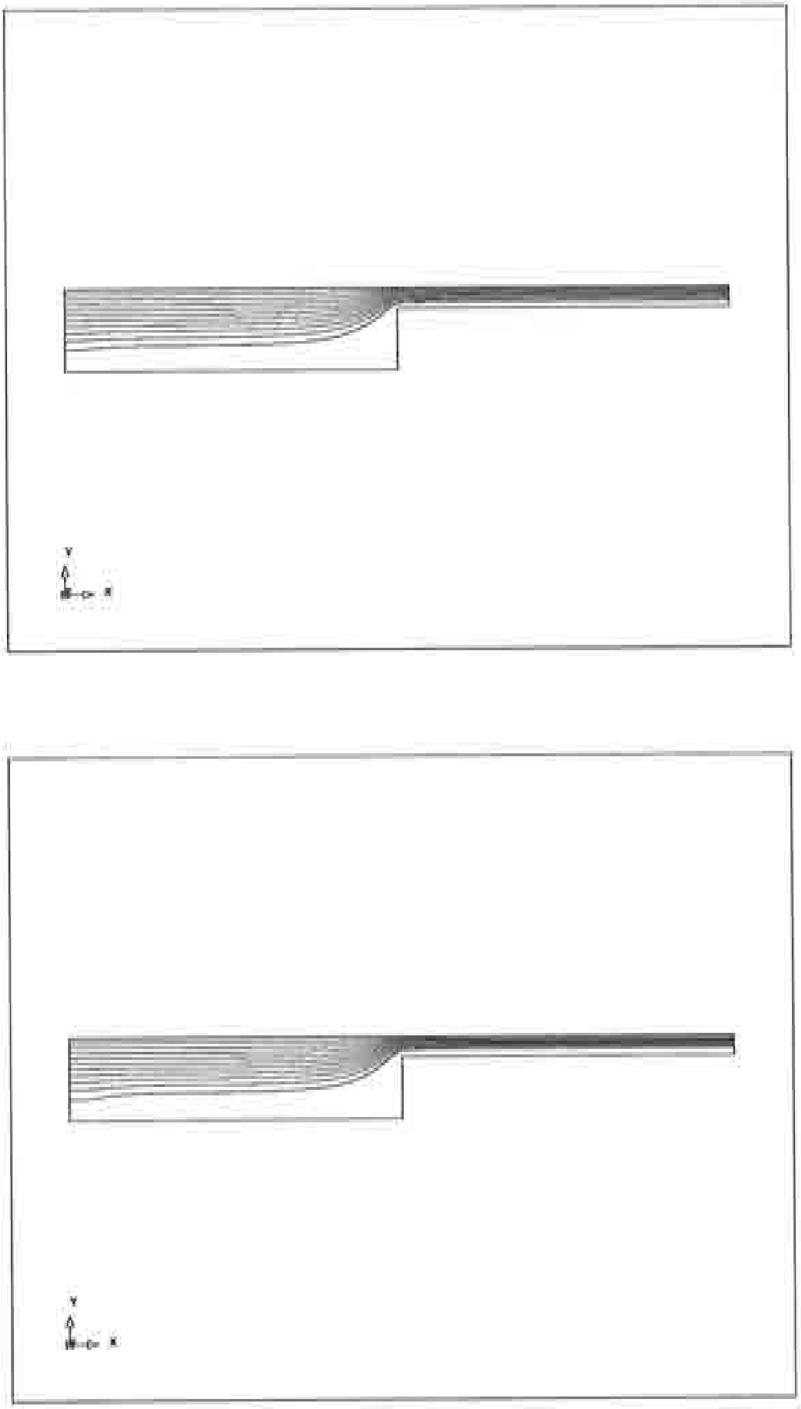

Figure 3.36 Streamlines for $\beta = 0$ (a) (thermally independent viscosity) and for $\beta = 2 \times 10^3$ (b) (thermally coupled flow). Observe the different curvature near the inflow vertical wall and the different gradient of the streamfunction in the exit channel (EPL).

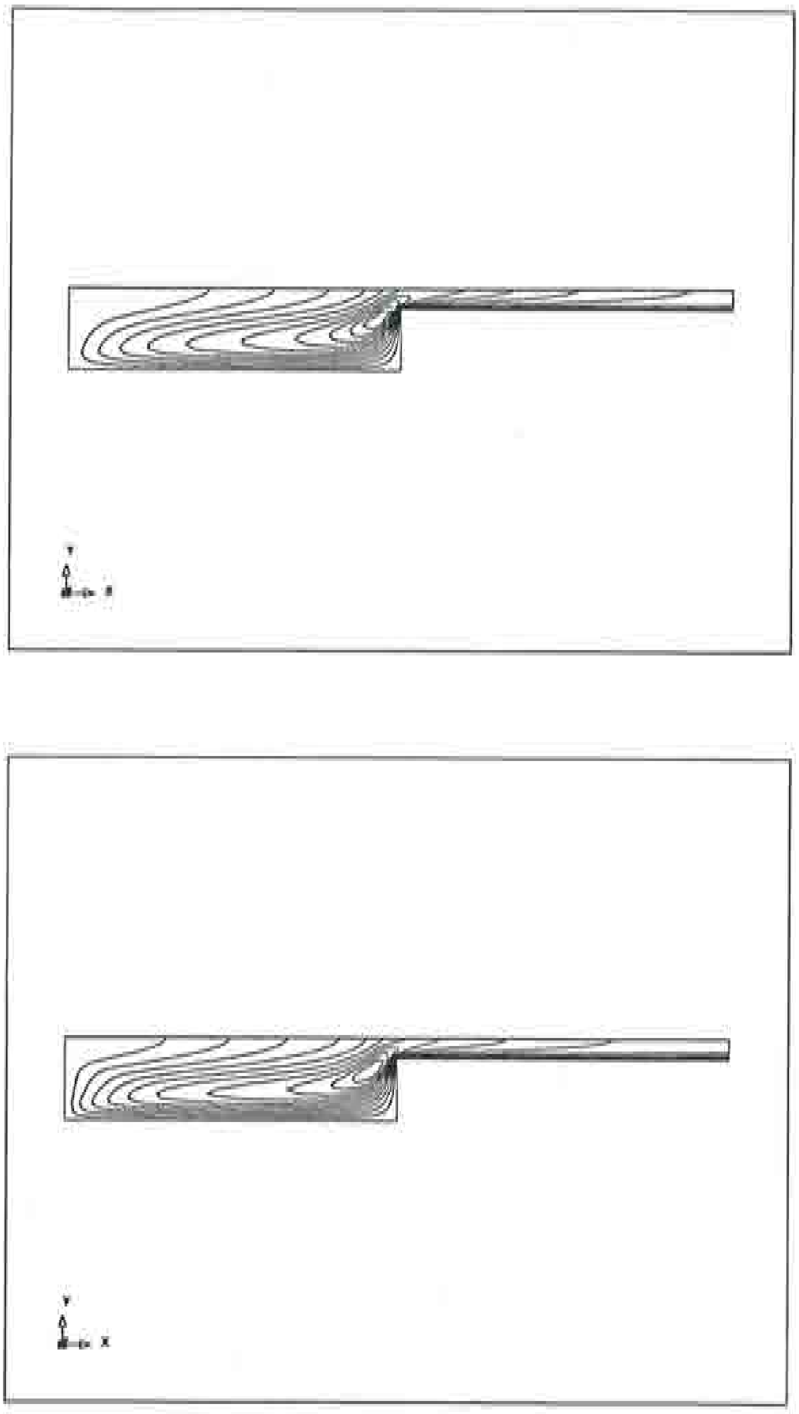

Figure 3.37 Temperature contours for $\beta = 0$ (a) (thermally independent viscosity) and for $\beta = 2 \times 10^3$ (b) (thermally coupled flow) (EPL).

In this expression, $K_0, n$ and $\beta$ are physical constants ($K_0$ is the material consistency and $n$ the rate sensitivity) and $\vartheta$ is the temperature. The power law given by Eqn. (3.50) has been combined with an exponential thermal dependence as dictated

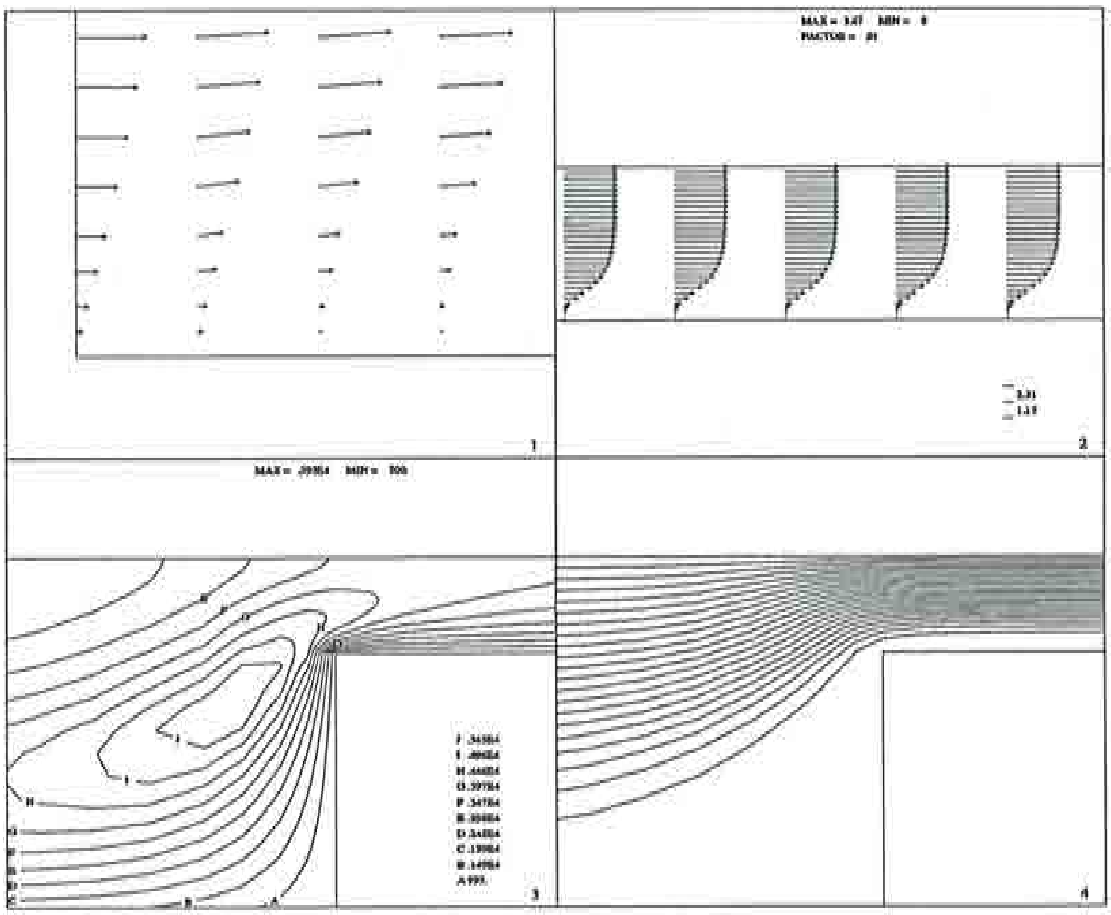

Figure 3.38 Details of the flow for $\beta = 0$ (EPL). (1): Accomodation of the parabolic velocity profile, corresponding to a Newtonian fluid, to the non-Newtonian velocity profile near the bottom left corner. Observe that velocity vectors have and positive $y$−component; (2): Velocity vectors in the exit channel. The shear thinning effect is apparent; (3): Temperature contours near the corner of the step; (4): Streamlines near the corner of the step.

by Eqn. (3.60), with a suitable identification of the physical parameters.

The values of the physical constants we have used are (all in SI units): $\rho = 1200$ (density), $c_p = 10$ (specific heat), $k = 2$ (thermal conduction coefficient), $K_0 = 10^6$ (material consistency) and $n = 0.2$ (rate sensitivity). For this value of $n$ the effect of the non-constant viscosity is very pronounced. The values of the thermal properties are non-physical, but they have been used to accentuate the temperature effect on the viscosity. Numerical experiments have also been conducted with larger values of $n$, in which case convergence is easier to achieve. Since the expression of the viscosity (3.81) tends to infinity when $I_2(\varepsilon)$ tends to zero, we have introduced a cut-off value $\mu_c = 10^{11}$ for $\mu$. The values of the viscosity for the converged solutions are always below this limit, except in isolated points.

The physical results for this problem are presented if Figures 3.36 to 3.43 (coordinates are given in decimeters. The problem has been identified with the acronym 'EPL', standing for plane Extrussion of a Power-Law fluid). Figure 3.36 shows the streamlines

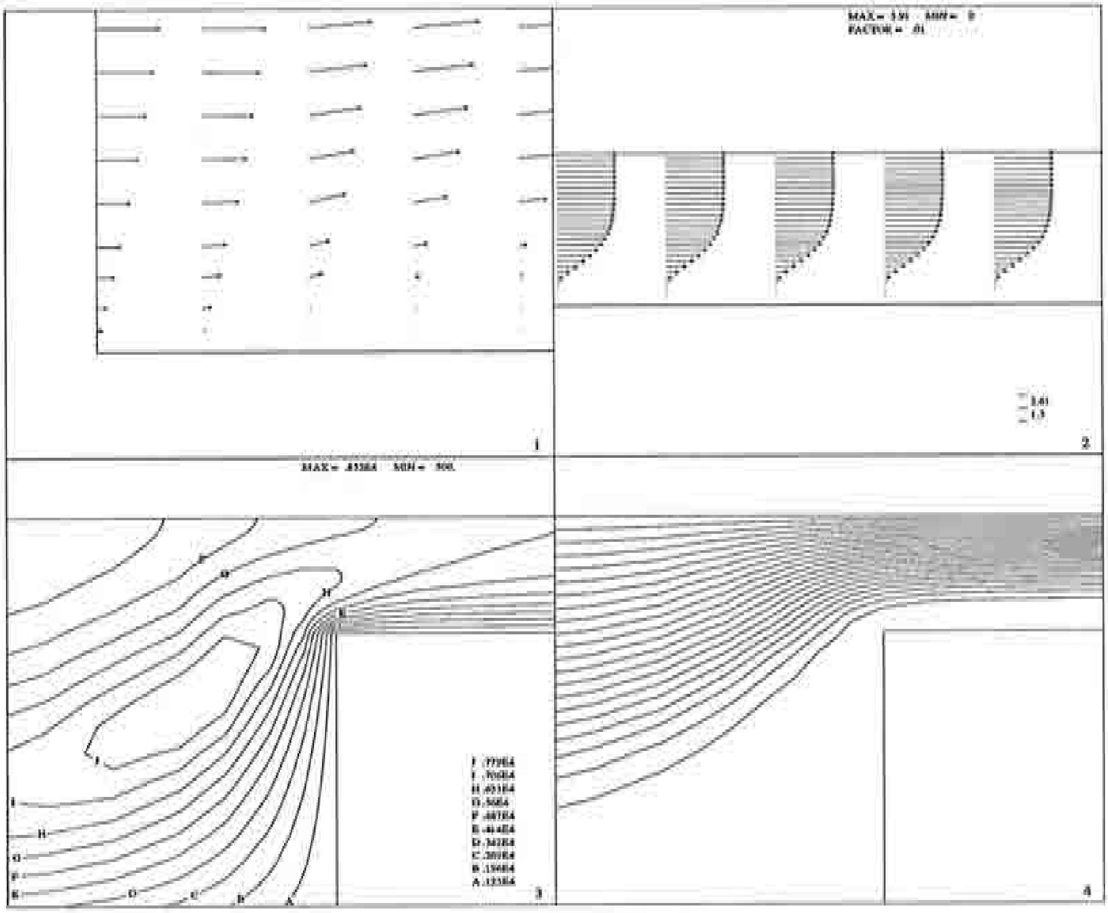

Figure 3.38 Details of the flow for $\beta = 2 \times 10^3$ (EPL). (1): Accomodation of the parabolic velocity profile, corresponding to a Newtonian fluid, to the non-Newtonian velocity profile near the bottom left corner; (2): Velocity vectors in the exit channel. The shear thinning effect is more pronounced than for $\beta = 0$; (3): Temperature contours near the corner of the step; (4): Streamlines near the corner of the step.

for $\beta = 0$ (thermally uncoupled flow) and for $\beta = 2 \times 10^3$, where the effect of the temperature on the viscosity (and thus on the velocity) is apparent. The temperature contours are plotted in Figure 3.37. From Eqn. (3.63) it is clear that the temperature will rise where the internal mechanical work is higher, that is, in the zones with high strain rate. This happens near the corner $(x, y) = (16, 3)$.

A detail of the flow features for both $\beta = 0$ and $\beta = 2 \times 10^3$ is shown in Figures 3.38 and 3.39, respectively. It is observed that the effect of the temperature on the viscosity for the latter case results in an even more pronounced shear thinning.

Figures 3.40, 3.41 and 3.42 show the variation of the $x$−velocity component and the viscosity along the sections $AA$, $BB$ and $CC$ indicated in Figure 3.35. The approximation of the viscosity in the $AA$ section is not very good for $0 \leq y \leq 3$. As it has been already said, the discretization there is poor. However, the variation of the $x$− and $y$−velocity components (Figures 3.40 and 3.43) is smooth, since the shear thinning effect is not important in this section.

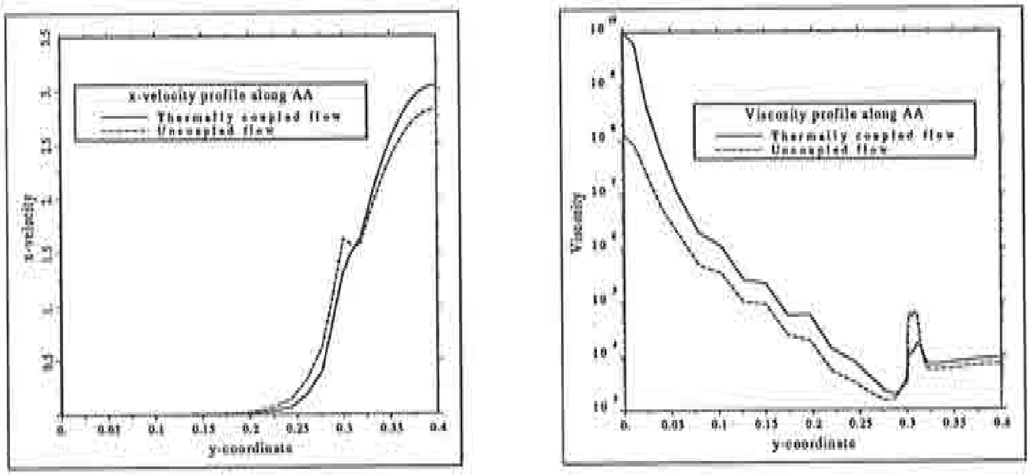

Figure 3.40 $x-$velocity and viscosity profiles along section $AA$ for $\beta = 0$ and $\beta = 2 \times 10^3$ (EPL).

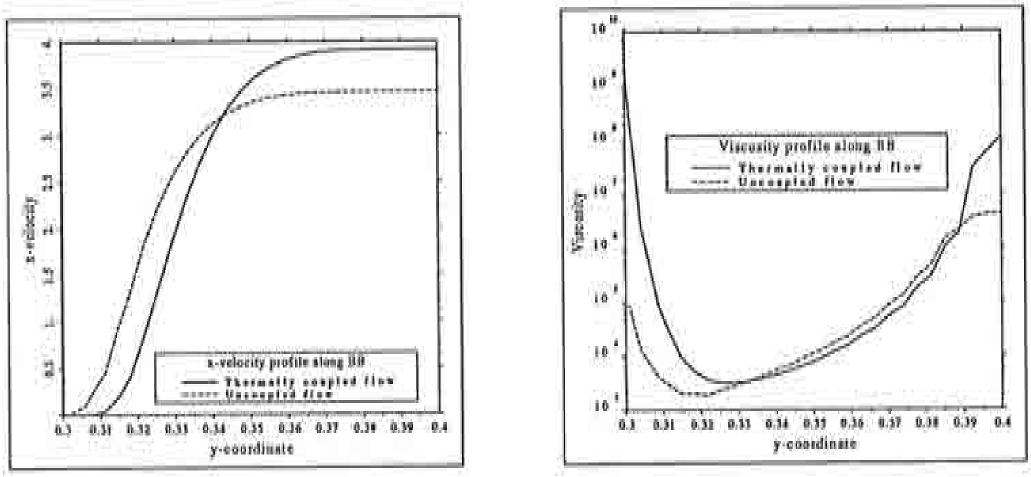

Figure 3.41 $x-$velocity and viscosity profiles along section $BB$ for $\beta = 0$ and $\beta = 2 \times 10^3$ (EPL).

Let us discuss now the performance of the iterative penalization. For values of $\beta$ between 0 and $2 \times 10^3$ the convergence history of the numerical simulation is similar. However, for larger values of $\beta$ lack of convergence can occur. We have failed to obtain converged solutions for $\beta = 5 \times 10^3$, both for the standard penalty method and for the iterative version. As proposed in Reference [ZOH], under-relaxation techniques may be required when the dependence of the viscosity on the temperature is very pronounced. The convergence of the algorithm will be discussed in the case in which $\beta = 2 \times 10^3$, that is, when the viscosity depends on the temperature (thermally coupled flow).

Figure 3.44 shows the evolution of the discrete $L^2$ norm of the velocity residuals over the norm of the actual velocity (in %). As usual, this has been taken as the

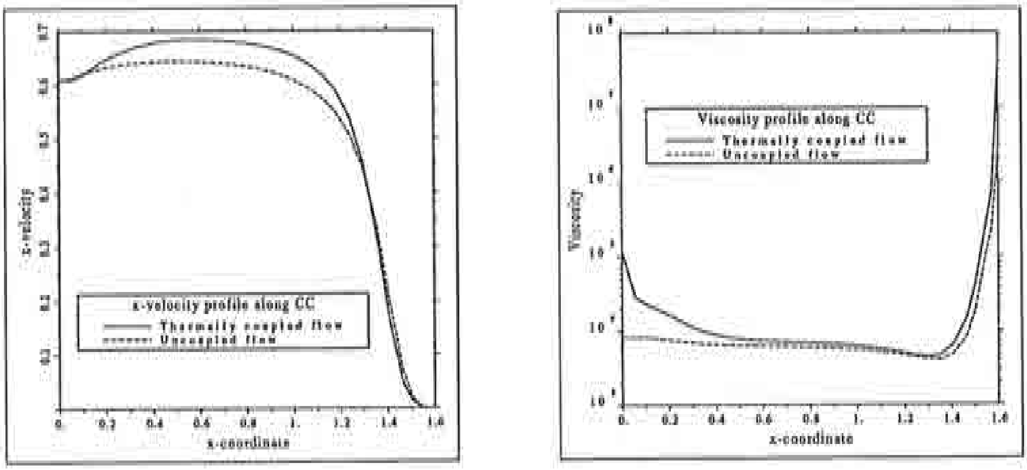

Figure 3.42 $x$−velocity and viscosity profiles along section $CC$ for $\beta = 0$ and $\beta = 2 \times 10^3$ (EPL).

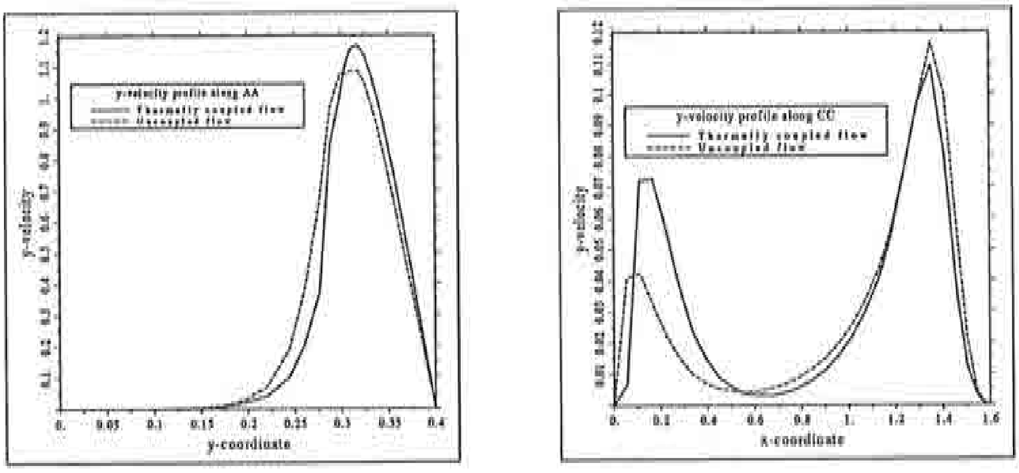

Figure 3.43 $y$−velocity profiles along sections $AA$ and $CC$ for $\beta = 0$ and $\beta = 2 \times 10^3$ (EPL).

parameter to decide whether convergence has been achieved or not. Both the curves corresponding to the classical and the iterative penalty methods have been plotted. Here, the penalty parameter that has been used is $\epsilon = 10^{-12}$. In the first iteration, the viscosity is set to its cut-off value. Thus, the effective initial guess for the second iteration is the Newtonian solution with this viscosity. A real non-Newtonian behavior will be first encountered in this second iteration and from there onwards iterations are required to reach the prescribed convergence tolerance. However, we see that one more iteration is needed if the iterative penalization is employed. The explanation we give is that in this method the second pass of the algorithm uses the Newtonian pressures obtained in the first one, and thus the complete non-Newtonian approximation is not

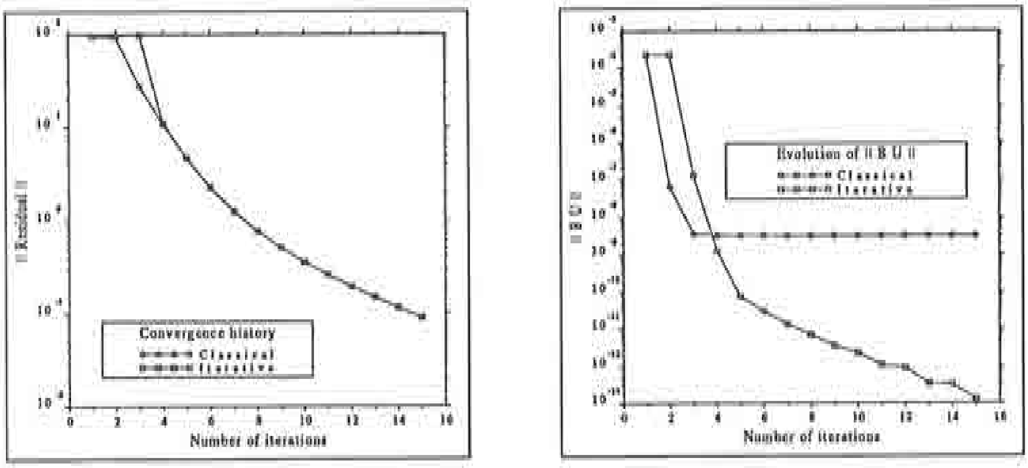

Figure 3.44 Convergence history and evolution of the incompressibility constraint for $\epsilon = 10^{-12}$ and $\beta = 2 \times 10^3$ (EPL).

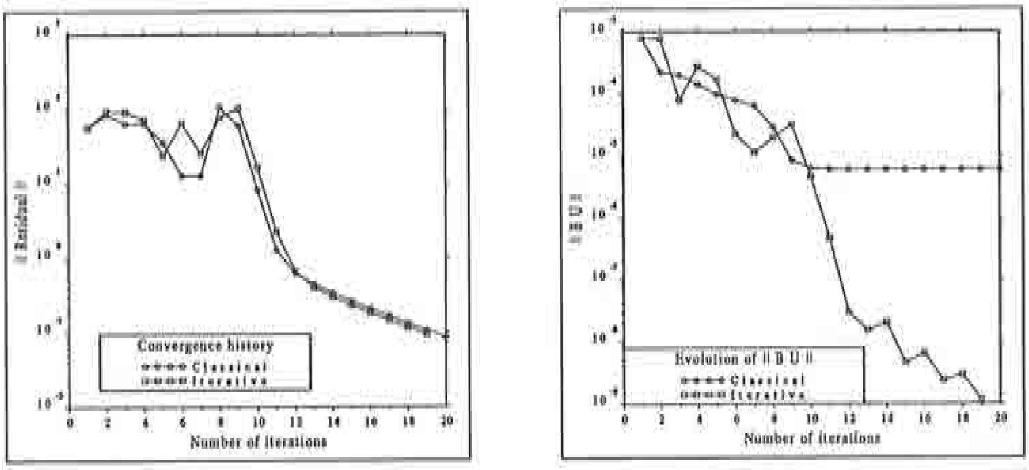

Figure 3.45 Convergence history and evolution of the incompressibility constraint for $\epsilon = 10^{-9}$ and $\beta = 2 \times 10^3$ (EPL).

obtained until the third iteration. In any case, it is interesting to observe that the final convergence rate and the number of iterations needed to achieve convergence have not been deteriorated because of the iterative penalization.

The important issue is to determine how well the incompressibility constraint has been approximated. The evolution of $\|\mathbf{BU}\|$ ($\mathbf{B} = \mathbf{G}^T$, with the notation used earlier) as the iterative procedure goes on has been plotted in the second box of Figure 3.44 (we have normalised this norm by dividing it by $N_{tp}^{1/2}$). Observe that this value keeps constant for the classical penalty method and that it decreases uniformly up to a value of order $10^{-13}$ in 15 iterations if the iterative penalization is used. One might think that the value of order $10^{-8}$ obtained with the classical penalty method is a good enough

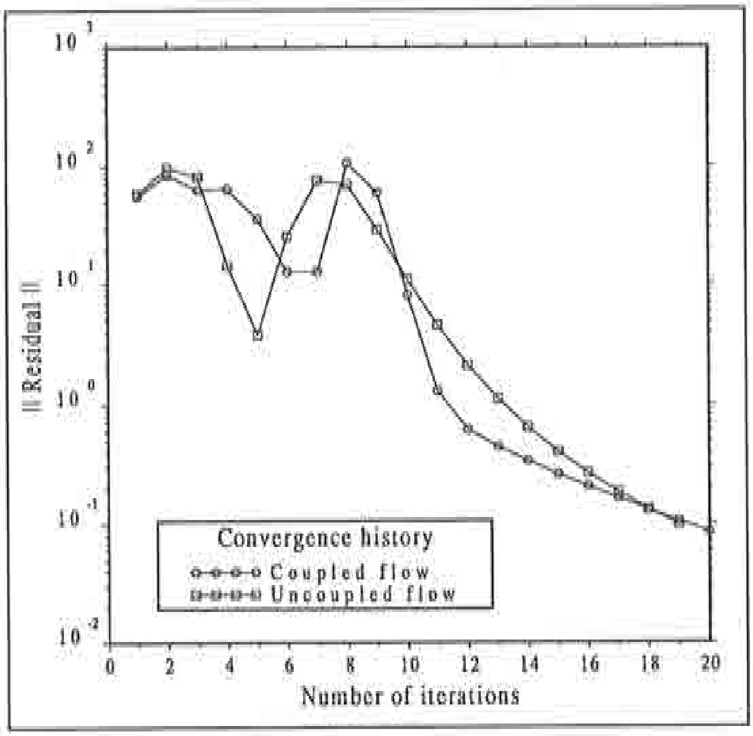

Figure 3.46 Convergence history for $\epsilon = 10^{-9}$ for thermally coupled flow ($\beta = 2 \times 10^3$) and uncoupled flow ($\beta = 0$) (EPL).

approximation. However, this may be somehow misleading, since the smallest value of the final viscosity, say $\mu_1$, is of order $10^3$, and thus $\epsilon \approx 10^{-9}\mu_1^{-1}$ whereas the largest viscosity value, say $\mu_2$, is of order $10^9$ and then $\epsilon \approx 10^{-3}\mu_2^{-1}$. Thus, the parameter $\bar{\epsilon}$ introduced earlier is of order $10^{-9}$ in the low viscosity zones and of order $10^{-3}$ in the high viscosity zones. Recalling that the approximation of the incompressibility constraint is driven by $\bar{\epsilon}$, we may expect a much better satisfaction of this constraint in the low viscosity regions than in the zones where the viscosity is high. If smaller penalty parameters are employed, the solution is affected by the ill-conditioning of the stiffness matrix, even for the direct solver we use. For $\epsilon = 10^{-16}$ this ill-conditioning is so important that the algorithm fails to converge.

The same experiments discussed above have been performed using a penalty parameter $\epsilon = 10^{-9}$ and the results are presented in Figure 3.45 (convergence history and evolution of the $L^2$ norm of the discrete divergence). The conclusions are similar to the previous case. Observe now that oscillations are found for the first eight iterations and then the iterates converge uniformly. The reason for this behavior is the high value of $\epsilon$, that is of the same order as $\mu_2^{-1}$, the inverse of the maximum viscosity, and 100 times higher than $\mu_c^{-1}$, the inverse of the cut-off value. To see that this behavior of the iterative procedure is not due to the block iterative algorithm (see Box 3.2), the convergence history for $\beta = 0$ (uncoupled flow) and $\beta = 2 \times 10^3$ (coupled flow) has been plotted in Figure 3.46. In both cases oscillations appear for the first eight iterations, although the final convergence rate of the uncoupled flow is slightly higher than for the coupled flow for the last iterations.

Concerning the computational cost of the simulation, the CPU required per iteration has been 24.41 seconds for $\beta = 2 \times 10^3$ and 18.58 seconds for $\beta = 0$. For the first case, the solution of the temperature equation needs the 20.46% of CPU time and the solution of the momentum equations (Stokes problem) the 74.85%. Most of the computing time now is needed to solve the linear algebraic system (about a 75%), both for the Stokes and the energy equation. Updating the physical properties and performing the smoothing technique explained in Chapter 2 in order to obtain nodal values of the viscosity and the pressure is inexpensive: these operations only need the 1.6% of CPU time.

## 3.6 Summary and conclusions

The basic numerical method described in Chapter 2 has been applied here to solve thermally coupled flows and flows of non-Newtonian fluids. The first issue to be considered is the algorithm used to couple the energy equation with the Navier-Stokes equations. This has been done by means of a block iterative coupling. Although its use seems to be quite 'natural', an effort has been made to analyse how can it be interpreted and to place it in the general framework of iterative algorithms. In particular, it has been proved for Newtonian fluids that the solution of the energy equation using the actual iterate of the velocity field can be thought of as a Newton-Raphson linearization of the convective term in this equation coupled with a Gauss-Seidel block iterative technique. In more general situations, numerical experiments have indicated that this coupling between the thermal and mechanical problems is very efficient from the computational standpoint.

The extension of the numerical methods used for the Navier-Stokes equations to the problems considered here has proved to be effective. In particular, the Streamline Diffusion method has proved to work very well when div-stable velocity-pressure finite element interpolations are used. Numerical results have demonstrated that a consistent Petrov-Galerkin weighting yields very accurate solutions, without any oscillations.

Concerning the time stepping algorithm, the Crank-Nicolson method has been found to be very sensitive to the convergence tolerance adopted within each time step. Using the block iterative technique, the coupling between the thermal and mechanical problems is only accomplished up to a certain tolerance and thus a certain stability limit will exist for the time step size. Using the backward Euler scheme no stability problems have been encountered in the numerical tests.

Perhaps the behavior of iterative penalization is the most salient result. It was derived and analysed for a much simpler problem than the one considered here (stationary Navier-Stokes equations with constant viscosity and under conditions that ensure uniqueness of solution) but happens to perform very well for thermally coupled flows and, what is more important, for non-Newtonian fluids. In this last case, the classical penalization is inappropiate due to the high variation of the viscosity in the fluid domain, and therefore either the incompressibility constraint is poorly approximated or the final stiffness matrix is ill-conditioned. The iterative penalty method allows to circumvent both problems using relatively high values of the penalty parameter.

## References

[BN] J. Baranger and K. Najib. Analyse numérique des écoulements quasi-Newtoniens dont la viscosité obéit à la loi puissance ou à la loi de carreau. *Numer. Math.*, vol. 58 (1990), 35–49

[BL] J. Boland and W. Layton. An analysis of the finite element method for natural convection problems. *Numer. Meth. for Partial Diff. Eqns.*, vol. 2 (1990), 115–126

[BLL] Y.A. Bukhman, V.I. Lipatov, A.I. Litvinov, B.I. Mitelman and Z.P. Shulman. Rheodynamics of nonlinear viscoplastic media. *Journal of Non-Newtonian Fluid Mechanics*, vol. 10 (1982), 215–233

[BP] M.B. Bush and N. Phan-Thien. Drag force on a sphere in creeping motion through a Carreau model fluid. *Journal of Non-Newtonian Fluid Mechanics*, vol. 16 (1984), 303–313

[CWJ] G.F. Carey, K.C. Wang and W.C. Joubert. Performance of iterative methods for Newtonian and generalized Newtonian flows. *Int. J. Numer. Meth. Fluids*, vol. 9 (1989), 127–150

[CO] J.L. Chenot and E. Oñate (eds.). *Modelling of metal forming processes.* Proceedings of the Euromech 233 Colloquium, Sophia Antipolis, France (Kluwer Academic Publishers, 1988).

[CC] L. Choplin and P.J. Carreau. Excess pressure losses in a slit. *Journal of Non-Newtonian Fluid Mechanics*, vol. 9 (1981), 119–146

[Co] R. Codina. *A finite element model for the numerical solution of the convection-diffusion equation.* (CIMNE Monograph Num. 14, 1992)

[CCO] R. Codina, M. Cervera and E. Oñate. A penalty finite element method for non-Newtonian creeping flows. *CIMNE Report Num. 13* (1991) (Submitted to *Int. J. Numer. Meth. Engrg.*)

[Cu] C. Cuvelier. Résolution numérique d'un problème de control optimal d'un couplage des équations de Navier-Stokes et celle de la chaleur. *Calcolo*, vol. 15 (1978), 345–379

[CSS] C. Cuvelier, A. Segal and A. van Steenhoven. *Finite element methods and Navier-Stokes equations* (Reidel, 1986).

[DT] H.H. Dannelongue and P.A. Tanguy. An adaptive remeshing technique for non-Newtonian fluid flow. *Int. J. Numer. Meth. Engrg.*, vol. 30 (1990), 1555–1567

[DK] H.D. Doctor and N.L. Kalthia. Spline collocation in the flow of non-Newtonian fluids. *Int. J. Numer. Meth. Engrg.*, vol. 26 (1988), 413–421

[DR] A. Dutta and M.E. Ryan. A study of parison development in extrusion blow molding. *Journal of Non-Newtonian Fluid Mechanics*, vol. 10 (1982), 235–256

[EP] G. Evans and S. Paolucci. The thermoconvective instability of plane Poiseuille flow heated from below: A proposed benchmark solution for open boundary flows. *Int. J. Numer. Meth. Fluids*, vol. 11 (1990), 1001–1013

[GR] K.S. Gage and W.H. Reid. The stability of thermally stratified plane Poiseuille flow. *J. Fluid Mech.*, vol. 33 (1968), 21–32

[Gu] M. Gunzburger. *Finite element methods for viscous incompressible flows* (Academic Press, 1989).

[He] J.C. Heinrich. A finite element model for double diffusive convection. *Int. J. Numer. Meth. Engrg.*, vol. 20 (1984), 447–464

[HTB] P. Hurez, P.A. Tanguy and F.H. Bertrand. A finite element analysis of die swell with pseudoplastic and viscoplastic fluids. *Comput. Meths. Appl. Mech. Engrg.*, vol. 86 (1991), 87–103

[IOS] V.P. Isachenko, V.A. Osipova and A.S. Sukomel. *Heat transfer* (Mir, 1977).

[Jo] D.D. Joseph. *Stability of fluid motions* (Springer-Verlag, 1976).

[Ke] R. Kessler. Nonlinear transition in three-dimensional convection. *J. Fluid Mech.*, vol. 174 (1987), 359–379

[LL] L.D. Landau and E.M. Lifshitz. *Mécanique des fluides* (Mir, 1969).

[Li] J.L. Lions. *Quelques méthodes de résolution des problèmes aux limites non lineaires* (Dunod, 1968).

[LLH] T.J. Liu, H.M. Lin and C.N. Hong. Comparison of two numerical methods for the solution of non-Newtonian flow in ducts. *Int. J. Numer. Meth. Fluids*, vol. 8 (1988), 845–861 (1988)

[MV] A.A. Mohamad and R. Viskanta. Transient natural convection of low-Prandtl-number fluids in a differentially heated cavity. *Int. J. Numer. Meth. Fluids*, vol. 13 (1991), 61–81

[Oñ] E. Oñate. *Plastic flow in metals, I: Thermal coupling behaviour, II: Thin sheet forming.* Ph. D. Thesis. University College of Swansea (1978).

[OH] D.R.J. Owen and E. Hinton. *Finite elements in Plasticity* (Pineridge Press, 1980).

[PF] K.C. Park and C.A. Felippa. Partitioned analysis of coupled systems. In: *Computational methods for transient analysis.* T. Belytschko and T.J.R. Hughes (eds.) (Elsevier, 1983).

[SY] A.J.M. Shih and H.T.Y. Yang. Experimental and finite element simulation methods for rate-dependent metal forming processes. *Int. J. Numer. Meth. Engrg.*, vol. 31 (1991), 345–367

[SB] J. Stoer and R. Burlisch. *Introduction to Numerical Analysis* (Springer-Verlag, 1983).

[Ta] R.I. Tanner. *Engineering Rheology* (Clarendon Press, 1985).

[TNB] R.I. Tanner, R.E. Nickell and R.W. Bilger. Finite element methods for the solution of some incompressible non-Newtonian fluid mechanics problems with free surfaces. *Comput. Meths. Appl. Mech. Engrg.*, vol. 6 (1975), 155–174

[TWZ] E.G. Thompson, R.D. Wood, O.C. Zienkiewicz and A. Samuelson (eds.). *Numiform 89.* Proceedings of the 3rd International Conference on Numerical Methods for Industrial Forming Processes, Fort Collins, Colorado, USA (A. Balkema, 1989).

[TTK] D.M. Tidd, R.W. Thatcher and A. Kaye. The free surface flow of Newtonian and non-Newtonian fluids trapped by surface tension. *Int. J. Numer. Meth. Fluids*, vol. 8 (1988), 1011–1027

[WTS] K. Wisniewski, E. Turska, L. Simoni and B.A. Schrefler. Error analysis of staggered predictor-corrector scheme for consolidation of porous media. In: *Finite elements in the 90's.* E. Oñate, J. Periaux, A. Samuelson (eds.) (Springer-Verlag/CIMNE, 1991)

[Zi] O.C. Zienkiewicz. Coupled problems—A simple time-stepping procedure. *Comm. Appl. Numer. Meth.*, vol. 1 (1985), 233–239

[ZG] O.C. Zienkiewicz and P.N. Godbole. Flow of plastic and viscoplastic solids with special reference to extrusion and forming processes. *Int. J. Numer. Meth. Engrg.*, vol. 8 (1974), 3–16

[ZJO] O.C. Zienkiewicz, P.C. Jain and E. Oñate. Flow of solids during forming and extrusion: some aspects of numerical solution. *Int. J. Numer. Meth. Engrg.*, vol. 14 (1978), 15–38

[ZOH] O.C. Zienkiewicz, E. Oñate and J.C. Heinrich. A general formulation for coupled thermal flow of metals using finite elements. *Int. J. Numer. Meth. Engrg.*, vol. 17 (1981), 1497–1514

[ZMS] A.I. Zografos, W.A. Martin and J.E. Sunderland. Equation of properties as a function of temperature for several fluids. *Comput. Meth. Appl. Mech. Engrg.*, vol. 61 (1987), 177–187

# *CHAPTER 4*

# MOULD FILLING SIMULATION

## 4.1 Introduction

This chapter will be devoted to present a specific application of the numerical tools developed previously: the numerical simulation of mould filling processes. Mould filling is an integral part of the casting process, an ancient metal forming technique. It starts with the pouring of a molten metal into a mould until it is filled and it is concluded when the solid nature of the metal is restored. The complete numerical simulation of these processes involves modelling of mould filling, prediction of thermal stresses in a solidifying material and micro-macro modelling in order to predict material micro-structure. Besides the inherent difficulty to model all these physical phenomena, another problem arises because of the identification of material properties, for which delicate experiments are needed. Mould filling as the first stage of the casting process will be the subject of this chapter.

The main difficulty for simulating the flow of a molten metal in a mould is the modelling of free surfaces. Most of the numerical approaches to this problem have been limited to simple geometries, due to the high computational cost of this simulation and that numerical models have been mainly based on finite difference techniques. Because of the available computer potential, it has become possible to deal with more complicated geometries for which finite element models are especially well suited. The representation of feeders, gating systems, risers and the overall mould geometry does not offer any difficulty using finite elements. Proper evaluation of the position of the melt during the transient analysis is the most important problem.

The model that we shall use here to track the free surface of the fluid is based upon the pseudo-concentration technique, which employs a fixed mesh. The moving fluid may fill the elements partially or fully. The version of this method we shall use is due to Thompson [Th1], [Th2], [TS], although it has also been used under the names *volume of fluid method* (VOF) [HN] or *saturation method* [SW]. The basic idea is to introduce a scalar function which is advected according to the velocity flow field obtained from the solution of the Navier-Stokes equations. This function is defined on the whole computational domain. A certain isovalue contour is used to define the front of the 'real' fluid. The unfilled region is assumed to be occupied by a fictious material whose physical properties are such that its motion does not affect the dynamical behavior of the fluid under consideration. To fix ideas, we shall consider that this fictious material is air.

There are other popular methods to track free surfaces. One of them is the updated Lagrangian approach, in which the mesh moves with the fluid [Zi]. The main disadvantatge of this method is that the mesh becomes distorted during the analysis and eventually remeshing is needed. Only when small distortions occur the method is successful [LDD], [ZJO], [ZOH]. A second approach is the Arbitrary Lagrangian-Eulerian method (see, e.g., References [Hu], [SFD]). In this method, a velocity is assigned to the mesh which is independent of the fluid velocity except at the boundary, and is chosen in order to minimize the mesh distortion and/or the convective terms. This requires some *a priori* knowledge of the fluid flow.

The pseudo-concentration technique has been used by several authors to follow free surfaces of creeping flows and viscoplastic flows in the context of metal forming processes, such as extrusion, forging or rolling. See, e.g., References [AI], [AID], [DP], [TS]. For applications of this method to mould filling, see References [DGB], [HS], [LUC].

This chapter is organized as follows. The basic pseudo-concentration technique is described in Section 4.2, whereas Section 4.3 is concerned with some problems encountered when this method is employed. These problems are either practical, arising from the computer implementation of the method, or conceptual. The coupling between the Navier-Stokes and energy equations with the free surface tracking is considered in Section 4.4. Practical numerical examples are presented in Section 4.5. The numerical simulation of two mould filling problems is first discussed. The final example is the classical lamination of a metal flat plate, now analysing the transient mechanical and thermal evolution since the metal contacts the roll until it leaves it.

## 4.2 The pseudo-concentration method

### 4.2.1 Basic formulation

The basic idea of the pseudo-concentration technique is to define a scalar function, say $\psi(\mathbf{x})$, over the computational domain $\Omega$ in such a manner that its value at a certain point $\mathbf{x} \in \Omega$ indicates the presence or absence of fluid. This function may be considered as a fictious fluid property. For instance, we may assign the value 1 to regions where the fluid has already entered and the value 0 to air-filled regions. The position of the fluid front will be defined by the isovalue contour $\psi(\mathbf{x}) = \psi_c$, where $\psi_c \in [0,1]$ is a critical value defined *a priori*. We usually take $\psi_c = 0.5$. This value is immaterial if $\psi$ is a true step function, but is needed in the finite element discretization and for the smoothing to be described later.

The conservation of the pseudo-concentration in any control volume $V_t \subset \Omega$ which is moving with the velocity field $\mathbf{u}$ leads to

$$\frac{d}{dt}\int_{V_t} \psi \, d\Omega = 0$$

If we further assume that $\psi$ is smooth and $\mathbf{u}$ is divergence-free, this implies that

$$\partial_t \psi + (\mathbf{u} \cdot \nabla)\psi = 0 \qquad \text{in } \Omega,\ t \in (0,T) \tag{4.1}$$

where, as usual, $(0,T)$ denotes the time interval where the problem is to be solved. Equation (4.1) is hyperbolic and therefore boundary conditions for $\psi$ have to be specified at the inflow boundary, that is,

$$\psi(\mathbf{x},t)=\bar{\psi}(\mathbf{x},t), \qquad \mathbf{x}\in\Gamma_{inf}, \;\; t\in(0,T) \tag{4.2}$$

where

$$\Gamma_{inf}:=\{\mathbf{x}\in\partial\Omega \mid \mathbf{u}\cdot\mathbf{n}<0\}$$

and $\bar{\psi}$ is a given function. Finally, an initial condition of the form

$$\psi(\mathbf{x},0)=\psi_0(\mathbf{x}), \qquad \mathbf{x}\in\Omega \tag{4.3}$$

has to be appended to (4.1)–(4.2), $\psi_0(\mathbf{x})$ being chosen in order to define the initial position of the fluid front.

Solving problem (4.1)–(4.3) the position of the fluid will be identified by the values $\psi(\mathbf{x},t)>\psi_c$ and the position of the air by $\psi(\mathbf{x},t)<\psi_c$.

### 4.2.2 Numerical solution of the pseudo-concentration problem

The numerical techniques introduced in the previous chapters will be applied to the numerical solution of problem (4.1)–(4.3). Time derivatives will be discretized using the generalized trapezoidal rule and the Streamline Diffusion (SD) formulation will be employed for the space discretization.

The time discretization of Eqn. (4.1) leads to the following problem: Given $\psi^0(\mathbf{x})=\psi_0(\mathbf{x})$, for $n=1,2,...,N$ find $\psi^n(\mathbf{x})$, approximation to $\psi(\mathbf{x},t^n)$, such that

$$\psi^n+\theta\Delta t(\mathbf{u}^n\cdot\nabla)\psi^n=\psi^{n-1}-(1-\theta)\Delta t(\mathbf{u}^{n-1}\cdot\nabla)\psi^{n-1} \tag{4.4}$$

After choosing a suitable finite element partition $\{\Omega^e\}$, $e=1,...,N_{el}$, of the domain $\Omega$, the SD method applied to Eqn. (4.4) leads to the variational equations

$$\begin{aligned}\int_\Omega \phi_h\psi_h^n d\Omega+\theta\Delta t\int_\Omega \phi_h(\mathbf{u}_h^n\cdot\nabla)\psi_h^n d\Omega+\sum_{e=1}^{N_{el}}\mathcal{S}_f^{n,e}(\mathbf{u}_h,\psi_h;\phi_h)\\ =\int_\Omega \phi_h\psi_h^{n-1}d\Omega-(1-\theta)\Delta t\int_\Omega \phi_h(\mathbf{u}_h^{n-1}\cdot\nabla)\psi_h^{n-1}d\Omega\end{aligned} \tag{4.5}$$

where the test functions $\phi_h$ and the trial solutions $\psi_h^n$ belong to $H^1(\Omega)$, the former satisfying homogeneous boundary conditions on $\Gamma_{inf}$ and the latter the essential boundary conditions (4.2). The SD term in Eqn. (4.5) is given by

$$\begin{aligned}\mathcal{S}_f^{n,e}(\mathbf{u}_h,\psi_h;\phi_h):=\int_{\Omega^e}\tau_f^e(\mathbf{u}_h^n\cdot\nabla)\phi_h[\psi_h^n-\psi_h^{n-1}\\ +\theta\Delta t(\mathbf{u}_h^n\cdot\nabla)\psi_h^n+(1-\theta)\Delta t(\mathbf{u}_h^{n-1}\cdot\nabla)\psi_h^{n-1}]d\Omega\end{aligned} \tag{4.6}$$

The intrinsic time $\tau_f^e$ is computed as explained in Reference [Co] using a Péclet number $\gamma=\infty$ (see Box 1.1 in the quoted reference) to compute the upwind function.

Let us denote by $\mathbf{M}_f$ the 'mass' (or Gramm) matrix for the pseudo-concentration interpolation and by $\mathbf{J}$ the matrix arising from the convective term in Eqn. (4.5) (considering both the Galerkin and the SD contributions). The matrix version of Eqn. (4.5) will read as follows:

$$\mathbf{M}_f \cdot \mathbf{\Psi}^n + \theta \Delta t \mathbf{J}(\mathbf{U}^n) \cdot \mathbf{\Psi}^n = \mathbf{M}_f \cdot \mathbf{\Psi}^{n-1} - (1-\theta)\Delta t \mathbf{J}(\mathbf{U}^{n-1}) \cdot \mathbf{\Psi}^{n-1} \qquad (4.7)$$

the capital letter $\mathbf{\Psi}$ denoting the vector of nodal unknowns of the pseudo-concentration function. The dependence of matrix $\mathbf{J}$ on the velocity has been explicitly indicated.

**Remarks 4.1**

(1) The parameter $\theta$ of the generalized trapezoidal rule may be set different to that employed for the Navier-Stokes or the energy equations. In fact, when $\psi$ is a step function or with a high gradient at the fluid front, the backward Euler scheme ($\theta = 1$) is inappropiate due to its high dissipation, even though it may be used for the Navier-Stokes and energy equations. In this case, the Crank-Nicolson scheme ($\theta = 1/2$) should be employed. However, this problem does not appear if the pseudo-concentration is a smooth function, since the position of the critical contour $\psi_c$ will be advected properly, because the error of the backward Euler scheme is basically an amplitude error and not a phase error.

(2) In our calculations we have chosen for the pseudo-concentration $\psi$ the same finite element interpolation as for the components of the velocity field and the temperature. □

## 4.3 Some numerical techniques

### 4.3.1 General considerations

The use of the pseudo-concentration method described above provides a basic technique to track free-surfaces of viscous incompressible flows, although several problems appear when it is implemented in a computer code.

The first problem encountered is merely for post-processing the results. If the no-slip boundary condition is prescribed for the velocity field, the pseudo-concentration values for points of the finite element discretization located at the boundary of the computational domain will never be advected and therefore the final value obtained for them will be given by the initial condition $\psi_0(\mathbf{x})$. Assume that this initial value is zero. If fluid enters and occupies the neighboring nodal points, located at a distance $h$ from the boundary, the pseudo-concentration value for them will be 1. When the discrete function $\psi_h$ is interpolated, the critical contour $\psi_c$ will be placed between the boundary and the contiguous points. In particular, for $\psi_c = 0.5$ the predicted position of the front will be at a distance $h/2$ from the boundary.

A possible way to artificially overcome this problem is to modify the pseudo-concentration values of the boundary nodal points. We have implemented the following method. Let $\psi_m$ be the mean value of the function $\psi$ for an element $\Omega^e$ adjacent to the boundary. The condition $\psi_m \geq \psi_c$ will indicate that most of the nodes of the element have already been filled. In this situation, the value of the pseudo-concentration for a node located at the boundary, $\psi_b$, is modified as follows:

$$\psi_b \leftarrow \psi_b + \rho(\psi_m - \psi_b) \qquad (4.8)$$

where $0 \leq \rho \leq 1$. The constant $\rho$ may be adjusted in order to control when the boundary nodes have to be considered part of the fluid or part of the air. As time advances, the application of (4.8) will yield a value 1 for $\psi_b$ if this procedure enters the calculation, although it may also be used as a post-processing facility.

There are two more problems to be considered for the implementation of the pseudo-concentration technique. One of them is the choice of the function $\psi$. If we take a step function, as indicated before, numerical problems may be encountered when it is transported. It is explained in Reference [Co] why small oscillations in the vicinity of sharp gradients still remain using the SD formulation. These oscillations may propagate and yield to distorted front shapes, especially near corners. Since the basic idea of the method does not depend on the choice of the function $\psi$, it is preferable to use a smooth function instead of one whith abrupt changes. The smoothing technique we employ will be discussed below. Nevertheless, we have found that if the peaks encountered when dealing with a step function are just eliminated for each time step, an accurate tracking of the front is obtained using the SD method.

The last problem to be considered is the evacuation of air bubbles. Since we deal with incompressible flows, air cannot shrink and air bubbles near the corners will remain if a method to evacuate them is not devised. In practice, moulds are made of porous materials, usually sand in casting applications. Therefore, air can leave the mould without resistence. Numerically, a possible way to evacuate air is to introduce holes on the boundary and to block them when the fluid touches the wall. This method will also be explained in the following.

### 4.3.2 Smoothing of the pseudo-concentration surface

Even if the initial condition $\psi_0(\mathbf{x})$ is a smooth function, if the pseudo-concentration is mantained unmodified over several time steps it may begin to lose its smoothness and numerical problems may be encountered. Since the only important factor is the location of the critical contour that defines the front, it is possible to smooth $\psi$ while maintaining the position of this critical contour. Following Thompson [Th1], this can be performed redefining the pseudo-concentration for each node of the finite element mesh according to the following expression:

$$\psi = \psi_c + \mathrm{sgn}(\psi_o - \psi_c)\ \sigma\ d \tag{4.9}$$

where $\psi_o$ stands for the calculated value of $\psi$, $\sigma$ is a given constant, $d$ is the distance from the node under consideration to the front and $\mathrm{sgn}(\cdot)$ is the signum of the value enclosed in the brackets.

Equation (4.9) indicates that the smoothed pseudo-concentration is obtained adding or substracting to the critical value a quantity proportional to the distance to the front, according to which material occupies the point (the fluid analysed or air). The constant $\sigma$ is the slope of the new pseudo-concentration surface in the direction normal to the front.

The crucial point is how to calculate the distance $d$ from a point under consideration to the front. We have tested several possibilities that will be briefly described now.

*Nodal-based distance*

To calculate the distance $d$, we may first identify the points surrounding the front. This can be easily done by checking if their pseudo-concentration value is close to $\psi_c$, i.e., $|\psi - \psi_c|$ is less than a given tolerance that depends on the diameter of the elements and the constant $\sigma$. Once these points surrounding the front are identified, the required distance from a point of interest to the front is evaluated as the minimum of the distances to these points. We have found that this method yields a somehow ondulated (and therefore inappropiate) representation of the front, especially for coarse meshes. Moreover, the tolerance to be used depends strongly on the element dimensions and the slope of the pseudo-concentration surface.

*Integration-points-based distance*

Instead of using the nodal points surrounding the front to calculate $d$ for a given point, we may also employ the integration points. Apart from this, the idea is the same as before and the problems encountered are also the same, perhaps to a lesser extend.

*Interpolation of a straight line*

Once we know the values of the pseudo-concentration for all the nodal points, it is possible to calculate the position of the points of the front located at the sides of the elements. This can be done by checking if the sign of $\psi - \psi_c$ changes when passing from a certain node of an element to the adjacent one. When this happens, the position where the value $\psi_c$ is attained can be computed using a linear interpolation between the values of $\psi$ at the two nodes identified and the coordinates of these two nodes. In the most common case in which only one front crosses the element, two front points which are part of the element sides will be found. Between these two points, the position of a specified number of additional front points may be calculated by interpolating the front within each element by a straight line. If more than a single front crosses the element, an even number of front points lying on the element sides will be found. The way to connect pairs of them is easily established by moving along the boundary and checking the sign of $\psi - \psi_c$.

When the process just described is finished, the front will be represented by a set of points lying on straight segments within each element. The distance $d$ from a considered point to the front is then computed as the mimimum of the distances to all these front points.

The accuracy of this method depends on the smoothness of the front (not on the pseudo-concentration), as well as on the number of front points to be interpolated within each element. Clearly, if the front presents a sharp corner within a certain element, the approximation by a straight segment will be indeed poor. Moreover, advancing in time the approximation error will sum up and the final representation of the front may be completely wrong. In these cases the smoothing of the pseudo-concentration is not recommended. We have solved some problems of this kind just using a step function for $\psi$ and without smoothing. However, when the front is smooth, this method has proved to be quite effective. In general, we have found that four or five additional front points interpolated within each element are needed when quadratic elements are used.

For the particular case of finite elements with interior nodes, such as the $Q_2/P_1$ or the $P_2^+/P_1$ pairs, this smoothing technique has an additional problem that we have observed while running some test cases. Let us consider the situation illustrated in Figure 4.1 for the two-dimensional $Q_2/P_1$ element.

The nodes of the element have been denoted by $N1,\ N2, ..., N9$, the front points

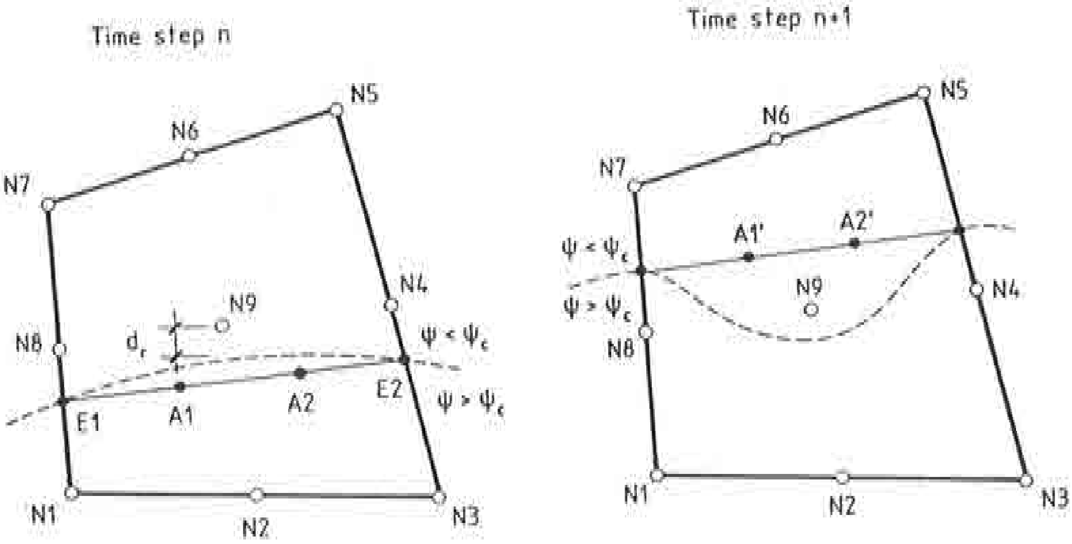

Figure 4.1 Formation of spurious air-bubbles for interior nodes. The dashed line denotes the critical contour $\psi_c$.

located on the sides of the element by $E1$, $E2$ and the additional front points by $A1$, $A2$. In the situation of the picture on the left of Figure 4.1, application of Eqn. (4.9) computing the distance $d$ as explained above will lead to

$$\begin{aligned}\psi_9^n &= \psi_c - \sigma \min\{\text{dist}(N9, A1), \text{dist}(N9, A2)\} \\ &< \psi_c - \sigma\ d_r\end{aligned} \tag{4.10}$$

where $d_r$ is the 'real' distance from node $N9$ to the front. Inequality (4.10) indicates that we are underestimating the value of $\psi$ at node $N9$. The error will be much smaller for nodes $N4$ and $N8$. After solving the transport equation for the pseudo-concentration it may happen that nodes $N4$ and $N8$ are already part of the fluid whereas node $N9$ remains in the unfilled region (see the picture on the right of Figure 4.1). Since the fluid front will be again approximated by a straight segment, node $N9$ may be situated at the wrong side of this. Applying again (4.9) we will obtain

$$\psi_9^{n+1} = \psi_c - \sigma \min\{\text{dist}(N9, A1'), \text{dist}(N9, A2')\} < \psi_c$$

It is even possible that $\psi_9^{n+1} < \psi_9^n$. In any case, there exists the possibility that as the fluid front advances a spurious bubble around node $N9$ be left behind. We have observed this misbehavior in practice.

The way to circumvent this problem is quite simple. Once the values of the smoothed pseudo-concentration for the nodes lying on the element sides have been calculated using Eqn. (4.9), the value for the interior node is computed from interpolation. The serendipid interpolation ($Q_2^-$) is used for the biquadratic element ($Q_2$) and the quadratic simplicial interpolation ($P_2$) for the enriched simplex $P_2^+$.

### 4.3.3 Air release—Introduction of holes

It has already been said that in practical problems air can leave the mould through its porous walls. Numerical models must incorporate a facility to evacuate air in order to prevent the appearence of air bubbles, especially near the corners.

The basic idea of the method to be described now is to place some holes in the walls of the mould and to block them when the fluid reaches these walls. Thus, air will be allowed to leave the mould but the fluid analysed will not.

To motivate the basic inconvenience of this method, let us describe how boundary conditions are implemented in the computer code developed in this work. If a boundary node has a Neumann type prescription, its velocity is one of the unknowns of the problem. But if a Dirichlet condition is prescribed there, the velocity vector is known. The columns and rows corresponding to the node under consideration of the assembled matrix of the final algebraic system are not needed. The product of the columns by the velocity components of the node are moved to the right-hand-side. The matrix of the resulting reduced system, say $\mathbf{A}$, will be smaller than if these columns and rows are not eliminated. Since we work with dynamic memory allocation, the dimension of matrix $\mathbf{A}$ has to be known before starting the analysis, after reading the data of the problem. Hence, the change of a node from a Neumann boundary condition to a Dirichlet boundary condition during the analysis is not so simple as it might seem at first glance.

In order to avoid the need for changing the size of the problem, we leave the nodes located at the holes always free. When the fluid reaches them, the velocity (or perhaps only the component normal to the wall) is prescribed to zero not exactly, but through penalization.

To describe this method, let us consider a generic linear system of the form

$$\mathbf{A}\mathbf{x} = \mathbf{b} \tag{4.11}$$

where $\mathbf{x}$ is a vector of $n$ unknowns. Suppose that the $i$−th component of $\mathbf{x}$ is to be prescribed to a value $\bar{x}$, i.e., $x_i = \bar{x}$. From Eqn. (4.11) we will have that

$$a_{ii}x_i = b_i - \sum_{j=1, j\neq i}^{n} a_{ij}x_j \tag{4.12}$$

Assume that the component $a_{ii}$ of matrix $\mathbf{A}$ is not zero and replace

$$\begin{aligned} a_{ii} &\leftarrow a_{ii}(1+\lambda) \\ b_i &\leftarrow \bar{x}a_{ii}(1+\lambda) \end{aligned} \tag{4.13}$$

From Eqn. (4.12) we will have that

$$x_i = \bar{x} - \frac{1}{a_{ii}(1+\lambda)} \sum_{j=1, j\neq i}^{n} a_{ij}x_j \tag{4.14}$$

from where it follows that $x_i \rightarrow \bar{x}$ as $\lambda \rightarrow \infty$.

In practice, we have observed that values of $\lambda$ of order $10^6$ yield a good enough approximation to the prescription to be imposed (observe that $\lambda$ is dimensionless).

The way to block the holes is now clear. For a certain time step, the value of the pseudo-concentration at the point of interest is computed. If this value $\psi$ is lower than $\psi_c$, $\lambda = 0$ is taken for the system analogous to (4.11) arising from the fully discrete and linearized Navier-Stokes equations and the redefinition (4.13) is not performed. Otherwise, a high value of $\lambda$ is selected, taking $\bar{x} = 0$ in (4.13).

Consider now the transport equation for the pseudo-concentration. If for a certain time step the velocity at a node lying on the hole is left free, it may point into the mould due to suction effects. In this situation, the hole must be considered as a part of the inflow boundary $\Gamma_{inf}$ and therefore the function $\psi$ must be prescribed there. Otherwise, it may happen that values of $\psi$ higher than $\psi_c$ be transported into the mould, thus introducing spurious fluid. The situation is similar to what happens for the one-dimensional hyperbolic equation

$$\partial_t \psi + u \partial_x \psi = 0, \qquad 0 < x < 1$$

If $u > 0$ and the value of $\psi$ at $x = 0$ is not prescribed, the solution is simply $\psi(x,t) = \psi_0(x - ut)$, where $\psi_0(x)$ is the initial condition extended by periodicity to the whole real line $\mathbb{R}$.

There is another way to see that if $\psi$ is not prescribed at the nodes for which the velocity points into the mould then spurious material will be introduced. Let $V_t$ be any control volume surrounding this node. Multiplying Eqn. (4.1) by $\psi$, integrating over $V_t$ and using the fact that $\mathbf{u}$ is divergence-free yields

$$\frac{d}{dt} \int_{V_t} \psi^2 d\Omega = -\frac{1}{2} \int_{\partial V_t} (\mathbf{n} \cdot \mathbf{u}) \psi^2 d\Gamma$$

If $\psi$ is not prescribed where $\mathbf{n} \cdot \mathbf{u} < 0$, the integral of $\psi^2$ over $V_t$ may increase as time goes on, and this happens for any control volume $V_t$, that is, a spurious fluid-filled region may appear around the hole.

Having these considerations in mind, it is clear that the pseudo-concentration must be prescribed at the temporary free wall nodes where $\mathbf{n} \cdot \mathbf{u} < 0$. For a certain time step, the value of the prescription will be the value obtained in the previous one. The way to implement this is the same as for the velocities in the Navier-Stokes equations. Let $\psi_b^{n-1}$ the value of the pseudo-concentration at the node under consideration for time step $n - 1$. Considering that the system to be solved to find $\psi$ for time step $n$ is (4.11), the redefinition (4.13) will be employed, with $\bar{x} = \psi_b^{n-1}$. Again, we have found that good results are obtained taking $\lambda$ of order $10^6$.

The checks to be performed for temporary free boundary nodes are summarized in Box 4.1. It is understood that all the variables (pseudo-concentration and velocity) refer to a certain node and that Dirichlet boundary conditions are prescribed according to the penalty technique described here.

**Box 4.1 Checks for temporary free wall nodes**

```
• IF $\psi_b^{n-1} < \psi_c$ then
      • IF $\mathbf{n} \cdot \mathbf{u} < 0$ then
            Prescribe $\psi_b^n$ to $\psi_b^{n-1}$
        ELSE
            Leave $\psi_b^n$ free
        END
      • Leave $\mathbf{u}$ free (Neumann type condition)
  ELSE
      • Prescribe $\mathbf{u} = \mathbf{0}$
      • Leave $\psi_b$ free
  END
```

## 4.4 The Navier-Stokes equations with a moving free surface

### 4.4.1 Statement of the problem

In Section 3.4 we have considered the general problem for an incompressible fluid in laminar regime and taking into account thermal effects. Now we will include the existence of a free surface within the domain $\Omega$, which will be tracked using the techniques described in this chapter.

The mechanical and thermal equations describing the problem are (3.73), viz.

$$\begin{aligned} \rho[\partial_t \mathbf{u} + (\mathbf{u} \cdot \nabla)\mathbf{u}] - 2\nabla \cdot [\mu \boldsymbol{\varepsilon}(\mathbf{u})] + \nabla p = \rho \mathbf{f} \qquad & \text{in } \Omega,\ t \in (0,T) \\ \nabla \cdot \mathbf{u} = 0 \qquad & \text{in } \Omega,\ t \in (0,T) \\ \rho c_p[\partial_t \vartheta + (\mathbf{u} \cdot \nabla)\vartheta] - \nabla \cdot (k \nabla \vartheta) = Q \qquad & \text{in } \Omega,\ t \in (0,T) \end{aligned} \tag{4.15}$$

It has been already explained in Section 3.4 the interest of considering the physical properties and the forcing terms as variable. The boundary conditions for the velocity and the temperature to be considered here are

$$\begin{aligned} \mathbf{u} = \bar{\mathbf{u}} \qquad & \text{on } \Gamma_{du},\ t \in (0,T) \\ \mathbf{n} \cdot \boldsymbol{\sigma} = \bar{\mathbf{t}} \qquad & \text{on } \Gamma_{nu},\ t \in (0,T) \\ \mathbf{u} \cdot \mathbf{n} = \bar{u}_n, \quad \mathbf{n} \cdot \boldsymbol{\sigma} \cdot \mathbf{g}_1 = \bar{t}_1, \quad \mathbf{n} \cdot \boldsymbol{\sigma} \cdot \mathbf{g}_2 = \bar{t}_2, \qquad & \text{on } \Gamma_{mu},\ t \in (0,T) \\ \vartheta = \bar{\vartheta} \qquad & \text{on } \Gamma_{dt},\ t \in (0,T) \\ -k\mathbf{n} \cdot \nabla \vartheta = \bar{\varphi} \qquad & \text{on } \Gamma_{nt},\ t \in (0,T) \end{aligned} \tag{4.16}$$

where the notation is the same as in Chapters 2 and 3. In particular, the boundary $\partial\Omega$ has been considered split into three sets of disjoint components $\Gamma_{du}$, $\Gamma_{nu}$ and $\Gamma_{mu}$, the latter being the part of the boundary where mixed conditions are prescribed: the normal velocity and the tangent stresses. Vectors $\mathbf{g}_1$ and $\mathbf{g}_2$ (for the three-dimensional case) span the space tangent to $\Gamma_{mu}$.

The initial conditions for Eqns. (4.15) are

$$\begin{aligned} \mathbf{u}(\mathbf{x},0) &= \mathbf{u}_0(\mathbf{x}) \quad \text{in } \Omega \\ \vartheta(\mathbf{x},0) &= \vartheta_0(\mathbf{x}) \quad \text{in } \Omega \end{aligned} \tag{4.17}$$

The definition of the position of the fluid front will be given by the physical properties. Let $\pi$ be any of these, i.e., density ($\rho$), viscosity ($\mu$), specific heat ($c_p$) or conduction coefficient ($k$). We will have that

$$\pi(\mathbf{x},t) = \begin{cases} \pi_{fluid}(\mathbf{x},t) & \text{if } \mathbf{x} \in \Omega_t \\ \pi_{air} & \text{if } \mathbf{x} \in \Omega \setminus \Omega_t \end{cases} \tag{4.18}$$

where

$$\Omega_t := \{\mathbf{x} \in \Omega \mid \psi(\mathbf{x},t) \geq \psi_c\} \tag{4.19}$$

and the pseudo-concentration function $\psi$ is the solution of the following problem:

$$\begin{aligned} \partial_t \psi + (\mathbf{u}\cdot\nabla)\psi &= 0 && \text{in } \Omega,\ t \in (0,T) \\ \psi &= \bar{\psi} && \text{on } \Gamma_{inf},\ t \in (0,T) \\ \psi(\mathbf{x},0) &= \psi_0(\mathbf{x}) && \text{in } \Omega \end{aligned} \tag{4.20}$$

This is the formulation of the pseudo-concentration method. In Eqn. (4.18), the property $\pi$ for the fluid-filled region is allowed to depend on the unknowns of the problem, whereas it has been considered constant for the air, i.e., for the fictious fluid. Observe that since the physical properties will be discontinuos across the fluid front, the differential equations (4.15) will not exactly describe the conservation of momentum, mass and energy, since the jump of these properties has been simply ignored.

A particular case of the mixed boundary condition on $\Gamma_{mu}$ will be employed here, namely, the von Karman law for the shear stress, also used in References [DGB] and [LUC] (see Reference [FCT] for another friction law for Bingham fluids). Introducing the tangent stress vector

$$\bar{\mathbf{t}}_\tau = \bar{t}_1\mathbf{g}_1 + \bar{t}_2\mathbf{g}_2$$

and the tangent velocity

$$\mathbf{u}_\tau = (\mathbf{u}\cdot\mathbf{g}_1)\mathbf{g}_1 + (\mathbf{u}\cdot\mathbf{g}_2)\mathbf{g}_2$$

the expression of this law is

$$\bar{\mathbf{t}}_\tau = -\rho\frac{|\mathbf{u}_\tau|}{(u^+)^2}\mathbf{u}_\tau \tag{4.21}$$

where the dimensionless friction coefficient $u^+$ depends on the rugosity of the wall and the position of the point considered through the relation

$$u^+ = A\log(y^+) + B$$

$A$ and $B$ being physical parameters. As in Reference [DGB] we will take $A = 2.5$, $B = 5.5$ (smooth walls) and $y^+ = 100$, yielding $u^+ = 17.01$.

Friction laws of this type are normally applied to turbulent flow problems, trying to emulate the frictional effect of boundary layers. As in the above quoted references, we shall use (4.21) to obtain tangencial tractions at the walls of the mould.

### 4.4.2 Numerical treatment

It has already been explained in detail in Chapter 3 how to solve problem (4.15)–(4.17) and in Section 4.2.2 the numerical solution of problem (4.20). It only remains to link both problems through the updating of the physical properties given by Eqn. (4.18) for the continuous problem. First, let us discuss how to compute the matrices involving any of these properties. For example, consider the matrix $\mathbf{K}_d$ arising from the viscous terms of the Navier-Stokes equations (see Box 4.2). Neglecting the contribution of the SD term, this matrix comes from $2\int_\Omega \mu\boldsymbol{\varepsilon}(\mathbf{u}) : \boldsymbol{\varepsilon}(\mathbf{v})d\Omega$. Using numerical integration within each element of the finite element partition with $N_{gp}$ integration points of positions in the parent domain $\boldsymbol{\xi}_k$ and weights $w_k$, $k = 1, ..., N_{gp}$, we will have that

$$\begin{aligned}\int_\Omega \mu\boldsymbol{\varepsilon}(\mathbf{u}_h) : \boldsymbol{\varepsilon}(\mathbf{v}_h)d\Omega &= \sum_{e=1}^{N_{el}} \int_{\Omega^e} \mu^e \boldsymbol{\varepsilon}(\mathbf{u}_h^e) : \boldsymbol{\varepsilon}(\mathbf{v}_h^e)d\Omega \\ &\approx \sum_{e=1}^{N_{el}} \sum_{k=1}^{N_{gp}} w_k \mu^e(\boldsymbol{\xi}_k)\boldsymbol{\varepsilon}[\mathbf{u}_h^e(\boldsymbol{\xi}_k)] : \boldsymbol{\varepsilon}[\mathbf{v}_h^e(\boldsymbol{\xi}_k)]|J^e(\boldsymbol{\xi}_k)|\end{aligned}$$

where $J$ is the Jacobian determinant of the isoparametric mapping. It is therefore clear that the viscosity must be computed and stored for each integration point of each element. The same holds true for the rest of physical properties. Let us denote by $\pi$ any of them and by $\pi_k^e$ its value at the $k-$th integration point of the $e-$th element. To determine how to calculate it we first must know the value of the pseudo-concentration at this point, $\psi^e(\boldsymbol{\xi}_k)$, which is easily calculated from the standard interpolation from the nodal values of $\psi$ for the element. Then,

$$\pi_k^e = \begin{cases} \pi_{fluid}^e(\boldsymbol{\xi}_k) & \text{if } \psi^e(\boldsymbol{\xi}_k) \geq \psi_c \\ \pi_{air} & \text{if } \psi^e(\boldsymbol{\xi}_k) < \psi_c \end{cases} \tag{4.22}$$

The property $\pi$ for the fluid analysed may depend on the velocity and the temperature. For the 'air', it may be any constant provided that the motion of the resulting fictious fluid do not affect the motion of the 'real' fluid. There is always the possibility of using the real air properties.

The final transient and iterative algorithm is given in Box 4.2. Only the basic steps of the scheme presented in Box 3.2 for the general problem of thermally coupled flows and nonlinear materials are indicated. The basic calculations needed to track the free surface are included.

**Remarks 4.2**

(1) In Box 4.2 it is assumed that the Navier-Stokes equations are solved first and then the solution of the energy equation is performed. As mentioned in Chapter 3, there is no difficulty in swapping the order of block iterations.

(2) The pseudo-concentration may be calculated at the begining of the time step or at the end (staggered with respect to the other problems). This last choice is considered in Box 4.2. Both options are equally valid, but one must keep in mind that if the former is chosen the front will be 'delayed' one time step with respect to the velocity, pressure and temperature, whereas if the second possibility is adopted the situation will be the inverse. It could also be possible to include the calculation of the pseudo-concentration within the block iterative loop. We have found that this leads to convergence problems, which are due to the fact that an

integration point may belong to the fluid in a certain iteration and to the air in the next one, thus having different physical properties from iteration to iteration.

(3) The parameter $\theta$ of the generalized trapezoidal rule for the three different transient problems to be solved (velocity-pressure, temperature and pseudo-concentration) may be different and chosen according to the accuracy in time required for each problem.

(4) In Box 4.2, it is understood that the boundary conditions for the temporary free wall nodes are always adjusted using the penalization method described in Section 4.3.3.

(5) In the most common situation, the fluid front will cross an element. For some of its integration points the properties of the fluid will be used and for the others the properties of the air. Clearly, the accuracy of the integration rule will be poor for these elements, although this should not affect much the global accuracy. Also, there will be a jump in the fluxes of temperature and stresses that we have not considered. Let us denote by $\Gamma^e_f$ the part of the front crossing element $e$. Considering for example the temperature equation, this jump (arising from the application of the divergence theorem) will be

$$\int_{\Gamma^e_f} \eta \left[ k_{fluid}\mathbf{n} \cdot (\nabla\vartheta)_{fluid} - k_{air}\mathbf{n} \cdot (\nabla\vartheta)_{air} \right] d\Gamma$$

where $\eta$ is the test function for the temperature. For the finite element discretization, the derivatives of $\vartheta$ within each element will be continuous, i.e., $(\nabla\vartheta)_{fluid} = (\nabla\vartheta)_{air}$, and therefore this integral will not vanish if the diffusions are different. The continuity of heat fluxes for the continuous problem implies that the bracketed term must be zero. The influence of the inclusion of the jump in the finite element problem is an aspect that deserves greater attention.

(6) The use of the friction law given by Eqn. (4.21) will introduce another nonlinearity in the problem. Even if the Newton-Raphson linearization is employed for the convective term of the Navier-Stokes equations, this term is linearized only up to first order, since its influence is not very important, as we shall show in a numerical example. Moreover, the value of the friction at time step $n-1$ is considered to be approximately the same as for time step $n$ when the equations are written for this time step (this is the same approximation used for the density; see Section 3.4.2). This approximation is obviously unnecessary when the backward Euler scheme is used for the Navier-Stokes equations. Let us denote by $\mathbf{F}_{fric} = \mathbf{F}_{fric}(\mathbf{u})$ the contribution to the discrete forcing vector for Eqn. (3.78) arising from the friction law (4.21) (omitting the dependence on the SD contributions). The approximations just mentioned can be expressed as

$$\theta \mathbf{F}^n_{fric}(\mathbf{u}) + (1-\theta)\mathbf{F}^{n-1}_{fric}(\mathbf{u}) \approx \mathbf{F}_{fric}(\mathbf{u}^{n,i-1})$$

where $n$ and $i$ are the actual time step and iteration, respectively.

(7) The iterative penalty method has proved to be a fundamental ingredient for the success of the pseudo-concentration technique. In practical situations, especially for highly viscous flows, the viscosity of the fictious material will be several orders of magnitude smaller than that of the fluid analysed. Even if the exact value for the air is not used, it must be between 3 and 5 orders of magnitude smaller. Hence, choosing *a priori* a penalty parameter for the classical penalty method will yield unavoidably a poor approximation to the incompressibility constraint or to

ill-conditioning. This is aggravated by the fact that contiguous elements may have stiffness matrices of an order of magnitude completely different. We have observed from several numerical experiments that if $\epsilon$ is taken as $\epsilon = 10^{-n}\mu_{fluid}^{-1}$ (assuming the fluid viscosity to be constant) and $\mu_{air} = 10^{-3}\mu_{fluid}$, ill-conditioning is observed for values of $n$ as small as 3 (we have used the check proposed in Reference [ZT], Chapter 15, for ill-conditioning). □

**Box 4.2 General algorithm including free-surface tracking**

```
• Set the initial condition $\mathbf{U}^0$, $\mathbf{P}^0 = 0$, $\mathbf{\Theta}^0$ and $\mathbf{\Psi}^0$
• $n := 0$
• WHILE $n < N$ and (non-stationary) DO:
    • $n \leftarrow n + 1$
    • $i := 0$
    • WHILE (not converged) DO:
        • $i \leftarrow i + 1$
        • Solve the Navier-Stokes equations (3.78)–(3.79)
        • Update the physical properties and forcing terms
        • Solve the temperature equation (3.80)
        • Update the physical properties and forcing terms
        • Check convergence
      END while (not converged)
    • Check the sign of $\mathbf{n} \cdot \mathbf{u}$ for the temporary free wall nodes
      and adjust the boundary conditions for $\psi$ (see Box 4.1)
    • Solve the pseudo-concentration equation (4.7)
    • Smooth the pseudo-concentration (see Eqn.(4.9))
    • Update the physical properties according to (4.22)
    • Check whether $\psi \geq \psi_c$ or $\psi < \psi_c$ for the temporary free wall nodes
      and adjust the boundary conditions for $\mathbf{u}$ (see Box 4.1)
    • Check if the steady-state has been reached
  END while $n < N$ and (non-stationary)
  END
```

## 4.5 Application to some practical problems

The numerical model to simulate the mould filling process presented in this chapter will be applied now to three different problems. The first has been taken from Reference [DGC] and consists in the filling of a cavity due to the gravity acceleration. In the second problem the mould is filled by imposing an inflow velocity at the entrance of the cavity. The last problem is not directly related to the mould filling simulation, but demonstrates the possibility to apply the model described here to another metal forming problem: the plane strain hot rolling of a metal slab.

As in the two previous chapters, the numerical calculations have been carried out on a CONVEX-C320 computer using double arithmetic precision.

### 4.5.1 Mould filling by gravity

The problem definition for this first example is sketched in Figure 4.2. The mould is filled by a fluid that enters through the left vertical channel due to the action of the gravity acceleration. The data of the problem and the physical properties are those used in Reference [DGC]. In particular, the density and viscosity have been taken as $\rho_1 = 100$, $\mu_1 = 0.2$ for the fluid analysed (in SI units) and $\rho_2 = 0.1$, $\mu_2 = 0.02$ for the air (fictious material). Part of the top wall of the square cavity has been left free in order to allow the air evacuation. No temporary holes have been used for this example.

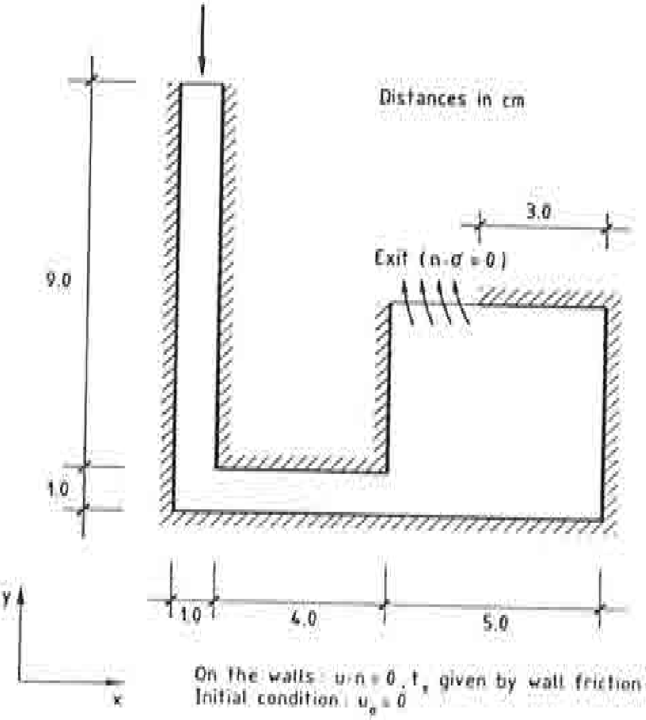
Distances in cm
3.0
Exit $(n \cdot \sigma = 0)$
9.0
5.0
1.0
1.0
4.0
5.0
y
x
On the walls: $u \cdot n = 0$, $t_s$ given by wall friction
Initial condition: $u_0 = 0$

Figure 4.2 Geometry and boundary conditions for the problem of mould filling by gravity (MFG).

The boundary conditions for the Navier-Stokes equations are zero normal velocities and tangent stresses given by the wall friction law (4.21), with $u^+ = 17.01$. The initial condition is zero velocity everywhere and the fluid front located at the entrance of the left vertical channel. No thermal analysis will be performed for this example.

The computational domain has been discretized using a rather uniform mesh of 280 $Q_2/P_1$ elements (see Figure 4.3), yielding 1233 nodal points. The iterative penalty method has been employed with a penalty parameter $\epsilon = 10^{-4}$. The algorithmic constants of the SD formulation have been taken as $\alpha_0 = 0.5$ and $h_0 = 2$. The backward Euler scheme has been used to advance in time for the Navier-Stokes equations and the Crank-Nicolson method for the transport of the pseudo-concentration, the time step size being $\Delta t = 0.01$ in both cases.

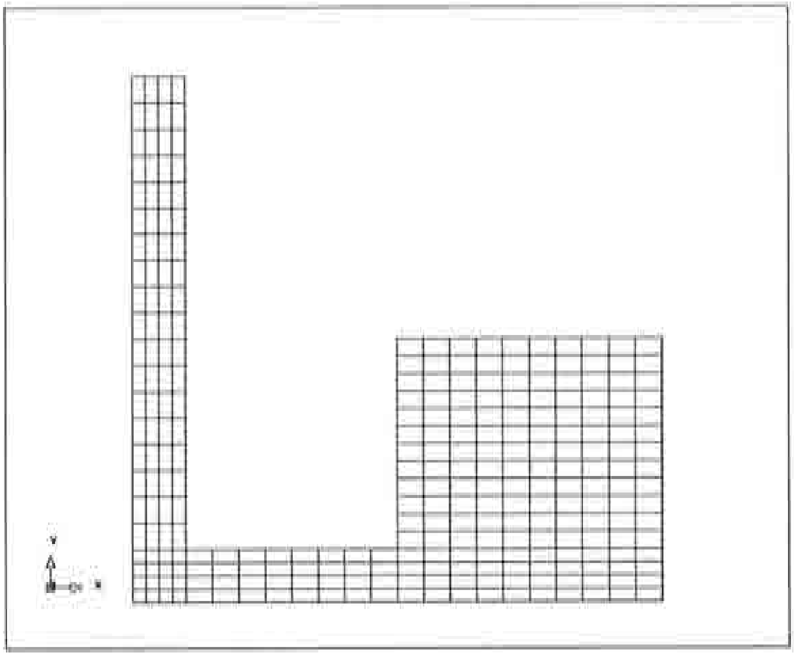

Figure 4.3 Finite element mesh for the problem of mould filling by gravity (280 $Q_2/P_1$ elements, 1233 nodal points) (MFG).

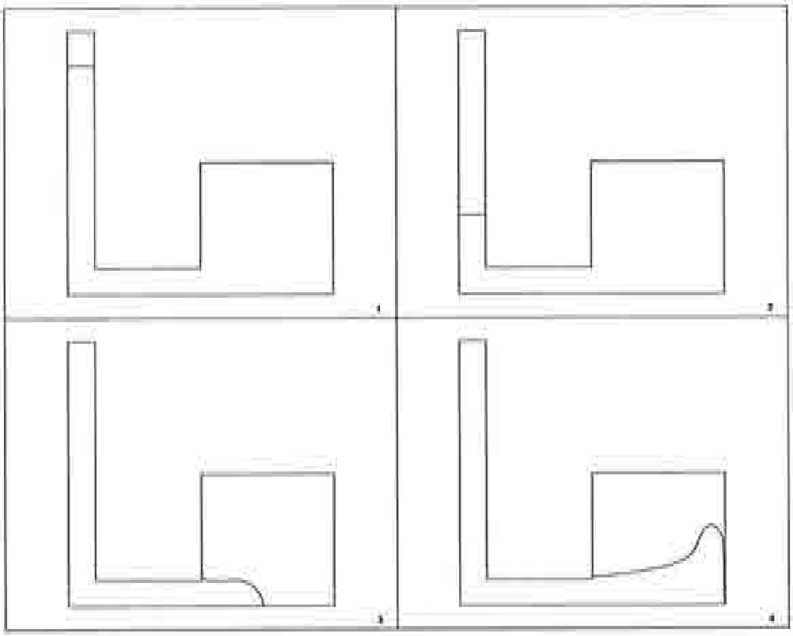

Figure 4.4 Positions of the fluid front using the $Q_2/P_1$ element (MFG). (1): $t = 0.1$; (2): $t = 0.2$; (3): $t = 0.3$; (4): $t = 0.4$.

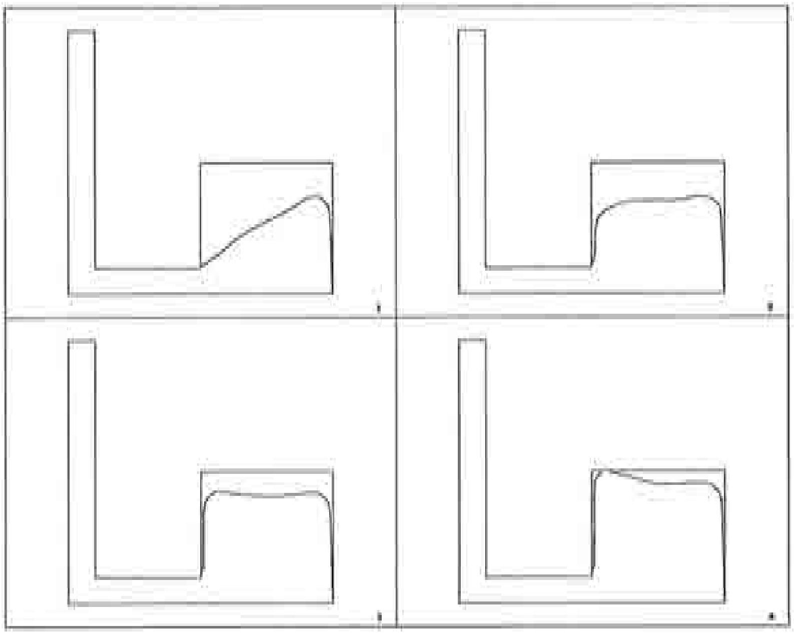

Figure 4.5 Positions of the fluid front using the $Q_2/P_1$ element (MFG). (1): $t = 0.5$; (2): $t = 0.6$; (3): $t = 0.7$; (4): $t = 0.8$.

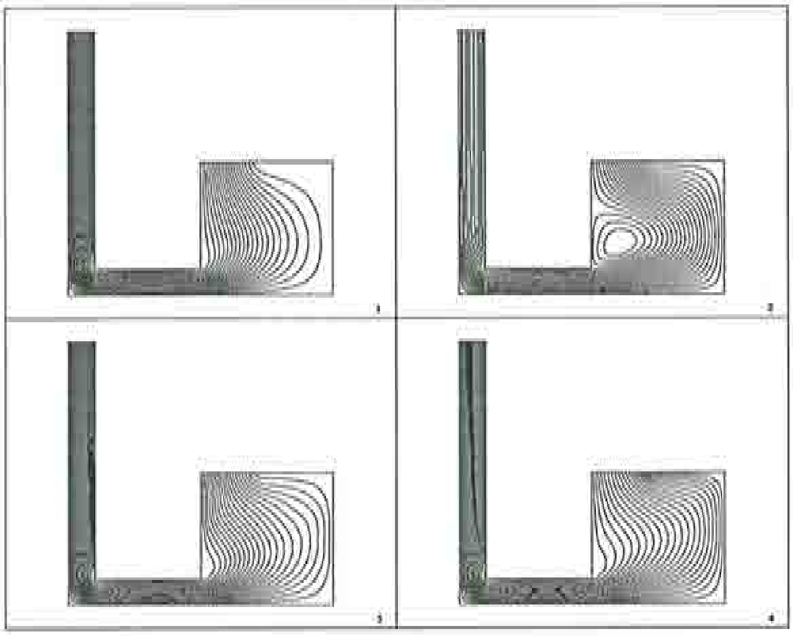

Figure 4.6 Evolution of the streamlines using the $Q_2/P_1$ element (MFG). (1): $t = 0.2$; (2): $t = 0.4$; (3): $t = 0.6$; (4): $t = 0.8$.

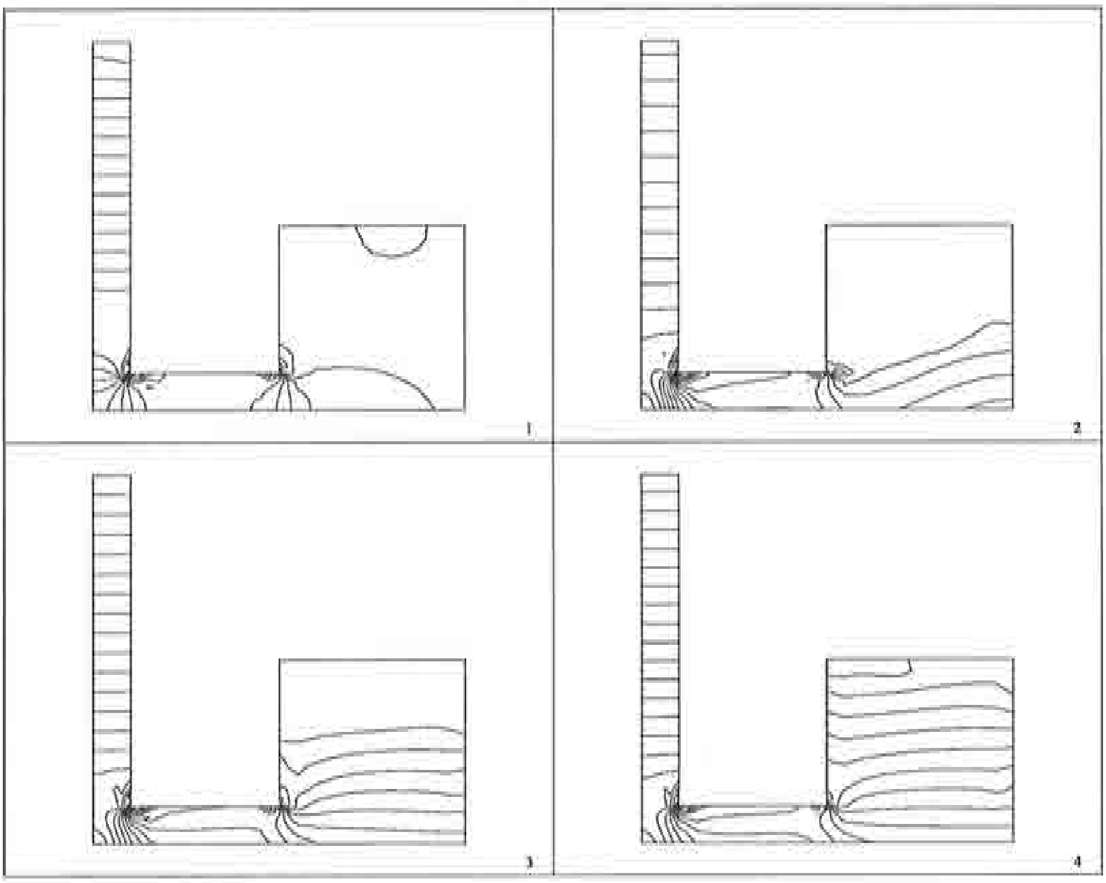

Figure 4.7 Evolution of the pressure contours using the $Q_2/P_1$ element (MFG). (1): t = 0.2; (2): t = 0.4; (3): t = 0.6; (4): t = 0.8.

Within each time step the convergence tolerance has been taken as 0.1%, first solving the transport of the pseudo-concentration and then iterating (using the Picard method) until a converged solution of the Navier-Stokes equation is found. Two iterations have been needed per time step. The final value of the norm of the incompressibility constraint has been found to be of order $10^{-11}$ for all the time steps.

Once the pseudo-concentration is calculated, the smoothing technique described in Section 4.3.2 has been employed, with a slope $\sigma = 1$ (see Eqn. (4.9)) and using five points within each element to compute the distace $d$.

Numerical results are shown in Figures 4.4 to 4.8. The evolution of the fluid front is depicted in the first two of them. In general, our results agree very well with those presented in Reference [DGC], although they are delayed since the initial position of the front is different and we have solved first the transport of the pseudo-concentration (cf. Remark 4.2.(2)). Looking at Figures 4.4.(1) and 4.4.(2) it is observed that the influence of the friction is very little at the walls of the vertical channel, since the shape of the front is almost straight there. To give a qualitative explanation to this fact, let us consider a single particle in contact with the walls and neglecting the effect of the contiguous particles, i.e., just considering the gravity acceleration. Denoting by

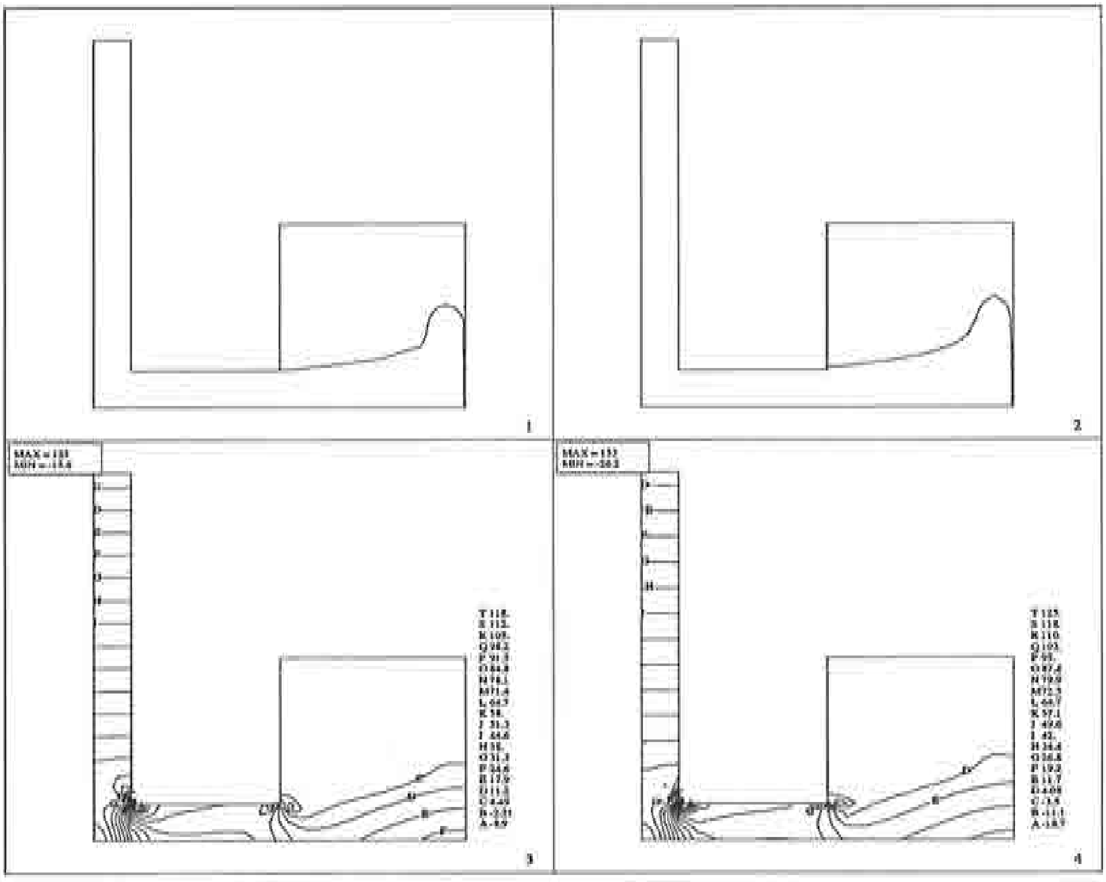

Figure 4.8 Comparison of the results obtained using the $Q_2/P_1$ and the $Q_1/P_0$ elements at time $t = 0.4$ (MFG). (1): Position of the front using the $Q_1/P_0$ element; (2): Position of the front using the $Q_2/P_1$ element; (3): Pressure contours using the $Q_1/P_0$ element; (4): Pressure contours using the $Q_2/P_1$ element.

$x = x(t)$ its vertical position measured from the entrance of the channel, this function will be the solution of the following non-linear equation

$$\ddot{x} = -\alpha(\dot{x})^2 + g \tag{4.23}$$

where $\alpha = (u^+)^{-2} \approx 3.46 \times 10^{-3}$ and $g$ is the gravity acceleration. Assuming initial conditions $x(0) = 0$ and $\dot{x}(0) = 0$, the solution of Eqn. (4.23) is

$$\dot{x}(t) = \sqrt{\frac{g}{\alpha}} \tanh(\sqrt{g\alpha}\; t) \tag{4.24}$$

$$x(t) = \frac{1}{\alpha} \log\left(\cosh(\sqrt{g\alpha}\; t)\right) \tag{4.25}$$

Expanding the velocity given by (4.24) in Taylor series in the neighborhood of $t = 0$ (or $\alpha = 0$) it is found that

$$\dot{x}(t) = g\left[t - \frac{1}{3}\alpha g t^3 + O(\alpha^2 g^2 t^5)\right]$$

from where it follows that for $\alpha$ small or $t$ small the influence of the friction is negligible with respect to the gravity effect. Friction will only be important once the vertical channel is completely filled. We have solved numerically the falling of the fluid in a very long channel (2 meters) and the position of the front agrees extremely well with the results predicted by Eqn. (4.25).

Let us return now to the discussion of the physical results. The evolution of the streamlines is shown in Figure 4.6. From the second box it is observed that a vortex is induced in the air due to the transmision of shear stresses from the fluid to the air. When the cavity is filled, this vortex disappears.

Pressure contours at different times are plotted in Figure 4.7. These contours allow to check the influence of the air on the motion of the fluid that fills the mould. Pressure gradients should be rapidly dissipated in the region occupied by the fictious material and this in fact is observed to happen (see the positions of the front in Figures 4.4 and 4.5 corresponding to the plots of Figure 4.7).

A comparison between the behavior of the $Q_2/P_1$ and the $Q_1/P_0$ elements is shown in Figure 4.8. For the latter element, the mesh has been built up by splitting each element of the mesh used for the former into four bilinear quadrilaterals and the SD parameters have been taken as $\alpha_0 = 1$ and $h_0 = 2$. Apart from this, the numerical strategy is the same in both cases. From the first and second boxes of Figure 4.8 it is observed that the $Q_1/P_0$ element shows a stiffer behavior than the $Q_2/P_1$ pair, for which the fluid front is smoother. Pressure contours in both cases are similar (slightly smaller absolute values are obtained using the $Q_1/P_0$ element). The possible stability problems that could be found using the bilinear-constant pair have not been observed for this particular example.

The cost of the numerical simulation is significantly smaller using the $Q_1/P_0$ than the $Q_2/P_1$ element. This is basically due to the formation and storage of the element matrices. The elemental stiffness matrix for the $Q_2/P_1$ element has $18 \times 18 = 324$ components, whereas four matrices for the $Q_1/P_0$ element have $4 \times 8 \times 8 = 256$ components. Also, the bandwidth of the assembled global matrix for the $Q_1/P_0$ pair is smaller than for the $Q_2/P_1$. Using a profile storage, the maximum column height (after renumbering the equations) for the problem now considered is 96 for the former and 163 for the latter. The total memory required is 2.44 and 2.13 Mega-bytes, and the CPU time per iteration 10.8 and 7.8 seconds, respectively. Finally, let us mention that the tracking of the free surface has a very reduced computational cost compared to the solution of the Navier-Stokes equations (the 16.36% of the total CPU time for the $Q_2/P_1$ element).

### 4.5.2 Injection mould filling

In this second example the numerical simulation of the filling of the mould shown in Figure 4.9 is considered. The geometry and experimental results for this problem have been provided by RENAULT (Reference [RA]). The experiments have been carried out using Gallium, a metal well suited to experimentation because it has a low fusion point (30° C) and therefore it is easy to use it in the laboratory and to recover it once the experiments are finished. Moreover, its properties are close enough to those of the alluminium and other metals used in casting applications.

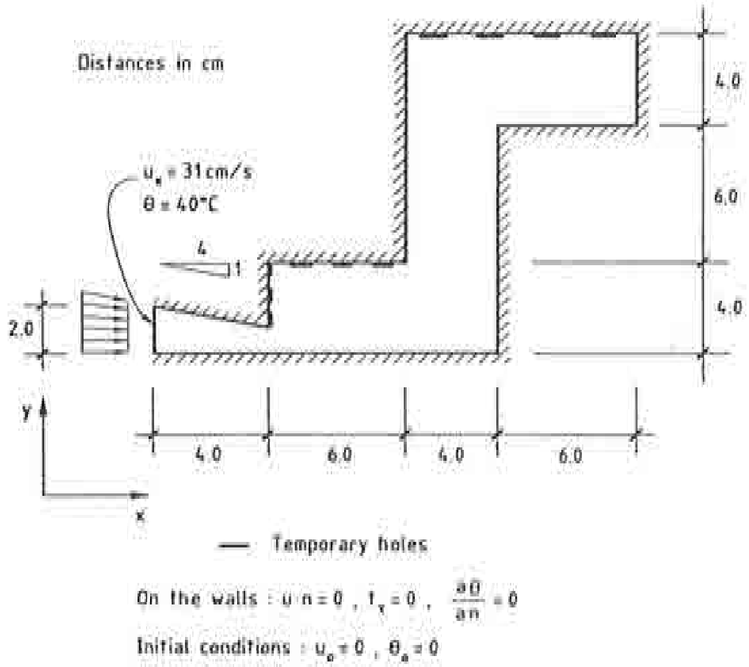
Distances in cm
$u_x = 31$ cm/s
$\theta = 40$°C
4
1
2.0
4.0
6.0
4.0
4.0
6.0
4.0
6.0
y
x
— Temporary holes
On the walls : $u \cdot n = 0$ , $t_y = 0$ , $\frac{\partial \theta}{\partial n} = 0$
Initial conditions : $u_o = 0$ , $\theta_o = 0$

Figure 4.9 Geometry and boundary conditions for the problem of injection mould filling (IMF).

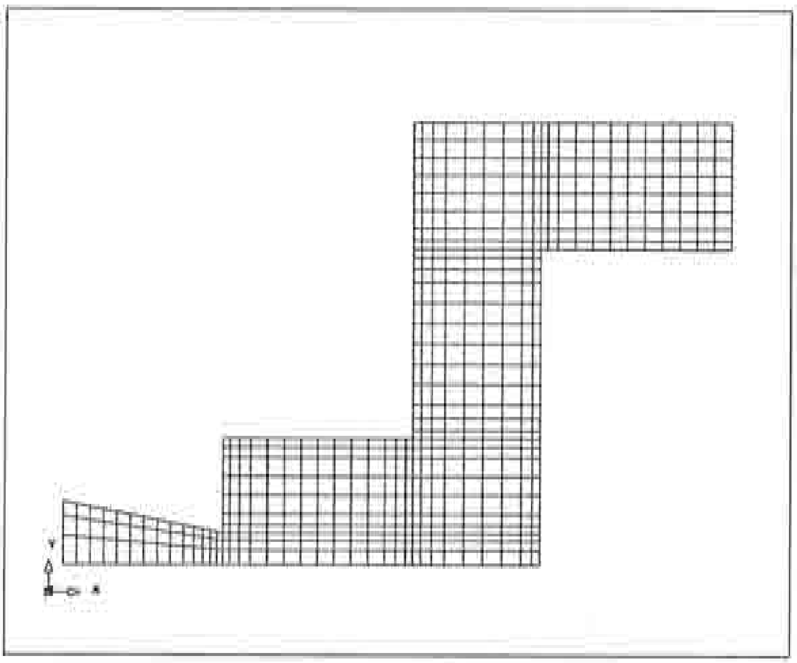

Figure 4.10 Finite element mesh for the problem of injection mould filling (548 $Q_2/P_1$ elements, 2351 nodal points) (IMF).

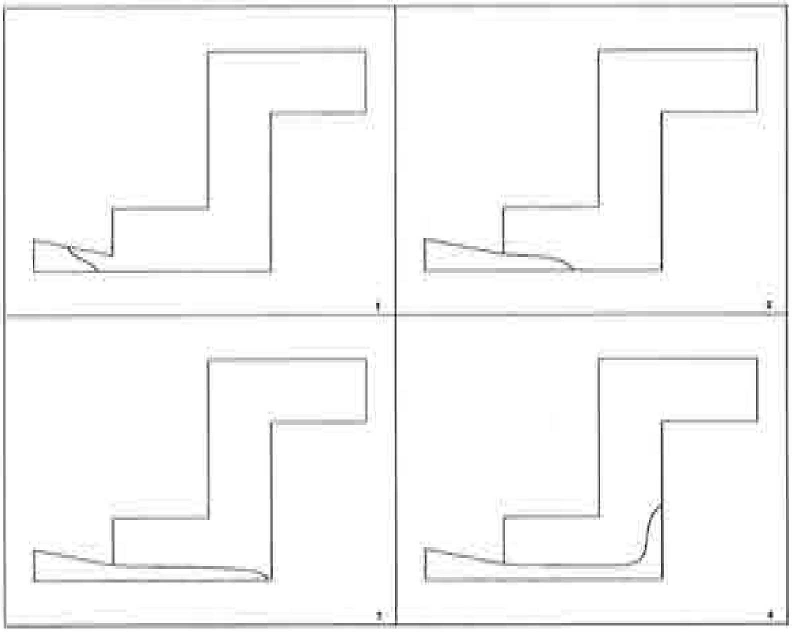

Figure 4.11 Positions of the fluid front (IMF). (1): t = 0.1; (2): t = 0.2; (3): t = 0.3; (4): t = 0.4.

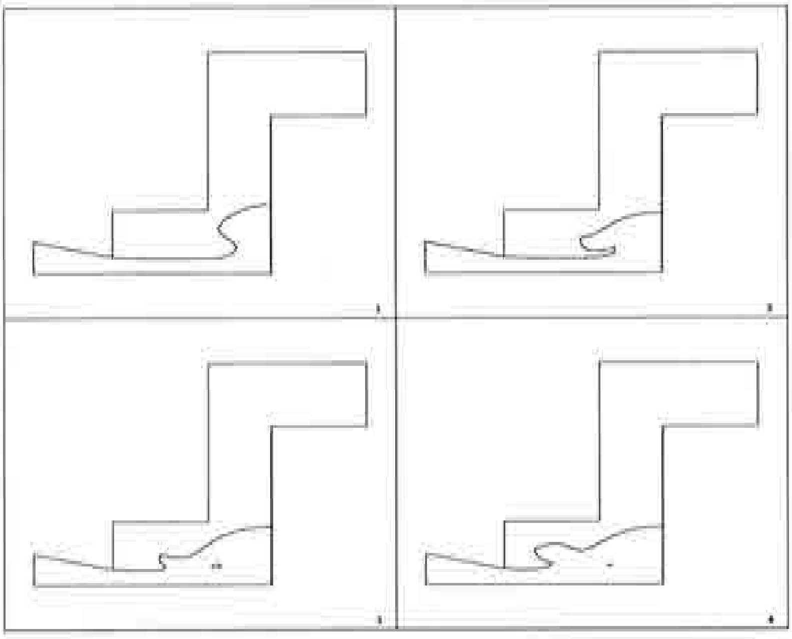

Figure 4.12 Positions of the fluid front (IMF). (1): t = 0.50; (2): t = 0.55; (3): t = 0.60; (4): t = 0.65.

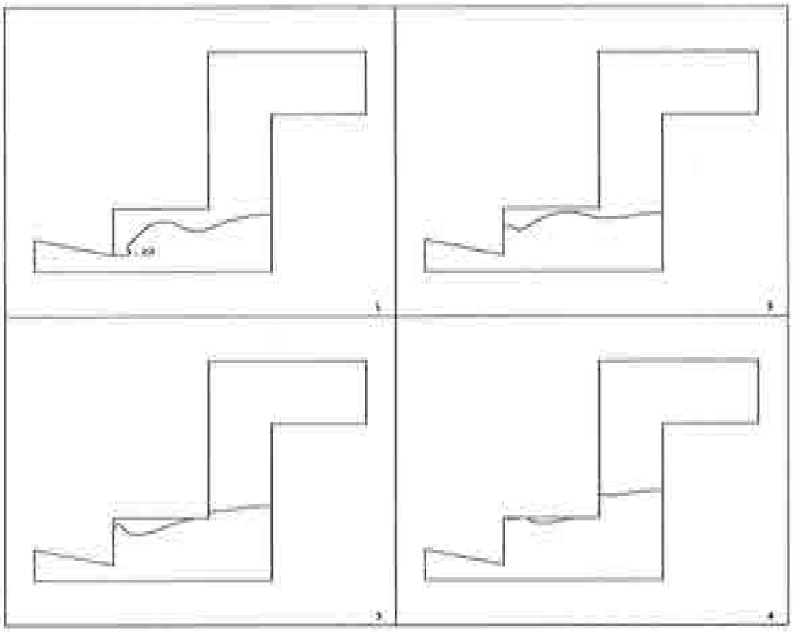

Figure 4.13 Positions of the fluid front (IMF). (1): $t = 0.7$; (2): $t = 0.8$; (3): $t = 0.9$; (4): $t = 1.0$.

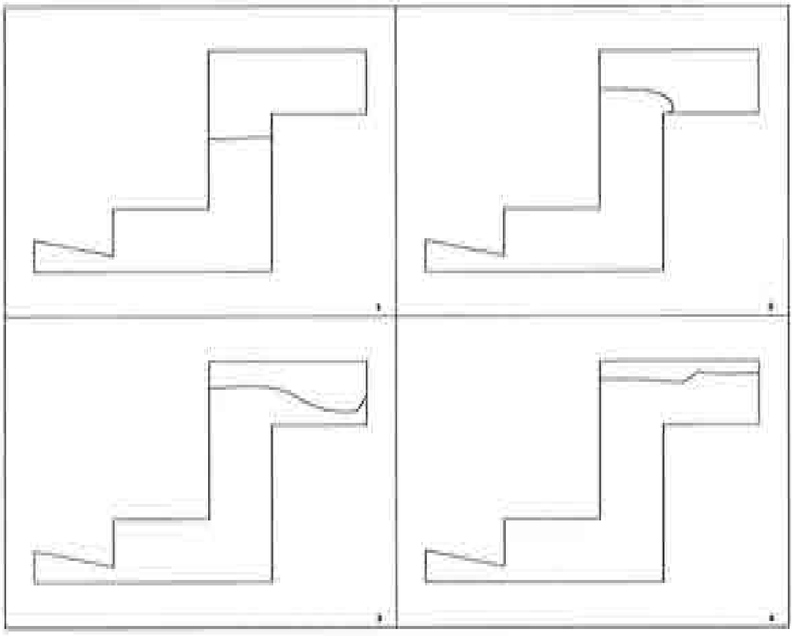

Figure 4.14 Positions of the fluid front (IMF). (1): $t = 1.2$; (2): $t = 1.4$; (3): $t = 1.6$; (4): $t = 1.8$.

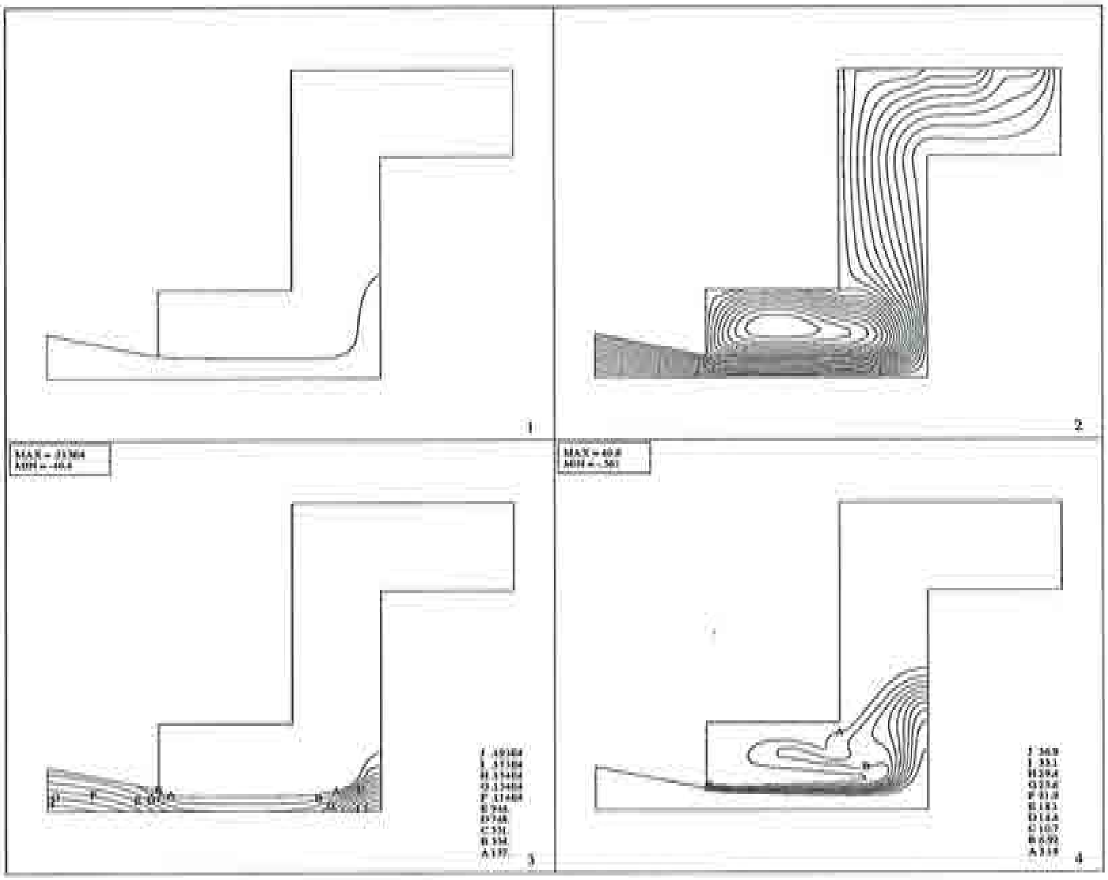

Figure 4.15 Some relevant physical results at $t = 0.4$ (IMF). (1): Position of the front; (2): Streamlines; (3): Pressure contours; (4): Temperature contours.

The molten metal enters through the left gate shown in Figure 4.9 with a horizontal velocity of 0.31 m/s. The vertical velocity is accomodated to the slope of the top wall of the entering gate. The physical properties of the molten Gallium at 55° C are (all in SI units) $\rho = 5.9 \times 10^3$ (density), $\mu = 1.9 \times 10^{-3}$ (dynamical viscosity), $k = 30.4$ (thermal conduction coefficient) and $c_p = 250$ (specific heat at constant pressure). Thus, the Reynolds number based on the velocity that enters the cavity (0.62) and its longitudinal length (0.1) is $Re = 1.93 \times 10^5$. The flow is clearly turbulent for such a high Reynolds number and it is impossible to simulate it with a laminar model as ours. The physical properties of air are $\rho = 1.2$, $\mu = 1.8 \times 10^{-5}$, $c_p = 1005$ and $k = 0.0256$. In order to reproduce the relative importance of all the physical effects, we have used the real properties of the Gallium and the air except for the dynamical viscosity, which has been taken $10^n$ times higher for both the Gallium and the air. Results are qualitatively similar for $n = 3$ and $n = 2$. We have failed to obtain a converged solution for lower values of this exponent.

The boundary conditions for this problem are zero normal velocities at the walls and zero tangent stresses, i.e., no friction with the walls is considered. The fluid is

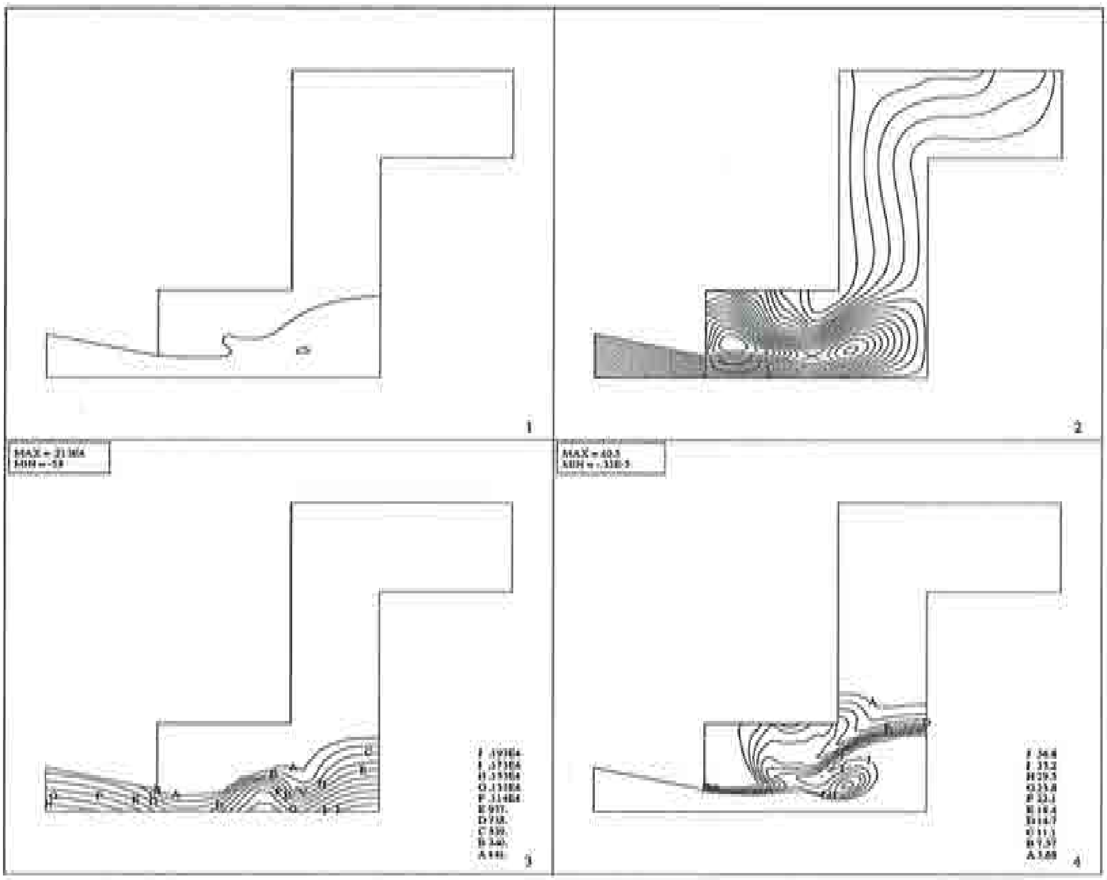

Figure 4.16 Some relevant physical results at $t = 0.6$ (IMF). (1): Position of the front; (2): Streamlines; (3): Pressure contours; (4): Temperature contours.

assumed to be initially at the entrance of the left gate. A thermally uncoupled flow model will be adopted. Therefore, it is possible to deal with relative temperatures. The temperature of the Gallium has been assumed to be 40° C higher than that of the air (i.e., 60° C for standard laboratory conditions). The walls of the mould have been assumed to be adiabatic.

The finite element mesh designed for this problem is shown in Figure 4.10. It consists of 548 $Q_2/P_1$ elements and 2351 nodal points. The iterative penalty method has been employed, using a penalty parameter $\epsilon = 10^{-4}$. The algorithmic constants of the SD method have been taken as $\alpha_0 = 0.5$ and $h_0 = 2$. The backward Euler scheme has been employed to advance in time for the three transient problems to be solved (velocity-pressure, temperature and pseudo-concentration). The smoothing technique described in Section 4.3.2 has been used, with $\sigma = 1$ and five additional points within each element to compute the distance $d$ (see Eqn. (4.9)). Within each time step, of size $\Delta t = 0.01$, the advection of the pseudo-concentration has been solved first and then iterations have been carried out (between three and four) to obtain a converged solution of the Navier-Stokes equations (with a tolerance 0.1%). Finally, the temperature equation has been solved.

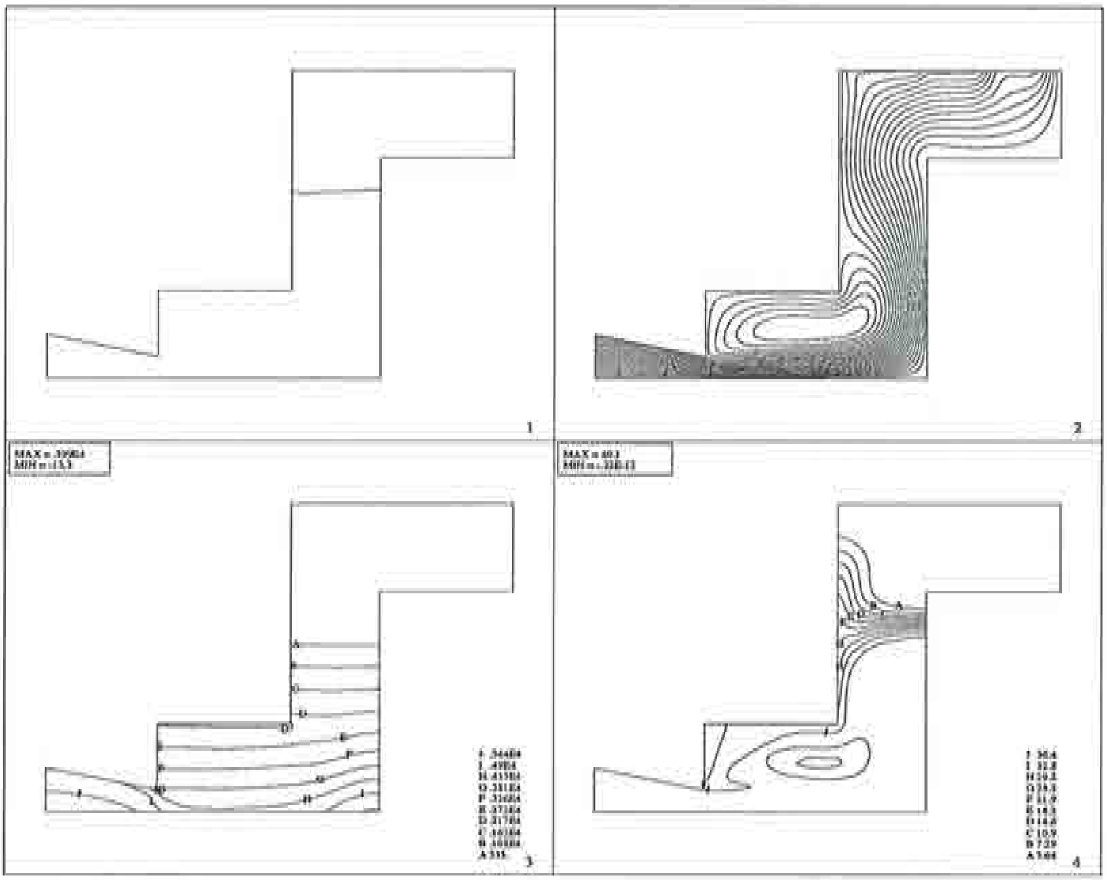

Figure 4.17 Some relevant physical results at $t = 1.2$ (IMF). (1): Position of the front; (2): Streamlines; (3): Pressure contours; (4): Temperature contours.

In order to allow the air evacuation, some holes have been introduced on the walls of the mould. They are schematically shown in Figure 4.9 (three or four nodes of the finite element discretization correspond to each hole). The parameter $\lambda$ to block them when the Gallium touches the wall (see Section 4.3.3) has been taken as $\lambda = 10^6$.

Numerical results are shown in Figures 4.11 to 4.20. The position of the fluid front at different times is depicted in Figures 4.11 to 4.14. It is observed how several air bubbles appear in the Gallium. This fact is also observed in the experimental results [RA], with which the numerical simulation shows a good qualitative agreement. The differences should be attributed to the different Reynolds number of the numerical calculation. Air bubbles disappear as time goes on due to the artificial effect of the smoothing technique. Observe from Figure 4.1 that the interpolation of the front by a straight segment within each element will advance or delay artificially the front depending on its curvature. Physically, air bubbles disappear because air can escape through the porous lateral walls of the sand mould.

Figures 4.15 to 4.18 show the position of the fluid front, the streamline pattern, the pressure contours and the temperature contours at different times. From the streamline plots, it is observed how air enters or leaves the mould through the holes, as well as

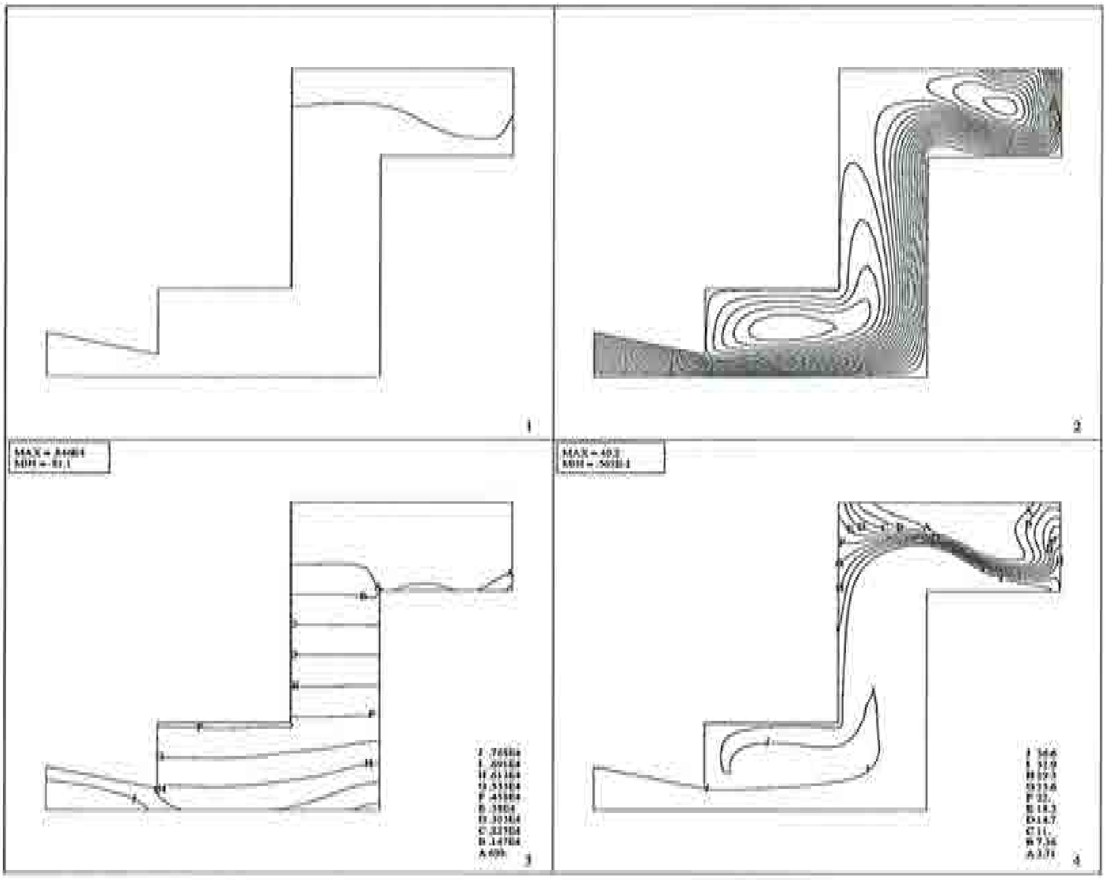

Figure 4.18 Some relevant physical results at $t = 1.6$ (IMF). (1): Position of the front; (2): Streamlines; (3): Pressure contours; (4): Temperature contours.

the creation of vortices due to the transmision of shear stresses. All these results are in accordance with what physical intuition predicts. From the pressure plots it is seen that pressure gradients are rapidly dissipated in the air region. This indicates that the motion of air does not influence much that of the Gallium. Isotemperature curves show how heat is basically transported through convection. Conduction transport is only apparent in regions occupied by Gallium that has first entered the cavity. It is remarkable to note the high temperature gradients that the numerical method is able to capture at the interface between hot Gallium and cold air.

Velocity vectors at times $t = 0.6$ and $t = 1.6$ are plotted in Figures 4.19 and 4.20, respectively. From the former it is observed how air enters the mould through the holes placed at the top wall and leaves it through the holes of the bottom left corner. The pseudo-concentration is prescribed at the temporary inflow using the penalization technique described in Section 4.3.3. Otherwise, spurious fluid would enter the cavity. The effect of the blocking of the holes when Gallium contacts the walls is clearly appreciated from Figure 4.20. It is also observed that a vortex remains in the fluid-filled region.

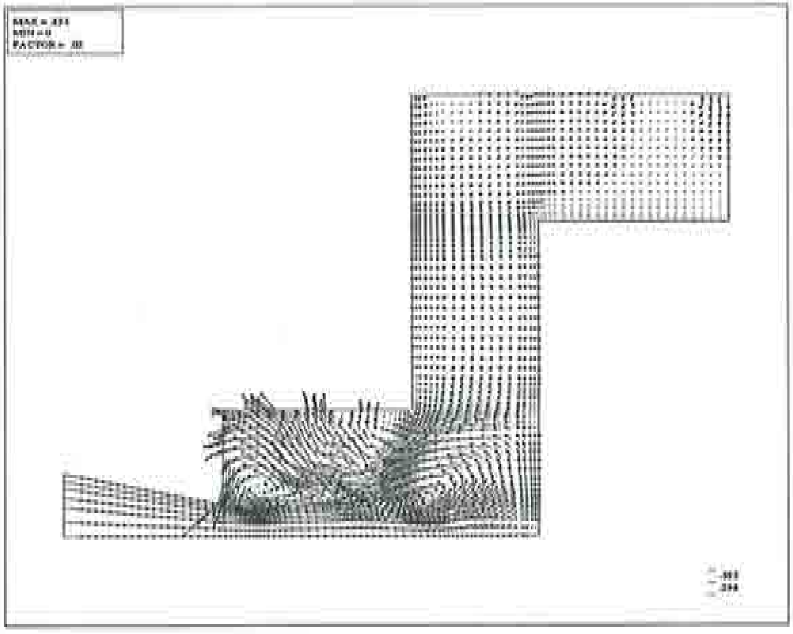

Figure 4.19 Velocity vectors at $t = 0.6$ (IMF).

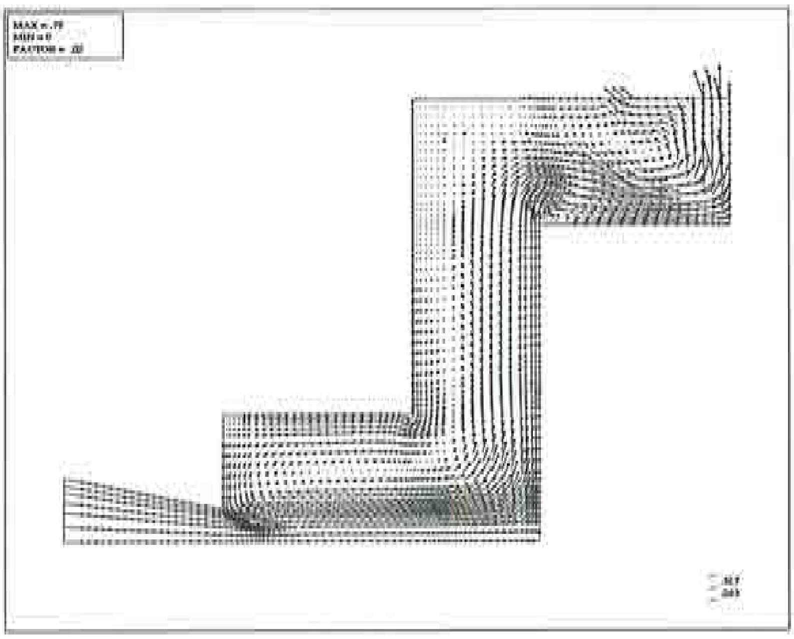

Figure 4.20 Velocity vectors at $t = 1.6$ (IMF).

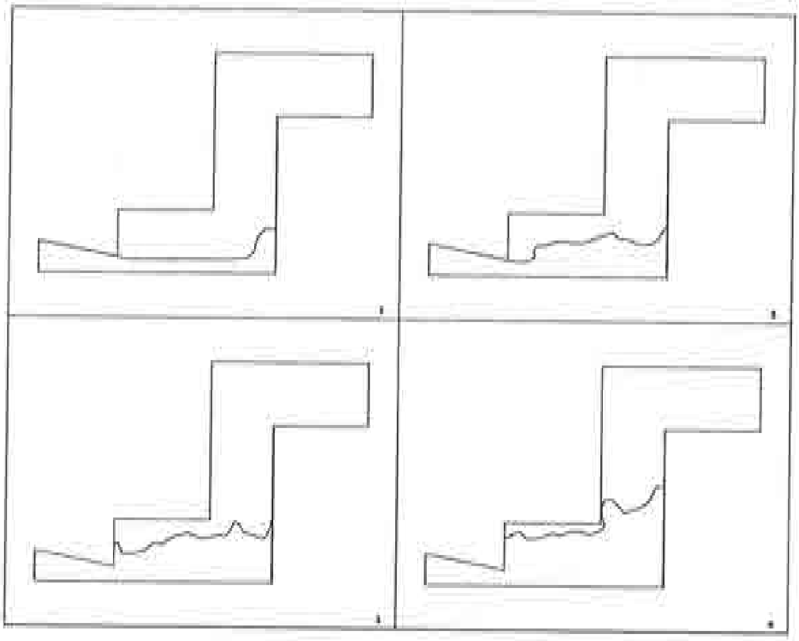

Figure 4.21 Positions of the fluid front without the introduction of holes on the walls (IMF). (1): t = 0.5; (2): t = 1.0; (3): t = 1.5; (4): t = 2.0.

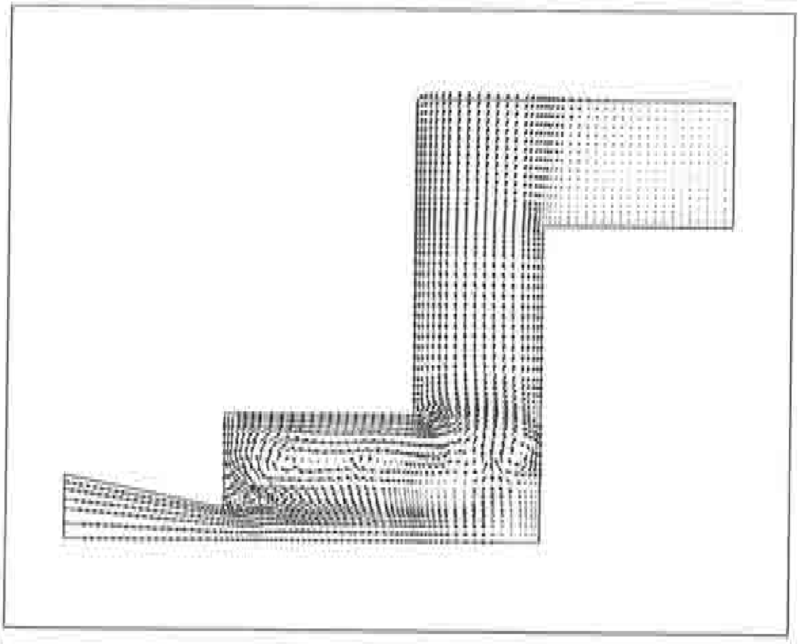

Figure 4.22 Velocity vectors at $t = 1.0$ without the introduction of holes on the walls (IMF).

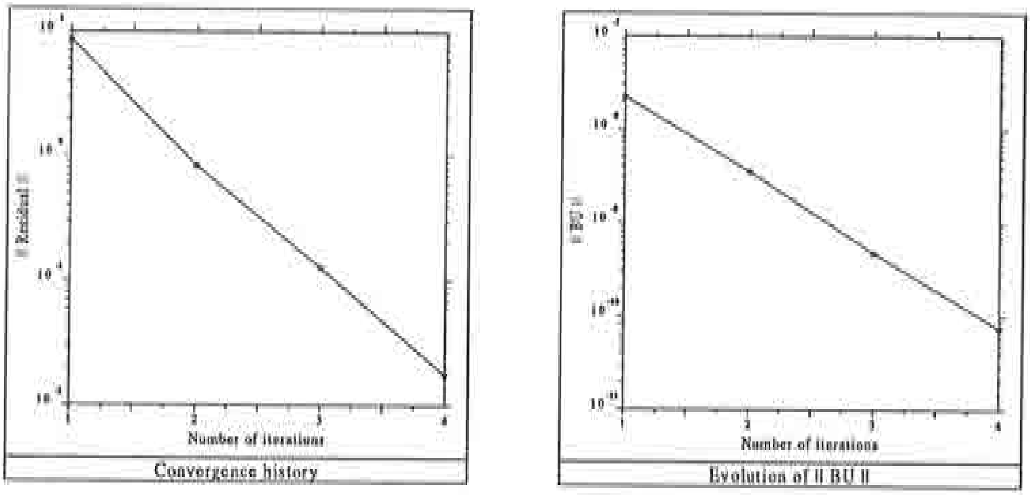

Figure 4.23 Convergence history and evolution of the norm of the incompressibility constraint for time step number 77 (IMF).

If air is not allowed to escape, the flow features are much more complicated. If only the top wall is left free, the position of the fluid front at different times is depicted in Figure 4.21. It could be argued that the ondulations of the fluid surface are due to a misbehavior of the pseudo-concentration technique. To show that this is not the case, the velocity vectors for $t = 1.0$ have been plotted in Figure 4.22. It is observed how small recirculation zones are created in the air region, thus inducing the shape of the fluid front.

Referring now to some computational aspects of the calculation, the behavior of the iterative penalty method has been found to be again very effective. The convergence history and the evolution of the norm of the incompressibility constraint for time step number 77 are shown in Figure 4.23. It is observed that this norm decreases almost three orders of magnitude in four iterations. This decrease is even more accentuated for the first time steps (not shown). Starting from a value of order $10^{-7}$, a final value of order $10^{-11}$ is obtained in four iterations.

Most of the computational cost of the simulation is due to the solution of the Navier-Stokes equations. The CPU time per iteration has been 24.27 seconds (54.96% for the formation of the element matrices, 44.96% for the solution of the linear system). The pseudo-concentration and the temperature are solved only once per time step. The CPU time needed has been 5.03 (11.54% for the element matrices, 52.98% for the linear system, 35.48% for the smoothing and updating of physical properties) and 3.05 seconds (24.83% for the element matrices, 75.16% for the linear system), respectively.

### 4.5.3 Hot rolling of a rectangular slab

The plane stress hot rolling of a metal has been chosen for this last example. The problem definition is sketched in Figure 4.24. All the data except for slight changes in the geometry have been taken from Reference [ZOH]. In particular, the constitutive law (3.58) has been adopted for the metal, with $\gamma = \infty$ (pure plastic flow) and $\sigma_y$

depending on the temperature through the following empirical law:

$$\sigma_y = \frac{1}{C_1}\left[\left(\frac{Z}{C_2}\right)^{1/C_3} + \sqrt{\left(\frac{Z}{C_2}\right)^{2/C_3} + 1}\right] \tag{4.26}$$

with

$$Z := \sqrt{3}\bar{\varepsilon}\exp\left(\frac{C_4}{R\vartheta}\right) \tag{4.27}$$

The parameter $\bar{\varepsilon}$ is defined by Eqn. (3.57) and the experimental constants $C_i$, $i = 1, 2, 3, 4$, and $R$ are

$$\begin{aligned} C_1 &= 0.01901 && \mathrm{m^2/MN} \\ C_2 &= 7.92 \times 10^8 && \mathrm{s^{-1}} \\ C_3 &= 5.0 && \\ C_4 &= 1.39 \times 10^5 && \mathrm{J/g\ mole} \\ R &= 8.311 && \mathrm{J/g\ mole\ K} \end{aligned}$$

The use of the pseudo-concentration technique will allow us to follow the metal since it first contacts the roll until the steady-state is reached. Besides the inherent interest of this numerical simulation, a classical problem concerning free surfaces will be solved: the swelling problem (see, e.g., Reference [WC] and references therein).

The values of the physical properties we have used are the following:

| | Metal | Fictious fluid |
|---|---|---|
| $\rho$ Kg/cm$^3$ | 0.00275 | 0.001 |
| $k$ cal/cm s K | 0.4302 | 0.01 |
| $c_p$ cal/Kg K | 239.01 | 1000.0 |
| $\mu$ N s/cm$^2$ | | 1.0 |

For the viscosity law (3.58), a cut-off value $\mu_c = 10^5$ has been chosen. The viscosity values in the metal for the converged solution are always below this limit, except where the strain rate is small, i.e., in regions where the flow approach used here is not valid. This happens before the metal contacts the roll. Since we assume that the initial position of the metal is the first contact with this roll (see Figure 4.24), this simplification is immaterial for the results.

In practice, there is no rigid contact between the metal and the roll. In order to simulate the friction between them, we have just assigned a smaller viscosity (100 times smaller) to a boundary zone defined by very narrow elements (see Figure 4.25). In Reference [ZOH], the friction was introduced by means of a law relating $\sigma_y$ with the pressure and using a somehow arbitrary friction coefficient. The introduction of proper friction laws between roll and slab surfaces is an aspect that deserves further investigation.

Not all the plastic work has been considered to be transformed into heat, but only the 90%. Therefore, the source term for the energy equation given by expression (3.63) has been multiplied by 0.9.

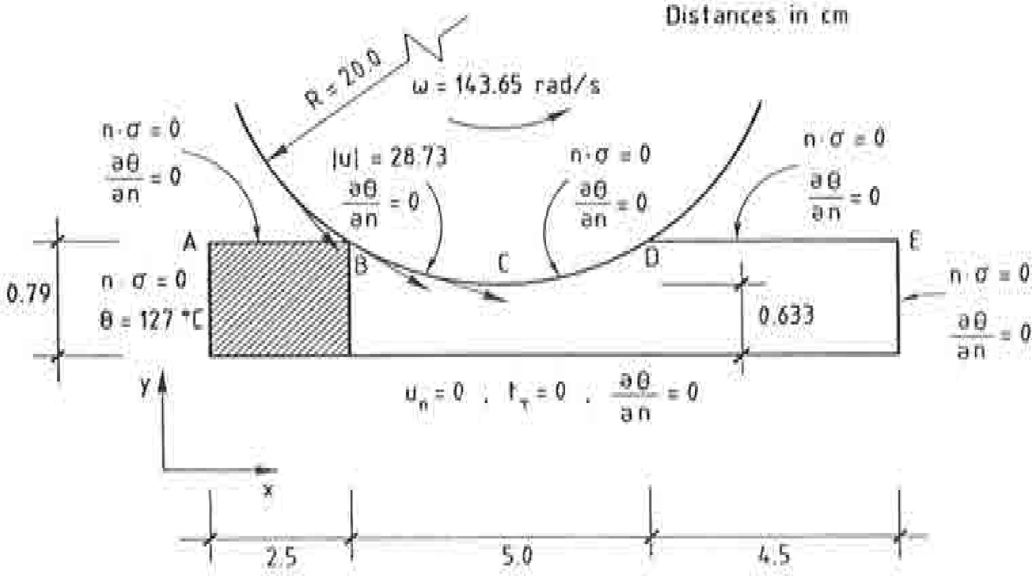

Figure 4.24 Geometry and boundary conditions for the problem of hot rolling of a metal slab (HRM).

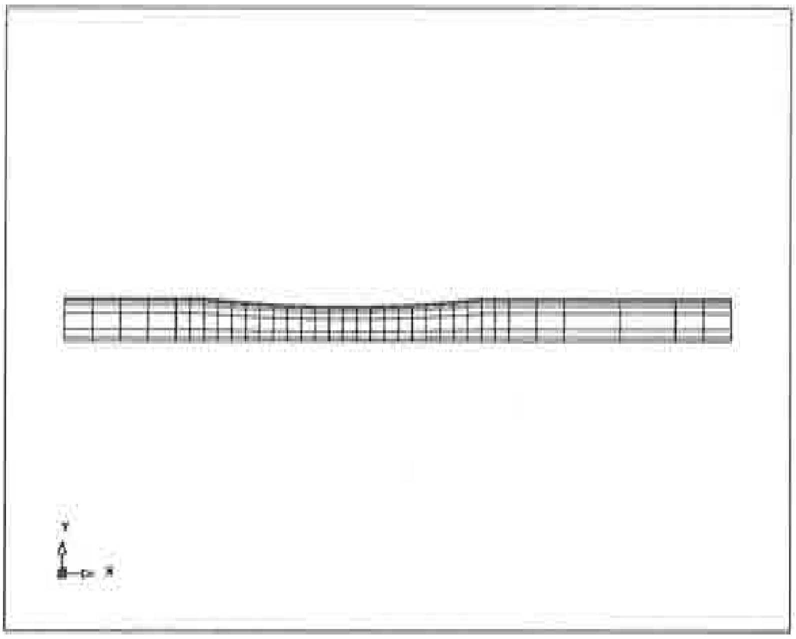

Figure 4.25 Finite element mesh for the problem of hot rolling a metal slab (HRM) (340 $Q_2/P_1$ elements, 1449 nodal points).

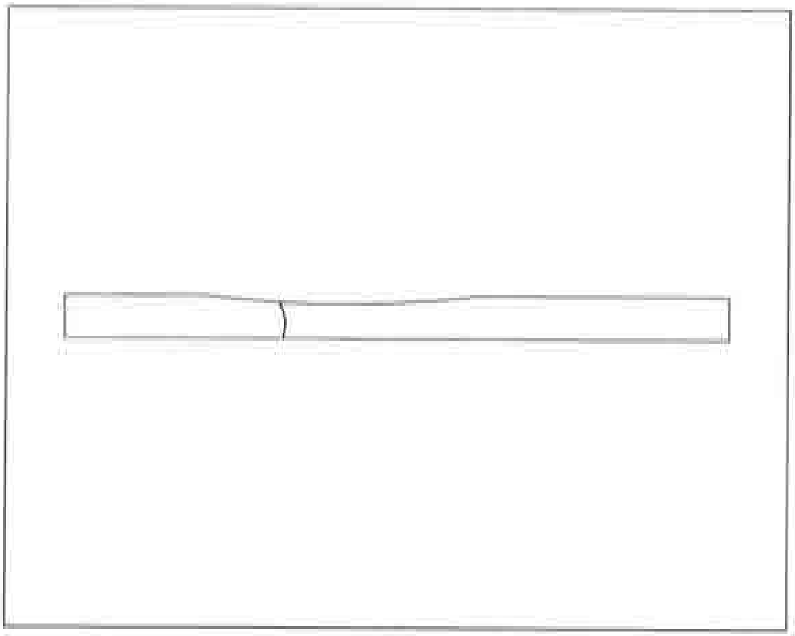

Figure 4.26.(a) Position of the metal front at $t = 0.5$ (HRM).

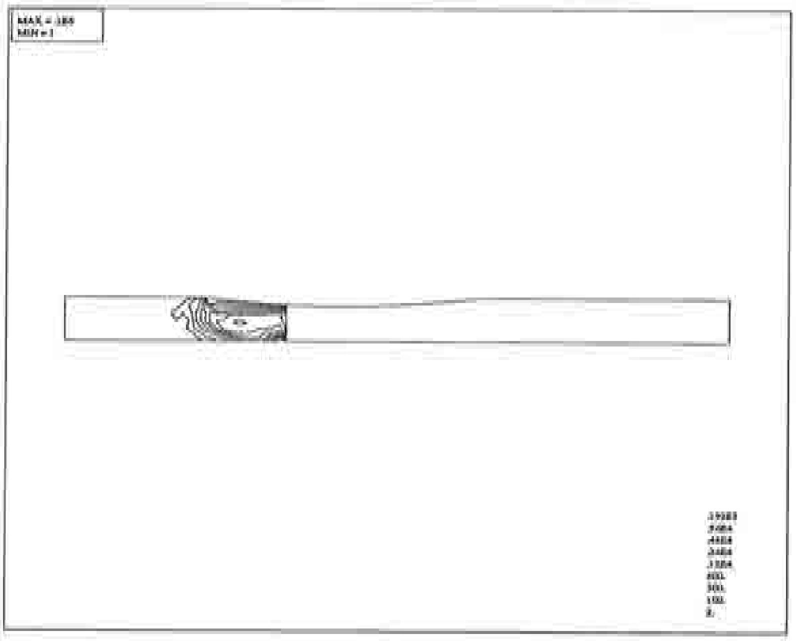

Figure 4.26.(b) Some viscosity contours at $t = 0.5$ (HRM).

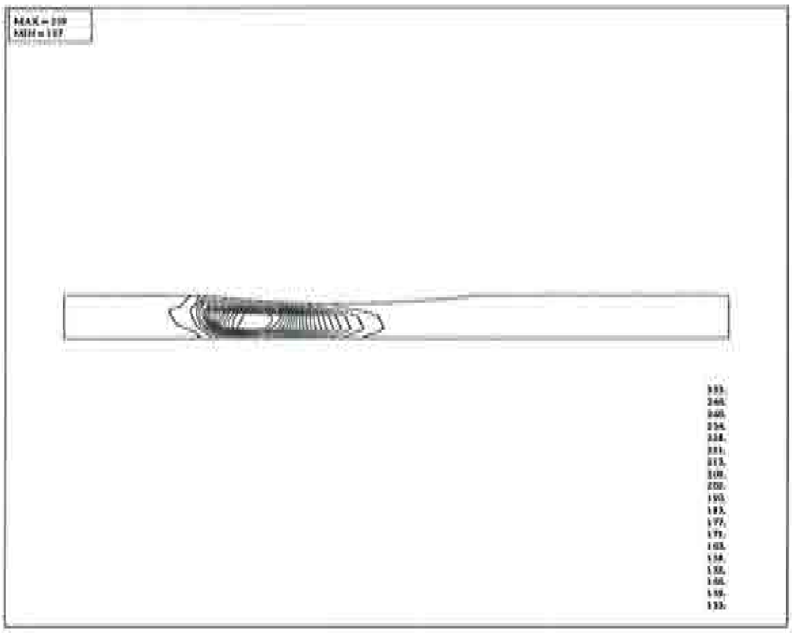

Figure 4.26.(c) Temperature contours at $t = 0.5$ (HRM).

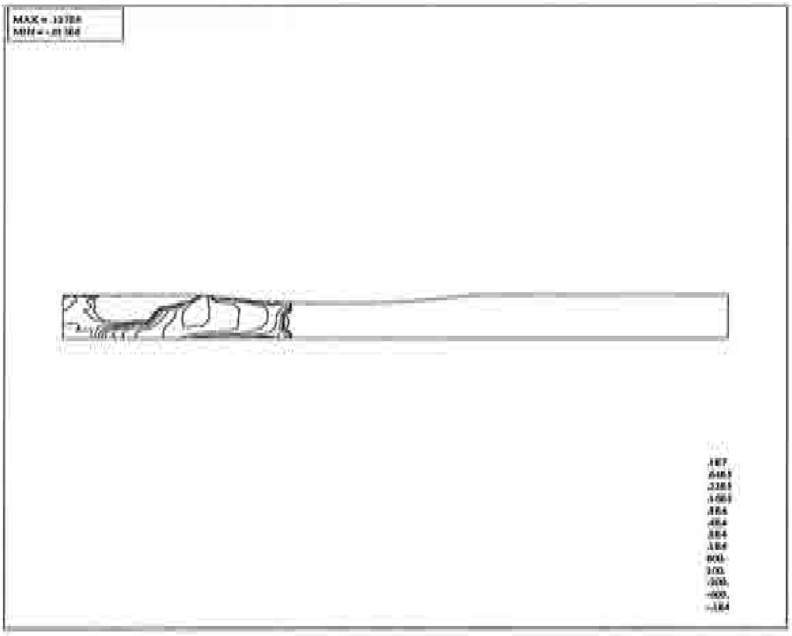

Figure 4.26.(d) Some pressure contours at $t = 0.5$ (HRM).

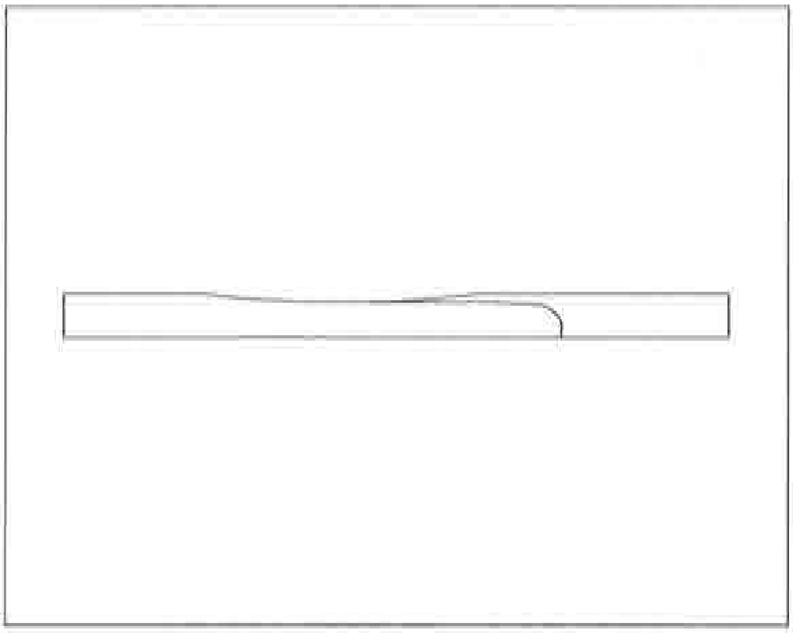

Figure 4.27.(a) Position of the metal front at $t = 2.0$ (HRM).

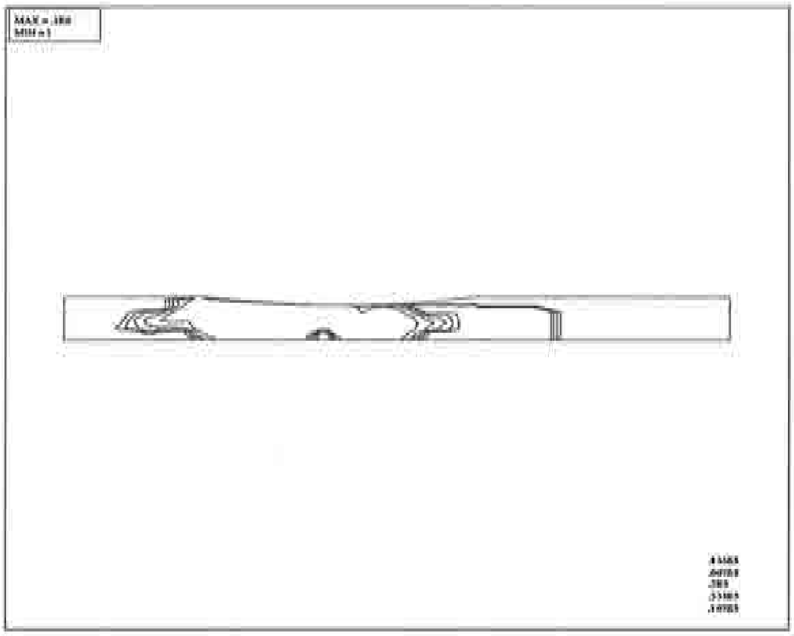

Figure 4.27.(b) Viscosity contours at $t = 2.0$ (HRM).

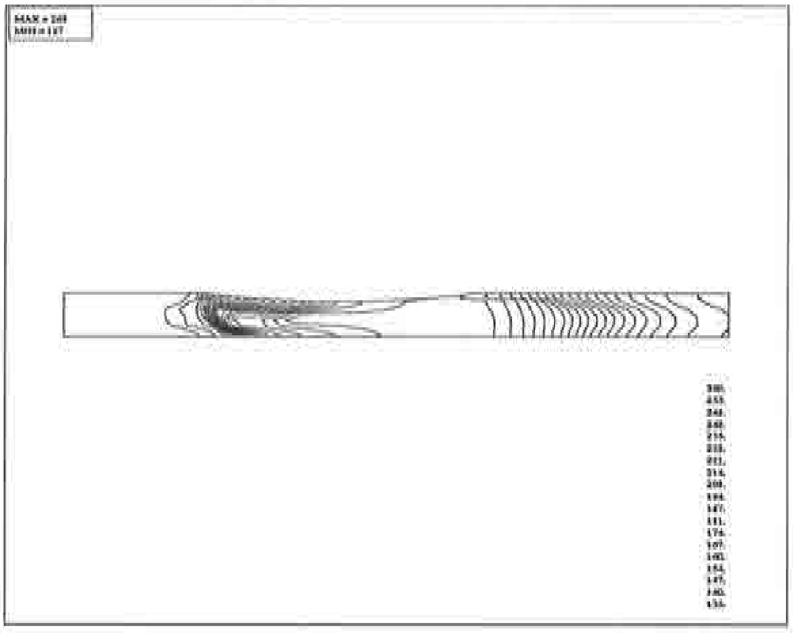

Figure 4.27.(c) Temperature contours at $t = 2.0$ (HRM).

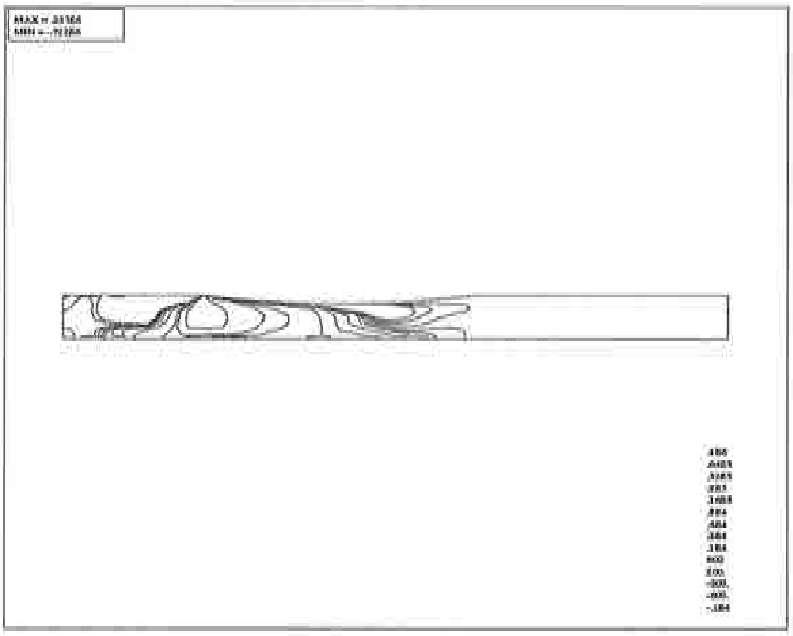

Figure 4.27.(d) Some pressure contours at $t = 2.0$ (HRM).

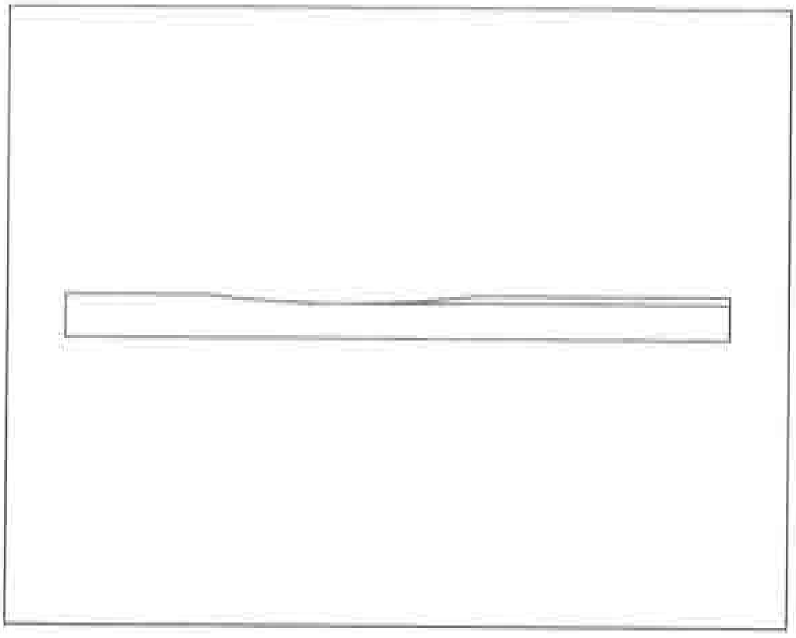

Figure 4.28.(a) Position of the metal front at $t = 5.0$ (HRM).

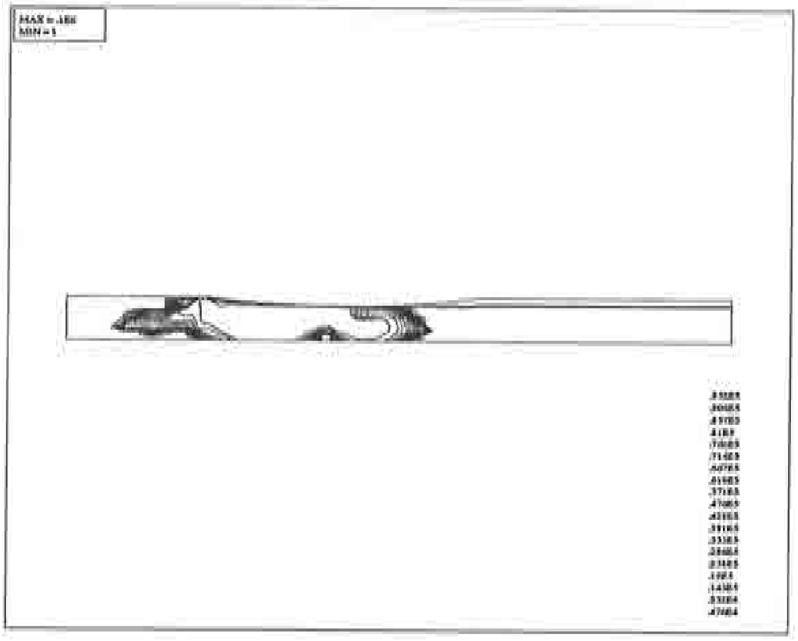

Figure 4.28.(b) Viscosity contours at $t = 5.0$ (HRM).

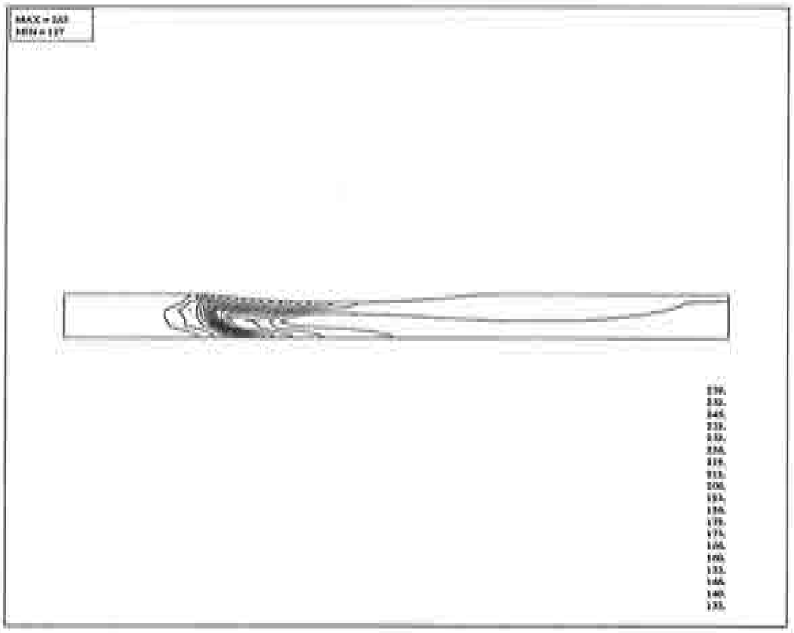

Figure 4.28.(c) Temperature contours at $t = 5.0$ (HRM).

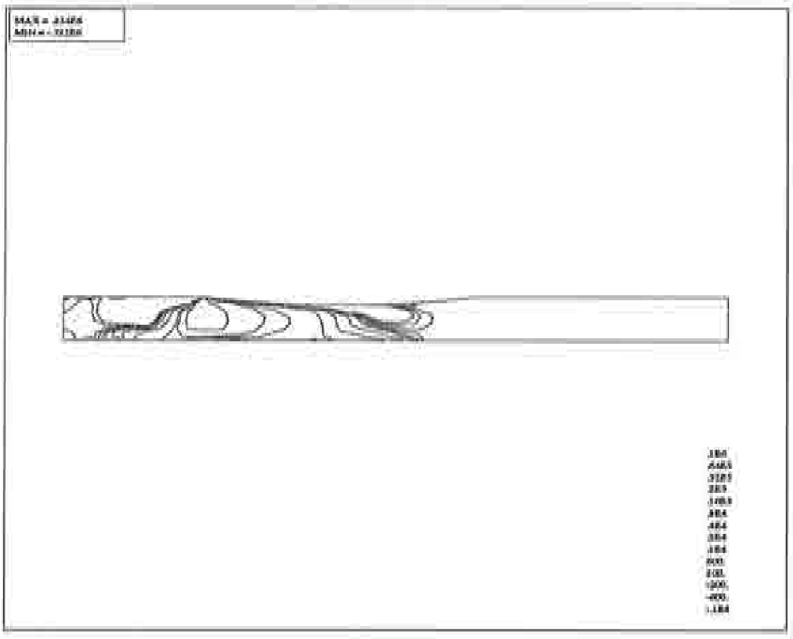

Figure 4.28.(d) Some pressure contours at $t = 5.0$ (HRM).

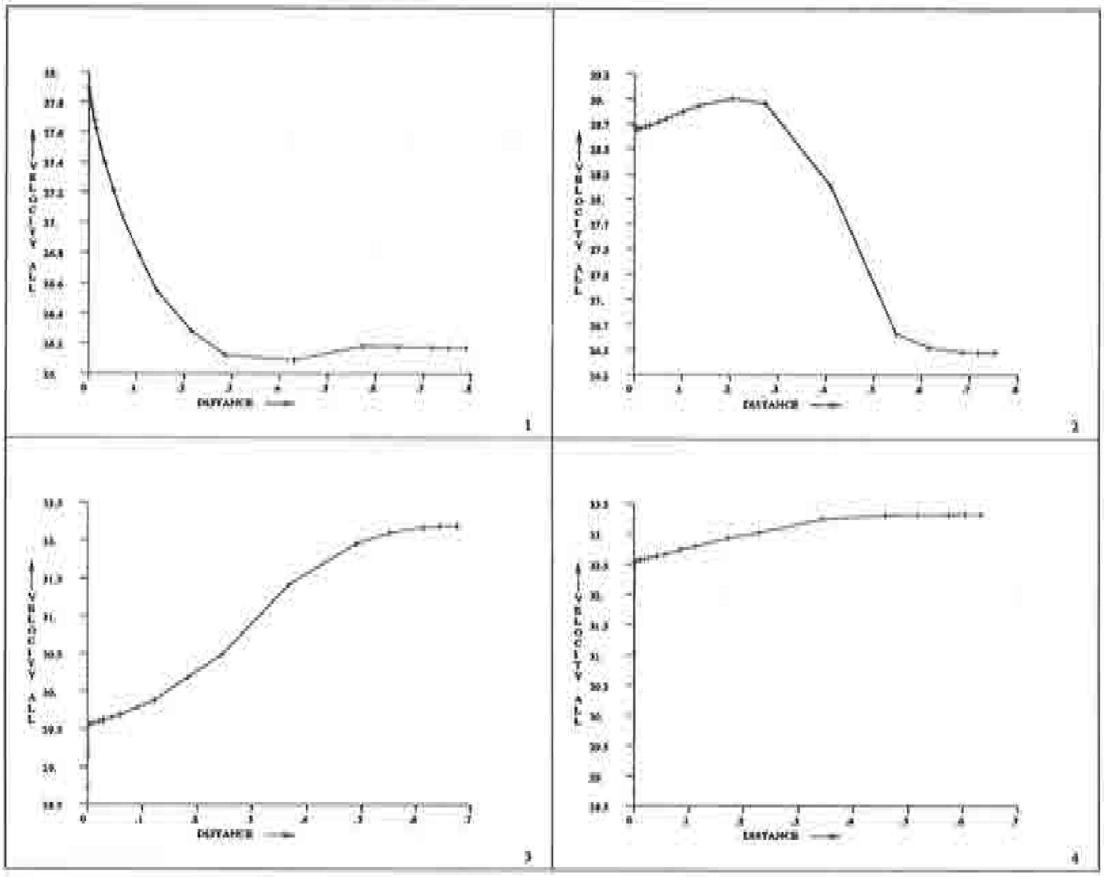

**Figure 4.29** Velocity profiles (norms) for some vertical sections at $t = 5.0$ (HRM). (1): Contact with the roll ($x = 2.5$); (2): $x = 3.125$; (3): $x = 3.750$; (4): Center of the roll ($x = 5.0$).

The computational domain has been discretized using the mesh shown in Figure 4.25. It consists of 340 $Q_2/P_1$ elements, with 1449 nodal points. A parameter $\epsilon = 10^{-9}$ has been used for the iterative penalty method. Convective terms for the Navier-Stokes equations have been neglected (creeping flow). Since convection is not very important for the temperature equation either, the Galerkin approach has been used to solve it. The transport of the pseudo-concentration has been solved using the SD formulation, with $\alpha_0 = 0.5$ and $h_0 = 2$. As for the previous examples, within each time step this transport equation is solved first. Since now the flow is thermally coupled, the block iterative scheme described in Chapter 3 has been employed to deal with the mechanical and thermal problems. The time step size has been taken as $\Delta t = 0.01$, using the backward Euler scheme to advance in time. Now, *no smoothing* of the pseudo-concentration has heen performed, i.e., a true step function is transported. The metal is defined by the value 1 and the 'air' for the value 0. The metal front is assumed to be defined by $\psi_c = 0.5$.

In all the previous examples, no comment has been made about the numerical integration rule. We have always used the Gauss-Legendre 3 × 3 integration for the 2D

$Q_2/P_1$ element. However, when the viscosity at the nodes of the mesh is computed using the least-squares smoothing technique described in Chapter 2, oscillations appear in the vicinity of sharp viscosity gradients, i.e., at the metal front in this case. This problem was not encountered for the problem solved in Section 3.5.3 because the variation we obtained for the viscosity was smooth. In order to avoid this problem, for this particular example we have used the nodal $3 \times 3$ rule (Lobatto), i.e., with the integration points placed at the nodes of the elements. Therefore, no smoothing is needed to obtain nodal viscosity values.

Numerical results at different times are shown in Figures 4.26 to 4.28. The position of the metal front, some viscosity contours, temperature contours and pressure contours are plotted for each case. It is observed that the viscosity is low where the temperature is high, in accordance with the constitutive law given by Eqns. (3.58), (4.26) and (4.27). High temperatures appear in the region where the strain rate is higher, arising from the transformation of plastic work into heat. From Figure 4.19 it is observed how the swelling effect is perfectly well reproduced using the pseudo-concentration technique.

The velocity profiles for different sections $x = const.$ are shown in Figure 4.29. Recalling that the velocity of the roll is 28.73 cm/s, it is observed that the no-slip point is placed approximately at $x = 3.125$. The relative velocity between the roll and the metal depends on the friction coefficient to be used for the narrow elements in contact with the roll.

We have also computed the roll force and the roll torque, assuming as in Reference [ZOH] that the former acts midway along the angular arc of contact and that it is directed towards the roll center. The values we have obtained are $F = 0.4955$ N for the force and $T = 0.1207$ N cm for the torque.

Concerning the numerical behavior of the algorithm, between three and six iterations have been needed to convergence for a tolerance of the 0.1% in the relative $L^2$ norm. The iterative penalty method yields a value of order $10^{-8}$ for the norm of the incompressibility constraint, starting from a value of order $10^{-5}$

The computational cost of the simulation has been of 14.16 CPU seconds per iteration (solution of the Stokes problem, temperature equation and updating of the physical properties, including the calculation of the viscosity). The 68.77% of the total CPU time has been needed to solve the Stokes equations, the 19.64% for the temperature equation and the 8.69% for the pseudo-concentration transport equation.

## 4.6 Summary and conclusions

In this chapter we have given a complete description of the pseudo-concentration technique as a numerical method to track free surfaces of viscous incompressible flows. Besides the application of the techniques developed in the previous chapters applied now to the solution of its transport equation (Streamline Diffusion formulation, generalized trapezoidal rule to advance in time), some specific issues have been introduced here. The most important one is with no doubt the introduction of temporary holes on the walls in order to allow the air release, an essential ingredient for the success of this method. Two aspects have to be considered when one deals with temporary free wall nodes. The first is that one must check whether the fluid has touched the wall or not and, if so, to block the holes. The other is that the sign of the normal velocity has to be computed. If the velocity points into the computational domain, the temporary free node is part of the inflow boundary and thus the pseudo-concentration must be prescribed there. We have used a penalty technique to prescribe both the velocity and the pseudo-concentration when necessary.

Also related to the free surface tracking, some problems arising from the smoothing technique described here have been noticed. In particular, special reference has been given to the calculation of the distance from a certain point to the fluid front.

Concerning the solution of the Navier-Stokes and temperature equations when a free surface has to be simulated, a comprehensive description of the transient algorithm, its implications and some approximations has been given. Once again, the numerical methods developed previously have demonstrated their robustness for the problem considered in this chapter. The SD formulation and the iterative penalty method have been shown to be extremely effective.

The main interest of this chapter relies however on the numerical results that have been presented. They show that the pseudo-concentration technique is an effective method to track free surfaces with complicated shapes. If the physical properties of the fictious material are properly chosen, its motion does not affect that of the fluid that one wishes to analyse. It is observed that pressure gradients are rapidly dissipated in the region occupied by this fictious fluid. Moreover, an accurate thermal analysis can be performed. This is an aspect of vital importance in casting applications, the subject that has motivated the work presented in this chapter.

## References

[AI] H.J. Antúnez and S.R. Idelshon. Using pseudo-concentrations in the analysis of transient forming processes. *Engineering Computations* (to appear).

[AID] H.J. Antúnez, S.R. Idelshon and E.N. Dvorkin. Metal forming analysis by Fourier series expansion and further uses of pseudo-concentrations. *Computers & Structures* (to appear).

[Co] R. Codina. *A finite element model for the numerical solution of the convection-diffusion equation.* (CIMNE Monograph Num. 14, 1992)

[DGB] G. Dhatt, D.M. Gao and A. Ben Cheikh. A finite element simulation of metal flow in moulds. *Int. J. Numer. Meth. Engrg.*, vol. 30 (1990), 821–831

[DP] E.. Dvorkin and E.G. Petöcz. On the modelling of 2D metal forming processes using the flow formulation and the pseudo-concentration technique. In: *COMPLAS III.* Proceedings of the 3rd International Conference on Computational Plasticity, Barcelona, Spain (Pineridge Press/CIMNE, 1992).

[HN] C.W. Hirt and B.D. Nichols. Volume of fluid (vof) method for the dynamics of free boundaries. *J. Comput. Phys.*, vol. 39 (1981), 201–225

[Hu] J. Huetink. Anlysis of metal forming processes based on a combined Eulerian-Lagrangian finite element formulation. In: *Numerical analysis of forming processes.* J.F.T. Pittman, O.C. Zienkiewicz, R.D. Wood and J.M. Alexander (eds.) (Wiley, 1984).

[HS] W.S. Hwang and R.S. Stoehr. Molten metal flow prediction for complete solidification analysis of near net shape castings. *Materials Science Technology*, vol. 4 (1988), 240–250

[FCT] A. Fortin, D. Cote and P.A. Tanguy. On the imposition of friction boundary conditions for the numerical simulation of Bingham fluid flows. *Comput. Meth.*

*Appl. Mech. Engrg.*, vol. 88 (1991), 97–109

[LDD] Y.S. Lee, P.R. Dawson and T.B. Dewhurst. Bulge predictions in steady state bar rolling processes. *Int. J. Numer. Meth. Engrg.*, vol. 30 (1990), 1403–1413

[LUC] R.W. Lewis, A.S. Usmani and J.T. Cross. Finite element modelling of mould filling. In: *Finite elements in the 90's.* E. Oñate, J. Periaux, A. Samuelson (eds.) (Springer-Verlag/CIMNE, 1991)

[RA] P. Le Roy and P. Angibault. Remplissage d'un 1/2 moule sable par du Gallium: mesures, visualisations et comparaisons avec le calcul. *Direction de Méthodes Organes Mécaniques, RENAULT - Service 0968.* Note de Service N° 90/299.

[SW] T.J. Smith and D.B. Welbourn. The integration of geometric modelling with finite element analysis for the computer-aided design of castings. *Applied Scientific Research*, vol. 44 (1987), 139–160

[SFD] A. Soulaimani, M. Fortin, G. Dhatt and Y. Ouellet. Finite element simulation of two- and three-dimensional free surface flows. *Comput. Meth. Appl. Mech. Engrg.*, vol. 86 (1991), 265–296

[Th1] E. Thompson. Use of pseudo-concentrations to follow creeping viscous flows during transient analysis. *Int. J. Numer. Meth. Fluids*, vol. 6 (1986), 749–761

[Th2] E. Thompson. Transient analysis of metal forming operations using pseudo-concentrations. In: *Numiform 86.* Proceedings of the 2nd International Conference on Numerical Methods for Industrial Forming Processes, Göteborg, Sweden (A. Balkema, 1986).

[TS] E. Thompson and R.E. Smelser. Transient analysis of forging operations by the pseudo-concentration method. *Int. J. Numer. Meth. Engrg.*, vol. 25 (1988), 177–189

[WC] O. Wambersie and M.J. Crochet. Transient finite element method for calculating steady-state three-dimensional free surfaces. *Int. J. Numer. Meth. Fluids*, vol. 14 (1992), 343–360

[Zi] O.C. Zienkiewicz. Flow formulation for the numerical solution of forming processes. In: *Numerical analysis of forming processes.* J.F.T. Pittman, O.C. Zienkiewicz, R.D. Wood and J.M. Alexander (eds.) (Wiley, 1984).

[ZJO] O.C. Zienkiewicz, P.C. Jain and E. Oñate. Flow of solids during forming and extrusion: some aspects of numerical solution. *Int. J. Numer. Meth. Engrg.*, vol. 14 (1978), 15–38 (1978)

[ZOH] O.C. Zienkiewicz, E. Oñate and J.C. Heinrich. A general formulation for coupled thermal flow of metals using finite elements. *Int. J. Numer. Meth. Engrg.*, vol. 17 (1981), 1497–1514

[ZT] O.C. Zienkiewicz and R.L. Taylor. *The Finite Element Method.* Fourth Edition, vol. 1 (McGraw-Hill, 1989)